



**This electronic thesis or dissertation has been  
downloaded from Explore Bristol Research,  
<http://research-information.bristol.ac.uk>**

*Author:*  
**Mulakkal, Manu**

*Title:*  
**Development of Bio-inspired Cellulosic Smart Composites for Morphing**

**General rights**

Access to the thesis is subject to the Creative Commons Attribution - NonCommercial-No Derivatives 4.0 International Public License. A copy of this may be found at <https://creativecommons.org/licenses/by-nc-nd/4.0/legalcode>. This license sets out your rights and the restrictions that apply to your access to the thesis so it is important you read this before proceeding.

**Take down policy**

Some pages of this thesis may have been removed for copyright restrictions prior to having it been deposited in Explore Bristol Research. However, if you have discovered material within the thesis that you consider to be unlawful e.g. breaches of copyright (either yours or that of a third party) or any other law, including but not limited to those relating to patent, trademark, confidentiality, data protection, obscenity, defamation, libel, then please contact [collections-metadata@bristol.ac.uk](mailto:collections-metadata@bristol.ac.uk) and include the following information in your message:

- Your contact details
- Bibliographic details for the item, including a URL
- An outline nature of the complaint

Your claim will be investigated and, where appropriate, the item in question will be removed from public view as soon as possible.

# Development of Bio-inspired Cellulosic Smart Composites for Morphing

---



Manu Charles Mulakkal

A dissertation submitted to the University of Bristol in accordance with the requirements for award of the degree of Doctor of Philosophy (PhD) in the Faculty of Engineering, School of Civil, Aerospace and Mechanical

Engineering

July 2018

63,905



# ABSTRACT

---

Materials capable of self-actuation and architectures facilitating re-configuration are highly valued and profoundly sought-after for numerous applications in the fields of robotics, deployable and morphing structures. Here, a bio-inspired approach to realising a programmable materials system capable of morphing was explored and implemented with a specific focus on the sustainability of the material components.

The deployment of manually folded paper architectures using a fluid medium as the morphing stimulus presents a simple and inexpensive methodology capable of self-actuation. The materials-based as well as the stimuli parameters of this system were found to be programmable to control the actuation response of folded paper architectures. These results confirmed the suitability of cellulose as a cost effective and sustainable smart material capable of further functionalisation, and thus justified its consideration in developing programmable morphing systems. Following nature's inspiration, a strain-gradient mediated methodology for self-folding paper architectures was realised by locally patterning 'fold-lines' with a compatible hydrogel system. The architectures were designed to actuate along the principles of paper folding techniques such as origami and kirigami thus providing proven and elegant programmability and actuation attributes. As such, a novel methodology for self-folding and subsequent stimuli responsive deployment of cellulosic architectures was established.

The developments in 3D printing (3DP) technology allow the controlled placement of building materials in 3D space and this feature was harnessed to complement the strain-gradient mediated actuation of the cellulosic substrates. Therefore, a bespoke bio-inspired cellulose-hydrogel (carboxymethyl cellulose - CMC) composite for 3D printing was developed which can morph in the time domain (4D) according to the design rules developed from the previous chapters to mimic the actuation of responsive cellulosic structures observed in nature. Consequently, these responsive materials permit 4D printing - a process which pertains the transformation of 3D printed forms with respect to time. In this material system, the cellulose-hydrogel composite constitutes the programmable substrate and the CMC hydrogel acts as the localised component responsible for actuation. The strategy of drying and crosslinking following 3D printing results in a high fibre volume fraction cellulosic composites. The versatility of the materials and fabrication strategies demonstrated here enables the development of complex morphing architectures from computer aided design files with the tuneable material and structural features permitting programmability of the actuation responses. As such, this project demonstrates the realisation of sustainable cellulosic architectures capable of morphing via 4D Printing.



# DEDICATION

---

TO MY PARENTS CHARLES AND PHILOMINA

&

GOD



# ACKNOWLEDGEMENTS

---

A number of people have been crucial in the fulfilment of this project. First and foremost, I would like to express my sincere gratitude to my supervisor, Dr Annela Seddon for her support and guidance throughout this project. I would also like to thank Professor Richard Trask for introducing me to the topic for the XP project and also for his supervision during the first year of this project. I would also like to thank Dr George Whittell and Professor Ian Manners for their support during the XP and first year of this project. I would like to sincerely thank Dr Valeska Ting for her support and guidance during the crucial stages of this project and also for her supervision during the later stages of this project. I sincerely appreciate your flexibility and willingness to help.

I would like to acknowledge the ACCIS CDT for giving me the opportunity to pursue such an interesting and diverse project and the EPSRC for supporting my work. I would also like to thank Ms Jo Brooks for guiding me through the CDT application procedures and being patient with me throughout the process. I would like to acknowledge the support of Mr Giampaolo Ariu, Miss Laura Beckett, Mr Jamie Hartley and Mr Shashitha Kularatna from my cohort (DTC 13) during the course of this project. I would like to extend my gratitude to ACCIS lab support team, especially to Mr Ian Chorley and Dr Steven Rae for their assistance in the lab. I would like to thank the lab support teams at the School of Physics and School of Chemistry for providing me the training and access to the research facilities.

I would also like to acknowledge my friends in general for their understanding and patience for the lack of commitment from my part to the friendships, especially during the final stages of this project. I would like to thank my sister Dr Nitha Mulakkal for giving me an insight into the highs and lows of PhD research and helped me to mentally prepare for the life as a research student. Finally, I would like to thank my parents for supporting me throughout my education and other endeavours.





# AUTHOR'S DECLARATION

---

I declare that the work in this dissertation was carried out in accordance with the requirements of the University's Regulations and Code of Practice for Research Degree Programmes and that it has not been submitted for any other academic award. Except where indicated by specific reference in the text, the work is the candidate's own work. Work done in collaboration with, or with the assistance of, others, is indicated as such. Any views expressed in the dissertation are those of the author.

Manu C Mulakkal

July 2018



# DISSEMINATION

---

Aspects of the work presented in the thesis has been disseminated through a variety of papers and presentations.

## Journal papers

MC Mulakkal, AM Seddon, G Whittell, I Manners, RS Trask. 4D fibrous materials: characterising the deployment of paper architectures. *Smart Materials and Structures* 2016;25:095052. doi:10.1088/0964-1726/25/9/095052. (Published)

*MCM carried out the research, experiments and wrote the paper. GW and IM contributed to the discussions and experiment designs. AMS and RST provided supervision and corrected the initial drafts.*

MC Mulakkal, RS Trask, VP Ting and AM Seddon. Responsive Cellulose-Hydrogel Composites for 4D Printing. *Materials and Design* 160 (2018) 108–118 (Published)

*MCM carried out the research, experiments and wrote the paper. AMS and VPT provided supervision, checks and feedback on the initial drafts.*

## Conference papers

MC Mulakkal, RS Trask, and AM Seddon. Smart Cellulose-Hydrogel Composites for 4D Printing. 8th Conference on Smart Structures and Materials, SMART 2017 and 6th International Conference on Smart Materials and Nanotechnology in Engineering, SMN 2017

*MCM carried out the research, experiments and wrote the paper. RST checked the initial draft. AMS provided supervision, checks and feedback on the initial drafts.*

## Presentations

Smart Cellulose-Hydrogel Composites for 4D Printing. 8th Conference on Smart Structures and Materials, SMART 2017 (Oral presentation)

Creating folds: Origami inspired morphing. 6th Annual Conference of the CDT in Advanced Composites for Innovation and Science, 2017. (Oral and Poster presentation)

4D Fibrous Materials: Characterising the Deployment of Paper Architectures. 5th Annual Conference of the CDT in Advanced Composites for Innovation and Science, 2016 (Poster presentation)

Programmable deployment of origami architectures. 4th Annual Conference of the CDT in Advanced Composites for Innovation and Science, 2015. (Oral and Poster presentation)

Programmable deployment of origami architectures. University of Bristol Three Minute Thesis (3MT) Semi-finals, 2015. (Oral presentation)



# DATA AVAILABILITY STATEMENT

---

All data created during this research are openly available from the University of Bristol Research Data Storage Facility (RDSF) archive.

This data is also available from the following location:

[https://drive.google.com/open?id=12Po3UXcFGZgbafBHt163Cah\\_c7iq7loU](https://drive.google.com/open?id=12Po3UXcFGZgbafBHt163Cah_c7iq7loU)

All the raw data used to generate the results in this thesis are also available from the above location from folder titled 'Appendix'. These are organised chapter-wise and the link to this data is also included as an Appendix to this report



# TABLE OF CONTENTS

---

Chapter 1	Introduction.....	1
1.1	Background to nature-inspired smart composites .....	1
1.2	Composites: An overview .....	4
1.2.1	Composite reinforcements.....	7
1.2.2	Composite matrices.....	8
1.2.3	Significance of the reinforcement-matrix interface.....	8
1.2.4	Future of advanced composites .....	9
1.3	Morphogenesis manufacturing .....	9
1.4	Bio-inspiration .....	10
1.5	Smart materials .....	17
1.5.1	Response based classification of smart materials .....	18
1.5.2	Soft smart materials .....	20
1.5.2.1	Shape memory polymers.....	21
1.5.2.2	Shape changing polymers.....	22
1.5.2.3	Hydrogels.....	24
1.5.2.4	Hydrogel composites.....	26
1.6	3D and 4D printing .....	28
1.6.1	Shape memory materials-based approach to 4D printing.....	31
1.6.2	Expanding gels-based approach to 4D printing.....	34
1.6.3	Composites-based approach to 4D printing.....	36
1.7	Additive manufacturing with cellulose .....	38
1.8	Summary .....	39
1.9	Outline of the thesis .....	41
Chapter 2	Morphogenesis through folding – Potential of paper .....	44
2.1	Introduction .....	44





2.2	Characterisation of paper deployments.....	48
2.2.1	Materials .....	48
2.2.2	Paper Microstructure .....	49
2.2.3	Contact angle measurements of paper substrates.....	50
2.2.4	Shape selection .....	52
2.2.5	Actuation media .....	53
2.3	Fold Lines.....	55
2.4	Fold recovery upon drying.....	57
2.5	Factors affecting deployment.....	60
2.5.1	Microstructure .....	60
2.5.2	Temperature .....	63
2.5.3	Surfactants .....	65
2.6	Multi-layered composite paper systems .....	66
2.7	Reversible deployment through functionalisation .....	68
2.7.1	Thermoresponsive functionalisation of paper substrates .....	69
2.7.1.1	Materials .....	70
2.7.1.2	Substrate selection and preparation .....	70
2.7.1.3	Immobilisation of initiator on paper substrate.....	71
2.7.1.4	Grafting of N-Isopropylacrylamide from initiator functionalised substrate	71
2.7.2	Contact angle measurements of modified paper substrate .....	72
2.7.3	Actuation of functionalised paper substrates.....	74
2.8	Discussion and Conclusion .....	75
Chapter 3	Realising 4D architectures through strain differential.....	80
3.1	Introduction .....	80
3.2	Classification of folds in origami inspired stimuli responsive morphing.....	81
3.3	Significance of simplistic approaches in materials and fabrication .....	84
3.4	Harnessing volumetric changes in cellulosic hydrogels for morphing.....	88
3.4.1	Factors affecting fold creation on paper substrates.....	90



3.4.1.1	Substrate stiffness .....	90
3.4.1.2	Amount of gel per unit area .....	91
3.4.1.3	Distribution of hydrogel (spread) .....	93
3.4.1.4	Open area to be folded .....	94
3.4.1.5	Interface between the hydrogel and substrate .....	96
3.4.1.6	Strain potential of the gels .....	97
3.4.2	Dynamics of hydrogel dehydration and hydration .....	98
3.5	Examples of shrinking driven morphing on fibrous structures .....	99
3.5.1	Independent morphing response .....	100
3.5.2	Coupled morphing response .....	103
3.6	Potential of strain differential beyond hydrogel on paper systems .....	105
3.7	Discussion and Conclusion .....	105
Chapter 4	Cellulose – hydrogel composites for 4D Printing .....	108
4.1	Introduction .....	108
4.1.1	Cellulose as a smart material .....	109
4.1.2	Cellulose fibres .....	110
4.1.3	Enabling functional cellulose 3D printing .....	110
4.2	Development of hydrogel composite .....	112
4.2.1	Materials and formulation .....	112
4.2.2	Processing .....	113
4.2.3	Stability of hydrogel composites .....	116
4.3	Characterisation of material formulations .....	120
4.3.1	Rheology .....	120
4.3.1.1	Strain sweep .....	121
4.3.1.2	Frequency sweep .....	123
4.3.1.3	Shear rate .....	125
4.3.1.4	Stress ramp .....	126
4.3.2	Swelling ratio .....	128



4.3.3	Shrinking ratio .....	129
4.3.4	Force characterisation .....	132
4.3.4.1	Experimental set-up .....	133
4.3.4.2	Swelling force .....	135
4.4	Strain differential mediated morphing of cellulosic architectures .....	137
4.5	Discussion and conclusion .....	138
Chapter 5 Cellulosic composites and 4D transformations .....		142
5.1	Introduction .....	142
5.2	Enabling additive layer manufacturing (ALM) of cellulose .....	142
5.2.1	Specifications.....	143
5.2.2	3D Printer hardware .....	143
5.2.3	Design of paste extruder .....	145
5.2.4	Printer and extruder set up .....	148
5.2.5	Print results .....	149
5.2.6	4D printing of cellulosic composites.....	150
5.3	Characterisation of 3D printed cellulosic composites .....	152
5.3.1	Microscopy .....	152
5.3.2	Contact angle measurements of 3D printed formulations .....	153
5.3.3	Fibre alignment in-print.....	155
5.3.4	Mechanical characterisation of printed composites – Tensile testing .....	158
5.3.4.1	Test standards .....	159
5.3.4.2	Tensile testing of composite samples.....	160
5.3.4.3	Sample details .....	160
5.3.4.4	Sample preparation.....	162
5.3.4.5	Test details .....	163
5.3.4.6	Data post-processing.....	163
5.3.4.7	Results .....	165
5.4	Shape transformations .....	167



5.4.1	Connected concentric annuli.....	168
5.4.2	Connected annulus-coil.....	169
5.5	Discussion.....	170
Chapter 6	Conclusions and Future work.....	173
6.1	Conclusions.....	173
6.2	Suggestions for future work.....	176
6.2.1	Improved material strategies.....	176
6.2.2	Sequential actuation.....	177
6.2.3	Extruder upgrades for reliable and integrated multi-material printing.....	177
6.2.4	Structures with increased complexity in form and actuation response.....	179
References	.....	180
Appendix	.....	193
A.1.	Optimisation of paste extruder and print settings to for 3D printing.....	193
A.1.1.	Introduction to stepper motors.....	193
A.1.2.	Optimisation of print parameters.....	194
A.2.	Raw data.....	195





# LIST OF FIGURES

---

Figure 1.1: (top row) Constituents in the composite. (bottom row) Typical arrangement in a composite.....	6
Figure 1.2: Hierarchical structure of (a) bones (top row). Images adapted from [20] with permission from Springer Nature. (b) Skeletal muscle (bottom row). Images adapted from [21] under Creative Commons Attribution License 4.0 from OpenStax.....	13
Figure 1.3: Examples of actuation in plant kingdom. (Top row) Pinecone; Open (dry) to closed (wet); Differential cellulose fibril winding in the top and bottom layers results in anisotropic swelling upon water absorption resulting in the closure of scales. (Bottom row) Touch-me-not plant ( <i>Mimosa pudica</i> ); Mechanical stimuli induces a signal potential towards pulvinus which in turn initiate action potential and movement of ions from extensor cells to flexor resulting in the loss of turgidity through diffusion of water out of the cells and results in dropping of pulvinus and closing of leaves. ....	15
Figure 1.4: Structure of cellulose.....	16
Figure 1.5: (top row) Transformation of SMP (shape memory polymer) composite from (a) flat to (b) 3D configuration. (bottom row) (c) Schematic of detailed hinge design as fabricated and after activation. Images adapted from [51] with permission from IOP Publishing. ....	21
Figure 1.6: Morphing responses of liquid crystalline polymer films (top) to linearly polarised light: (a) Polymer film as fabricated. (b) Bending towards the incident light after irradiated with light polarised in $0^\circ$ . (c) Recovered flat film following irradiation with visible light of wavelength greater than 540 nm. (d) Bending response to $-45^\circ$ polarised light. (e) Response to $-90^\circ$ polarised light. (f) Response to $-135^\circ$ polarised light. Images adapted from [52] with permission from Springer Nature. (bottom) to uniform heating. (g) Representative photograph of film with +1 topological defect arranged in 9 voxels as observed between crossed polarisers. (h) Orientation of the directors around the defect. (i) Polymer film as fabricated. (j) Actuation response after heating. Images adapted from [53]with permission from The American Association for the Advancement of Science. ....	23
Figure 1.7: Examples of 4D printed transformations. (a) Linear expansion of a 3D printed shape upon swelling in water. Image adapted from [94] and reproduced under Creative Commons Attribution-NonCommercial-NoDerivatives 4.0 International License. (b) 1D-2D transformation upon swelling in water. (c) 1D-3D transformation upon swelling in water. Images adapted from [89] with permission from John Wiley and Sons. (d) 2D-2D transformation of square lattice structure upon heating and cooling resulting in the release of internal strain. (Scale bar = 20 mm). Image adapted from [104] and reproduced under Creative Commons Attribution 4.0 International License. (e) 2D-3D transformation of multi-material sheet into a box upon heating. Image adapted from [101] and reproduced under Creative Commons	

Attribution 4.0 International License. (f) 3D-3D transformation of cuboid by active preferential swelling in solvent. (Scale bar = 10 mm). Image adapted from [108] and reproduced under Creative Commons Attribution 4.0 International License. .... 30

Figure 1.8: Sequential folding of programmed SMP component. (a) Schematic of the component as printed indicating the hinge locations. This was followed by the programming stage of coil being flattened. (b) Response of a control strip with uniform hinges to heating by submersion in water at 90 °C. (c) Response of the sample with graded hinges upon heating by submersion in water at 90 °C. Image adapted from [101] and reproduced under Creative Commons Attribution 4.0 International License. .... 32

Figure 1.9: Actuation response of FFF printed spring demonstrating shape memory effect. (a) The spring as printed. (b) After the programming step of deforming at elevated temperature followed by cooling. (c) Recovered shape after heating by immersion in hot water at at 70 °C. (Scale bar = 10 mm). Image adapted from [103] with permission from ACS Publications. .... 33

Figure 1.10: Formation of 3D petal architecture from planar sheet. (a) The initial planar shape of composite sheet. (b) Intermediate shape of the petal architecture when placed on a hot-plate at 105 °C (c) The final 3D petal architecture after cooling. (Scale bar = 20 mm). Images adapted from [104] and reproduced under Creative Commons Attribution 4.0 International License. .... 34

Figure 1.11: Detailed hinge design of PolyJet printed morphing shapes. (a) Hinge as printed. (b) Deformed hinge after swelling in water. Image adapted from [94] and reproduced under Creative Commons Attribution-NonCommercial-NoDerivatives 4.0 International License. ... 35

Figure 1.12: Actuation of cuboid with magnetically aligned platelets upon swelling in a solvent (Scale bar = 10 mm). Image adapted from [108] and reproduced under Creative Commons Attribution 4.0 International License. .... 36

Figure 1.13: Morphing response through the alignment of particulates in a composite gel. (a) Schematic showing the shear induced alignment of cellulose nanofibrills (CNF) as it exit the deposition nozzle.(b) A flower architecture as printed through bio-4D printing. (c) Morphed state of the printed form after swelling in de-ionised water. (d) Series of photographs showing the morphing response from flat to 3D over time when immersed in water. (White scale bar = 5mm; yellow scale bar = 2.5 mm). Image adapted from [93] with permission from Springer Nature. .... 37

Figure 2.1: Examples of folding in nature. (a) Schematic (Side view) of flat trilaminar embryonic disk forming embryo. (b) Closed and open petals of Bindweed (*Calystegia sepium*). Image adapted from [118] (c) Formation of mountain folds through the movement of tectonic plates. Image adapted from Wikipedia under GNU Lesser General Public License. (d) Stowed away and deployed wing of Rove beetle (*Cafius vestitus*) [119]. .... 44

Figure 2.2: (a) Basic origami folds. (b) Miura-ori basic unit and corresponding fold pattern. (c) Folded Miura-ori (top view). (d) Folded Miura-ori pattern (side view). (Scale bar = 25 mm). 45

Figure 2.3: Examples of origami inspired self-actuation. (a) Actuation of a Ni-rich TiNi shape memory stent at 319 K. Image adapted from [122] with permission from Elsevier. (b) Self folding origami robot: [i] composite hinge scheme; PSPS-pre-stretched polystyrene, [ii] flat configuration and [iii] folded configuration. Image adapted from [51] with permission from The American Association for the Advancement of Science. (c) Actuation of 4D printed (rigid phase + hydrophilic) polymeric box. Image adapted from [89] with permission from John Wiley and Sons. (d) Pneumatic actuation of locally reinforced silicone kirigami cell. Image adapted from [128] with permission from IOP Publishing. ....	47
Figure 2.4: Sequential deployment of hierarchical paper folds in water (Scale bar = 10 mm) – Flotilla [132].....	48
Figure 2.5: Microstructure of paper types. (a) Printer paper 90 gsm, (b) Lokta 60 gsm, (c) Lokta 30 gsm and (d) Sekishu 30 gsm. (White scale bar = 10 mm; Green scale bar = 50 $\mu$ m; Red scale bar = 10 $\mu$ m). ....	50
Figure 2.6: Contact angle.....	51
Figure 2.7: Stable contact angle of different paper types during droplet absorption as a function of time.....	52
Figure 2.8: Deployment sequence (a-d) of the folded profile of Sekishu paper. (Scale bar = 15 mm).....	53
Figure 2.9: Saturation in printer paper 90 gsm and subsequent deployment. (a) Development of low resistance flow paths. (b) Close-up view. Blue arrows indicate deployment direction. (c) Cracks formed in printer paper as the consequence of folding. (Scale bar = 20 $\mu$ m).....	55
Figure 2.10: Folding in handmade paper types -Sekishu 30 gsm. (a) Before folding. (b) Fold scheme. (c) Fold line visualisation and (d) close-up of outside of the fold line (Gold scale bar = 100 $\mu$ m and Green scale bar = 50 $\mu$ m). ....	57
Figure 2.11: Shape recovery after deployment in a water bath at room temperature and drying overnight. (a) Printer paper 90 gsm, (b) Lokta 60 gsm, (c) Lokta 30 gsm and (d) Sekishu 30 gsm. (Scale bar = 15 mm).....	58
Figure 2.12: (Top row) Twist and recovery observed in five printer paper samples after drying following deployment – top view. (Bottom row) Planar deformations in handmade samples after drying following deployment – side view. (Scale bar = 15 mm).....	59
Figure 2.13: Recovery of sample architectures after deployment. (a) Printer paper 90 gsm, (b) Lokta 3x30 gsm and (c) Lokta 30 gsm. (Scale bar = 15mm). ....	60
Figure 2.14: SEM image of (a) dry fibres and (b) fibres after hornification at 500x magnification showing the effects of hornification. (Scale bar = 50 $\mu$ m).....	62

Figure 2.15: Schematic of diffusion dominant water transport in fibre capillaries. ....	63
Figure 2.16: Variation of 1 <sup>st</sup> actuation time at a range of temperatures. The insert image shows an enlarged snapshot of the 1 <sup>st</sup> actuation time of the handmade specimens below 55 °C. ....	64
Figure 2.17: Variation of 2 <sup>nd</sup> actuation times at a range of temperatures. ....	65
Figure 2.18: Variation of actuation time for corresponding % volume concentration of surfactants (a) Printer paper 90 gsm (2 <sup>nd</sup> actuation) (b) Lokta 30 gsm (1 <sup>st</sup> actuation). ....	66
Figure 2.19: Flow characteristics: (a) Lokta 30 gsm; (b) Printer paper 90 gsm; (c) Lokta 3 x 30 composite. (Scale bar = 15 mm). ....	67
Figure 2.20: Comparison of 1 <sup>st</sup> actuation time and 2 <sup>nd</sup> actuation time for different paper types. (The average and standard deviation is of 5 specimens). ....	68
Figure 2.21: Schematic of ATRP reaction carried out on paper substrate. ....	69
Figure 2.22: FTIR spectra of the paper types and the close-up of OH stretch region is shown in insert. ....	70
Figure 2.23: FTIR spectra of Sekishu 30 gsm (Control) and Sekishu 30 gsm grafted with PINAAPm. ....	72
Figure 2.24: SEM images of Sekishu 30 gsm paper (a) before and (b) after grafting with PNIPAAm. (Scale bar = 50 µm). ....	72
Figure 2.25: Experimental set-up for contact angle analysis at elevated temperatures. ....	73
Figure 2.26: Contact angle measurements for polymer grafted samples above and below the LCST along with control. ....	74
Figure 3.1: Classification of fold and related terms with their characteristic features. ....	82
Figure 3.2: Examples of morphing responses from open literature; (a) Morphing of pre-stretched polystyrene (Shrinky-dinks) patterned with black ink due to localised heat absorption. Image adopted from [124] with permission from Royal Society of Chemistry (b) Morphing response of a UV crosslinked composite (regions of primary gel and binary gel achieved by the use of photo mask) hydrogel sheet to the stimuli of heat or iconicity. Image adopted from [166] with permission from Springer Nature (c) Formation of a helix through ionoprinting on an interpenetrating polymer network hydrogel and morphing response above and below LCST in 0.1 M LiCl solution. Image adopted from [167] and reproduced under Creative Commons Attribution 4.0 International License. (Scale bar = 10 mm). ....	86
Figure 3.3: (top) Schematic of folding with hydrogels; (bottom) Examples of crease and bend fabricated as per the schematic. (Scale bar = 10 mm). ....	89

Figure 3.4: Actuation response of different paper substrates to same amount of hydrogel. (Scale bar = 10 mm).....	90
Figure 3.5: Relationship between amount of hydrogel and resulting fold angle. (Scale bar = 10 mm).....	91
Figure 3.6: Fold angle as a function of relative amount of hydrogel confined to the fold line. ....	92
Figure 3.7: Effect of Hydrogel distribution (spread) in folding. (Scale bar = 10 mm).....	93
Figure 3.8: Effect of fold region width (hydrogel spread) and facet width on folding.....	94
Figure 3.9: Fold angle as a function of facet width and gel spread. Method of determining fold angle is shown in insert. ....	96
Figure 3.10: Hydrogel-paper interfaces. (a) Separated after drying and crosslinking. (b) Separated after saturation of crosslinked samples in water. (Scale bar = 10 mm).....	96
Figure 3.11: Effect of shrinking/swelling potential on realising folds (a) Fold at room temperature (b) Increased folding after drying at elevated temperatures (ET) (c) Fold deployed to flat configuration once fully immersed in water (d) Further unrestricted swelling results in transverse fold.....	98
Figure 3.12: Schematic of independent morphing response of shrinking hydrogels on paper. Arrows indicate membrane forces of shrinking.....	100
Figure 3.13: (Top row) Schematic of helix and its geometrical parameters. (Bottom row) Schematic of fold line and geometrical parameters of paper strip to fold a helix.....	101
Figure 3.14: Programmable self-folding helices. Geometric parameters such as fold line angle ( $\theta$ ) and spacing (a) are varied to create helices of varying diameter (D) and length (L). Images are presented in black and white to enhance the visibility of gel placements on fold lines. (Scale bar = 25 mm). ....	102
Figure 3.15: Morphing of annular strip. (a) Schematic of paper annulus. (b) Morphed saddle after drying of the hydrogel at room temperature (21°C). (c) Front view (d) Side view. (Scale bar = 10 mm). ....	102
Figure 3.16: Schematic of Coupled morphing response.....	103
Figure 3.17: Hydrogel shrinking initiated pop-up morphing response. Transformation of (a) flat floral configuration into (b) pop-up configuration in response to the stimuli of heat. (c) Individual unit isolated from the floral architecture. (d) Resilient individual unit supporting mass much greater than itself. (e) Cut-open square pillow structure showing locked in curvatures after transformation. (Scale bar = 30 mm). ....	104

Figure 4.1: Schematic of hierarchical structure of cellulose fibres. (Scale bar = 100 $\mu$ m). ...	109
Figure 4.2: (top) Processing of cellulose fibres from pulp linters. (a) Pressed pulp linters as received. (b) Pieces of pulp linters saturating in reagent grade water prior to breaking up and (c) scraped up pulp in the process of drying at room temperature. (bottom) Schematic of the preparation of hydrogel composite and (d) final mix shown in insert. (Scale bar = 20 mm).	114
Figure 4.3: Pulp-CMC composite films illustrating the improvements in pulp dispersion as a result of optimised mixing strategies: (a) Mechanical agitation with spatula, (b) Ultrasonication, (c) Shear mixer and (d) Non-contact planetary shear mixer. (Scale bar = 10 mm). .....	115
Figure 4.4: Self-crosslinking induced charring (a) before crosslinking (b) after crosslinking at 180 C for 30 minutes (c) after swelling in reagent grade water for 24 hours. (Scale bar = 20 mm). .....	117
Figure 4.5: Cracking observed in PAA crosslinked samples after swelling. (Scale bar = 20 mm). .....	119
Figure 4.6: Amplitude sweep data showing (top) Elastic modulus ( $G'$ ) and (bottom) phase angle ( $\delta$ ) as the function of shear strain.....	123
Figure 4.7: Frequency sweep data showing (top) Elastic modulus ( $G'$ ) and (bottom) phase angle ( $\delta$ ) as a function of frequency.....	124
Figure 4.8: Steady state (top) shear viscosity ( $\eta$ ) and (bottom) shear stress ( $\tau$ ) as a function of shear rates. ....	126
Figure 4.9: Stress ramp plots showing Yield Stress of formulations at peak viscosity.....	127
Figure 4.10: Typical thermal data of the samples indicating distinct weight loss regions (0-1, 1-2 and 2-3) during the analysis steps. ....	130
Figure 4.11: TGA curves (a) Weight (%) expressed as function of time. (b) First derivative ( $d(TG)/dt$ ) of weight (%) expressed as a function of temperature.....	131
Figure 4.12: Schematic of experimental set-up for force characterisation using rheometer with close-up of the top-plate and sample is shown in insert. ....	133
Figure 4.13: Series of images showing the sample set-up for characterising swelling force (a) empty petri dish (b) with glue applied in the middle. (c) Final set-up with a Composite+Clay+CA sample fixed at the base of petri dish. (Scale bar = 10 mm). ....	134
Figure 4.14: Typical swelling force response over time for the investigated formulations. Each chart shows the response of one sample. ....	136

Figure 4.15: (top) Schematic of flower architecture fabrication (bottom) Actuation of flower architecture. (a) During drying at RT (21 °C) (b) dried at RT –initiation (c) after drying at elevated temperature– fixing shape (d) deployed back to flat configuration in water at RT. (Scale bar = 20 mm).....	138
Figure 5.1: (a) Cartesian style Prusa i3 MK2S (b) A generic delta-style 3D printer. (Image adapted from source: <a href="http://www.alibaba.com">www.alibaba.com</a> ).....	143
Figure 5.2: Schematic of MIni-RAMBo v1.3 a. (Image adapted from source: <a href="http://www.matterhackers.com">www.matterhackers.com</a> ).....	144
Figure 5.3: (a) Direct mount belt driven Universal Paste extruder. Image adapted from [190]. (b) Off-axis direct driven syringe extruder. Image adapted from [191] and reproduced under Creative Commons Attribution-NonCommercial-ShareAlike 2.5 Generic License. ....	145
Figure 5.4: Paste extruder. (a) Key components, (b) loaded with syringe containing hydrogel composite, (c) female luer barb lock and PTFE tubing assembly, (d) male luer nozzle assembly and a selection of nozzle sizes, and (e) Push-fit nozzle assembly into the housing attached to the X carriage. ....	146
Figure 5.5: 3D printer and extruder set-up; Extruder housing is shown in insert.....	147
Figure 5.6: 3D printing of a cylinder (dimensions in mm) using paste extruder. (a) CAD design with dimensions. (b) Sliced layer by layer profile of the cylinder. (c) 3D printing of the cylinder using Composite+Clay+CA formulation. ....	150
Figure 5.7: Fabrication of petal architecture. (a) Generated print-path from CAD model. (b) 3D printed form. (c) Drying at room temperature initiating morphing. (d) After crosslinking to maximise and fix the 3D shape. (e) Deployed to flat configuration upon hydration and (f) drying (dehydration) recovers the 3D petal shape. The side views are shown in inserts. (Scale bar = 10 mm). ....	151
Figure 5.8: Microscope images of 3D printed specimens. (a)Single extrusion line of Composite+Clay+CA (1-layer). (b) Overlapping lines of Composite+Clay+CA (1-layer) and (c) Gel+CA laid on top of Composite+Clay+CA defining fold line. (Scale bar=200 µm).....	152
Figure 5.9: Example of substrate swollen into the droplet for Gel+CA. ....	153
Figure 5.10: Contact angle of the substrates investigated in this study. ....	154
Figure 5.11: Schematic (top down view) of 3D printer bed and principal printing direction relative to the nozzle movement. (Insert) Microscopic image (10x) of the 3D printed cellulose-hydrogel composite line. ....	156
Figure 5.12: Directionality histograms for the various nozzle diameters investigated showing the dominant alignment direction and the relative amount. ....	158



Figure 5.13: (top row) Test specimen dimensions as per ASTM D638 Type V (dimensions in mm). (bottom row) Print-path and stacking sequence of the samples fabricated for each set. .... 162

Figure 5.14: Samples before being tested to failure in tension. (a) Longitudinal orientation, (b) Transverse orientation and (c) Symmetric cross-ply orientation relative to print direction. (Scale bar= 10 mm)..... 162

Figure 5.15: Samples after testing to failure in tension. (a) Longitudinal orientation, (b) Transverse orientation and (c) Symmetric cross-ply orientation relative to print direction. Highlighted are the discarded samples as they failed to meet the validation criteria. (Scale bar = 10 mm)..... 166

Figure 5.16: Connected concentric annuli. (a) CAD with blue lines indicating curved fold line. (b) 3D printed architecture after drying and crosslinking. Morphing response when submerged in water (c) Side view and (d) Top view. (Scale bar = 10 mm). .... 168

Figure 5.17: Connected annulus-coil. (a) CAD with blue indicating fold lines. (b) Slicer generated print path for the fold lines (dark blue - extruding moves; green - non-extruding moves) (c) 3D printed architecture after drying and crosslinking. Morphing response when submerged in water (d) Side view and (e) Top view. (Scale bar = 10 mm). .... 170

Figure 6.1: Schematic of suggested multi-material paste extrusion set-up with finer deposition. (a) Visualisation of the print-head with Prusa MK2S (b) close-up view of the print-head housing motor and deposition nozzle (c) cross-section view of the print-head showing the extruder chamber during multi-material printing with an empty chamber shown in insert..... 178

Figure A.1: Internal components of a generic stepper motor showing the phases and coil windings - Front view. (Image adapted from source: [www.pololu.com](http://www.pololu.com)) ..... 194



# LIST OF TABLES

---

Table 2.1: Summary of paper type actuation in different liquid mediums at room temperature (25 °C) .....	54
Table 2.2: Average recovery angle in printer paper for folds 1-6 .....	58
Table 2.3: 1 <sup>st</sup> and 2 <sup>nd</sup> actuation times for different paper types at R.T (25 °C) .....	62
Table 2.4: Summary of multi-layered paper composites .....	67
Table 2.5: Actuation times for single fold of PNIPAAm grafted paper .....	75
Table 4.1: Sample nomenclature and respective formulations .....	121
Table 4.2: Yield Stress of the formulations .....	128
Table 4.3: Equilibrium swelling ratio of formulations with CA after crosslinking.....	129
Table 4.4: Summary of thermal analysis results .....	131
Table 4.5: Summary of swelling force generated by the formulations after an hour .....	135
Table 5.1: Aligned direction of the cellulose fibres and the amount of alignment for different nozzle diameters.....	157
Table 5.2: Tensile testing results.....	165
Table A.1: Summary of G-codes used and its function .....	194





---

## Chapter 1 Introduction

---

### 1.1 Background to nature-inspired smart composites

Despite the multitude of scientific and technological advances since the discovery of fire, humans have never managed to successfully alleviate the associated risks and consequences of that development. There can be no doubt that the advancements especially since the second industrial revolution of the 19<sup>th</sup> century have made our lives more comfortable and easier. Innovations that not just benefitted the growth and prosperity of some communities or countries but transformed the way we live across the globe are plentiful. However, it is hard to deny that the innovations which lead to these developments were often carried out with less regard for the environment, natural resources, future generations and ultimately our planet. In the wake of strong evidence implying polluted habitats, depleting natural resources and ailing planet, we must place nature at the centre of our efforts for further development. Nature had always inspired the creative minds and its influence in the fields of science and arts are evident. Perhaps the solutions to aforementioned challenges could also be drawn from nature and its synergy with science and arts.

Justifiably, there is a growing trend among researchers to seek inspiration from nature not just to solve modern-day challenges but also to complement and enhance the prevailing technological feats. After all, nature has indeed perfected its design solutions over billions of years through adaptation and evolution. Nature's solutions to the challenges of life, sustenance and survival are characterised by its efficiency through multi-functionality and smart design (through evolution) and has endured the test of time. In comparison, human solutions lack the simplicity in materials and the complexity in functionality of natural counterparts. A typical example would be a human solution for transportation which consists of discrete systems for sensing, power, transmission and movement without sufficient coherence amongst them. A wider range of materials with varying properties are required to realise motion and integration between these sub-systems are not optimal compared to the standards observed in biological world enabling the same function. It is apparent that in nature, there is a positive synergy between form, functionality and materials, whilst utilising a smaller palette of materials than humans. Scientists are actively considering nature's solutions to solve modern day challenges in an efficient and effective manner. Such efforts are broadly classified under bio-inspiration and bio-mimicry. Synthetic systems leave a lot of to be desired such as integrated sensing, self-healing and stimuli responsive actuation which are the hallmarks of biological systems. Shape transformations or morphing in biological world

particularly in the plant kingdom are of great interest as they embody multiple useful shape configurations that can be passively activated. For example, the opening and closing of pinecones and the seed burial mechanisms in wheat awns requires no energy expenditure from the organisms [1,2] but are regulated through the synergy between constituent materials, their arrangement and interaction with the environment. Such levels of operational independence are highly desirable for any system as it can lead to self-sustainable structures, eliminating the need for external or embedded power sources and associated sub-systems to realise certain functionalities. Another crucial feature to be desired from nature which should be central to bio-inspiration and bio-mimicry is the low environmental impact of such systems throughout their realisation, operational cycle and beyond. This feature will ensure that the future generations can also enjoy the merits of the technologies developed today rather than be adversely affected by them.

Unlike metallic structures, modern composite structures are inspired by the plant kingdom such that strength and stiffness are present in regions that require them the most to realise a viable structure. For example, plants can grow high and branch out wide without the need for considerable vertical supports through local control over reinforcing elements and the strength and stiffness tailoring approaches utilised in advanced fibre reinforced composites captures the same concept. In addition to novel battery and kinetic energy-recovery technologies, fibre reinforced composites are heralded as the solution to greater fuel efficiencies and consequently lesser emissions and pollutants from combustion in automobiles. Currently, carbon fibre reinforced composites find application in automotive, aerospace and niche sports industries. There is a push by the composites industry to widen its market share to a variety of applications for the obvious benefits of specific strength and stiffness properties; additionally, in the hope that economies of scale will drive the current production costs down. Traditionally, carbon fibres and its supporting matrix materials are made from unsustainable fossil fuel derived monomers. The process of converting carbon fibre precursors to the final product is also energetically very demanding. If widely adopted, the environmental cost of producing and recycling carbon fibre composites is very high, perhaps even to offset the aforementioned efficiency gains. Advanced composite materials still lack integrated functions like sensing, self-healing, movement and growth that define biological systems. The recyclability of the modern composite materials is currently limited and their potential impact on the environment due to their wider adoption in their current form will be adverse. Currently, material systems capable of meeting multiple requirements (structural or functional) on demand does not exist and there is a growing interest among

researchers in developing novel material systems with such capabilities. Multi-functionality in general can lead to improved overall system efficiencies minimising or eliminating the need for auxiliary sub-systems and as such there have been numerous approaches in imparting properties such as sensing and self-healing to advanced composites. However, in most cases these functionalities currently being investigated and developed are lacking in terms of eco-friendliness mainly due to the additives or reactions required to impart and integrate these added functionalities into the host materials. Unfortunately, this holds true even for non-structural materials (*i.e.* soft materials). Consequently, there is a real need for sustained and focused research action to develop multi-functional materials with minimum ecological footprint.

Spatial arrangement of functional building blocks in a pre-defined manner is crucial to achieving multi-functionality in nature. Growth as a manufacturing process is key to achieving this multi-functionality as it enables controlled placement of building blocks following the design embedded in DNA and develop essential attributes influenced by the internal and external environments. Such control of microstructure which is imperative for multi-functionality cannot be achieved by today's top down manufacturing processes, whereas, additive manufacturing processes demonstrate immense potential in the controlled placement of multiple materials in 3D space for fabrication. Together with novel smart material systems, additive manufacturing processes could be developed to realise structures that emulate biological systems with regard to integrated sensing, repair, growth and shape transformations. 4D printing is a relatively new approach to manufacturing transformable materials utilising 3D printing technologies with the 4<sup>th</sup> dimension being the time domain. There is huge potential for developing a manufacturing philosophy emulating growth through 4D printing where the functional materials (with low ecological footprint) can be precisely configured in 3D space to fabricate forms or structures. Furthermore, additive manufacturing processes has the potential to produce less waste and offers control of geometrical features not just on the exterior but on the inside of a structure as well.

The significance of arts in science has been emphasised by the likes of Leonardo da Vinci and Albert Einstein with the latter going on to remark the following in 1923; *"After a certain high level of technical skill is achieved, science and art tend to coalesce in esthetics, plasticity, and form. The greatest scientists are always artists as well"* (Einstein Archive 33-257). Even the sheer observation and examination of art than the act of creating can strengthen and develop one's scientific intuition. Whilst an artist captures the beauty and form of nature in canvas or in clay, a scientist tries to understand its secrets and disseminate that knowledge. An engineer



then seeks to incorporate the knowledge of nature's intricacies, its form and function into new creations that are in unison with the environment. Nature's influence on arts and science is undeniable and thus parallels can be made between the two. There are plenty of examples where the distinction between an art form and scientific invention can no longer be made as the boundaries were amalgamated in realising something unique. Origami, the age-old art form of folding paper into recreational shapes is a recent example of how art can influence science, especially mathematics and engineering. This applies to kirigami as well, a variant of origami where cutting of the paper is permitted. The principles of these folding techniques are applied to deployable structures, where antagonistic features of compactness and maximum surface typically needs to co-exist [3,4] and to morphing structures, where switching between multiple physical configurations leads to performance advantages [5]. Origami inspired engineering examples can be found across the length scales. This is a symbiotic relationship where mathematics applied to origami enables creation of complex forms on paper that were not formerly realised. There are software programs (such as Treemaker [6], Freeform Origami [7], Origamizer [8], and Rigid Origami Simulator [9]) that generate fold patterns for any given 3D model transcribed to a given sheet of paper. For morphing or deployable applications, origami and associated folding techniques such as kirigami offer efficient shape configurations and proven actuation pathways that are simple as well as elegant. The actuations or motions are realised differently in comparison to the traditional types of motions that we are familiar with. This artistic practice when combined with the power of mathematics offers a powerful tool for engineers to simultaneously realise system properties that were deemed antagonistic in nature such as compactness and maximum surface area. This strong relationship's proven outcomes are systems that are not only efficient by being functional at different spatial configurations but also pleasing aesthetically.

## 1.2 Composites: An overview

Composites can be defined as a material that consists of two or more discrete phases within itself. Thus, the first use of composite materials can be accredited to the Mesopotamians in 3400 BC who used plywood prepared by gluing thin pieces of wood together. Egyptians are credited with combining wet mud and straw to create bricks for buildings *circa* 1500 BC. This particular method of construction is still in use today across numerous parts of the world. The modern era of composites began in the 1900's following the discovery of polymers and glass fibres. Since the discovery of carbon fibres and improved plastics in the 1970's, composites began to gain traction as improved replacements for metals. Currently, composite materials

---

find increasing application in aerospace, marine, defence, automotive, energy, sports and other markets.

Composite materials are sought for their specific properties which means they often have lower weight penalty compared to other material options in meeting a specific requirement. Weight savings leads to greater efficiencies and ultimately results in lower overall costs. Composites achieve their unique properties by virtue of their constituent parts namely reinforcements and the matrix. Reinforcements are the structural and load carrying component whereas the matrix holds them in place. A key feature of composites unlike engineered alloys is that their constituents do not dissolve in each other and retain their form in final part. With regard to modern composites, the reinforcements used are generally high aspect ratio fibres such as carbon, glass or aramid fibres as opposed to particulates or reinforcements of other geometries such as spheres owing to structural motives. The reinforcement and matrix are not limited to polymers, but metals and ceramics are also used in composite form for some niche applications such as high temperature components in engines and heat-shields in spacecrafts.

The desire for a sustainable way of living and to reduce the over-dependency on petroleum products have resulted in a major shift in looking at the raw materials required to produce chemicals. In some cases, long sighted policies and much required initial investments have resulted in the development of thriving and viable bio-based chemicals industries. Scott *et al.* reports numerous bio-resources and their platform chemicals which can be used to produce higher value derivatives [10]. Fibres and matrix polymers derived from sustainable bio-mass are also gaining interest among industry and academic researchers alike. These bio-composites are seen as a part-solution to the challenges of recyclability and sustainability with regard to traditional advanced composite components. The current European Union's End of Life Vehicle (ELV) directive requires manufactures to reuse, recover or recycle up to 95 % of end of life vehicles and bio-composites are seen as the ideal candidate to offer the benefits of composites whilst meeting the directives targets. This has led to an increased use of bio-composites and innovations in the field as more and more Original Equipment Manufacturers (OEM) are taking a keen interest in bio-composites for automotive sector [11]. As a result, bio-composites (both bio-based reinforcements and matrix polymers) are emerging as a practical alternative to glass fibre composites [12]. The research into converting bio-derived pre-cursors as opposed to petroleum based precursors into carbon fibres is also gathering momentum and could reduce the environmental impact of advanced composites [13,14]. Nanocomposites are an emerging class of composite materials where the reinforcements have at least one of

its dimensions in the order of  $10^{-9}$  m. These reinforcements can be nano-clay, carbon nanofibers and carbon nanotubes. Their superior mechanical properties are attributed to the lack of defects and greater surface area of the nano-scale reinforcements and their interaction with the matrix phase. Apart from improved mechanical properties, inclusion of appropriate functional nano phase materials could also lead to improved thermal, electrical, optical and magnetic properties of the composites. As a result, nanocomposites are extensively looked at to impart the aforementioned multi-functional properties to the composites.

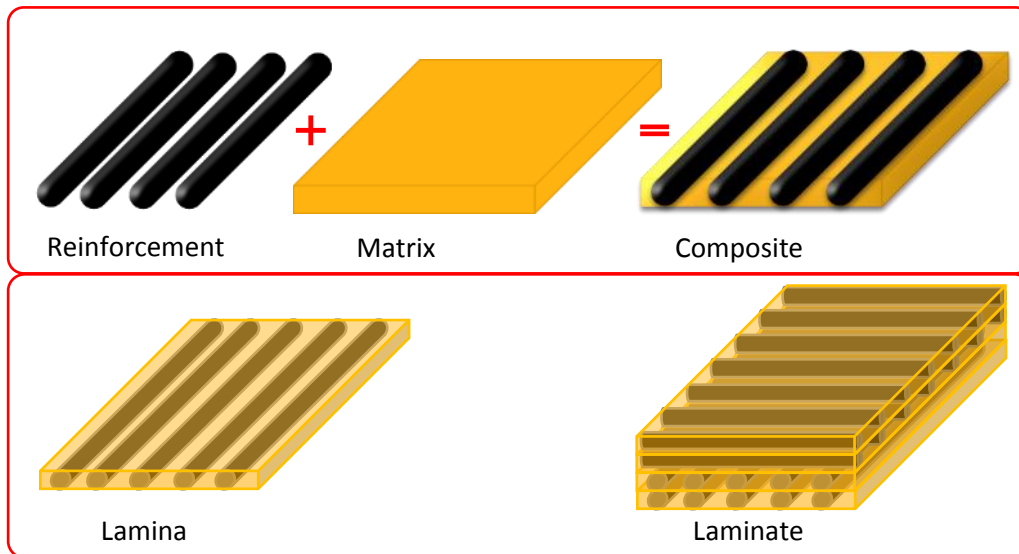


Figure 1.1: (top row) Constituents in the composite. (bottom row) Typical arrangement in a composite.

Figure 1.1(top row) shows the basic organisation of constituents in a composite. This arrangement is scalable across the length scales. Typically, composites are arranged in a layered fashion and the basic unit (single layer) is termed as lamina. When grouped together to meet the requirements of the structure, they are called a laminate (Figure 1.1(bottom row)). As mentioned earlier, the unique properties of composite materials are by virtue of its constituent phases namely reinforcement and matrix. For structural requirements such as high rigidity, composites with a sandwich construction are also used where a low-density core is embedded between two laminates on either side. This structural feature is by virtue of the geometrical arrangement (*i.e.* separation of laminates away from the principal axis) of laminates than the nature of core material. Therefore, comprehensive understanding of the roles played by the reinforcement and matrix phases and their synergy is essential. The properties of composites are not only a function of their constituent components but also depend on their arrangement and how well they are combined.

### 1.2.1 Composite reinforcements

Reinforcements can be defined as the discontinuous phase in a reinforced composite which is combined with the embedding matrix phase during various composite processing techniques resulting in the manufacture of a part or structure. Their primary function is to contribute towards the structural properties of the final part after manufacture and thus carry the operational loads. They can be seen as to provide the strength and stiffness to the part. High aspect ratio fibres are the most common reinforcement type used and their composites are typically referred to as fibre reinforced plastics (FRP) or advanced composites. Short fibres and particulates of various geometrical shapes such as ovals and spheres are also used as the discontinuous phase in composites. In structural composite parts, the reinforcements carry up to 70-90% of the loads. The anisotropy of composites originates from the directionality of reinforcements. Therefore, the selection of reinforcement type, its volume (volume fraction  $V_f$ ), length and orientation are imperative as it influences the key final properties of the composites [15].

The most commonly used reinforcement type is glass fibres owing to their relatively low cost and they find application in glass fibre reinforced plastics (GFRP) for the marine industry. Carbon fibres have exceptionally high tensile strength and tensile modulus for their weight and their composites are used in more structurally demanding applications especially in aerospace and automotive industry. However, the high cost of carbon fibres has limited their widespread adoption and has been primarily restricted to aerospace and premium automotive industry where the weight savings are deemed more critical than the cost. Aramid fibres represent another class of fibres widely adopted to manufacture composites. They are highly crystalline aromatic polyamide fibres and Kevlar is the trade name of one of the most commonly used aramid fibres. Unlike carbon and glass fibres, failure in aramid fibres is preceded by longitudinal fragmentation, splintering and even localised drawing. This non-catastrophic failure mode makes them an ideal choice of reinforcement for impact resistant applications such as body armour. There exist other reinforcement types such ceramics and metals, however they have limited and more specialised applications [15,16]. Natural fibres such as jute, flax, hemp, remi, sisal and coir represent the commonly used bio-fibres. The principal component of bio-fibres are cellulose microfibrils dispersed in an amorphous matrix of lignin and hemicellulose. Natural fibres are limited by their low tensile strength, thermal stability and hygroscopic nature, but are finding increasing applications such as for non-structural automotive parts to meet regulations concerning recyclability and sustainability. Albeit lacking in mechanical properties when compared to carbon and glass fibres, natural

fibres are gaining attention not only for their sustainable aspects but also due to its potential for further modification. Highly reactive groups present in bio-fibres could be utilised to functionalise the fibres imparting multiple additional properties.

### 1.2.2 Composite matrices

The matrix is the material that surrounds the reinforcement in reinforced composites and the phase that gives form to the final manufactured composite part. The main roles of the matrix in composite materials are: (i) keep the reinforcements in place giving form to the part and govern manufacturing parameters (ii) facilitate load transfer between reinforcements and (iii) offer protection to the part from mechanical degradation and adverse environmental elements. The selection of matrix has a huge influence on the compressive, interlaminar shear and in-plane shear properties of the composites. The matrix function of 'keeping fibres in place' couples with providing lateral support against buckling of fibres under compressive loading, thus contributing towards the compressive strength of the composite. Typically, the matrix is the limiting phase with regard to operational temperature and stiffness, but it should be adequate to provide uniform loading of the reinforcements under operational loads. Therefore, the interaction between the reinforcements and matrix must be taken into consideration in the design of composite structures. The choice of matrix material also dictates the processing route for the manufacture of the composite part. Polymers, metals and ceramics are some of the commonly used matrix materials. Polymers derived from sustainable biological sources are also currently being utilised as matrix materials to improve recyclability and reduce the ecological footprint of composites especially in the automotive industry. This aspect of utilising polymers derived from sustainable sources was explored in this project.

### 1.2.3 Significance of the reinforcement-matrix interface

A coherent interface between reinforcement and matrix is crucial to realising the full potential of composites. Poor interface between the constituents would limit the stress transfer between the reinforcements, thus impairing the performance of the composite structure. Advanced fibre reinforcements typically undergo a sizing treatment to enhance their interface compatibility with the matrix. For glass and carbon fibres, the reactive groups are rendered inert during the fibre manufacturing process to achieve better mechanical (stiffness and strength) properties and minimise defects. Therefore, a suitable sizing (surface treatment) specific to the chosen matrix is essential to ensure coherent interface with the matrix. Other strategies in aid of better interfaces include nano-additives (*e.g.* graphene or carbon nano-rods) in resin and hairy fibres where secondary and tertiary fibrous growth from the reinforcement surfaces are realised to increase the fibre-matrix interface area. A coherent

interface between the reinforcement and matrix components was also prioritised in this project, but adept material selection was employed ensure coherent interfaces utilising the inherent reactive groups to form bonds as opposed to the aforementioned strategies.

#### 1.2.4 Future of advanced composites

Clearly, the fibre and matrix types currently in extensive use are primarily optimised for mechanical properties rather than further functionalities such as coherent interface, self-healing and responsiveness. The next stage in the development of composites will see added capabilities and functionalities alongside the critical mechanical properties. Significant progress has been made in terms of realising better constituent interfaces and self-healing in composite materials. The next frontier will be responsive/reactive composites where the sensory elements form part of the structure itself and initiates a proportionate response from the structure. The greatest benefit with any attempts to impart multi-functionality is the overall efficiencies in system weight and resources used through integrated functional systems. Further developments in this direction could realise sentient composites with inherent intelligence of the structure guiding its response to stimuli. The research carried out in this project falls within the subset of responsive/reactive composites where the response to the sensory input is programmable self-actuation resulting in a different shape configuration. This novel functionality was given priority over mechanical properties so as to advance the scientific understanding of imparting additional functionalities particularly sensory aspects and self-actuation. Here, the programmable self-actuation was harnessed to create shape-changing (morphing) composites through additive manufacturing which can transform between multiple configurations through programmed actuation pathways in response to the incumbent stimuli.

### 1.3 Morphogenesis manufacturing

The term morphogenesis originates from the Greek *morphe* (meaning shape) and *genesis* (creation) and concerns the origin of shapes, forms and patterns. In biology, morphogenesis is a fundamental process concerning developmental biology through which an organism develops its shape and form. In geology, the term refers to the formation of landscapes or geographical structures. The characteristic feature when looking at the 'origins of shape and form' in natural world is that the materials come together (grow) rather than being removed. The process is additive as opposed to subtractive like some of the commonly used manufacturing routes in synthetic world such as milling, cutting and shaping. Another distinct feature of morphogenesis is that the form is influenced by its environments and stimuli

(external and/ internal). Nature's approach to realising a functional form can be captured by three key points: (1) inherent design either embedded into organisms' genetic code or shaped through the interacting natural forces; (2) core building materials embedded with multi-functionality; (3) growth as a process enabling precise placement of various building blocks in hierarchical order to realise form as per the embedded design under the influence of environmental stimuli.

Morphogenesis manufacturing envisages a 'bottom-up' additive manufacturing using materials beyond the readily available in nature or engineering. This is achieved through hierarchical arrangement of building blocks leading to unique material configurations during the additive process giving rise to previously inaccessible properties or functionalities in the bulk material or fabricated architecture. Such a process should draw its inspiration from nature not only in its additive nature to construct form but also in terms of the fundamental ecological and functional characteristics of the building materials found in nature. Therefore, morphogenesis manufacturing can be thought of as a nature inspired manufacturing philosophy where functional forms are fabricated through additive processes using sustainable and eco-friendly material systems where the functionalities of the form are not only a function of its constituent materials but also by virtue of their arrangement. Developing such materials aligning with the philosophy of morphogenesis manufacturing requires an in-depth understanding of nature's systems, advancements in biological sciences and advanced materials. Furthermore, a re-imagining of current manufacturing practices are also required. This manufacturing philosophy would be reflective of nature's process where specific materials seamlessly form part of a hybrid structure displaying synergy between form and function without having to attach onto or carve out materials at later stages to realise various functionalities and architectures.

#### 1.4 Bio-inspiration

Nature's materials possess a multitude of desirable properties and integrated features that leave synthetic materials lacking. Self-healing, regeneration, self-cleaning, adaptability and morphing are some of the characteristic features of materials and lifeforms (systems) in nature. Consequently, there have been enormous initiatives not only in achieving these unique properties but also in terms of mimicking the method with which these functionalities are realised in nature. Irrespective of the complexity of the organism, nature provides an array of material systems with various embedded functions that are tailored to suit specific organisms to survive in their habitat. In nature, complex structures or life forms are designed and realised from the molecular level up; integrating multiple functionalities within the

materials itself. This holistic approach is a far cry from the typical bolt-on approach employed by humans in realising functional structures. This is particularly true regarding structural forms where strength bearing elements (either tensile or compressive) are added on as required in man-made structures as opposed to developing strength (either tensile or compressive) by means of mineralisation from a molecular level or through strength and stiffness tailoring as observed in natural forms. As specialised and complex as living organisms can be, there are some distinct features that apply to most of nature's systems. Understanding these features and how they differ from current synthetic approaches to realising similar features are key to developing a morphogenesis approach to manufacturing. P. Chen *et al.* [17] summarised these desirable and distinguishable properties of biological material systems as follows:

- *Self-assembly* - Biological forms are assembled from the bottom up, with the building blocks following a prescribed genetic code which was perfected over the years through evolution and influenced by its environment. Self-assembly is observed across the length-scales in nature. The formation of molecules to specific proteins essential to life is one of such examples. The basic building blocks assemble through specific and local interactions between components and is controlled at each of the higher length scales in the structure.
- *Mild synthesis conditions* - Even though some basic life forms are known to exist in extreme conditions, most biological organisms develop at atmospheric pressure and temperatures. This is different to the extreme conditions required to make and process synthetic materials. Granted the full development of biological organisms takes longer and is thus arguably more energy demanding, the milder synthesis conditions are desirable with regard to the synthesis and processing of synthetic materials as they are more sustainable. Another interesting point to note here is that out of hundreds of stable elements in the periodic table, only about 10 % are being utilised as building blocks in biological world [17]. The common structural elements such as iron and aluminium are only present in minute quantities and also for enabling highly specialised functionalities. Nature utilises a limited palette of elements to realise its unique set of properties in comparison to synthetic approaches.
- *Hierarchy* - Most of the functional biological components are highly organised from the molecular level onwards adhering to specific design at each of the higher length scales. Each of these levels are critical in imparting distinct properties which complement the features from other levels within the hierarchy. In hierarchical structures, structural properties arise due to the orientation of structural phases resulting in anisotropy.



Functionalities like self-cleansing and adhesion also arise by virtue of geometry and hierarchical arrangement. Typical examples of hierarchical structures in nature are gecko feet [18], nacre [19], bone [20] (Figure 1.2a) and skeletal muscles [21] (Figure 1.2b).

- *Multi-functionality* - Many biological parts/ organs meet multiple requirements. This highly efficient evolutionary design enables organisms to be proficient in their environment. For example, the primary function of vertebrates' skeletal system is to support the body and protect the vital internal organs. However, specialised adaptations of skeletal systems can be found across the animal kingdom to serve additional functions. The bones in birds are optimised to be light-weight and flexible to aid flight [19]. The flexible spine in cheetahs allows them to coil whilst sprinting and results in longer strides to propel them forward at great speeds.
- *Hydration* - Water is the most abundant substance on planet earth and is vital for all known life forms. Natural systems take advantage of this stimulus in regulating their adaptive features. Regulating water content in cells is one of the ways with which natural systems can realise variable strength and stiffness. Hydration or water transport also aids to regulate and balance physiological conditions of the organisms. Turgidity in plants is a direct consequence of water content in cells and it enables shape transformations as well as nastic movements in plants.
- *Evolution* - This characteristic feature is closely related to the self-assembly, hierarchical organisation and multi-functionality in natural world. The genetic code which determines the self and organisational assembly of building materials is constantly being updated through information collected during the life cycle which is then used to improve the succeeding designs. Vestigial organs and adaptations are prime examples of this feature. This feedback loop for efficient design over generations ensures that the adaptations are relevant to the organisms' habitat.

In nature, it is often the case that chemically identical materials could have diverse functions and properties either through association with another material or through different spatial arrangements. Alongside hierarchical arrangement of its building materials, hybridisation (integration of soft and stiff phases) is also crucial to the unique set of properties and multi-functionality observed in nature. For example, technological advancements in analysis have revealed how strength and stiffness requirements are met or have evolved in the biological world. The key function of bones and muscles is to provide stiffness and strength respectively and together they support, stabilise and assist in locomotion as part of wider musculoskeletal system. However, these contrasting functionalities can be attributed to the key process of bio-

mineralisation. Bio-mineralisation is the process through which hard composites of organic/inorganic minerals dispersed within biopolymers are formed. Figure 1.2 shows the organisational levels in bones and muscles respectively. It can be seen that both are comprised of fibres but the collagen fibrils in bone has undergone bio-mineralisation forming preferentially oriented hydroxyapatite ( $\text{Ca}_{10}(\text{PO}_4)_6(\text{OH})_2$ ) nano crystals. This combination of preferential alignment and mineralised phases imparts stiffness to the bone [20]. Even though myofibril is the primary protein present in skeletal muscles to realise contractile motions, these fibres are encapsulated in collagen and makes up to 6-8 % of skeletal muscles. Both of these proteins are not mineralised in skeletal muscles. The strength characteristics of muscles can be attributed to its organisational structure and its ability to relax and contract. This is a prime example of how functionality can be so diverse through incorporating a new phase in comparatively similar hierarchical structures comprising of fibres. As in the case of skeletal and muscular collagen, the effect of hybridisation resulting in comparable base materials serving diverse functions are evident. The robust interface between different material phases promotes self-healing, resilience and adaptability. Therefore, it can be concluded that hybridisation in nature is an effective means of realising different requirements with a limited material palette. Hybridisation is also an effective means to providing better interfaces within

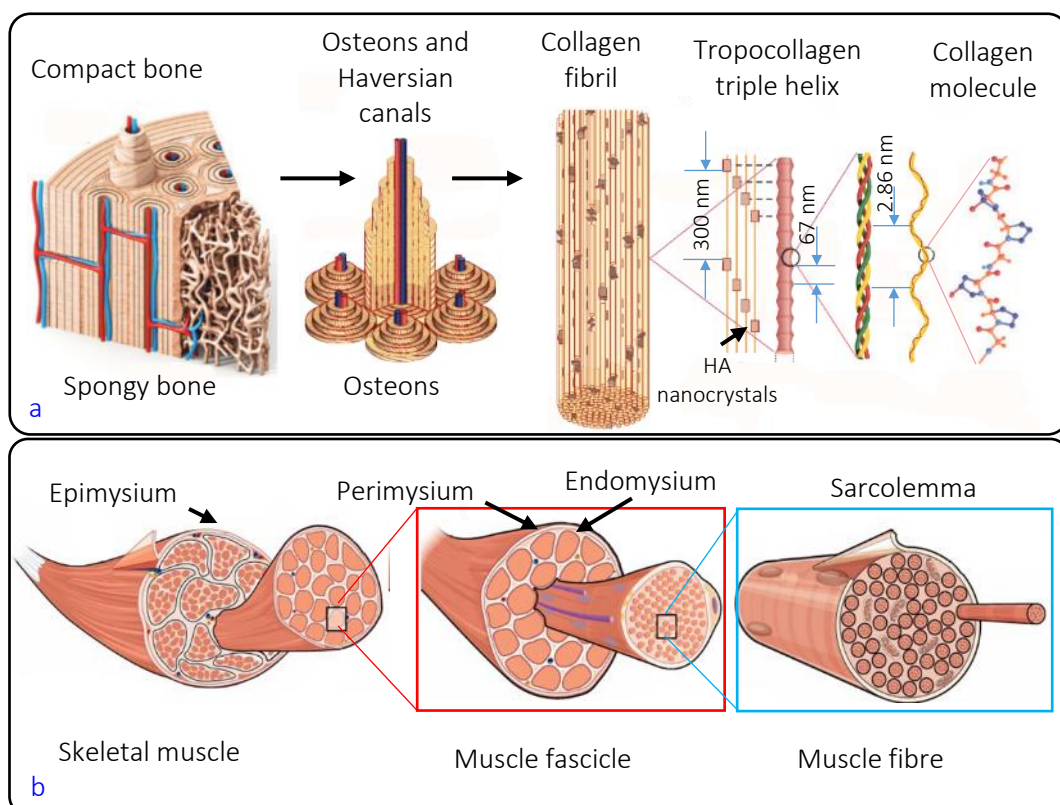


Figure 1.2: Hierarchical structure of (a) bones (top row). Images adapted from [20] with permission from Springer Nature. (b) Skeletal muscle (bottom row). Images adapted from [21] under Creative Commons Attribution License 4.0 from OpenStax.

a composite. The chemical homogeneity will ensure a coherent reinforcement and matrix interface whilst retaining the benefits of composite construction.

Advancements in microscopy and 3D imaging techniques permits a deeper understanding, especially the visualisation of these biological systems from nanoscale onwards. The chemical constituents and their respective functions can also be identified with good accuracy as a result of advancements in analysis techniques. Together with a greater understanding of the biological world, researchers are now in a better position to realise and even better the material features found in nature. The greater understanding of biological systems permitted by the advancements in analysing technologies has led to an increased number of bio-inspired designs from the early days of Velcro®, based on hooks in plant burrs and self-cleaning-hydrophobic surfaces, inspired by the lotus leaves [17]. Self-healing (vascular system), deployable structures (flowers), damage tolerance (nails and nacre) and adaptive structures (bird's wing) are some of the current and relevant bio-inspired research fields [17,19,20,22,23]. Amongst these, investigation into morphing and adaptive material systems presents an opportunity to incorporate sensory and actuation features to be stimuli-responsive or reactive to initiate the shape changes [1,24,25].

The ability to have multiple physical configurations within a single form activated on demand with each serving a distinct purpose is key to structural and resource efficiency. In nature, this ability to morph or adapt in response to stimuli is often key for survival and reproduction. Some examples of morphing/ adaptive forms in nature are as follows. The hygroscopic responses of pinecones (Figure 1.3 (top row)), sun tracking of Cornish Mallow (*Lavatera cretica*) and the tactile response of the 'touch-me-not' plant (*Mimosa pudica*) (Figure 1.3 (bottom row)) are some examples of reactive structures that respond to an array of stimuli. In pinecone scales, the tissues are visibly distinguishable and are arranged in a bilayer structure where the inner surface is made up of sclerenchyma and the outer surface consists of sclerids. The cellulose fibrils within the cell walls forming these tissues have different winding angles thus controlling the expansion of these cells during hydration. The fibrils in sclerids have a high winding angle and thus permit the cells on the outer surface to expand upon hydration. Whereas, the sclerenchyma cells have low fibril winding angle thus effectively restricting cell expansion (see schematic in Figure 1.3 (top row)). This anisotropic expansion results in the opening and closing of pinecone scales in response to dehydration and hydration. This actuation system is independent of the host plant's motor pathways and can operate passively [26]. However, in touch-me-not plant, the response is reliant on the motor pathways. Mechanical stimulation results in a signal being propagated from the site of origin towards the

pulvinus, which is located at the base of leaf and leaflets. The motor cells at the pulvinus are divided into flexor (dorsal side) and extensor (ventral side) cells. Upon receiving the signal, an action potential develops at these motor cells which initiates the differential transfer of  $K^+$  and  $Cl^-$  ions from extensor cells resulting in an increased water potential. The reverse ensues in flexor cells and consequently water flows from the extensor cells (shrinkage) to flexor cells (expansion) to balance the water potential (see schematic Figure 1.3 (bottom row)). This sudden loss of turgor pressure in the extensor cells results in the closing of leaves and dropping of pulvinus in *Mimosa pudica* [27,28]. Even though actuation in pinecones and *Mimosa pudica* are realised through the movement of water (external and internal), their reaction times are significantly different. The closing of leaves in *Mimosa pudica* is very fast (few seconds)

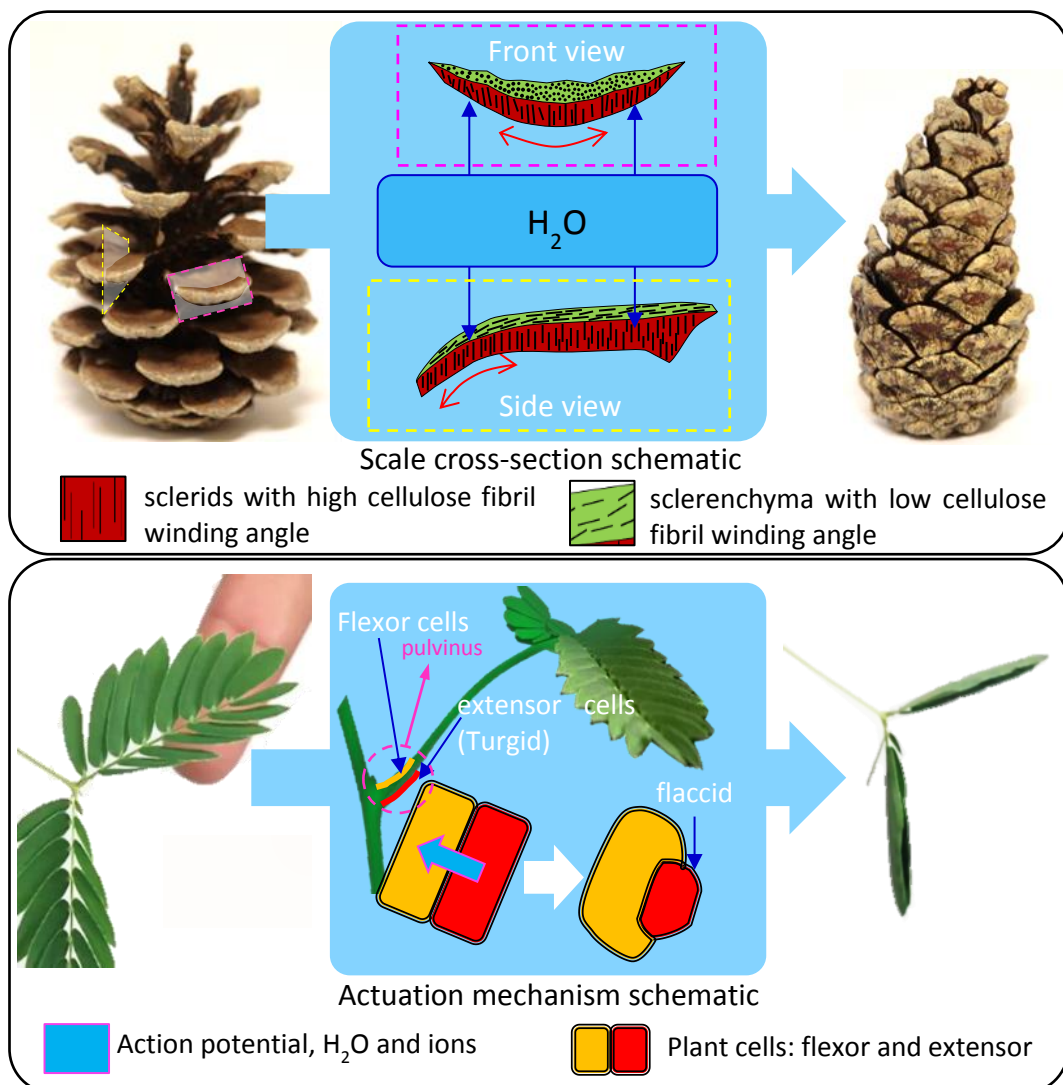


Figure 1.3: Examples of actuation in plant kingdom. (Top row) Pinecone; Open (dry) to closed (wet); Differential cellulose fibril winding in the top and bottom layers results in anisotropic swelling upon water absorption resulting in the closure of scales. (Bottom row) Touch-me-not plant (*Mimosa pudica*); Mechanical stimuli induces a signal potential towards pulvinus which in turn initiate action potential and movement of ions from extensor cells to flexor resulting in the loss of turgidity through diffusion of water out of the cells and results in dropping of pulvinus and closing of leaves.

compared to the actuation response of pinecone scales which takes several minutes to hours depending on the humidity levels in the surrounding environment.

Nature has devised these reactive systems by controlled arrangement of materials and simple responsive processes such as swelling. Anisotropic swelling occurring at cellular level is harnessed through hierarchical and programmed microstructure to realise morphing at a holistic level with respect to the plant organ. This reactive morphing is a consequence of not just stimuli responsive materials but also its arrangement from lower levels of cellular organisation onwards and together forms the morphing system. Consequently, there are significant research efforts and a large body of scientific literature [1,22–25,29–33] pertaining towards realising responsive systems akin to systems found in nature as opposed to just ‘smart’ materials or structures. It can be seen that cellulose fibrils and their arrangement is key to realising these morphing responses in these systems.

Cellulose is the most abundant bio-macromolecule in nature with desirable properties such as renewability, environmental friendliness and biodegradability [34–36]. Cellulose itself is a prime example of hierarchical arrangement of organisational units. Cellulose molecules consist of  $\beta$ -1,4-linked anhydro-D-glucose units in which every unit is inverted  $180^\circ$  with respect to its adjacent unit [37,38]. The presence of hydroxyl groups (OH) in the molecule results in hydrogen bonding between molecules leading to the formation of fibrils which further associate to form fibres in a true hierarchical fashion. The nature of hydrogen bonding and the arrangement of sub-units results in crystalline and amorphous phases within cellulose structure [38]. Furthermore, the presence of hydroxyl groups on cellulose chains permit further modification through derivatization and graft copolymerisation techniques. In addition to hydroxyl groups, there are other sites in the cellulose molecule that enable further modification. Therefore, utilising cellulose and its derivatives in the manufacturing of engineering polymers have been rigorously investigated [39] and implemented for a range of applications in pharmaceuticals [40], viscosity modification for flow control and tissue engineering [41] due to the aforementioned benefits and increasing concerns on the over-dependency on traditional petroleum resources.

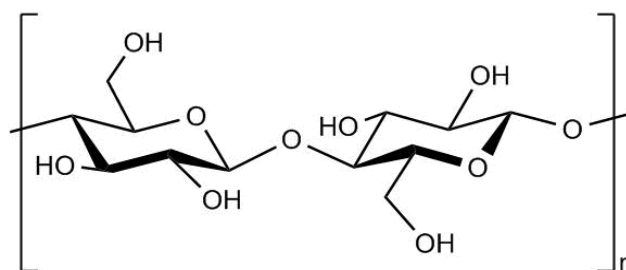


Figure 1.4: Structure of cellulose

## 1.5 Smart materials

The materials whose properties can be altered in a controlled fashion in response to external stimuli are typically referred to as smart materials. Sentient structures which incorporate sensory functions as well as proportionate mechanical responses within itself are widely touted to be the systems for the future. Sentience as in the ability to feel and perceive subjectively might be far from being accomplished within a material system without simultaneous developments in artificial intelligence (AI) research. However, the current crop of smart materials can be programmed to sense directional stimuli and output a proportional response. The design rules for such systems could be expanded to realise what could perhaps be classified as rudimentary sentience. There have been a multitude of approaches in order to realise the goal of developing such smart structures. Whether it be the miniaturisation of existing sensory, electrical and mechanical systems by virtue of the advancements in robotics and nanotechnology or through the development of novel material chemistries, the research community has been actively looking for solutions to tackle this particular challenge [24]. Fortunately nature has already solved this challenge as evidenced by a myriad of examples presented in the earlier Section *1.4 Bio-inspiration*.

It is no straightforward task to define what qualifies the material to be smart or intelligent in unambiguous terms as the words smart and intelligent are used in a much broader sense. A material's response to stimulus alone cannot constitute towards intelligence as almost all materials will respond to some stimulus in one way or the other. However, a directional, reliable, reproducible and proportionate response of the material to stimuli contribute towards smartness and such a smart material can be programmed by varying its physical or chemical parameters to harness the desired response. Whether just this ability to sense and respond contribute towards sentience as manifested in nature is debatable even though the term sentient materials have been used to describe smart or intelligent materials or systems embedded with an array of sensors measuring various system aspects and draws a particular system response [42]. Such materials, perhaps less complex and capable, have already been developed with shape memory materials being the most common of them all. The response of these materials to external stimuli is inherent to the material itself than realised solely through embedded mechanical, electronic, hydraulic or pneumatic sub-systems. The distinction between smart materials and smart structures must be stressed. Synthetic smart structures can be envisaged as systems capable of sensing and responding through the integration of sensory and actuation subsystems which can be comprised of smart materials. The integration is realised by means of dedicated control and feedback streams. However, to

---

be sentient as observed in nature, the smart materials or systems will have to do more than sense and respond. Greater understanding of the inherent mechanisms or means with which the material experiences the stimuli, the relative response and the programmability of both sensory and response aspects of the smart material are certainly leading towards sentient materials. It must be noted that without incorporating some form of intelligence which operates a feedback loop constituting a record or memory of previous encounters with the stimuli and adjusting the material behaviour respectively over time, true sentience in materials cannot be achieved. Programmability of smart materials could be seen as a precursor to or rudimentary sentience/ intelligence. It is envisaged that in future, inherent intelligence of the materials can not only adjust the material response based on historical data but can be passed on to improve the next generations analogous to adaptation (genetic programming) in life forms improved through evolution. This project however pertains to identifying smart materials demonstrating the potential of morphing whilst adhering to morphogenesis manufacturing philosophy and to develop design rules to program/ govern the way it senses and responds to stimuli. Such programmability is hoped to pave way for complex morphing systems and serve as forerunner to sentient materials of the future.

#### 1.5.1 Response based classification of smart materials

Smart materials can be classified based on their function and incumbent stimuli. There exists a wide variety of smart materials and an in-depth understanding of the underlying principles with which they respond to their environment is vital for the successful implementation of these materials. There also exists a sub-division of smart materials characterised by their physical nature, *i.e.* soft smart materials. A smart material's response can often be reversed once the incumbent stimulus is removed. As there exists a plethora of smart materials exhibiting a range of transformative properties, it is impossible to cover the full extent of these materials here. Therefore, the following sections present a concise review of smart materials with focus on its potential to realise morphing architectures in response to stimuli and the underlying principle behind their smartness and functionality.

There are multiple classifications of smart materials and the organisation based on the material response and stimuli are predominant. Chromic smart materials can change colour in response to a change in temperature (thermochromic) or UV - light (photochromic) [43]. There are also a wide range of chromic materials that can be electronically triggered. They are finding increasing applications in the field of architecture, aerospace, automotive and electronic displays. Electrophoretic media (also known as suspended particle devices (SPD)), phase dispersed liquid crystals (PDLC) and cholesteric liquid crystals (ChLC) are some examples

of electronically triggered chromic smart technologies [44]. The piezo-electric effect was discovered by Jacques and Pierre Curie in 1880 when they observed that an electrical output was produced when natural materials including quartz and Rochelle salt were mechanically strained (direct effect). These materials exhibited electromechanical coupling which meant the piezo electric effect could be reversed, *i.e.* a mechanical strain on the materials can be achieved by applying an electric field to it (converse effect). This reversed response is known as electrostrictive effect. The underlying principle for these effects are the inherent dipoles within the crystal structure of the materials orienting in response to mechanical or electric stimuli. Ionic polymers have also been shown to work in a similar way where an electric current passed through a conducting ionic polymer resulting in a change in its crystal structure and consequently in its shape [45]. Magnetostrictive materials responds to magnetic fields by developing mechanical strain within itself. Similar to dipoles within piezoelectric materials, magnetostrictive materials are made up to tiny ferromagnets which re-align itself with the applied field axis resulting in a strain response (either shrinkage or extension). Application of strain to these materials result in the reverse effect where a magnetic field is induced in the material and is known as Villari effect. Unlike some poled piezoelectric substances, magnetostrictive properties does not degrade over time as they are inherent to the material. As a transducer, these piezoelectric and magnetostrictive materials find application as sensors and actuators [45,46].

Shape Memory Alloys (SMA) are one of the most well-known type of smart materials. Even though shape memory effects (SME) were first observed in 1932, it wasn't until the discovery of Nitinol (an equiatomic alloy of nickel and titanium) SMA's began to find widespread applications. SME is a temperature effect where the material reverts its shape to a previous configuration (realised through prior programming of the material) at a specific temperature known as transition temperature which can be programmed by varying the ratio of constituting metals. Materials that can only display shape memory effect once are known as one-way SMA actuators. However, some alloys could be programmed (trained) to have two configurations. The alloy undergoes solid state phase transition at transition temperature from soft martensitic phase characterised by a zig-zag arrangement of atoms known as twins to an ordered and robust austenitic structure. Heating a deformed (fixed) shape in martensitic phase above the transition temperature removes the deformation and cooling below the temperature reverts the shape back to its deformed state. SMA find a range of applications; especially Nitinol, which is widely used in the medical field due to its biocompatibility. The excellent fatigue response of SMA makes them an ideal choice as an actuator [47].



### 1.5.2 Soft smart materials

There has been a significant and collective research effort into the development of smart soft matter which is at least in part inspired by the biological materials in nature, *e.g.* muscle fibres. Not only that the soft nature of these smart materials enables greater flexibility in adapting them to a variety of shape configurations, they present simpler material processing routes as well. Electro (ER) and magneto rheological (MR) fluids, ferrofluids, electromechanically active polymers (EAP), shape memory polymers and gels are some examples of smart soft matter materials. The flexibility in conforming these soft-matter materials to various configurations allows to develop the basic materialistic response to activating stimuli to manifest in complex ways. Through strategies such as functionalisation, photolithography and multi-layer construction more complex actuation responses could be programmed from these materials. This class of smart material is covered in the following sections to establish the direction of soft smart material research as it is vital in developing an understanding for the work carried out in this project.

Electro and magneto rheological fluids are suspensions of active micrometre sized particles within a non-active host (high density) fluid. These particles are responsive to the field effects of electricity and magnetism. They are used in applications where an instantaneous control of viscosity and flow behaviour are required, *e.g.* hydraulic valves and shock absorbers in suspension systems. Ferrofluids contains nanometre sized particles suspended in host fluids of comparatively lower density than ER and MR fluids. They find application as active liquid seals in electronic devices, lubricants for magnetic parts and in dampers. The nano-sized magnetic particles and relatively low density enable ferrofluids to re-organise and deform with respect to the applied magnetic field [45]. Electro active polymers (EAP) especially dielectric elastomers (DE) responds to voltage difference such that when placed between compliant electrodes, they undergo reduction in thickness and subsequent expansion of the area in order to maintain constant volume. They are transducers as they convert supplied electrical energy to mechanical energy. A critical feature is that the material response is greatest when the electrodes are close to each other, *i.e.* thin samples or membranes. They are characterised by large deformations, high energy density and fast response times and are actively researched upon for developing artificial muscles. However, large potential difference in the order of kilo-volts required to induce this response was seen as a limiting factor but strategies bypassing this limitation are evolving [48]. The soft nature and flexible electrodes allow for various configurations of DE materials such as rolls and stacks to be utilised as an efficient transducer.

### 1.5.2.1 Shape memory polymers

Shape memory polymers are an example of soft smart matter ideally suited to morphing applications. Shape memory polymers (SMP) are usually comprised of two networks; permanent chemical network composed of strong crosslinks dictating the primary equilibrium shape and the other network formed during programming or training step comprised of stimuli-responsive physical crosslinks which fixes the deformed shape. Similar to SMAs, SMPs have to undergo a pre-programming step to define the new shape where the secondary stimuli responsive network fixes the shape by storing the elastic energy of deformation. On the application of appropriate stimulus, the stored strain energy is released as the physical crosslinks fixing the new shape are cleaved. The restoring force generated by the primary network reverts to the equilibrium shape of the materials. Incorporating tertiary and further networks which could respond to different stimulus could be used to access multiple shape configurations within shape memory polymer [49]. Typically activated by means of heat, SMPs have been shown to be responsive to light, moisture and change in pH [50]. Strategies where SMP are realised as block-copolymers and composites have been employed to improve the properties and diversify SMP applications.

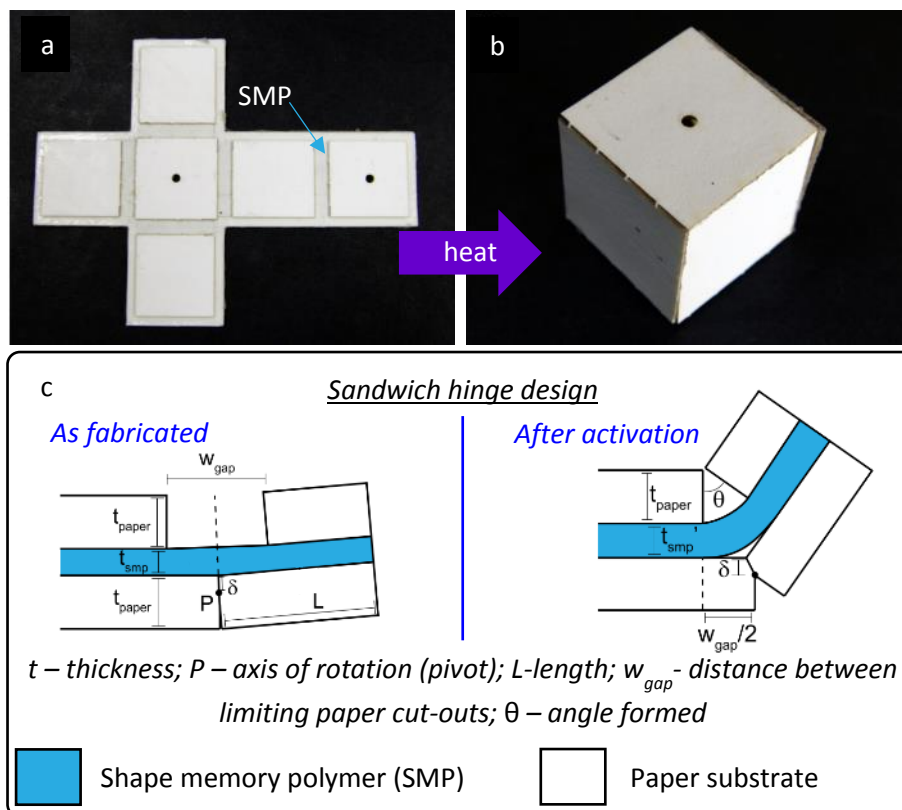


Figure 1.5: (top row) Transformation of SMP (shape memory polymer) composite from (a) flat to (b) 3D configuration. (bottom row) (c) Schematic of detailed hinge design as fabricated and after activation. Images adapted from [51] with permission from IOP Publishing.

Tolley *et al.* described the fabrication of shape memory composites through a sandwich construction of SMP embedded in between paper cut-outs [51]. Figure 1.5a and b show the transformation of such a patterned flat composite into a cube upon heating. Detailed design of the hinge forming the edges of the cube are shown in Figure 1.5c. Commercially available SMP, pre-strained polystyrene shrink films (Shrinky Dinks) were sandwiched between paper cut-outs using adhesives where the gap between the cut-outs dictated the extent of folding upon heat activation. Heating of the SMP composite release the internal locked in strain in SMP and the polymer tries to recover its original shape (prior to stretching) by shrinking, driving the paper cut-outs closer. As the bottom cut-outs only have rotational degree of freedom about the pivot  $P$ , the facets will rotate to accommodate the shrinking in SMP. The extent of this rotation (*i.e.* angle  $\theta$ ) is dictated by the gap ( $w_{\text{gap}}$ ) and thickness of adjacent cut-outs in top-layer (Figure 1.5c). Similar to SMA, the microstructural changes within the material are the driving force for shape memory behaviour in SMP. Polymers offer more versatility to engineer parameters such as glass transition ( $T_g$ ), melting and crystallinity as they are the predominant phase transitions occurring at the molecular level for activating shape memory effect.

#### 1.5.2.2 Shape changing polymers

Shape changing polymers undergo reversible shape alterations in response to specific stimuli. Unlike shape memory materials there is no pre-programming or fixing of a shape. Common mechanisms for shape change in polymers are (i) isomerisation (induced change in spatial conformation of atoms) (ii) liquid crystalline transitions and (iii) swelling of gels mediated by solvent gradients and crosslink density. Optically (UV light) activated shape changes through photoisomerisation in azobenzene based polymers have been widely reported. A trans-cis isomerisation at molecular level onwards results in macroscopic changes to the overall shape. Controlling the alignment of crystalline phases within the polymer have also been used to initiate shape changes in elastomeric polymers and could be triggered by a myriad of stimulus such as thermal, magnetic, chemical (pH, polarity or humidity) and optical. The alignment of these mesogens attached to compliant polymer backbone can be varied by applying appropriate field resulting in a change in its dimensions.

Yu *et al.* reports the guided bending of liquid crystal polymer film by means of polarised light, where the bending of the film occurs towards the direction of irradiation of the light and parallel to the direction of polarization as shown in Figure 1.6(top row) a-f. Here, the alignment of liquid crystals are macroscopically random and irradiation with linearly polarised light leads to selective absorption and trans-cis isomerisation of the azobenzene moieties aligned in that

direction [52]. The sensitivity of liquid crystalline materials to surface alignment has been exploited to fabricate patterned monolithic films capable of complex actuation responses (Figure 1.6g-i). This process typically involves aligning and fixing a photoalignment material (containing azobenzene moieties) to a desired topological defect pattern on a pair of glass slides to form liquid crystal cells. A nematic mixture of liquid crystalline monomers is then flooded into the cells through capillary action where the directors interact with the surface alignment of photoalignment material and orient in that direction through self-assembly (Figure 1.6g and h). This orientation is fixed by polymerisation and the resulting LCN film is removed from the glass cell (Figure 1.6i). A voxelated (grid based) approach of patterning multiple defects to form a monolithic LCN film was adopted by Ware *et al.* which demonstrated strains in the region of 55% for each voxel upon activation by heat due to the photoalignment of directors resulting in anisotropic volumetric changes [53]. The underlying photomechanical transduction of light into mechanical response is attributed to local strain generation in the glassy polymer caused by the reorientation and isomerization of the azobenzene chromophores. The actuation response of these LCN films are not limited to optical and heat

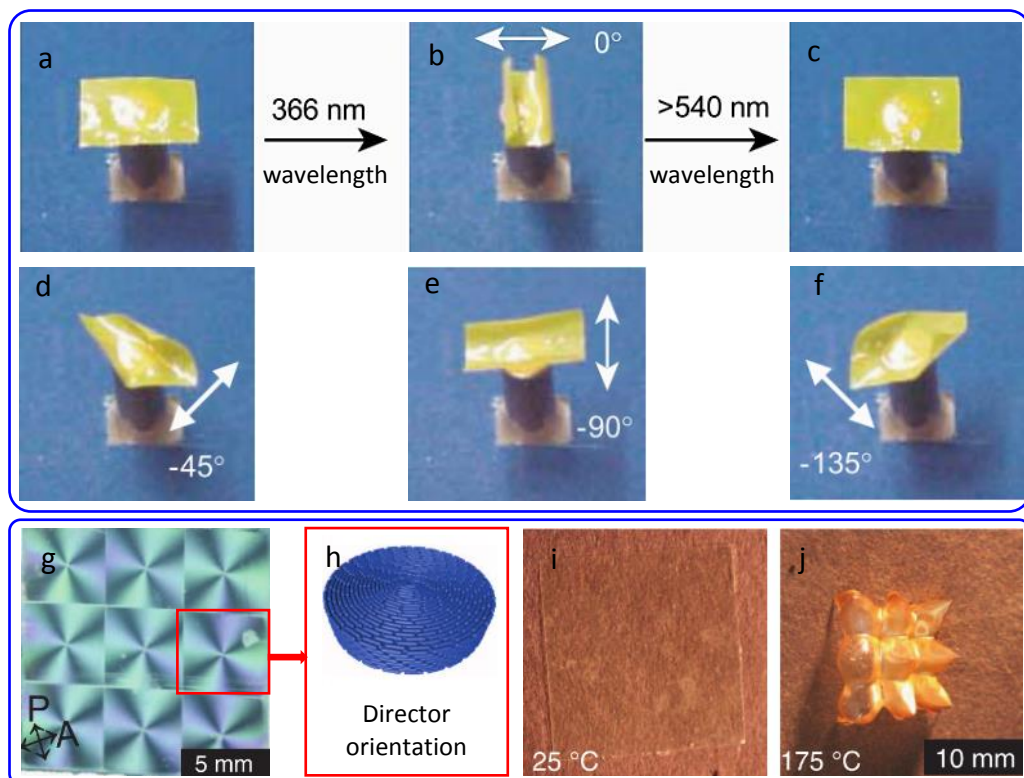


Figure 1.6: Morphing responses of liquid crystalline polymer films (top) to linearly polarised light: (a) Polymer film as fabricated. (b) Bending towards the incident light after irradiated with light polarised in  $0^\circ$ . (c) Recovered flat film following irradiation with visible light of wavelength greater than 540 nm. (d) Bending response to  $-45^\circ$  polarised light. (e) Response to  $-90^\circ$  polarised light. (f) Response to  $-135^\circ$  polarised light. Images adapted from [52] with permission from Springer Nature. (bottom) to uniform heating. (g) Representative photograph of film with +1 topological defect arranged in 9 voxels as observed between crossed polarisers. (h) Orientation of the directors around the defect. (i) Polymer film as fabricated. (j) Actuation response after heating. Images adapted from [53] with permission from The American Association for the Advancement of Science.

stimuli. As the alignment of crystals containing azobenzene chromophores were fixed within the films, swelling of the film in appropriate solvents also yielded strain and actuation response due to inherent anisotropy in the substrates.

### 1.5.2.3 Hydrogels

Swelling of polymer networks by a solvent typically results in isotropic changes in shape. The shape changes realised in polymers through these mechanisms represent the equilibrium state under the influence of stimulus. Swelling of polymers especially that of hydrogels are actively researched for numerous applications and are not limited to shape change. On comparison, they are relatively simple and benign in synthesis compared to the aforementioned shape memory and optically active moieties. Gels comprising of ionic liquid (IL) are another class of shape changing polymers. This class of gels are versatile as they can be synthesised to expand and shrink in a wide range of environments such as pH, electric field *etc.* As for the project carried out here, hydrogels and their ability to morph are more relevant due to the emphasis given in adhering to morphogenesis route to manufacturing.

Among polymers, hydrogels in particular have received great consideration in research due to their large homogeneous volumetric changes and resemblance to biological cytoplasm [54]. Hydrogels are defined as three-dimensional hydrophilic polymer networks that can retain large amount of water in their swollen state without completely dissolving. The mechanics of water absorption depends on interactions such as capillary forces, diffusion, osmosis and hydration. Synthetic hydrogels can be traced to the pioneering work of Wichterle and Lim [55] in 1960's. Since then, there has been an enormous interest as hydrogels exhibit characteristics closer to biological tissue with the ability to tailor these properties by selecting appropriate ingredients and processing routes. For example, incorporating thermosresponsive moieties such as poly(N-isopropylacrylamide) and optically responsive moieties such as azobenzene can impart thermal and optical responsivities to the hydrogel systems. Hydrogels find application in a myriad of technological scenarios such as contact lens, systems for controlled and localised drug releases and biomedical applications such as tissue engineering. The stability of these three-dimensional polymers very much depends on the presence of crosslinks in order to prevent dissolution into an aqueous state.

There exists a wide range of hydrogels which can be classified based on their source, polymeric composition, physical (micro) structure, network charge, and nature of crosslinks [56,57]. Hydrogels can be divided into two, namely natural and synthetic based on their source. Natural polymers such as proteins (collagen and gelatine) and polysaccharides (chitosan,

dextran, hyaluronate, and alginate) can be used to fabricate gels that are very suited to applications that require a high degree of biocompatibility and degradability. Hydrogels can be synthesised to have a multitude of desirable features such as long shelf-life, high capacity of water absorption, high gel strength, stimuli responsiveness and degradability. Synthetic hydrogels derived from biological sources such as cellulose are yet another interesting category of hydrogels. These derived polymers exhibit the features of natural materials such as bio-compatibility and sustainability whilst enabling further functionalisation to impart properties that are typical of synthetic gels [58]. Some examples of cellulose derived polymers forming hydrogels are hydroxypropyl cellulose (HPC), hydroxypropyl methylcellulose or hypomellose (HPMC), carboxymethyl cellulose (CMC), Hydroxyethyl cellulose (HEC), methyl cellulose (MC) and ethyl cellulose (EC) [36,59]. Most of these polymers find a wide range of applications as binder, rheological modifier, disintegrant and platform for controlled drug release [60]. Cellulose from plant source is isolated and removed of undesirable co-components such as hemicellulose and lignin. There are two main reactions involved in converting cellulose to the aforementioned polymers: (i) alkalization followed by (ii) treatment with strong base. The polar groups present in the derived polymer makes them soluble in water resulting in the formation of gel [61]. The solubility and viscosity of these cellulose derived polymers depend on the degree of substitution (DS) and degree of polymerisation (DP) [62].

Control of the composition of hydrogels by virtue of preparation leads to some main groups of hydrogels. Homopolymeric hydrogels refers to polymer networks where the basic structural unit comprises of a single species of monomer. When two or more different monomer species with at least one hydrophilic component are arranged in a random, block or alternating configurations along the polymeric chains forming the three-dimensional network, hydrogels thus formed are termed as co-polymeric hydrogels. Multi-polymer interpenetrating polymeric hydrogels are made up of two independently crosslinked synthetic and/ or natural component in a network form (IPN). When one of the components is non-crosslinked, the polymer networks are known as semi-IPN hydrogels. Based on their physical structure, hydrogels can also be classified into amorphous, semi crystalline, crystalline and hydrocolloid aggregates [56]. However, the physical structure and properties are often dependant on factors such as temperature and can be used to initiate shape memory behaviour by initiating a phase transition in gels as reported in [63]. The presence or absence of network charge leads to four groups of hydrogels, namely (i) non-ionic (neutral) (ii) ionic (either anionic or cationic) (iii) amphoteric (containing both acidic and basic moieties) and (iv) zwitterionic (containing both

anionic and cationic moieties). Hydrogels with their polymer chains held together by molecular entanglements, and or secondary forces (physical interactions) including ionic, H-bonding (hydrogen bonding) or hydrophobic forces are known as physical or reversible gels. These crosslink points are transient in nature. When the polymer chains forming hydrogels are covalently crosslinked they are known as permanent or chemical gels. A novel type of gel called topological gels have been developed where the polymer groups are neither covalently crosslinked nor physically interacting. Instead, the polymer chains are physically interlocked in figure-eight type of crosslinks which can slide along the polymer chain in response to the forces experienced within the gel [64]. Expansive hydrogel classifications based on physical appearance, nature and responsiveness also exists. Hydrogel films and microspheres based on appearance; tough double (DN) or interpenetrating (IPN) network hydrogels based on physical nature and chemically and physically responsive gels are some examples.

Characteristically, volumetric responses of hydrogels are isotropic in all directions. However, for effective morphing applications, directionality or anisotropy in volumetric changes are highly desirable to extract large localised strains. This is typically achieved by means of restricting changes in one or more directions allowing the dimensional changes in the free direction to be amplified. There are a multitude of ways to realise this: bi/multi-layer construction using hydrophobic or varying stiffness materials together with hydrophilic gel layers [65], restricting certain degrees of freedom by encapsulating the gel [66] or through introducing rigid phases via localised crosslinking [67,68] and forming composite gels with increased mechanical properties are a few examples.

#### 1.5.2.4 *Hydrogel composites*

The idea of a composite hydrogel is not new but combining materials to vary bulk composition via homogenous or composite construction extent the prospects of these swellable polymers beyond isotropic shape changes. Historically, several additives such as calcium phosphate and hydroxyapatite have been incorporated into base hydrogel in order to enhance their mechanical properties. As the field of soft materials mature, hydrogels with good mechanical properties are of great importance in many current and potential applications. Incorporation of layered silicates or clays at micro and nano scales have been implemented in order to enhance the mechanical performance of hydrogels. For example, the nanoscale dispersion of laponite [69,70] and montmorillonite [71–73] resulted in high tensile strength and elongation at break. Cellulosic materials such as nanocrystalline cellulose, microcrystalline cellulose, nano fibrillated and micro fibrillated cellulose are widely used as sustainable reinforcements in polymer composites [74]. The incorporation of nano-fibrillated cellulose (NFC) into polyacrylic

acid hydrogel followed by thermal crosslinking was reported to have enhanced the mechanical performance of these nanocomposites in aqueous environment [75]. The same researchers had previously reported a self-healing hybrid gel consisting of NFC, polyvinyl alcohol (PVA) and borax. NFC reinforcements within the hydrogel system contributed towards an enhanced gel content and compressive mechanical properties whilst restricting the swelling of hydrogel network [76]. Aspect ratio of the additives also plays a key role in the improvement of mechanical properties of the hydrogel. Hydrogel composites containing fibrous reinforcements have been reported for applications as diverse as controlled drug release, tissue constructs with tailorable mechanical properties and also to mediate actuation response. Han *et al.* reported a composite gel of poly( $\epsilon$ -caprolactone) (PCL) electrospun fibre mats coupled with poly(ethylene glycol)-poly( $\epsilon$ -caprolactone) diacrylate (PEGPCL) hydrogels for controlled and stable release of an enclosed model hydrophilic protein [77]. Schuurman *et al.* reported bio-printing of thermoplastic polycaprolactone (PCL) as fibres and cell laden alginate hydrogels in alternate layers to fabricate a tailorable stiffness tissue constructs [78]. Etches *et al.* investigated glass and carbon fibre reinforced epoxy hydrogel with improved structural properties and orthotropic actuation response realised by virtue of in-plane reinforcements promoting thickness swelling whilst limiting planar [79].

Aside from increased mechanical properties, the particulates can be multifunctional. Laponite and other modified clays carry negative charge on the surface and forms disc like particles in nano scale. This forms an intercalated network that stabilises the aqueous suspensions forming physical crosslinks between the polymer chains. Particulates can be used to form controlled and connected pore structure within the hydrogels there by increasing the surface area for the stimuli (water) to act on resulting in faster swelling response to the stimulus. These particles of particular size are usually known as diluents which then can be removed from the polymer network after gelation resulting in pores of pre-defined size. The inclusion of minerals was also shown to improve bio-compatibility for specific tissue engineering applications such as bone tissue mineralisation [80]. Hydrogel composite containing bisphosphonate functionalised hyaluronan with bioactive glass (Bioglass 45S5) or ceramics (hydroxyapatite) was reported to be excellent in promoting mineralisation for bone tissue-engineering applications [81,82]. Self-healing nanocomposite hydrogels containing calcium phosphate nanoparticles have also been reported [83]. Incorporating single walled carbon nano-tubes (SWNT) into thermoresponsive hydrogels based on poly(N-isopropylacrylamide) improves the response times of actuators fabricated with them [84]. Here, the strong absorption properties of SWNT are utilised to enable fast thermal and optical (through



infrared) response from actuating hinge regions resulting in shape change. It is evident that composite construction of hydrogels with functional reinforcements have benefits beyond anisotropic volumetric changes utilised to achieve morphing shapes. Therefore, the plurality of compliant materials and their spatial arrangement whether in a composite or multi-layered construction is critical and the manufacturing processes that facilitate these features are vital to developing morphing architectures.

## 1.6 3D and 4D printing

3D printing or more accurately additive manufacturing (AM) is a manufacturing process where a structure is realised from the bottom-up based on computer-aided designs (CAD) as opposed to traditional manufacturing routes such as moulding, milling and assembling. Plastics, metals and ceramics can be used with this process to fabricate structures of varying complexity. There are a wide variety of AM techniques enabling 3D printing of these material types. However, the process begins from a CAD model of the shape to be fabricated which is then digitally 'sliced' to be converted into layer-by-layer information as machine input. Some of the technologies and associated material formulations are proprietary. The common AM techniques are as follows. Selective laser melting (SLM) is an additive manufacturing process where a high powered laser is used to fuse and fabricate a shape from powdered particles. Selective laser sintering (SLS) is a similar technique where the particles are sintered rather than being melted. Parts fabricated using these techniques require further post processing to properly consolidate the shape. PolyJet is a proprietary printing technology from Stratasys where droplets of photopolymer are selectively deposited followed by photopolymerisation in a layer-by-layer fashion to make up the part. Stereolithography (SLA) is a technique of converting liquid materials contained in a resin bath to solid parts by selectively curing them using a light source in a layered fashion. The light source could be a UV laser, or a projector and the process is called photopolymerization. Once printed, the parts require post processing in a UV chamber to fully consolidate the crosslinks in printed parts. Direct Ink Writing (DIW) is a technique in which a compliant material is extruded from a small nozzle whilst being moved across the print platform following precise machine commands. DIW can be divided into filament-based approaches such as robocasting, micropen writing, and fused deposition and droplet-based approaches, such as hot-melt printing and ink-jet printing [85]. These techniques allow for a wide range of material types to be 3D printed. Fused filament fabrication (FFF) or fused deposition modelling (FDM) is a subset of DIW techniques where a continuous filament of thermoplastic polymer fed from a large coil is melted and deposited through a nozzle on to a print bed to fabricate the shape. On cooling, the printed part solidifies

on the print platform. This is by far the most extensively adopted 3D printing technique due to the low-cost nature of the open-source printers based on this technology [86,87].

Incorporating smart materials into the domain of 3D printing would enable time dependant transformation of the printed shapes. The fabrication of such responsive forms that can transform in the time domain is termed as 4D printing. Here, the reconfiguration as a function of time constitutes the 4<sup>th</sup> dimension alongside the 1-3 spatial dimensions. The exact nature of these 'transformations, or 'reconfigurations' needs to be established. Initially, only shape change was considered but now has been expanded to include physical or chemical changes within the printed form in response to the stimuli as reported in [88]. However, the term and process was initiated by a group in MIT [89] and has gained exceptional research interest utilising materials with shape memory and volumetric expansion properties with the reported forms ranging from micro to macro lengthscales [90–93]. The relevance and progression of this technology depend on the development of stimuli responsive smart materials, 3D printers and intelligent design as well as mathematical modelling of the actuation responses [92]. As form, structural properties and functionalities are closely related, 4D printing is envisaged to not only re-configure printed forms but also its properties and functionalities as well. 4D printing is essentially the re-configuration of a 3D printed shape regardless of whether the re-configuration occurs at 1D to 1D, 1D-2D, 1D-3D, 2D-2D, 2D-3D or 3D to 3D space. The transformation of some 4D printed examples are presented in Figure 1.7a-f. These examples and respective actuation mechanisms will be covered in detail in the following sections. 4D printing and morphing of smart materials share the same strategies such as shape memory materials, multi-material systems, composites (with active reinforcement and passive matrix or vice versa) and restricting isotropic swelling to realise morphing shapes

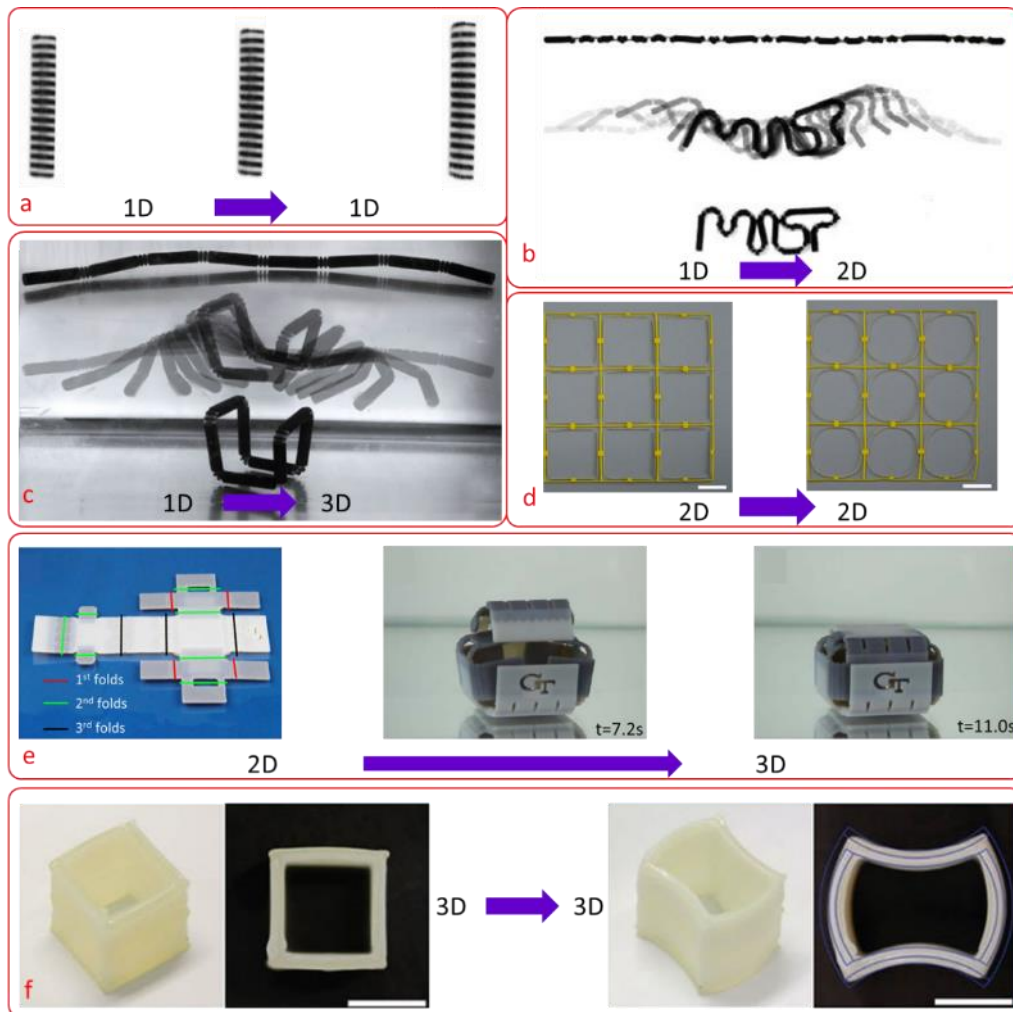


Figure 1.7: Examples of 4D printed transformations. (a) Linear expansion of a 3D printed shape upon swelling in water. Image adapted from [94] and reproduced under Creative Commons Attribution-NonCommercial-NoDerivatives 4.0 International License. (b) 1D-2D transformation upon swelling in water. (c) 1D-3D transformation upon swelling in water. Images adapted from [89] with permission from John Wiley and Sons. (d) 2D-2D transformation of square lattice structure upon heating and cooling resulting in the release of internal strain. (Scale bar = 20 mm). Image adapted from [104] and reproduced under Creative Commons Attribution 4.0 International License. (e) 2D-3D transformation of multi-material sheet into a box upon heating. Image adapted from [101] and reproduced under Creative Commons Attribution 4.0 International License. (f) 3D-3D transformation of cuboid by active preferential swelling in solvent. (Scale bar = 10 mm). Image adapted from [108] and reproduced under Creative Commons Attribution 4.0 International License.

The greatest advantage of 4D printing in realising morphing structures is that it offers great flexibility in terms of material placement in 3D space (by virtue of computer controlled additive manufacturing). This simplifies combining different types of compliant materials in 3D space to generate strain gradients (anisotropic response) from the fabricated parts in response to the stimuli. Furthermore, the design can be coded in digital format which aids visualisation of printed and actuated form (through appropriate modelling and simulation). A greater understanding of smart materials and its response mechanisms to the stimuli could lead to modelling of actuated structures or generate a specific shape to be printed to realise a target geometry through 4D printing. These modelling environments will permit 4D printed

geometries of increasing complexity to be efficiently created in the future minimising the need for physical experimentations to optimise the target form. Several approaches to model the behaviour of particular 4D systems have been employed. These can be classified as forward and inverse problem based approaches. Forward design problems look for the final desired shape after 4D printing given the material structure, material properties, print paths and stimulus properties. Whereas, inverse problem computes the material structure and print parameters required to realise a specific geometry for given material and stimuli [92–94]. Albeit being in its infancy, notable progress has been made by researchers on both fronts for specific material systems, but caution has to be applied when extending the underlying principles governing these models to wider smart material systems mainly due to the complexity of materials and physico-chemical processes involved in 4D printing. The following sections illustrate some examples of 4D printing approaches and resulting actuation based on the type of material used.

#### 1.6.1 Shape memory materials-based approach to 4D printing

Additive manufacturing with shape memory materials have been used to tailor the structural and functional properties. Shape memory alloys such as nickel-titanium (NiTi) have been used to fabricate structures through selective laser melting (SLM) process [95,96]. Incorporating a pre-fabricated shape memory alloy part during a PolyJet process to form actuated joints was reported by Meisel *et al.* [97]. Even though not strictly 3D printing of SMA, this strategy takes advantage of composite construction and layer-by-layer fabrication where the PolyJet process was paused to embed active SMA component followed by resumption of the printing process. The printed form is responsive in the time domain post-printing by virtue of its SMA component. Owing to inherent difficulties in preparing materials for SLM, progress on SMA 4D printing has been slow. Shape memory polymers (SMP) on other hand are actively investigated for 4D printing.

Compared to SMAs, SMPs are easier to engineer with the right attributes to enable 3D printing. Additive manufacturing techniques such as PolyJet [98], stereo lithography (SLA) [99] and fused filament fabrication (FFF) or fused deposition modelling (FDM)[100] can be utilised to fabricate SMP parts. Ge *et al.* fabricated polymer active composites (PAC) utilising proprietary digital materials such as Tangoblack, a rubbery material at room temperature containing urethane acrylate oligomer, Exo-1,7,7-trimethylbicyclo [2.2.1] hept-2-yl acrylate, methacrylate oligomer, polyurethane resin, and photoinitiator and Verowhite, a rigid plastic at room temperature containing isobornyl acrylate, acrylic monomer, urethane acrylate, epoxy acrylate, acrylic monomer, acrylic oligomer, and photoinitiator. The so-called digital

materials allow for these two base materials to be mixed at varying proportions to create new materials with properties in between the two. Tangoblack was used as the matrix where a mixture of Tangoblack and Verowhite (termed Gray 60) was used to fabricate the active shape memory fibres. Thus, the digital materials permit generation of materials with different glass transition temperatures ( $T_g$ ) and also to be incorporated within a single print. This strategy was employed by Mao *et al.* to fabricate sequential self-folding in response to uniform heating as shown in Figure 1.7e and Figure 1.8 [101]. Figure 1.8a shows the schematic of helical SMP component as printed with hinge locations. The programming step involves deforming the helical part to a flat strip. Figure 1.8b shows the activation response of the deformed flat strip with uniform hinges resulting in folding across all the hinges to occur at the same time. As for the sample printed with graded hinges,  $T_g$  of the hinges 1-9 ranges from 30 °C to 65 °C and fold in a sequential fashion upon activation. Figure 1.8c shows the actuation response when the hinges are graded. This resulted in sequential folding of the flat strip at the hinges in the order 1-9 as per the programmed  $T_g$  range. These samples were activated by submerging in hot water at 90 °C.

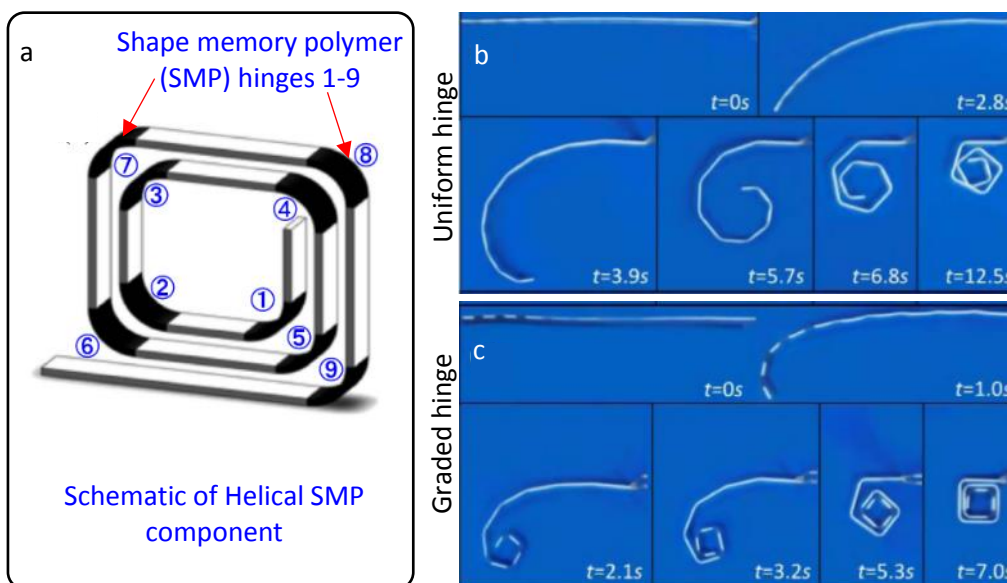


Figure 1.8: Sequential folding of programmed SMP component. (a) Schematic of the component as printed indicating the hinge locations. This was followed by the programming stage of coil being flattened. (b) Response of a control strip with uniform hinges to heating by submersion in water at 90 °C. (c) Response of the sample with graded hinges upon heating by submersion in water at 90 °C. Image adapted from [101] and reproduced under Creative Commons Attribution 4.0 International License.

Shape memory constructs based on polycaprolactone (PCL) fabricated through SLA was reported by Zarek *et al.* [99]. The custom oligomer melt containing PCL macromethacrylate was prepared by heating above its melting point followed by the addition of photoinitiator, inhibitor and dye. Once homogenously mixed, the melt was transferred to the resin bath of an SLA printer and kept at 90 °C during fabrication. Heating above the melting point of the

polymer renders the printed structure pliable and any deformation applied can be fixed by cooling below the melting temperature. Heating the structure above the melting temperature recovers the original shape. Multi-material SLA printing utilising SMP have been reported where the printer allows for automatic exchange of the resins baths during fabrication [102].

FFF/ FDM routes to 3D printing thermoplastic shape memory polymers have been demonstrated using commercially available polymers such as Surlyn 9520 from DuPont, a zinc-neutralised PEMA (poly(ethylene-co-methacrylic acid)) [103] and DiAPLEX MM-4520, a polyurethane elastomer from SMP technologies *Inc.* [100]. Polymer pellets were extruded to form filaments under controlled conditions which was then fed into an FDM printer to fabricate shapes. Figure 1.9a-c shows the transformation of a spring fabricated through FFF using Surlyn 9520 (zinc-neutralized poly(ethylene-co-methacrylic acid) (PEMA)). The printed shape (Figure 1.9a) was deformed at an elevated temperature of 70 °C and fixed in its new configuration by cooling it under load (Figure 1.9b). The printed shape was recovered when heated by immersion in water bath at 70 °C (Figure 1.9c). Shape memory materials can be triggered by a wide range of stimuli. Phase transition, the underlying mechanism for shape memory is activated by heat and can be supplied into the material through direct heating, indirect heating (temperature controlled fluid medium) or optically through infrared. However, the programming step of mechanical deformation at elevated temperature followed by cooling to fix the shape is essential for 4D printed shape memory materials regardless of the 3D printing techniques employed. Even though these examples demonstrate the potential of combining shape memory materials and 3D printing, the human interaction required to train or program (by deforming) is seen as a limitation of this approach with regard to truly stimuli responsive morphing systems.



Figure 1.9: Actuation response of FFF printed spring demonstrating shape memory effect. (a) The spring as printed. (b) After the programming step of deforming at elevated temperature followed by cooling. (c) Recovered shape after heating by immersion in hot water at at 70 °C. (Scale bar = 10 mm). Image adapted from [103] with permission from ACS Publications.

Zhang *et al.* reported a smart and inexpensive demonstration of 4D printing by means of printing thin polylactic acid (PLA) strips on paper substrates fixed on the print-bed using an FFF printer. This strategy utilises stored internal strain energy arising from the thermal expansion and contraction of polymers during the 3D printing process. The thermoplastic polymer has high co-efficient of thermal expansion (CTE) compared to paper substrate. When printed in molten form as longitudinal strips on the substrate at a lower temperature, the subsequent shrinking of PLA on cooling is resisted by the paper substrate setting up internal strain which is locked into this bi-layer configuration. Cutting the paper substrates to the perimeter of printed PLA form completes the fabrication of this composite sheet. A petal architecture thus fabricated is presented in Figure 1.10a. Heating the composite petal architecture on a hot plate above the  $T_g$  of the polymer (with PLA side up) releases the locked-in strain as PLA starts to expand more than paper resulting in a negative curvature as shown in Figure 1.10b. On cooling, PLA shrinks and hardens. As the paper substrate was not fixed to the print bed as it was during the printing stage, the petal architecture had to curl inwards (positive curvature) to balance the CTE of un-strained PLA resulting in the 3D shape shown in Figure 1.10c [104].

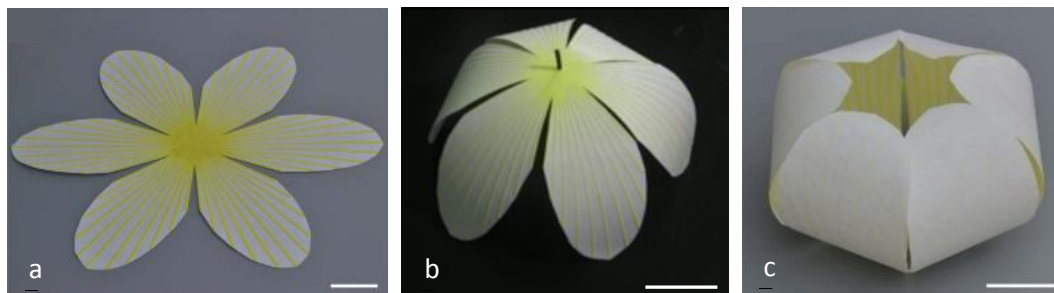


Figure 1.10: Formation of 3D petal architecture from planar sheet. (a) The initial planar shape of composite sheet. (b) Intermediate shape of the petal architecture when placed on a hot-plate at 105 °C (c) The final 3D petal architecture after cooling. (Scale bar = 20 mm). Images adapted from [104] and reproduced under Creative Commons Attribution 4.0 International License.

### 1.6.2 Expanding gels-based approach to 4D printing

3D printing of hydrogels have been actively explored for a multitude of applications especially in the biomedical field for tissue engineering [105,106]. Hydrogel based tissue scaffolds and gels laden with biological materials have been successfully printed using bio-3D printers leading onto attempts at printing replacement human organs known as organ printing [107]. The volumetric expansion of 3D printed hydrogels could be harnessed to realise 4D printing. Bakarich *et al.* demonstrated 4D printing of thermoresponsive alginate/ (poly(N-isopropylacrylamide) (PNIPAAm) ionic covalent entanglement (ICE) gels using an extrusion based 3D-Bioplotter. The bio-ink containing ICE gel and  $\alpha$ -keto glutaric acid as photoinitiator

amongst other ingredients was used to deposit layers according to the CAD model with UV light switched on in between the layers to cure the gels. The final form was then immersed in 0.1 M calcium chloride solution for 72 hrs to fully crosslink the alginate. When heated above the lower critical solution temperature (LCST) temperature ( $T_c \approx 32\text{--}35\text{ }^\circ\text{C}$ ) of PNIPAAm, the printed form shrunk (reversible) by repelling water owing to hydrophilic to hydrophobic (coil–globule) transition of PNIPAAm [90]. This resulted in the shape transformation of the printed form.

Multi-material 3D printing has been effectively used to restrict and guide the otherwise isotropic volumetric expansion of gel forming polymers. This strategy has been utilised to realise various shapes that transforms after 3D printing to the stimuli of water. PolyJet printing technology from Stratasys was used to fabricate shapes containing a rigid plastic and a hydrophilic material that expands up to 200% its original volume when exposed to water. This proprietary material has a composition of vinyl caprolactam (50%wt), polyethylene (30%wt), epoxy diacrylate oligomer (18%wt), Irgacure 819 (1.9%wt), and wetting agent (0.1%w) [94]. Figure 1.7a, b and c are some examples of shape changes realised through this strategy. Transformations were realised through appropriate hinge design as shown in Figure 1.11a, where rigid elements in combination with the expandable material realise programmable transformation of the 3D printed shape. Upon immersion in a water bath, the expandable material and bending element at the hinges behave like a bi-layer where the swelling of expandable material results in anisotropic expansion at the hinges causing it to bend. The spacing between the rigid elements at the hinges allows the deformation to reach the programmed level and locks it in place as shown in Figure 1.11b. This approach to programming is similar to the example presented in Figure 1.5 and have been adopted extensively to program or limit the morphing response of materials.

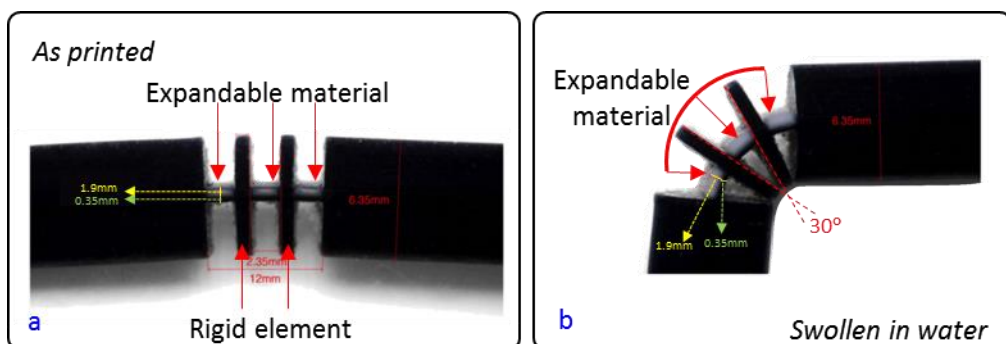


Figure 1.11: Detailed hinge design of PolyJet printed morphing shapes. (a) Hinge as printed. (b) Deformed hinge after swelling in water. Image adapted from [94] and reproduced under Creative Commons Attribution-NonCommercial-NoDerivatives 4.0 International License.



### 1.6.3 Composites-based approach to 4D printing

Composite construction of oriented anisotropic particles within a responsive matrix realised through 3D printing have been demonstrated to have morphing potential. Kokkinis *et al.* reported a multi-material magnetically assisted 3D printing (MM-3D) technique based on direct ink-writing system using a customised 3D Discovery, a bio-printer from regenHU Ltd [108]. Magnetically responsive ink preparation and multi-material capability are crucial to realising morphing with this strategy. The key constituents of the low-viscosity magnetic ink were polyurethane acrylate (PUA) oligomers, reactive diluents, photoinitiator, rheology modifier and modified alumina platelets as the magnetically responsive particles. Magnetisation was realised by means of adsorbing iron oxide nanoparticles on the surface of alumina platelets prior to ink formulation. A viscoelastic ink (shaping ink) without magnetic particles were deposited on the print bed defining the perimeter of the structure at each layer followed by the deposition of low viscosity magnetic ink within the boundary. This restricts the flow of deposited low viscosity magnetic ink. The resulting layer was positioned under a rotating magnetic field (achieved through customised modification to the printer) to orient all the platelets suspended in the magnetic ink in a specific direction. The low viscosity of the magnetic ink is necessary to allow the alignment of platelets to the magnetic field. Exposing the printed layer or part of it through a photomask to ultraviolet light polymerizes and crosslink the ink fixing the platelet orientation in the exposed region. This process was repeated layer by layer to realise the 3D shape with discrete layers of aligned anisotropic particles. When exposed to a suitable solvent (ethyl acetate), these aligned anisotropic particles limited the isotropic volumetric changes induced in the polymer and resulted in programmable actuation. Figure 1.12 shows the actuation of a cube thus fabricated and its actuation response due to anisotropic swelling in a solvent. This strategy is described by the authors as 5D printing where the localised control of materials (multi-material capability) and orientations constitutes the higher dimensions beyond 3D.

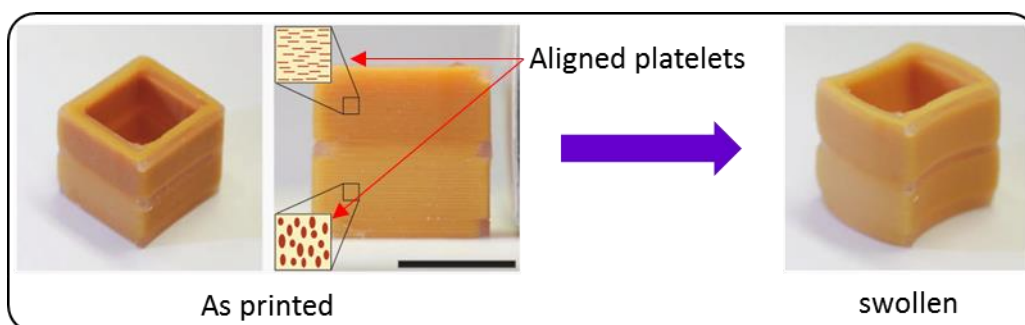


Figure 1.12: Actuation of cuboid with magnetically aligned platelets upon swelling in a solvent (Scale bar = 10 mm). Image adapted from [108] and reproduced under Creative Commons Attribution 4.0 International License.

Gladman *et al.* reported a biomimetic 4D printing system (bio-4DP) where local control of the orientation of cellulose nanofibrils within the hydrogel composite determined the elastic and swelling anisotropy when in contact with a solvent medium [93]. Here, the alignment of cellulose nanofibrils (NFC) was attained by virtue of shear alignment as the composite gel passed through the deposition nozzle of the 3D printer (Figure 1.13a). N,N-dimethylacrylamide or N-isopropylacrylamide based hydrogel containing NFC and photoinitiator (Irgacure 2959) amongst other ingredients were printed on a DIW based 3D printer. The NFC alignment along the print direction and custom print paths (through inverse problem modelling) resulted in programmed anisotropy within the printed form (Figure 1.13b). Once fabricated, the prints were cured under UV light and immersed in de-ionised water to allow swelling and shape change (Figure 1.13c). Figure 1.13b-d shows the printed petal architecture and its gradual morphing over time in de-ionised water. The isotropic swelling of hydrogels was restricted by aligned NFC and resulted in morphing. The incorporation of thermoresponsive N-isopropylacrylamide resulted in reversible shape change on varying the temperature of the water bath. The PNIPAAm moieties become hydrophobic and release water from the hydrogel system once the water bath was heated beyond the LCST of the polymer (32 °C). This reverts the anisotropic swelling and consequently returns the morphed shape back to original state.

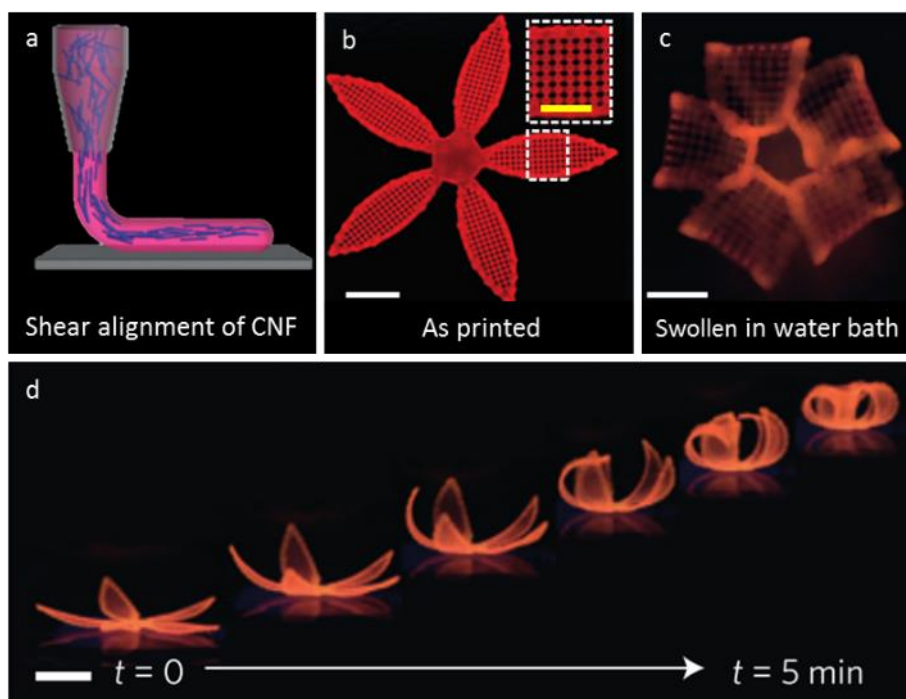


Figure 1.13: Morphing response through the alignment of particulates in a composite gel. (a) Schematic showing the shear induced alignment of cellulose nanofibrils (CNF) as it exit the deposition nozzle. (b) A flower architecture as printed through bio-4D printing. (c) Morphed state of the printed form after swelling in de-ionised water. (d) Series of photographs showing the morphing response from flat to 3D over time when immersed in water. (White scale bar = 5mm; yellow scale bar = 2.5 mm). Image adapted from [93] with permission from Springer Nature.

It can be seen that the developments in 4D printing are largely due to the recent advancements in multi-material 3D printing capabilities. Most of the aforementioned 4D printing examples were fabricated with multi-material 3D printing systems with some proprietary technologies and materials (*e.g.* PolyJet from Stratsys). It can be seen that greater understanding of the actuating principles and design rules allows one to utilise less complicated and economical 3D printers to achieve 4D printing as evidenced by the work of Zhang *et al.* using FFF printers [104]. This is an encouraging sign and will open up the research space for further developments in 4D printing. Besides bottom-up layer-by-layer manufacturing, 4D printing relies on sensory and actuation capabilities that are inherent to the material and structure as observed in nature. This eliminates the need for electrical parts and electro-mechanical systems directly resulting in fewer parts and faster assembly ultimately resulting in better integration between functionalities such as sensing and actuation. However, the current set of materials utilised for 4D printing are predominantly synthetic polymers. The shape memory effect in polymers are attributed to the presence of cyclic groups such as methacrylate which are known to have some health risks. Although it is essential to push the material boundaries to discover and realise the full potential of 4D printing, the importance of incorporating sustainable, natural or bio-derived smart materials to the domain of 4D printing must not be overlooked. 4D printing with such materials is ideally suited to the philosophy of morphogenesis manufacturing and will be pursued in this project

## 1.7 Additive manufacturing with cellulose

Cellulose and its potential as nature's smart material have been discussed before. As one of the most abundant, sustainable and functional material, the prospects of manufacturing using cellulose is very attractive for 3D printing as well as 4D printing. However, cellulose cannot be used with current additive layer manufacturing systems in its native form because it cannot be melted and extruded like typical 3D printing thermoplastics. There are examples of commercially available 3D printing filaments for FFF with cellulosic materials such as sawdust and recycled wood forming fillers within a polymer matrix such as polyester and PLA (Poly lactic acid) [109,110]. These materials have been used in fabricating responsive structures. This method however limits the exposure of cellulosic components to the environment/stimuli and such approaches are not ideal for responsive morphing applications. Correa *et al.* elucidated this point further in [111] where an off-the shelf wood filament was used to fabricate responsive forms due to lack of consistency in commercially available wood filaments. Anisotropic swelling in wood filaments to water/ moisture was also coupled with other 3D printing materials such as nylon and ABS through multi-material 3D printing to realise

actuating forms [111]. Markstedt *et al.* 3D printed cellulose by dissolution in ionic liquid (1-Ethyl-3-methylimidazolium, EmimAc) followed by coagulation in water resulting in 2D and multilayer 3D gel structures on a coagulating bed [112]. Håkansson *et al.* from Chalmers University of technology created composite printing inks by mixing cellulose nanofibrils in a hydrogel consisting of 95-99 % water. The 3D shape in dry state was achieved by means of removing the water through freeze drying from the final print [113]. Similar approaches in cellulose printing were also reported from Aalto University (Finland) and VTT research (Finland) as part of their joint Design Driven Value Chains in the World of Cellulose (DWOC) program [114]. The aforementioned composite approach of incorporating shear aligned NFC in bio-4DP by Gladman *et al.* showcased cellulosic component utilised as reinforcements restricting the swelling of N,N-dimethylacrylamide or N-isopropylacrylamide based hydrogels [93]. As such, research shows that adapting cellulosic materials to the 3D printing domain can be achieved but there is scope for discovery especially with regard to enabling 4D printing of cellulosic smart materials.

## 1.8 Summary

This chapter presented the concept of morphogenesis manufacturing along with some unique features of biological systems that enable them to have well integrated functionalities. Some of the examples presented in the review of smart materials have already taken advantage of these bio-inspired features such as hierarchical structures, multi-material configurations and composite constructions to have embedded sensory and actuation functionalities. Exploration of what constitutes smartness in a material system and the review of current set of smart materials shows that natural and bio-derived materials are unfavourably overlooked in terms of utilising their inherent smartness. This is not ideal in the long term and is the main reason to pursue the concept of morphogenesis manufacturing in realising smart material systems capable of shape change.

Nature's design philosophy for realising functional systems were summarised earlier in the chapter as follows: (1) inherent design either embedded into organisms' genetic code or shaped through the interacting natural forces (2) core building materials embedded with multi-functionality (3) growth as a process which enables precise placement of various building blocks in hierarchical order to realise form as per the embedded design under the influence of environmental stimuli. The 3D and 4D printing process are well suited to meet conditions (1) and (3) as it enables realisation of computer aided designs with unprecedented control of multiple materials in 3D space. Besides bottom-up and layer by layer manufacturing, 4D printing relies on sensing and actuation inherent to the materials as observed in nature.

---

For 4D printing to comply with the philosophy of morphogenesis manufacturing, a compliant smart material is required.

Amongst biological smart materials, cellulose and its derivatives stand out as a worthy candidate to meet the second criteria of core functional building material. As seen in some of the examples, the design of cellulosic fibrils to preferentially control the swelling of an embedding matrix is inspired by nature's design of pinecones [26,115]. Similar to pinecone design, combining a cellulose derived hydrogel with cellulosic reinforcements will permit the development a cost effective, cellulosic smart material. This will not only ensure sustainability of the material components but also guarantee responsiveness. Stimuli responsiveness alone does not contribute towards smartness. Programmability, reliability and repeatability of the material responses are key to smartness and thus serve as precursors to sentience in materials. Therefore, the stimuli responsive mechanisms at play and the design rules to programming in these bio-derived smart materials must be established and understood. Incorporating these materials into the domain of 4D printing is also crucial to exploit the full potential of these biological smart materials.

The potential of 4D printing in realising morphing architectures using a wide variety of material types is evident from the examples presented in Section *1.6 3D and 4D printing*. However, the novelty of the contemporary compliant materials for 4D printing and associated proprietary 3D printers renders the technology rather expensive for easier and widespread implementation. It can be seen from the relevant literature review presented in *1.6 3D and 4D printing* that the developments in 4D printing has been largely due to the advancements in multi-material 3D printing especially through PolyJet and SLA technologies. Unfortunately, the prohibitive costs and proprietary materials associated with 4D printing technology had hindered its extensive adoption and further advancements to an extent. 3D printing in general is experiencing a widespread popularity thanks to low cost 3D printers empowered through open-source projects such as RepRap [86,116]. This is driving down the cost of 3D printers and makes technologies such as FFF, SLA and SLM more accessible for researches and wider public alike. Apart from developing a bio-inspired smart material system capable of morphing that aligns to morphogenesis manufacturing, this project will also aim to address this issue by using materials and technologies that are sustainable, cost-effective and easily accessible.

The next generation of composites will be multi-functional in nature incorporating additional functionalities to structural requirements akin to natural systems. Perhaps the developments in the research towards artificial intelligence (AI) could see materials with inherent intelligence

---

beyond the responsiveness that we seek to impart to the composites or materials in general. This inherent intelligence could potentially pave way to systems with greater adaptability, self-sustainability and self-maintenance. It is envisaged that in future the boundaries between materials, form and function would be seamless and the synergy between these could lead not just to multi-functionality but to sentient material systems like the higher forms of life observed in nature. It is imperative that the material offerings developed for responsive systems are from sustainable resources and have low ecological footprint. The project undertaken here is characterised by bio-inspiration not only in terms of design, materials and function of the smart material system developed here but also in terms of its impact on the ecosystem. This material system is aimed for reactive morphing (sensing and actuation) applications and contributes towards the development of an open manufacturing process where the final structure is not limited to one configuration but has many. The transformations between the programmed configurations adhere to the principles of folding techniques such as origami and kirigami and are mediated through the material response to the stimulus of hydration. This thesis will report the work carried out on developing eco-friendly, sustainable smart material systems capable of programmable shape transformations inspired by the biological systems. These sustainable smart materials in combination with the additive manufacturing techniques are envisaged to result in programmable morphing architectures as realised in nature. Therefore, the process is aptly termed as Morphogenesis Manufacturing akin to the biological process of morphogenesis which concerns with the development of form in an organism and the functionalities arising from it.

## 1.9 Outline of the thesis

The primary objective of this project was to investigate new materials capable of shape transformation or morphing. The project began as an eXtended Project (XP) within the ACCIS CDT program and the work carried out during this short project is also included here for completeness. This report was assessed internally, but it did not contribute to academic credits. Examples of morphing are ubiquitous in nature and thus the research into bio-inspired engineering solutions and an in-depth understanding of morphing examples in nature were warranted to establish the direction of the project. The concept of Morphogenesis Manufacturing was developed and adopted to ensure the material and process developments undertaken to realise the primary objective are sustainable with minimum ecological impact. This thesis reports the work carried out in realising bio-inspired smart composite capable of programmable shape transformations.

This thesis is divided into six chapters.

---

Chapter 1 serves many functions. Firstly, a brief introduction of the key aspects of this project and its significance relative to the wider research landscape are presented. This is followed by an overview of composite materials and the philosophy of Morphogenesis Manufacturing as a sustainable route to achieving multi-functionality as observed in nature. Bio-inspiration in relevance to achieving multi-functionality especially morphing is then discussed. A review of smart materials, particularly soft-smart materials is presented to highlight the materials currently investigated to realise responsive morphing. The merits of additive manufacturing in realising morphing shapes and the current developments in the field of 4D printing are also discussed. This chapter essentially refines the project objectives by identifying the common strategies, potential materials and processes required to realise morphing architectures as envisaged in this project.

Chapter 2 explores the ubiquity of folding in nature and the potential of paper as a viable material for realising morphing architectures. Some of the work presented in this chapter was also reported in the XP project report in its basic form. They are clearly delineated in the chapter even though these works were expanded in its detail through further and in-depth investigation during the PhD project timeline. An in-depth characterisation of the deployment of manually folded paper architectures in water was performed and the related physical and chemical factors were identified. It was also demonstrated that these factors could be manipulated to control the actuation response of paper architectures presenting the possibility of realising programmable shape transformations. This chapter is supported by a journal paper titled *4D fibrous materials: Characterising the deployment of paper architectures*.

Chapter 3 provides an introduction into origami inspired responsive morphing and is aimed to familiarise the readers with the pertinent terms. A review of current approaches and scientific basis in realising origami-based responsive shape change is presented focussing on the complexity of materials or the strategies adopted in realising such forms. Programmable strain gradient/ differential as a powerful means to realise morphing is presented and validated through examples of morphing paper architectures realised through self-folding. Factors affecting the fold creation on paper substrates were identified culminating in the development of design rules for realising morphing architectures using cellulosic substrates. This chapter complements the work presented in Chapter 2 as it represents programmable self-folding of paper architectures whilst Chapter 3 transcribed subsequent deployment of folded substrates in response to the stimuli of water.

---

Chapter 4 presents the development and characterisation of a novel all cellulosic hydrogel composite and auxiliary hydrogel formulations to realise morphing by programming localised strain gradients in a global substrate. Based on the work carried out in Chapter 2 and 3, it was concluded that paper was not an ideal substrate for achieving reliable morphing responses and new means of processing the key cellulosic component are required to alleviate the limitations of paper. The hydrogels and hydrogel composites were specifically formulated to enable syringe-based 3D printing whilst providing necessary storage, aqueous and thermal stability. Some of the work reported in this chapter were presented (presentation and conference proceedings) at the 8<sup>th</sup> International ECCOMAS SMART 2017 Conference held in Madrid. This was further developed into a journal paper titled *Responsive Cellulose-Hydrogel Composites for 4D Printing* and was published.

Chapter 5 confirms the validity of the developed formulations by enabling 3D printing and also reports the custom work carried out in adapting an open-source 3D printer to print the material formulations. The fibre alignment during printing and the resulting mechanical properties relative to the print direction of 3D printed forms were also characterised. Some model morphing architectures were printed and their actuation in response to the stimuli of hydration were also presented confirming programmable shape transformation thereby meeting the objectives set out in this project.

Chapter 6 describes the summary and suggestions for future work which would refine the material and manufacturing processes developed in this project. The work carried out in this project merely demonstrates the potential of cellulose as a reliable, sustainable and cost effective smart material for programmable morphing. Future work as suggested in this chapter is essential to further the understanding of realising functional programmable architectures and to create bespoke forms capable of transforming in complex ways.



## Chapter 2 Morphogenesis through folding – Potential of paper

*The work reported in this chapter contributed towards the publication referenced in [117]*

### 2.1 Introduction

Folding is a key process at the heart of morphing or transformations that occur in nature. Whether it concerns the growth of an embryo into a complex organism or the formation of vast mountain ranges, folding is ubiquitous in nature. In both cases, a two-dimensional flat entity (embryonic disk or tectonic plate) transforms into a three-dimensional entity as a direct result of sequential folding. Other prominent examples of folding in nature are the formation of proteins from polypeptide sequences, insect wings during eclosion (emergence from the pupal case) and opening of petals of flowers such as morning glory and bindweed [118,119]. Figure 2.1 shows some examples of how nature takes advantage of folding to realise growth (3-D shape) and space-efficient deployable structures.

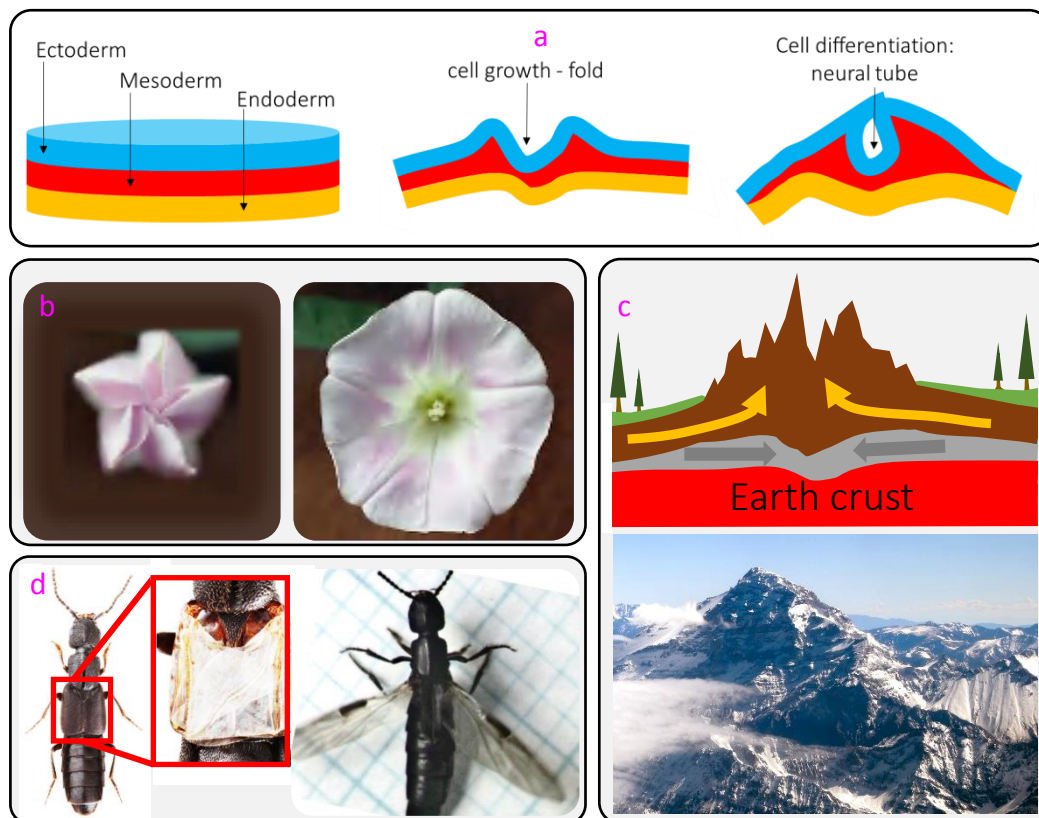


Figure 2.1: Examples of folding in nature. (a) Schematic (Side view) of flat trilaminar embryonic disk forming embryo. (b) Closed and open petals of Bindweed (*Calystegia sepium*). Image adapted from [118] (c) Formation of mountain folds through the movement of tectonic plates. Image adapted from Wikipedia under GNU Lesser General Public License. (d) Stowed away and deployed wing of Rove beetle (*Cafius vestitus*) [119].

The medium of paper has been in use since its invention in ancient China during the Han dynasty (206 BC-220 AD). The use of paper in art especially to create three-dimensional forms

also flourished soon after as the mass production of paper permitted greater affordability [120]. The significance of synergy between arts and science has been previously discussed. Inspired by the morphing examples found in biological world, Japanese scholars (and subsequently the rest of the world) have been developing the art form of origami since the 17<sup>th</sup> century. Today, the once recreational habit of origami has strong links to science and engineering and serves as an inspiration to material and design scientists alike. Hernandez *et al.* has reviewed a range of origami-inspired active structures from synthesis to the final form in [3]. The principles of origami offer unique foldable and compact designs to develop novel and simplistic approaches for manufacturing complex architectures (from 2-dimensional substrates) and also provide an inherent programmed morphing mechanism for active shape change or re-configuration. Forms with finer details and sophistication can also be realised through origami. Irrespective of its complexity, these forms can be reduced to its basics *i.e.* mountain folds and valley folds (Figure 2.2a). As a way of example, Figure 2.2b-d shows miura-ori pattern created from a sheet of paper through successive mountain and valley folds. Figure 2.2b shows the crease (fold) pattern to form miura-ori with a ‘tile’ highlighted. The folded form is shown in Figure 2.2c with the highlighted area showing the change in the basic tile as a result of folding. Whereas, Figure 2.2d shows the side view of miura-ori pattern.

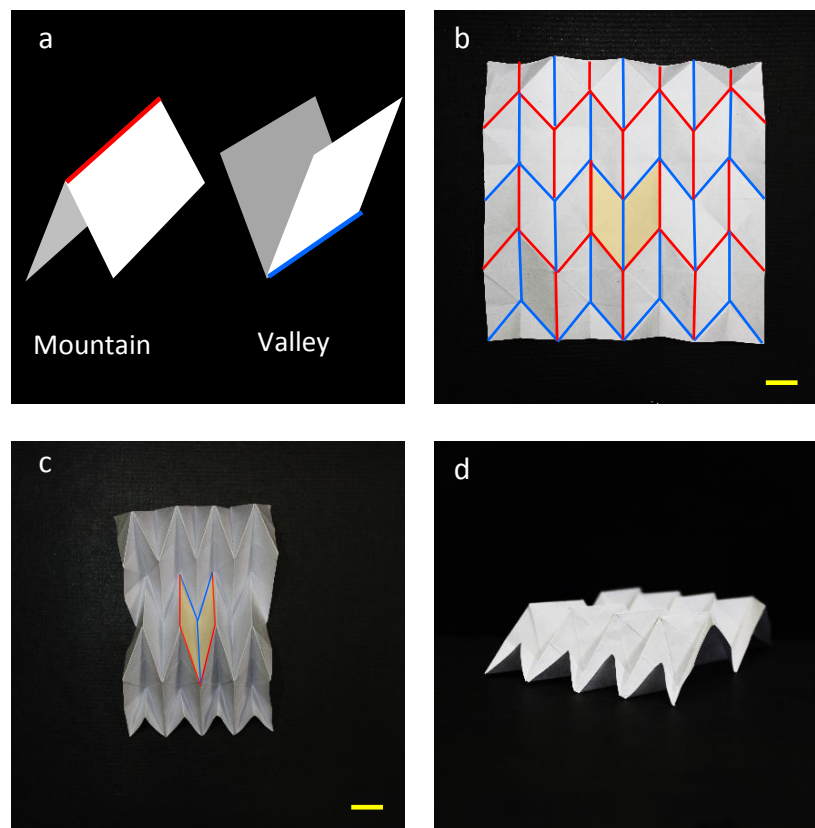


Figure 2.2: (a) Basic origami folds. (b) Miura-ori basic unit and corresponding fold pattern. (c) Folded Miura-ori (top view). (d) Folded Miura-ori pattern (side view). (Scale bar = 25 mm).

Advancements in mathematics has enabled further development of origami in terms of identifying the best possible transformation pathways for a planar sheet of paper to any 3D shape. The ‘Treemaker’ by Robert J Lang [6] and ‘Origamizer’ by Tomohiro Tachi [8] are mathematical programs that output the fold (crease) pattern for a given 3D geometry. These transformation (fold) pathways can be optimised for parameters such as least number of folds, smoothness and maximum stiffness through numerical simulations. The application of origami in engineering can be distinguished under origami engineering which is mainly concerned with deployable structures, morphing, auxetics and meta-material research. For example, researchers have been exploring these concepts for effective space saving solutions for deployable structures across a variety of length scales from Microelectromechanical systems (MEMS) to heart stents to space-masts/booms[121–123]. Origami and associated techniques such as kirigami (cutting paper) exploits traditional folding processes (*i.e.* mountain and valley folds) in realising elaborate forms that can morph through bi-stable or multi-stable configurations using low activation energies.

Combining self-actuation and morphing is an attractive prospect. The inherent ability of smart materials reviewed in Chapter 1 (*1.5 Smart materials*) to convert other forms of energy to mechanical work makes them ideally suited for self-actuating applications *i.e.* self-folding and un-folding. Self-actuating multi-material systems transforming through origami-inspired folding have been reported in the literature for diverse stimuli methods; for example, employing polymer swelling and shrinking [124], shape-memory materials [125] and magnetic materials [22]. To date, numerous stimulus have been reported in the open literature, such as water, light (photoactive), temperature, pH, electric field, specific solvent and enzymes [1,126,127]. Figure 2.3 shows some of the origami-inspired morphing examples reported in open literature. Whist the actuation examples presented in Figure 2.3a and c are stimuli responsive (to heat and water [89] respectively), Figure 2.3b and d requires external energy to be supplied (resistive heating [51] and pneumatics [128] respectively) to be actuated albeit all four examples adhering to origami or kirigami folding principles. The materials and strategies used to fabricate these examples (*i.e.* shape memory materials, hygroscopic polymers and bi-stable architectures) are being rigorously researched upon to develop new morphing or actuating forms. Paper, one of the ancient material produced can also be used to realise morphing architectures. Cellulose is the primary constituent in paper and the hygroscopic swelling of cellulose can be harnessed to manufacture self-actuating forms. For example, bi-layer natural cellulose composites (based on Timoshenko’s research on bimetallic strips [129]) have been studied to develop self-actuating components triggered by the swelling

differential across neighbouring layers. Similar to the bi-metallic strip, the cellulose bi-layer design results in a bending moment to accommodate the through-thickness induced strain in the material [130]. This approach has been reported for paper-plastic [115], wood veneer-glass epoxy composites [131] and natural fibre- maleic anhydride grafted polypropylene (MAPP) [25]. However, understanding and controlling the underlying principles of deployment of cellulose-based architectures are yet to be adequately fathomed.

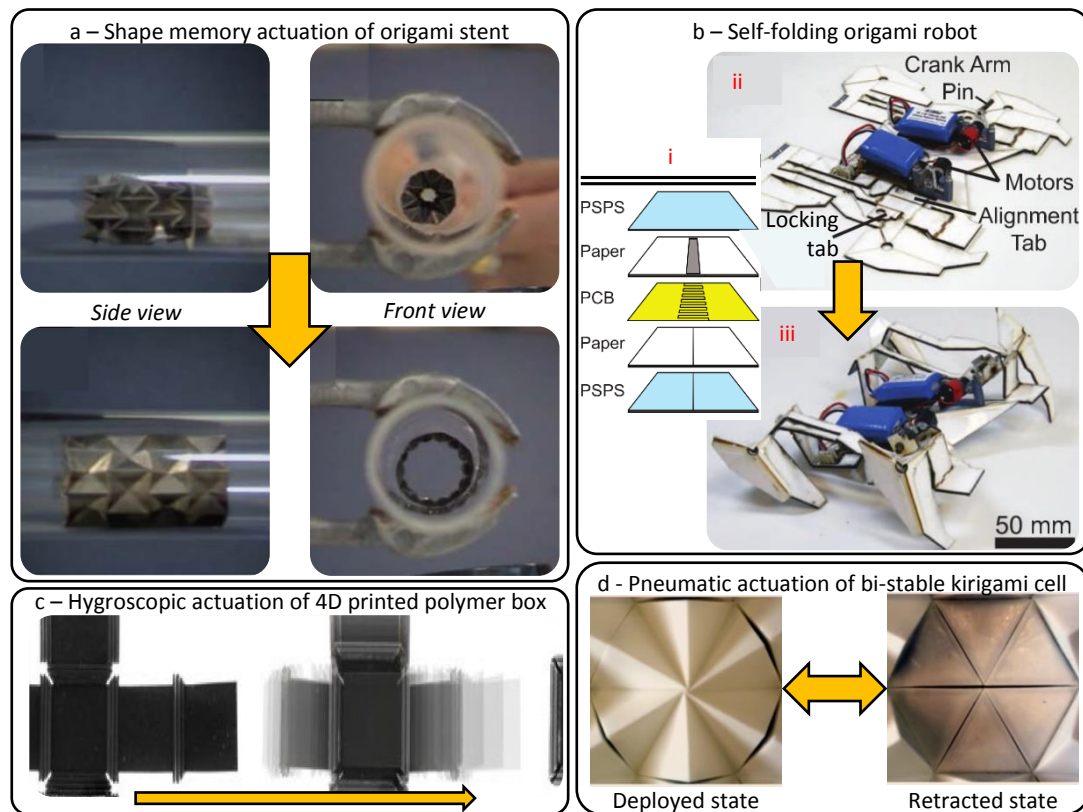


Figure 2.3: Examples of origami inspired self-actuation. (a) Actuation of a Ni-rich TiNi shape memory stent at 319 K. Image adapted from [122] with permission from Elsevier. (b) Self folding origami robot: [i] composite hinge scheme; PSPS-pre-stretched polystyrene, [ii] flat configuration and [iii] folded configuration. Image adapted from [51] with permission from The American Association for the Advancement of Science. (c) Actuation of 4D printed (rigid phase + hydrophilic) polymeric box. Image adapted from [89] with permission from John Wiley and Sons. (d) Pneumatic actuation of locally reinforced silicone kirigami cell. Image adapted from [128] with permission from IOP Publishing.

By way of example, the work by Etienne Cliquet (Figure 2.4) in his Flotilla art exhibition [132], show the unfolding deployment of multiple paper origami folds once in contact with water. Unlike the aforementioned bi-layer synthetic systems, this material lacks any distinct active or passive layers, or layered architecture as observed in pine cones [22] and wheat awns [2,26,133] controlling the through-thickness strain gradient, and yet still deploys in a timely fashion without the complexity of previous work. Understanding the science behind this actuation allows the development of simplistic approaches for engineering complex architectures (from 2D substrates) triggered by hydration for active shape change. Owing to

the scalability of origami, this has direct bearing on the development of self-actuating functional materials as effective space saving solutions for deployable structures across a range of length scales. This chapter aims to better understand and characterise the deployments of paper architectures through a model system. Since cellulose is the principal component of paper, the work carried out in this chapter will also further the understanding of responsive features of cellulose. Different types of paper substrates and stimuli were investigated in the following sections to interpret the physical and chemical parameters that dictates deployment in a model paper architecture. Factors affecting the deployment of paper architectures were also presented along with how variations in these factors affect the actuation time of the model architecture from concealed to fully deployed state. The inherent fold recovery of deployed model paper architectures was considered followed by the functionalisation of cellulose fibres to aid the fold recovery and also to facilitate greater control over the deployment response. The effect of hydration and deployment in multi-layered stacked paper architectures were also investigated.

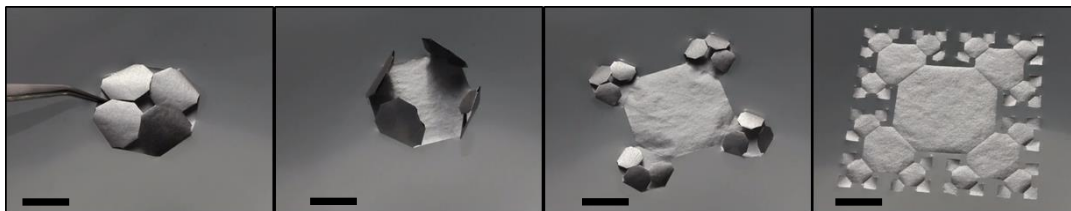


Figure 2.4: Sequential deployment of hierarchical paper folds in water (Scale bar = 10 mm) – Flotilla [132].

## 2.2 Characterisation of paper deployments

This section aims to characterise the deployment mechanisms for different paper architectures capturing the specific folding/unfolding design rules for future synthetic composite material systems. Understanding the role of the substrate, its architecture and the environmental stimulus is essential to decipher the science behind the deployment of paper architectures in water. The global microstructure of the substrate as well as the localised microstructure at the fold regions are also important. The following sections will systematically investigate the substrates, stimuli (actuating media) and the fold lines to understand the deployment behaviour exhibited by manually folded paper architectures

### 2.2.1 Materials

A number of commercial paper types characterised by their weight (usually referred to as grammage (gsm - grams/ square meter)) and origins were investigated to ascertain the effect of microstructure, filler, and fibre type on the rate of deployment. The paper types selected in this study were: Printer paper (90 gsm) (A4 Advanced Laser Paper) from Office Depot,

handmade Lokta (60 gsm), handmade Lokta (30 gsm), and handmade Sekishu (30 gsm) from Paper works ([www.paperworks.uk.com](http://www.paperworks.uk.com)). All paper types were used as received. Reagent grade water from Fisher Scientific was used as received for the actuation experiments. Scolacell (carboxymethyl cellulose sodium salt) was purchased from Scolaquip ([www.scolaquip.co.uk](http://www.scolaquip.co.uk)) and used as received. Methanol (99.8 %), Ethanol (99.5 %) and Glycerol (anhydrous,  $\geq 99.5$  %) were obtained from Sigma Aldrich and used as received. Household olive oil for cooking was purchased from local supermarket and used as such. Molecular sieves for adsorbing water from polar liquids (zeolite beads, 3Å) were obtained from Sigma Aldrich and activated by heating at 200 °C overnight followed by cooling to room temperature prior to use.

Along with its principal component cellulose pulp, commercial printer paper is manufactured with the addition of fillers (such as calcium carbonate, kaolin, talc and TiO<sub>2</sub> [134]) and sizing agents to improve the colour and ink absorption. Conversely, Lokta and Sekishu papers are handmade fine art papers made from the fibres of the Lokta plant (*Daphne papyracea*) from Nepal and the Kozo plant (*Broussonetia papyrifera*) from Sekishu region in Japan respectively. They are un-sized and lack any additional filler material. This spectrum of samples will elucidate the influence of grammage, origin, processing routes and fillers in governing the deployment of paper architectures.

### 2.2.2 Paper Microstructure

The physical construction of each paper type was characterised by light microscopy (Zeiss AX10) and scanning electron microscopy (JSM-IT300). Figure 2.5a-d shows the substantial differences in the microstructure and constituents across the 4 different sample types. From these observations, the printer paper can be considered an analogue to synthetic structural composite materials; where the fibres act as the reinforcement phase whilst the filler material forming the adjoining supporting matrix. Conversely, the handmade paper types essentially consist of a series of inter-connected short fibre bundles arranged in discrete layers. As the middle column in Figure 2.5 illustrates, the handmade papers have an open fibrous architecture showing excellent pore connectivity both intra-ply and inter-ply as evidenced by the free space in between the fibres in the micrographs.

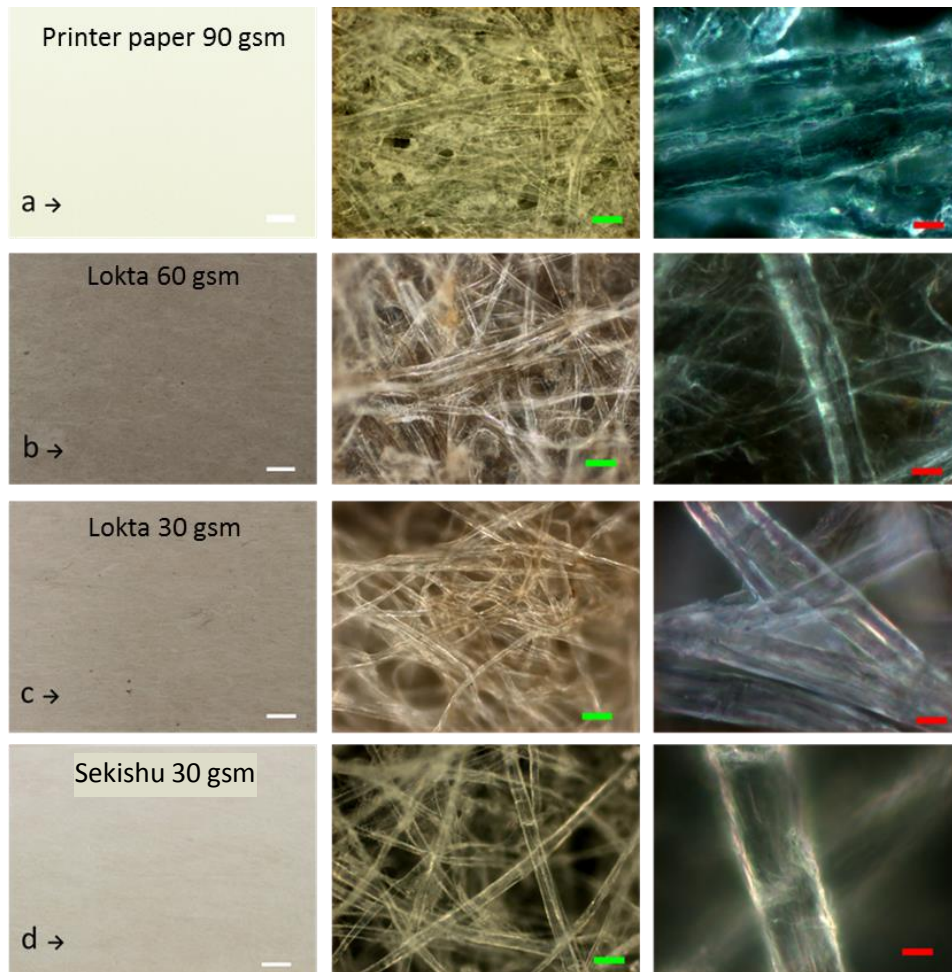


Figure 2.5: Microstructure of paper types. (a) Printer paper 90 gsm, (b) Lokta 60 gsm, (c) Lokta 30 gsm and (d) Sekishu 30 gsm. (White scale bar = 10 mm; Green scale bar = 50  $\mu\text{m}$ ; Red scale bar = 10  $\mu\text{m}$ ).

### 2.2.3 Contact angle measurements of paper substrates

Characterising the role of the stimulus in this model system (namely, the fluid-surface and fluid-transport interaction) is essential to understand and develop clear design guidelines concerning the specific folding/unfolding rules for future synthetic fibrous morphing material systems. Wetting and fluid impregnation are immensely dependent on the surface properties even in a molecularly homogenous substrate. Clearly, the surface properties of the different paper types will greatly affect the fluid transport on the surface as well as the transport mechanisms through and into the bulk of the material. The ease with which water can 'wet' or saturate a surface is dependent on the hydrophilicity of the substrate. Contact angle measurements provide a quantitative measure of the hydrophilicity and thereby wettability of a substrate. Contact angle ( $\theta$ ) is defined as the angle produced by a droplet of a fluid on the substrate under investigation (Figure 2.6). In essence, the angle formed is the consequence of equilibrium between the adhesive and cohesive forces within the surface and liquid. In these tests, complete wetting is defined when the contact angle reaches  $\theta = 0^\circ$ , whereas  $0^\circ < \theta <$

$90^\circ$  indicates that the surface is 'wetable' and  $\theta > 90^\circ$  signifies that a substrate is 'not wettable'. In order to quantify the 'wettability' of the surfaces under investigation, a series of contact angle measurements were carried out on the samples using a Drop Shape Analyser (KRÜSS DSA 100).

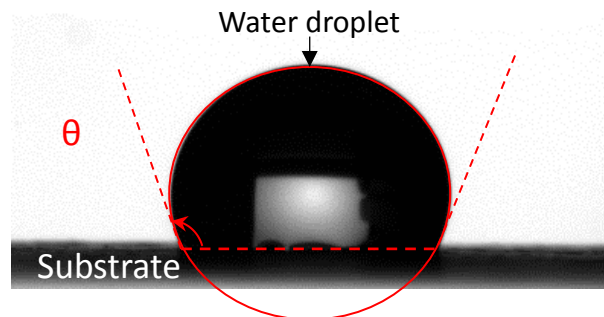


Figure 2.6: Contact angle.

Due to the inherent porosity and absorbing nature of the paper substrates, a static assessment of contact angle was not possible. However, in order to fully quantify the change in contact angle with time, a continuous assessment of droplet absorption over a set time period was undertaken. Figure 2.7 shows an average of five runs from various regions across two different samples of each paper type. The error bars represent the standard deviation of contact angle at the respective time frames. Error bars were selectively represented as shown in Figure 2.7 for clarity. The swelling and out-of-plane deformation (wrinkles) of the substrate generated by the absorbed droplet led to erroneous contact angle data being recorded towards the end of complete absorption and therefore, only stable regions were considered in Figure 2.7. The out-of-plane wrinkles were particularly disruptive on hand made paper specimens and resulted in erroneous high contact angle measurements - it was noted that the water droplet was eventually absorbed by all substrates but the decay in the contact angle was masked by the increase in swelling size of the substrate and wrinkles during hydration. The accompanying analysing software DSA4 from KRÜSS could not factor in the wrinkles and record the actual contact angle.

The contact angle values at time  $(t) = 0$  gives a comparative representation of factors such as roughness and surface chemistry, and thus wettability of the paper types investigated. Whilst great care was undertaken to test comparable specimens and regions of volume fraction, the tortuosity of the surface profile under the droplet will strongly influence the initial contact angle values. The recorded contact angle values for the Lokta 30 gsm and 60 gsm specimens at time  $(t) = 0$  confirms this, despite being produced from the same fibrous material (*i.e.* chemically similar). The change in contact angle with time is representative of the absorption of water into the paper substrates due to the internal microstructure and inherent porosity as



opposed to the molecular composition of the substrate. The variation in microstructure (porosity) owing to wrinkles is understood to be the source of high standard deviation at the later stages of absorption. It can be seen that the fillers and sized fibres in printer paper resist the droplet absorption into the substrate, which is evidenced by the very marginal time dependant change in contact angle observed in printer paper [135].

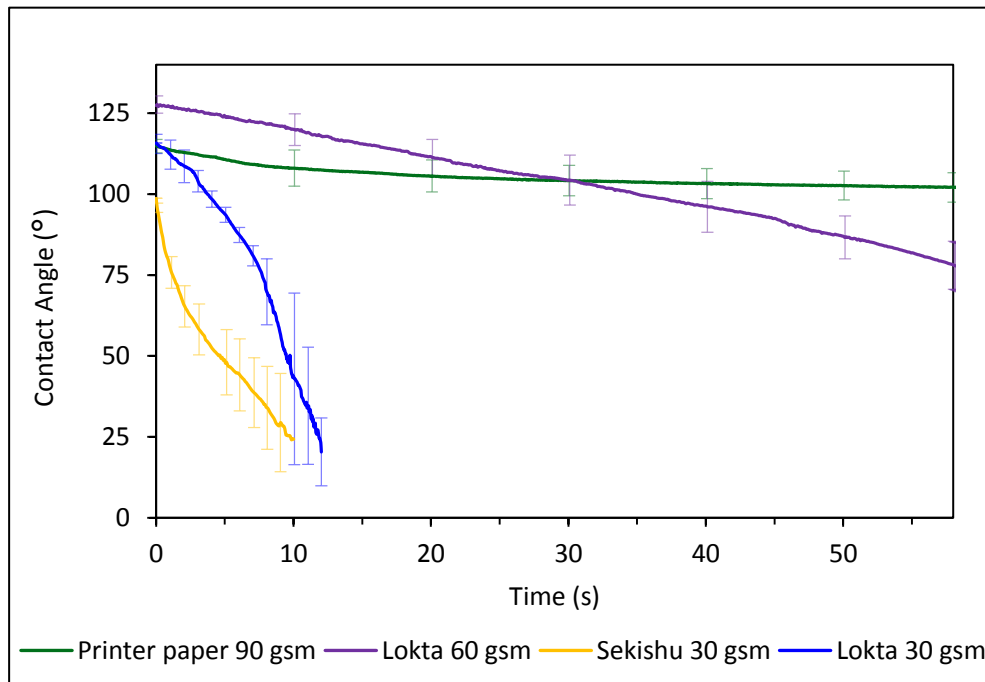


Figure 2.7: Stable contact angle of different paper types during droplet absorption as a function of time.

#### 2.2.4 Shape selection

To systematically characterise the folding/unfolding behaviour of the different paper microstructure, a model (manually folded) cross shape architecture (as shown in Figure 2.8) was chosen for evaluation. This geometrical shape simplifies the ‘valley’ fold creation, whilst also enabling the longitudinal and transverse ‘arms’ to be evaluated concurrently (thus demonstrating any fibre bias which might have occurred in the creation of the paper sheet). The profile dimensions were chosen so as to maximise the sample contact area with the fluid medium. The profile was generated in CAD, printed on an A4 sheet of paper using a laser printer, and then extracted. As for the handmade papers, the printed profiles were used as a stencil to extract samples. The extracted cross profile was then folded manually with three valley folds spaced 5 mm apart in each ‘leg’. The representative deployment sequence for a folded configuration is shown in Figure 2.8. The time taken to reveal the full profile from the folded shape was termed as actuation time and this will be the key parameter investigated in this study to understand the deployment of paper architectures. It was observed that natural drying (at room temperature, 21 °C) of the fully deployed samples resulted in partial shape

recovery of the original folded architecture; especially for the printer paper 90 gsm samples. This behaviour is advantageous and is investigated in greater detail in Section 2.4 *Fold recovery upon drying*.

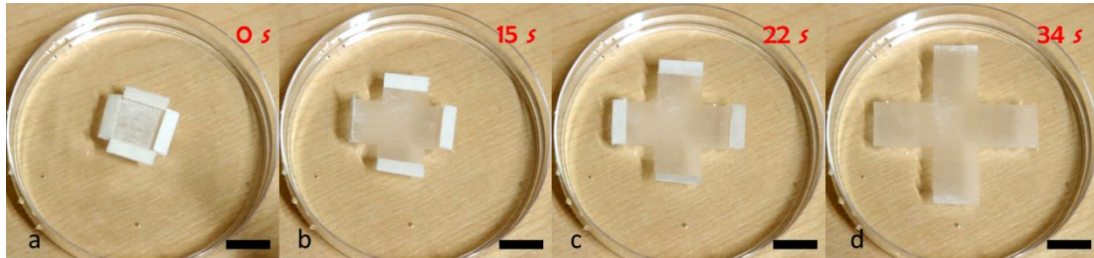


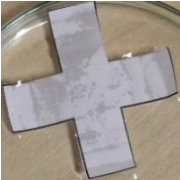



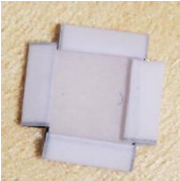
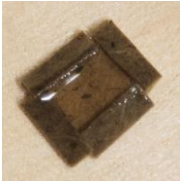


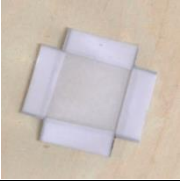
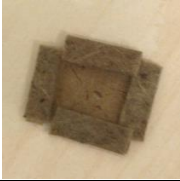
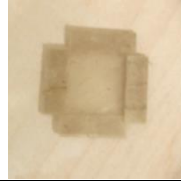
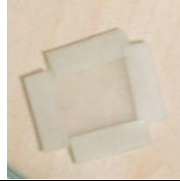

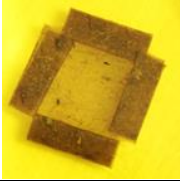
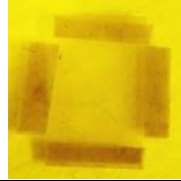


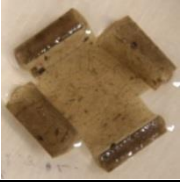


Figure 2.8: Deployment sequence (a-d) of the folded profile of Sekishu paper. (Scale bar = 15 mm).

### 2.2.5 Actuation media

In order to ascertain the relationship of microstructural permeability, chemical and physical interactions in structural deployment, a number of liquid media were used to actuate the different paper architectures, namely water (the primary stimulus), oil (olive oil with a viscosity of approximately 100 centistokes (cSt) [136]) and alcohol (methanol, ethanol, and glycerol). The results of these experiments are discussed in detail in the following sections.

A summary of deployment trials in a variety of actuation media is shown in Table 2.1. The average actuation time (from closed to fully deployed) in water for a minimum of 5 samples per paper type are presented in Table 2.1. The results indicate that printer paper took the longest to deploy to reveal the full profile, and had greater standard deviation compared to other paper types. It is speculated that the chemical treatments and additional fillers to improve ink absorption and arrest discolouration inhibit the water ingress, thus delaying the valley fold deployment. The greater standard deviation was attributed to the non-uniform microstructure resulting from the commercial printer paper manufacturing process. Due to the continuous nature of the process and various material constituents involved in printer paper manufacturing, the consistency can vary significantly, even in a single sheet of paper [137]. Printer paper is known to have a preferential fibre direction owing to the shear alignment of pulp fibres during the manufacturing process which is termed as machine direction. The orthogonal direction is referred to as cross direction. For example, a small difference of  $\pm 2$  seconds in the time required to open each of the folds in the transverse and longitudinal 'legs' (with respect to the machine direction in the global sheet of paper from which the samples were extracted) was observed for the 90 gsm printer paper in water; indicating a bias in fibre direction due to the processing method. Since this difference was minimal, the variation in actuation time as a result of fibre directionality bias was not explored further.

Table 2.1: Summary of paper type actuation in different liquid mediums at room temperature (25 °C)

	Printer paper	Lokta 60	Lokta 30	Sekishu 30
Water	Full deployment 313.1 ± 152.4 s 	Full deployment 132 ± 9.80 s 	Full deployment 25.2 ± 4.47 s 	Full deployment 37.6 ± 11.8 s 
Ethanol	sank without opening 	sank without opening 	sank without opening 	sank without opening 
Methanol	sank without opening 	sank without opening 	sank without opening 	sank without opening 
Olive Oil	sank without opening 	sank without opening 	sank without opening 	sank without opening 
Glycerol anhydrous (used as received)	sank and partially opened over night 	sank and partially opened over night 	sank and partially opened (4 hrs) 	sank and partially opened (6 hrs) 

It was observed that all the paper types could be deployed to some (partial) extent using a moist environment created using wet tissues in an enclosed chamber; in these environments, it was noted that the actuation time was higher, *i.e.* Lokta 30 gsm deployed in approximately 2 hours in a moist room temperature environment and for comparison only took 30 seconds when placed in a water bath. This response is clearly a function of the volume and rate of water required to permeate, react and soften the fibre architecture for deployment. Additionally, methanol (99.8 %), ethanol (99.5 %) and olive oil were investigated but it was noted that whilst they completely wetted out the samples, none of these systems were

capable of triggering the actuation sequence in any of the paper architectures considered here. On the other hand, glycerol did trigger a partial deployment sequence but only after specimen saturation had been attained (typically this took many hours). Table 2.1 summarises the final result/position of deployment trials for different liquid stimuli. The unfolding response is believed to be triggered by molecular interactions between cellulose fibres and that of water and glycerol rather than fluid flow and substrate saturation alone. The spectrum of actuation media investigated in this study alludes to the significance of molecular interactions alongside the effect of flow propagation, substrate saturation, viscosity and permeation in governing or triggering the actuation. Glycerol is reported to interact with the hydroxyl groups in the cellulose chains and is supported by its use as a softener for cellulosic fibres in paper making. In most applications, glycerol in conjunction with water act as humectant-plasticiser but is also reported to have a direct plasticising effect in conditions devoid of water as well [138]. Due to the hygroscopic nature of glycerol, it is possible for water to be present in glycerol. The experiments in glycerol were repeated using activated molecular sieves (diameter of 3 Å) that would absorb water in the actuation medium (glycerol) if present. Similar actuation response with regard to actuation time and extent of deployment were observed confirming that the actuation was in fact due to glycerol [135].

### 2.3 Fold Lines

The basic (mountain and valley) folds are key to realising the packing efficiency in origami based architectures. However, for paper architectures, folding involves permanently deforming the surface beyond its elastic limit. In origami terms, such folds are referred to as creases. From a structural point of view, this pre-stressing is detrimental and likely to result in internal defects which would typically limit the usefulness of the structure. When folds are created in paper, one side undergoes extension whilst the other exhibits localised compressive deformation. Understanding the nature and magnitude of the internal damage, and its role on the deployment kinetics, is essential in the design of multi-deployable architectures.

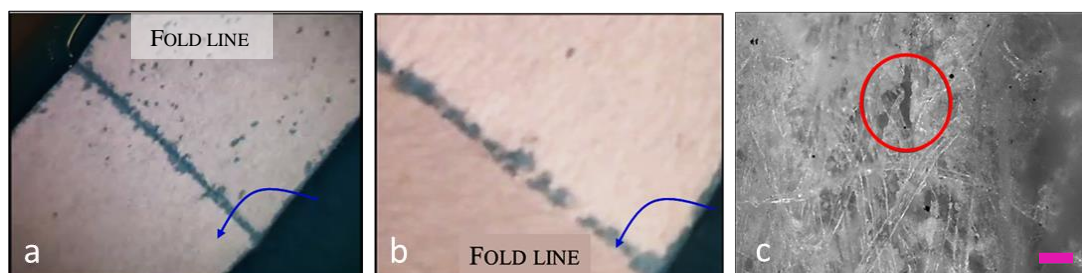


Figure 2.9: Saturation in printer paper 90 gsm and subsequent deployment. (a) Development of low resistance flow paths. (b) Close-up view. Blue arrows indicate deployment direction. (c) Cracks formed in printer paper as the consequence of folding. (Scale bar = 20  $\mu\text{m}$ ).

A comprehensive examination of the folded region revealed that the fibres are not torn when the folds are created but deform and re-position themselves to minimise the local strain field. The localised strain developed in printer paper during folding results in cracks being developed in filler materials as they are typically brittle and cannot absorb the energy of folding. These cracks then serve as a low resistance flow path for penetrating liquids as shown in Figure 2.9a-c. For improved visualisation, water was coloured with blue food dye. A number of global and local features (such as overlapping fibrous network and hierarchical cellulose fibres respectively) equips the fold line to withstand high local strains without failure. It is hypothesized that the overlapping fibre network (seen in Figure 2.5) provides pseudo-ductility by rearranging the local architecture to absorb the global energy of folding. Furthermore, the hierarchical nature of micro-fibrils provides flexibility to the individual fibres through stretching and/or twisting mechanisms at the nano scale. The localised delamination between the adjacent layers is another means of dissipating the energy of folding. These mechanisms operating on a nano, micro and macro level ensure that the fibres can withstand the sharp folds without premature failure. Contrary to synthetic man-made composites which rely on interfacial chemical bonding, the individual layers in paper are held together by means of hydrogen bonds which offer reversible adhesion by hydration and dehydration.

The actuation of paper folds can be compared to that of shape memory materials as the pre-programming step (pre-stretch) is analogous to manually creating crease lines and folding. In shape memory materials, the mechanical energy imparted is stored within the materials as molecular/ atomistic reorganisation which is then released in the presence of an appropriate stimuli. In paper architectures, the unique ability of the fibrous network to locally re-arrange itself along, and either side of, the valley fold line permits the creation of stored energy. The localised re-organisation in paper architectures develops to minimise local in-plane and out-of-plane bending stress. The stored energy is released for subsequent deployment of the folded region when triggered by the stimulus of hydration. In this system, deployment is governed by (1) the softening of the bonds between the fibres (and matrix for printer paper), which triggers both (2) the release of the stored elastic energy (to minimise the bending stress gradient within the folded region), and (3) the swelling of the fibre network resulting in a geometric change (strain gradient) propagating through the thickness of the folded region. To further elucidate this point, Figure 2.10a-d illustrates the changes in substrate microstructure due to folding in handmade Sekishu 30 gsm paper. It can be seen that the fibres are re-arranged in a manner that they are closely aligned to the direction perpendicular to fold line, thus increasing the fibre volume fraction locally and increasing the bending stiffness of this

region. The global fibre volume fraction ( $V_f$ ) across the folded region remains constant, despite the increase in  $V_f$  at the fold line; whilst in the outside adjacent regions, the  $V_f$  is lower creating a zone of graded permeability (and for this specific application, the creation of a low resistance flow path for any penetrating liquid, see Figure 2.10c). This observation holds true for all the handmade paper types investigated in this study [135].

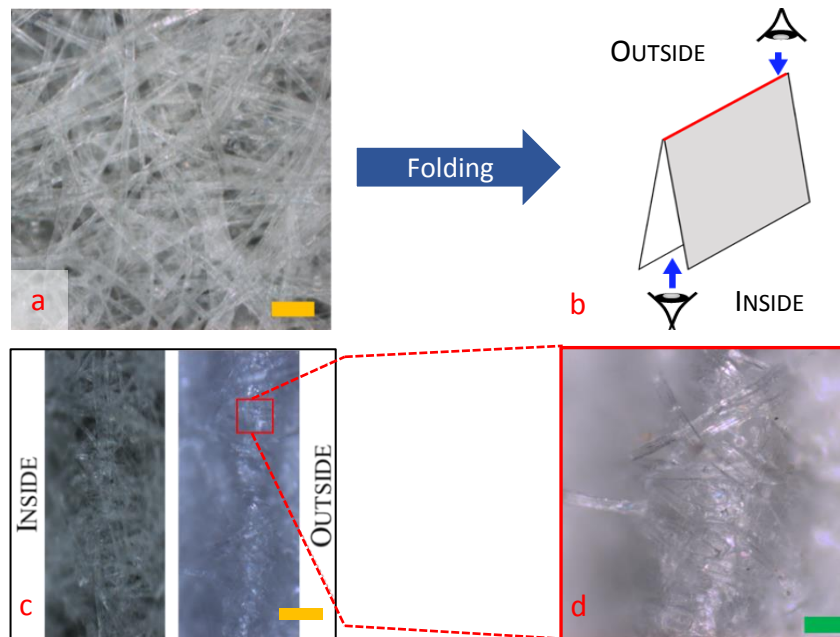


Figure 2.10: Folding in handmade paper types -Sekishu 30 gsm. (a) Before folding. (b) Fold scheme. (c) Fold line visualisation and (d) close-up of outside of the fold line (Gold scale bar = 100  $\mu\text{m}$  and Green scale bar = 50  $\mu\text{m}$ ).

## 2.4 Fold recovery upon drying

As noted in Section 2.2.4 *Shape selection*, natural drying at room temperature resulted in test specimens partially reverting to their initial folded configuration. Figure 2.11a-d shows the recovery attained in the paper types investigated. The printer paper samples showed the greatest recovery (Figure 2.11a), whereas the fold recovery in handmade paper types were not as distinct. The potential for controllable and reversible folding is of substantial interest to the engineering community to realise multiple actuation cycles and consequently a series of experiments were undertaken to quantify the physical and structural motives governing the angle 'recovered' (recovery angle) upon drying.

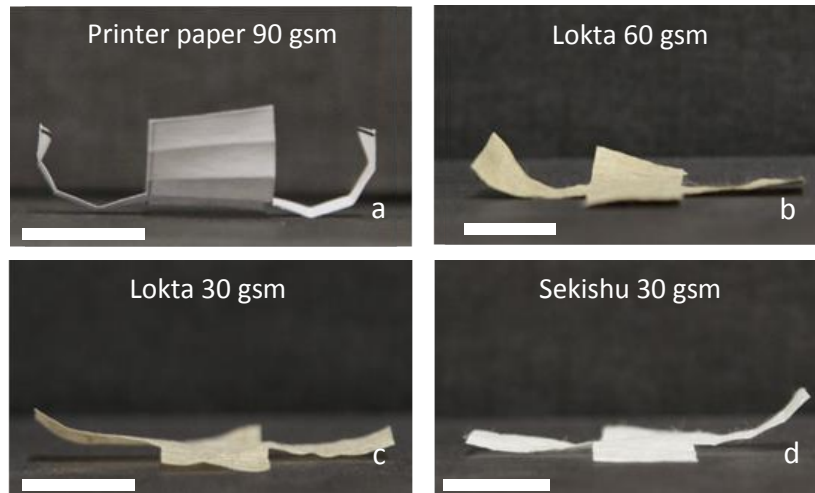
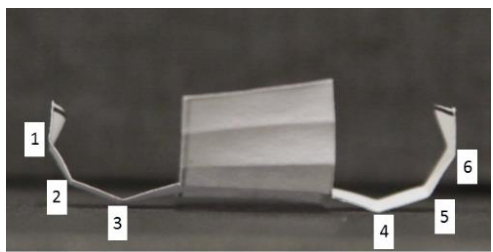


Figure 2.11: Shape recovery after deployment in a water bath at room temperature and drying overnight. (a) Printer paper 90 gsm, (b) Lokta 60 gsm, (c) Lokta 30 gsm and (d) Sekishu 30 gsm. (Scale bar = 15 mm).

To determine the extent of recovery, five samples of printer paper 90 gsm were deployed in a water bath, removed and then dried at room temperature overnight. These experiments were limited to printer paper 90 gsm as they demonstrated the greatest extent of recovery. Photographs from two directions (front view and side view) were taken to provide the means for calculating the recovery angle at each fold line for all four legs in each specimen. Image analysing software ImageJ (version 1.50g) was used to calculate the angle at every fold location. In stowed configuration, the angle between each facet forming the folds is  $0^\circ$ . Once fully deployed in water this angle reaches  $180^\circ$  as they lie flat on the water surface. The recovery fold angle  $\theta_R$ , as reported in Table 2.2, is determined from the difference between the fully deployed angle ( $180^\circ$ ) and the final resting position as shown below in equation 2.1.

$$\text{Recovery angle } (\theta_R) = 180^\circ - \text{angle measured from image analysis} \quad (2.1)$$

Table 2.2: Average recovery angle in printer paper for folds 1-6

for both directions		Average $\theta_R$ ( $^\circ$ )	Std-dev ( $^\circ$ )
	1	44.6	12.9
	2	42.8	8.7
	3	33.3	9.2
	4	39.0	14.7
	5	39.0	7.2
	6	44.8	11.3

The average recovery angle at each folds and the standard deviation were obtained for five samples. The recovery angle results summarised in Table 2.2 revealed an interesting observation concerning the repeatability of recovery angle in the same fold positions on different legs. For example, the outer folds in each leg (folds 1 and 6) and the middle folds in each leg (folds 2 and 5) have very similar values (see Table 2.2). Conversely, the inner folds (3 and 4) show the greatest discrepancy. This variation in ‘actuator’ response is speculated to be a function of the bending moment associated with each fold (which will be greatest at fold 4, since the majority of the paper (moment) arm is outside the fold) and the surface tension of water in ‘pinning’ the paper arm to the surface as it dries. Twisting of the samples upon drying as observed in Figure 2.12 (top row) resulted in a challenging scenario where the angle recovered at each fold line varied along the length of the fold line. Consequently, only one side (for each front and side view) was quantified in this study. This form of minor twisting is believed to be the result of the fibre direction bias and the physical changes occurring in the fibres as they move through the drying cycle (namely, Hornification; discussed in 2.5.1 *Microstructure*). Comparatively, the handmade paper types showed noticeable planar deformations (twisting and wrinkling) compared to more consistent twisting observed in the printer paper (Figure 2.12).

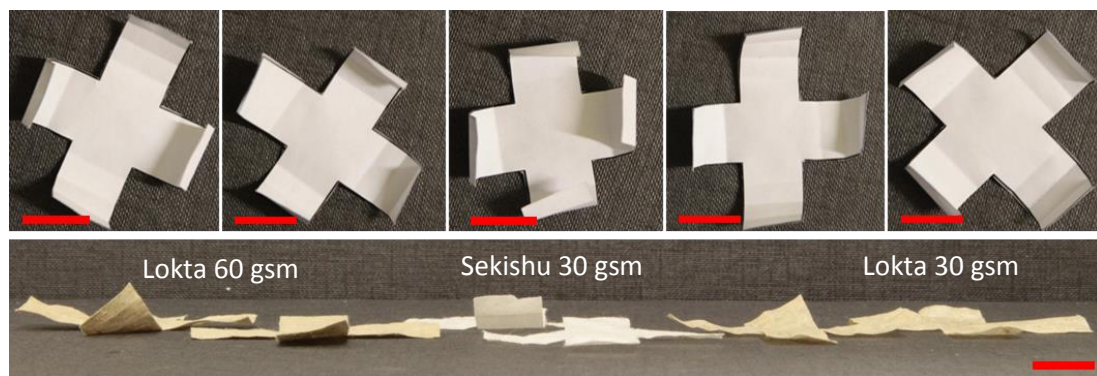


Figure 2.12: (Top row) Twist and recovery observed in five printer paper samples after drying following deployment – top view. (Bottom row) Planar deformations in handmade samples after drying following deployment – side view. (Scale bar = 15 mm).

To demonstrate the role of total fibre content (*i.e.* grammage) on fold angle recovery, a 90 gsm Lokta paper stack, akin to the printer paper 90 gsm, was prepared by combining three layers of Lokta 30 gsm paper. The layers were wetted out with water-based cellulose adhesive Scolacell (carboxymethyl cellulose sodium salt) and consolidated. Surplus adhesive from the stack was rinsed off with water and dried under light pressure to minimise wrinkles. After deployment in water and drying, it was observed that the recovery in these stacked Lokta 90 gsm samples were greater than that of the 30 gsm samples. A comparison of final recovered shape for printer paper 90 gsm, Lokta 90 gsm and Lokta 30 gsm can be seen in Figure 2.13. As



expected, the total fibre volume fraction significantly contributes towards the recovery of the initial folded (stressed) configuration. It should also be noted that fibre orientation, fibre-to-fibre connectivity and filler content, also play a significant role in fold recovery as evidenced by the greater recovery in printer paper samples in comparison with handmade paper types. The role of the filler materials (or a compliant matrix) should not go unacknowledged; it provides a mechanism for substrate stabilisation once hydrated and subsequently aids to minimise the wrinkles upon drying, resulting in greater and more effective shape recovery in the printer paper specimens than handmade paper types lacking a stabilising matrix. The stability of the host architecture when hydrated is also important as the fibre orientation and fibre-to-fibre connectivity (*i.e.* adhesion) in the design of any fibrous actuators based upon natural fibres especially from a cyclic and reusable perspective.

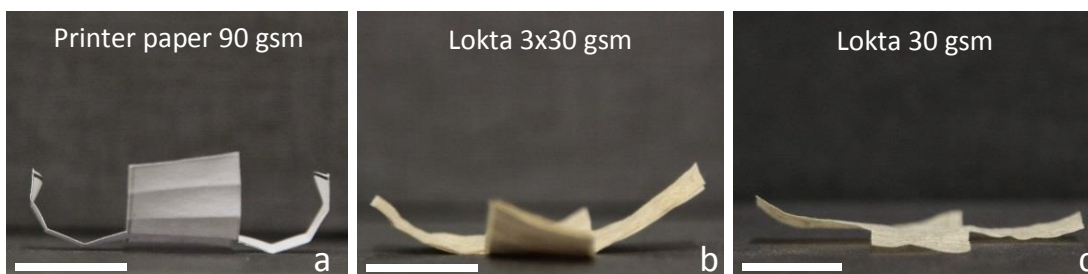


Figure 2.13: Recovery of sample architectures after deployment. (a) Printer paper 90 gsm, (b) Lokta 3x30 gsm and (c) Lokta 30 gsm. (Scale bar = 15mm).

## 2.5 Factors affecting deployment

The role of the physical architecture (shape, fold lines) and the environment (nature and chemical composition of the medium containing the stimulus) are all important regarding the active deployment of any morphing structure. In the previous section, consideration was given to specific variables, specifically the role of paper weight (gsm) and stimuli. This section extends the work and discussion further to contemplate the role of the microstructure, temperature, surface tension (*i.e.* varying surfactant concentrations) and the role of dehydration for subsequent redeployment. These parameters can be varied as required in a controlled way and consequently offer great potential to tailor the response of the folded cross architectures investigated in this study. Characterising the actuation response of the model architecture in response to the changes in these parameters will inform the future developments of actuators based on this system with regard to programmability.

### 2.5.1 Microstructure

Hydration and how quickly and easily water can hydrate the active regions (cellulose) in paper substrate is at the heart of actuations in folded paper architectures. The local and global

arrangement of the fibre architecture and inherent porosity within the fibrous medium greatly affects the ease with which water can saturate the substrate and consequently the actuation response. Manipulation of the fibre architecture (through either volume fraction or direction bias) or the porosity level (through the application of fillers and coatings) can be used to regulate water ingress into the substrate and thus control the rate of deployment. In any porous material, the pressure drop across the liquid-vapour interface within the pores is the driving force behind liquid penetration. This implies that greater the number of pores and pore volume, extra volume of liquid can penetrate the substrate at a faster rate until saturation. Additionally, as noted in Figure 2.11, upon drying, the unfolded architecture tries to recover its original stowed shape and filler materials play a significant role alongside fibres to realise such a response. It is therefore plausible that full recovery (back to the original shape) could be realised through the introduction of functional fillers. In this study of actuation with different paper types, the available microstructures are already set as they are unique to each of the paper types. However, the spectrum of paper types investigated permits the understanding of the influence of total fibre content ( $V_f$ ), fillers (matrix) and porosity on actuation time as well as fold recovery. Being able to control the microstructure, whether through manipulating fibres and/ fillers will have a compounded effect on the actuation response as it will not only control the water ingress but also the strain differential generated within the substrate which dictates the extent of swelling. Therefore, it is possible to selectively modify the microstructure in specific regions in a 2D substrate and trigger transformation into 3D shapes and forms upon hydration or dehydration. This method of strain differential control through microstructure modification in fabricating 3D forms will be explored further in Chapter 3 and Chapter 5. Applying these principles in the formation of the fibrous medium, coupled with an active matrix, offers considerable potential for future morphing design concepts. Pore features such as size, pore volume and distribution were not characterised and thus the extent to which these variables influence the deployment time is not known.

With regard to the cyclic actuation, the re-usability of actuated paper forms are critical. Hornification is a technical term used in the paper industry to distinguish the physical changes that fibres undergo upon recycling, *i.e.* wetting and drying [139]. The ability of paper architectures to recover its stowed away configuration raises the possibility of creating a paper architecture with the potential of multiple deployment scenarios. During the course of this experimental investigation, it was noted that the second actuation of the same specimen was considerably faster than the original deployment. The respective actuation times for a range

of samples carried out at room temperature (25 °C) are presented in Table 2.3. As can be seen from Table 2.3, the second actuation of the same specimens were significantly faster, and the deployment time decreased with further actuation attempts and eventually stabilised. The data presented in Table 2.3 is the average of 5 samples tested and the standard deviation is presented as error. The standard deviation within each sample group also decreased for subsequent actuations.

Table 2.3: 1<sup>st</sup> and 2<sup>nd</sup> actuation times for different paper types at R.T (25 °C)

	Lokta 30 gsm	Sekishu 30 gsm	Lokta 60 gsm	Printer paper 90 gsm
1 <sup>st</sup> (s)	25 ± 4.5	37.6 ± 11.8	132 ± 9.80	313.1 ± 152.4
2 <sup>nd</sup> (s)	12 ± 2.5	13 ± 3.4	30 ± 1.1	85 ± 15
% change	-51%	-65%	-77%	-73%

The permanent changes in the local fibre architecture at the folds and the global microstructure of paper were attributed to this decline in actuation times in subsequent deployments. Naturally, hornification induces both a reduction in internal fibre volume and change in fibre aspect ratio. This shrinkage is irreversible upon the introduction of water. Figure 2.14 shows an SEM image of Sekishu fibres before and after hornification with Figure 2.14b exhibiting a more relaxed microstructure as a result of hornification - characterised by the free spaces in between the fibres. It is evident that when the fibres shrink after each wetting and drying cycles, more free volume between the fibres are created, enhancing the permeability of the system, thus allowing the fluid medium to penetrate faster and further. This rapid penetration, and subsequent swelling of the cellulose fibres, results in quicker actuation times.

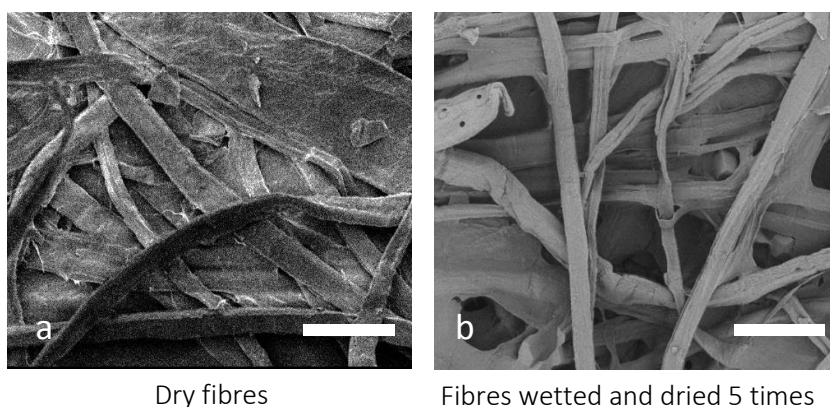


Figure 2.14: SEM image of (a) dry fibres and (b) fibres after hornification at 500x magnification showing the effects of hornification. (Scale bar = 50 µm).

The shrinkage in fibres is explained within two theoretical frameworks based on physical forces at play and cellulose chemistry. The first theory suggests that the cellulose micro-fibrils

are brought into close contact by the surface tension of water as drying progresses. This would close capillary voids on fibre surfaces permanently, resulting in irreversible volumetric changes. The second theory is based on the formation of lactones (a cyclic ester) when carboxyl groups present in cellulose react with the nearby hydroxyl groups [140,141]. It is proposed that the lactone would remain unbroken even after re-wetting and prevent the bound cellulose chains from separating and swelling. It must be noted that there is no hard evidence to validate lactone formation in cellulose during drying-wetting cycles [142,143]. The chemical or physical motives behind this phenomenon is beyond the scope of this project; however, hornification is an unavoidable reality in cyclic hydration of cellulosic fibres and must be accounted for in order to fully quantify the response of paper architectures or any cellulose fibre based actuators [135].

### 2.5.2 Temperature

Temperature of the actuating medium was found to have a significant effect on the actuation time. This is expected as the deployment actuation is the consequence of a diffusion-based absorption mechanism at the fluid-vapour interface. An increase in temperature elevates the molecules at the liquid-vapour interface to higher energy states to escape the liquid phase resulting in an increased concentration of vapour-phase water molecules within the capillaries formed by the fibrous network. The partial vapour pressure increases with number of molecules in the vapour phase and facilitates diffusion transport of water molecules away from the liquid front into the paper substrate. A schematic of this transport mechanism is presented in Figure 2.15. The water molecules then condense and adsorb on to the fibre surface leading to a decrease in interfacial tension between the fibres and vapour phase molecules, resulting in an increased wetting speed and faster substrate saturation [135,144,145].

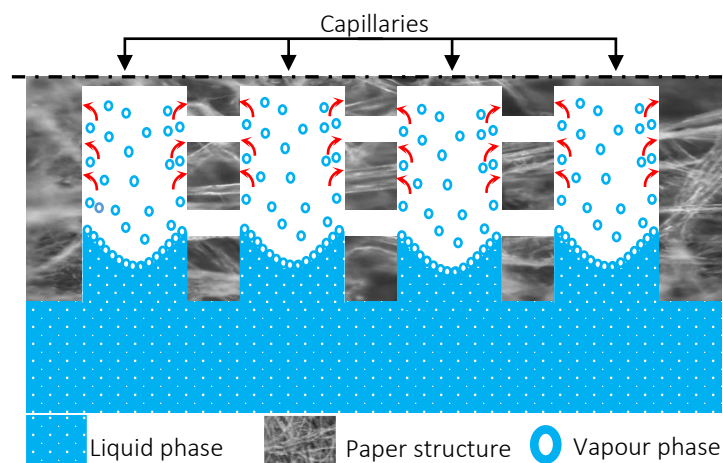


Figure 2.15: Schematic of diffusion dominant water transport in fibre capillaries.

The temperature-dependant variation of 1<sup>st</sup> actuation time for the paper types investigated is presented in Figure 2.16. The standard deviation at respective temperatures were presented as error. As can be seen from the figure, a significant reduction in actuation times were observed at higher temperatures for all paper types. The decay in actuation times are indicative of the faster fluid transport into the substrate as a result of a dominant diffusion-based absorption mechanism at higher temperatures [144,146]. It was also noted that at higher temperatures (> 75 °C), the steam from the water bath was sufficient to open up the samples clearly indicating that deployment is primarily due to chemical interaction as opposed to just physical flow through the capillaries.

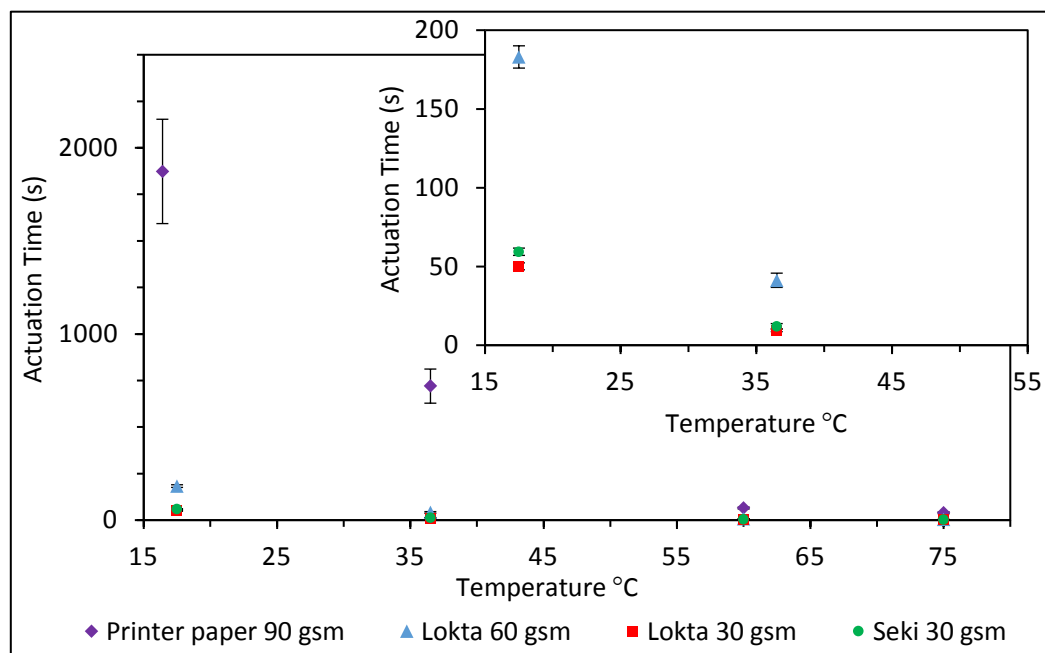


Figure 2.16: Variation of 1<sup>st</sup> actuation time at a range of temperatures. The insert image shows an enlarged snapshot of the 1<sup>st</sup> actuation time of the handmade specimens below 55 °C.

Figure 2.17 shows the variation of 2<sup>nd</sup> actuation time of different paper types across a range of temperatures. A comparison with Figure 2.16 illustrates that although all the handmade paper types decay, the 2<sup>nd</sup> actuation times of printer paper does not decay at the same rate. The effects of hornification and filler content in the printer paper at higher temperatures is clearly evident from the response noted in Figure 2.17. The effect of microstructure (*i.e.* hornification) was also observed to have a smaller influence between 1<sup>st</sup> and 2<sup>nd</sup> actuation times at higher temperatures (> 50 °C). It can therefore be concluded that the response of these paper architectures is very sensitive to temperature variations in the actuating medium and confirms that concentration gradient-driven diffusion is the dominant mode of fluid transport in paper architectures.

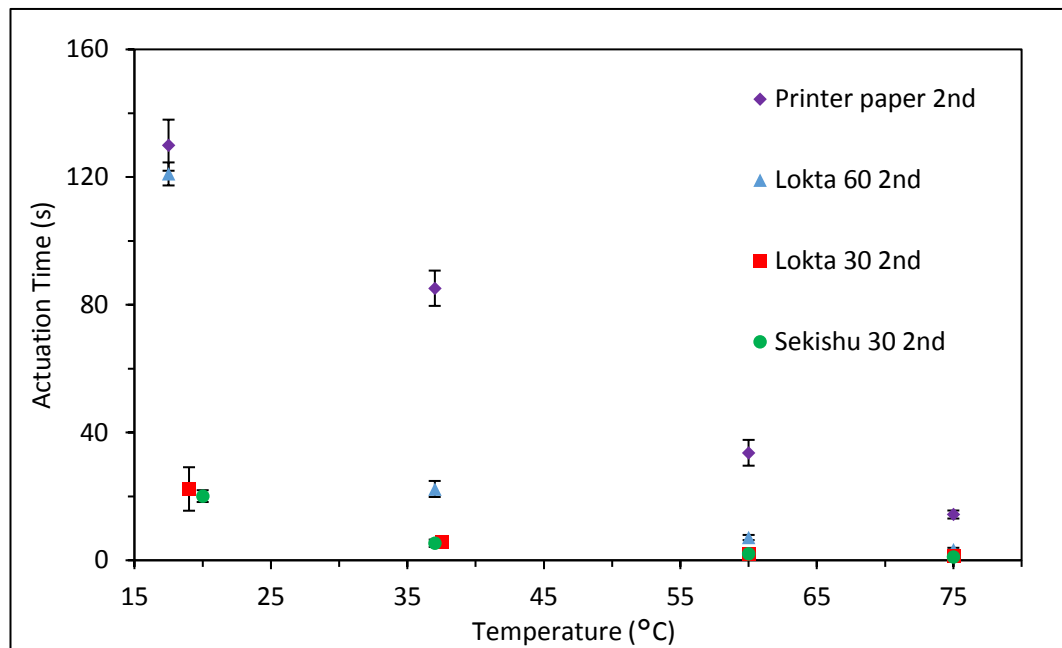


Figure 2.17: Variation of 2<sup>nd</sup> actuation times at a range of temperatures.

### 2.5.3 Surfactants

In order to further characterise the influence of actuation media, actuation experiments were carried out in “soapy water” and the deployment was found to be quicker than in water. Consequently, it was decided to explore this aspect of actuation media further in a systematic manner. The samples actuated faster in water containing varying surfactant concentrations. Sodium dodecyl sulfate (SDS) and Triton were added in concentrations of 1%, 0.1%, 0.01% and 0.001% by volume to the water bath. These surfactants were selected for this study as they differ in their nature as SDS is anionic and Triton is non-ionic. This choice would also inform about the influence of surfactant ionisation if applicable. Addition of surfactants results in the reduction of surface tension for an increasing concentration until the liquid surface becomes fully saturated with surfactant molecules. Continued surfactant addition leads to the aggregation of surfactant molecules resulting in micellar formation at critical micellar concentration (CMC). Further addition of surfactant above critical micellar concentration has minimal effect on the surface tension. It is evident from Figure 2.18 that there is minimal difference between the actuation times despite the variation in surface tension values of the different surfactants used at given concentrations. However, the decreasing trend observed in actuation times and surface tension suggests a positive correlation between the two. These results also imply that the actuation time is independent of surfactant type [135].

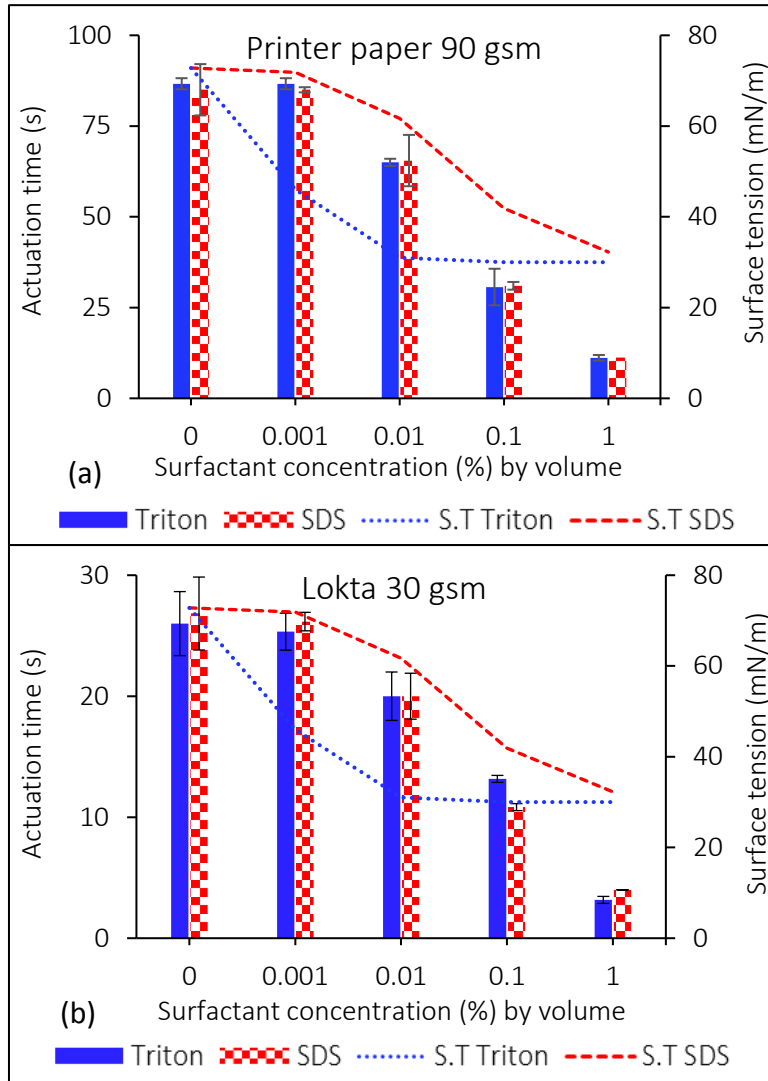


Figure 2.18: Variation of actuation time for corresponding % volume concentration of surfactants (a) Printer paper 90 gsm (2<sup>nd</sup> actuation) (b) Lokta 30 gsm (1<sup>st</sup> actuation).

## 2.6 Multi-layered composite paper systems

Morphing of paper laminates was also investigated where the composite form was prepared by stacking individual layers of paper. This approach enables the construction of laminates by utilising different paper types, their orientation and stacking sequence drawing parallels to the lay-up process in the fabrication of advanced composites. It was demonstrated in Section 2.3 *Fold Lines* that higher fibre content achieved by means of layering individual sheets improved the fold recovery in paper architectures. Similar multi-layered paper composites were prepared for this study using carboxymethyl cellulose sodium salt (CMC) as an adhesive inter-layer. Lokta 30 gsm was chosen as the base unit for these systems as they had the fastest rate of water absorption (Table 2.1) among the paper types investigated. The heavier variant of handmade Lokta paper, Lokta 60 gsm was also examined in order to study the influence of

base unit 'size'. An important objective of this element of the study, was to establish the role of the adhesive bond-line on (1) hornification of the cellulose fibres, (2) actuation times and (3) temperature. Table 2.4 shows the summary of the paper composites produced and their grammage.

Table 2.4: Summary of multi-layered paper composites

Configuration	2 x 30 gsm	3 x 30 gsm	2 x 60 gsm	4 x 30 gsm
Nominal	Lokta 60 gsm	Lokta 90 gsm	Lokta 120 gsm	Lokta 120 gsm
Measured gsm	73 ± 4	96 ± 0.2	105 ± 2	144 ± 6

As expected, the CMC adhesive layer acts as a buffer slowing down water permeation in the through-thickness direction. As the adhesive is hygroscopic, permeation of layers away from the water surface only occurs after the saturation of the layer itself in thickness direction. Interestingly, the presence of the CMC layer mediated a different permeation pathway in multi-layered substrates, as indicated in Figure 2.19. In the absence of a CMC inter-layer, water uniformly saturates the substrate in the through thickness direction as shown in Figure 2.19a and b; whereas in the Lokta composite, saturation proceeds from the free-edge boundary to the core (Figure 2.19c) as its offers least resistance to the flow front. Controlling the permeability of the different layers offers the potential for sequenced in-plane and out-of-plane deployment.

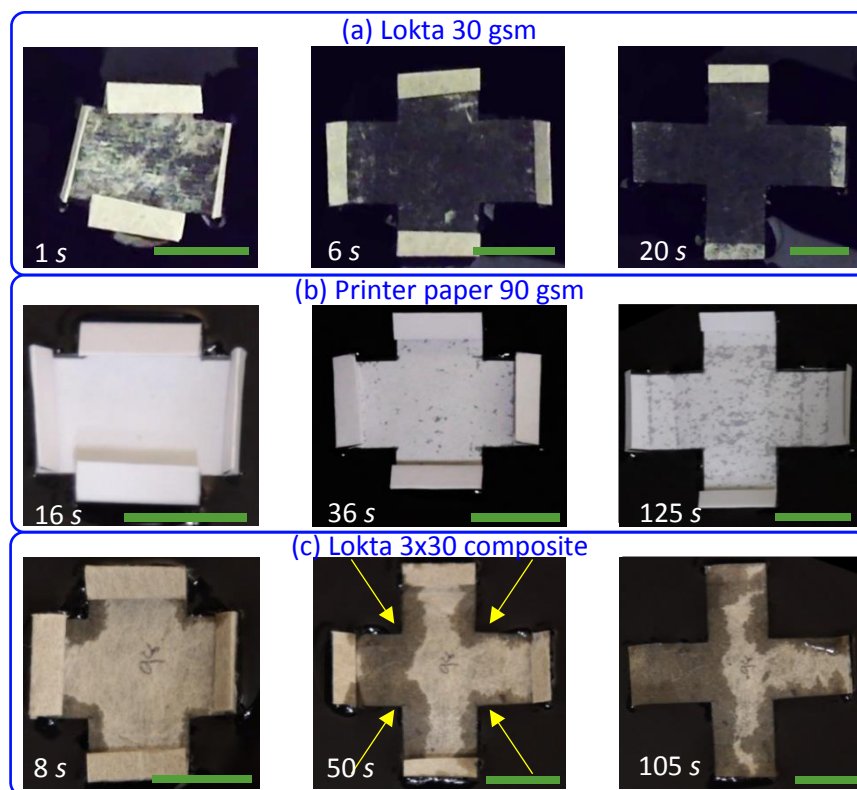


Figure 2.19: Flow characteristics: (a) Lokta 30 gsm; (b) Printer paper 90 gsm; (c) Lokta 3 x 30 composite. (Scale bar = 15 mm).



Comparable to the individual lamina sheet studies, the first and second actuation times at room temperature (24 °C) for the different paper composite configurations were characterised; these results are presented in Figure 2.20. Upon closer examination, a faster actuation was observed in Lokta 2 x 30 gsm and Lokta 4 x 30 gsm samples in comparison to the corresponding Lokta 60 gsm and Lokta 2 x 60 gsm systems. For the chosen materials, this clearly indicates that lighter base lamina assembled and consolidated to create a target gsm which is more efficient for morphing than the heavier base units, despite the introduction of additional adhesive inter-layers inhibiting through thickness water ingress. Regrettably, the presence of adhesive inter-layers did result in a non-uniform saturation across the paper composites even at full deployment, (see Figure 2.19c) and consequently led to non-uniform hornification effects. Clearly, this poses a significant challenge to developing a repeatable paper based composite actuator using this strategy unless full saturation of the actuator substrate is ensured prior to drying and subsequent deployments.

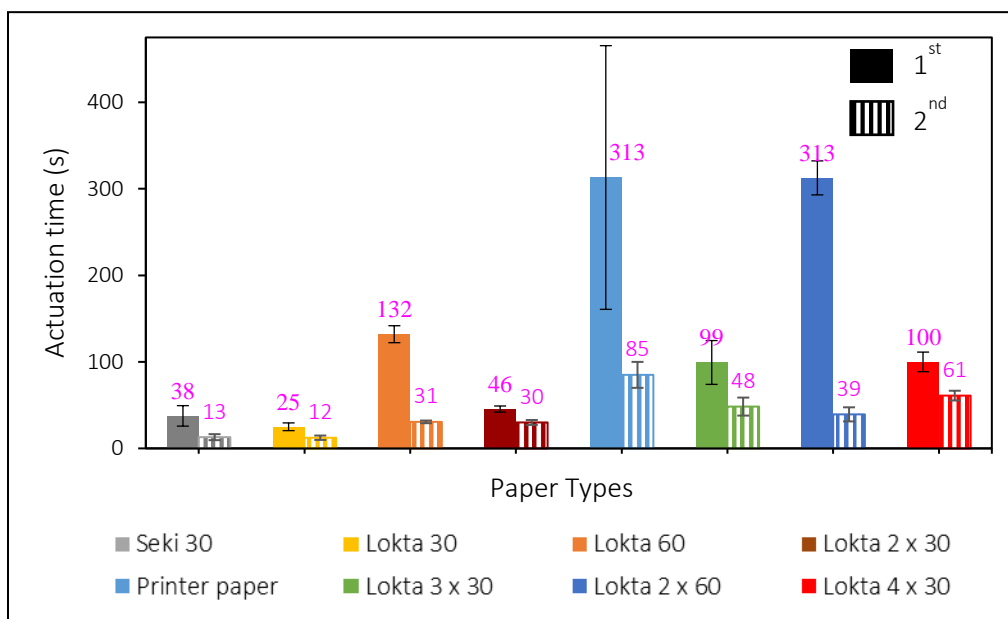


Figure 2.20: Comparison of 1<sup>st</sup> actuation time and 2<sup>nd</sup> actuation time for different paper types. (The average and standard deviation is of 5 specimens).

## 2.7 Reversible deployment through functionalisation

Ability of folded paper architectures to partially recover its stowed away configurations upon natural drying has been established and quantified. Albeit being very useful and inherent to the paper architectures, the over-dependency of fold recovery on time is less than ideal. The possibility of controlling the rate of actuation or indeed reversing the direction of actuation mid-deployment has been explored to complement and enhance the inherent recovery features of folded paper architectures. A key objective of this element of the study was not only to understand deployment but also to explore the potential of paper as raw material for

further improvement and to introduce programmability in actuation response. Cellulose has great potential to be chemically modified to bestow new functional properties due to its numerous hydroxyl groups. In order to achieve the objectives of reversible and controllable actuation, appropriate functionalisation of the cellulose fibres to facilitate accelerated drying (repelling water) was carried out. It was decided to chemically graft a thermoresponsive polymer on to the paper surface. The hydrophilic to hydrophobic transition of these polymers on fibre surface in response to a thermal trigger would control the rate of water ingress. It was envisaged that once hydrophobic after deployment, the substrate would repel water and return to its original folded state.

### 2.7.1 Thermoresponsive functionalisation of paper substrates

Several thermoresponsive polymers were considered. Poly (N-isopropylacrylamide) (poly (NIPAAm) or PNIPAAm) and polymers of oligo (ethylene glycol) methacrylate (POEGMA) were deemed most suitable due to their trigger temperature being close to room temperature. The bio-compatibility features of POEGMA were overlooked at this stage and PNIPAAm was chosen to be grafted on to cellulose as it was readily available. PNIPAAm is an amphiphilic stimuli responsive polymer characterised by its sharp hydrophilic to hydrophobic transition above its lower critical solution temperature (LCST) of 32 °C [147]. Atom Transfer Radical Polymerisation (ATRP) method was used to graft poly (N-isopropylacrylamide) from an initiator immobilised paper surface. The initiator was first immobilised by reacting with the OH groups on cellulose substrates where the OH groups were converted to tertiary bromoester groups. This was followed by aqueous surface initiated ATRP where the thermoresponsive polymer was grafted on to the cellulose backbone. The reaction procedures were obtained from [148,149] and adapted. Figure 2.21 shows the schematic of the reaction carried out. The following sections detail the procedures involved in functionalising a suitable paper type with N-Isopropylacrylamide (PNIPAAm) thermoresponsive polymer.

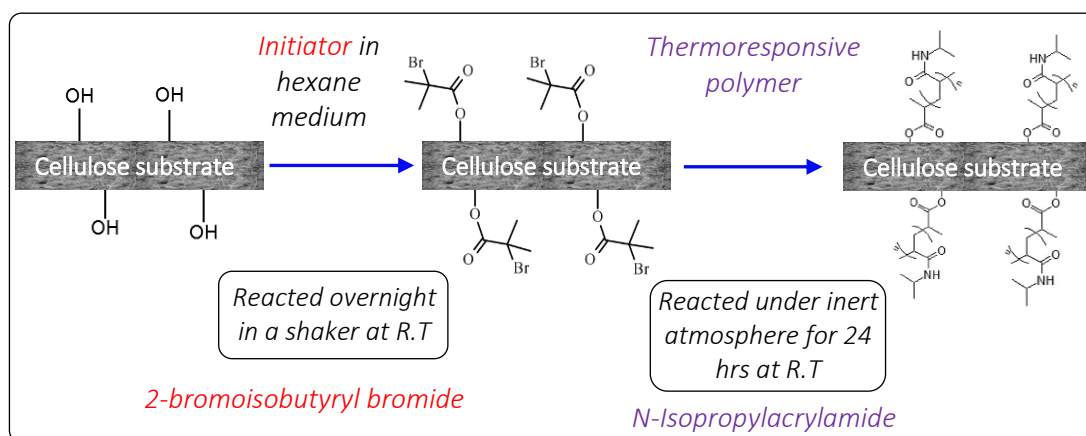


Figure 2.21: Schematic of ATRP reaction carried out on paper substrate.

### 2.7.1.1 Materials

Printer paper (90 gsm) was purchased from Office Depot, Lokta (60 gsm), Lokta (30 gsm) and Sekishu (30 gsm) were purchased from Paper works ([www.paperworks.uk.com](http://www.paperworks.uk.com)). Copper(I) bromide (CuBr, 99%), Triethylamine (TEA, 99.5%), 2-bromoisobutyl bromide (BiB, 98%), N-Isopropylacrylamide (PNIPAAm, 99%) and 1,1,4,7,10,10-Hexamethyltriethylenetetramine (HMTETA, 97%) were purchased from Sigma Aldrich. Reagent grade hexane, ethanol, acetone, tetrahydrofuran (THF) and dichloromethane were also obtained from Sigma Aldrich. Ultra-pure water was purified using Milli-Q Ultrapure purification system. All materials were used as received.

### 2.7.1.2 Substrate selection and preparation

FTIR (Fourier transform infrared spectroscopy) analysis on the paper substrates (dried overnight in vacuum oven at 40 °C) revealed the relative amount of OH group in each paper type. Figure 2.22 shows the averaged FTIR spectra (of 5 samples) of the various paper types investigated. The FTIR analysis indicated that the Sekishu 30 gsm paper had the most cellulose content (largest hydroxyl (OH) characteristic stretch) among the sampled paper types and was chosen as the substrate to carry out the grafting to maximise the grafted PNIPAAm density and thus the transition effect. Samples were cut as squares (4 cm x 4 cm) and rolled up as cylinders for ease of handling. These were then tied up with cotton threads to prevent them from opening up during the reaction stages. The following indicates the procedures used to graft 5 such rolled up samples. These samples were then washed in 100 mL of ethanol, acetone and THF respectively by sonicating at room temperature (RT 21 °C) for 2 minutes. The rolls were then opened up and dried in vacuum oven at 40 °C overnight.

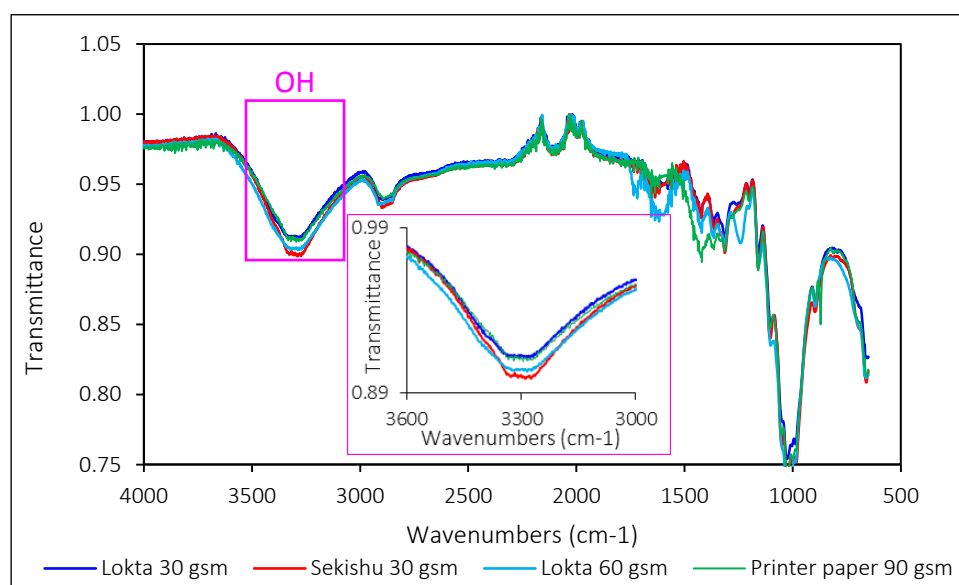


Figure 2.22: FTIR spectra of the paper types and the close-up of OH stretch region is shown in insert.

### 2.7.1.3 Immobilisation of initiator on paper substrate

Following drying, the samples were rolled and tied to form cylinders. The hydroxyl groups on the substrate were converted to ATRP initiator by reacting with 2-bromoisobutyryl bromide (BiB) in hexane (100 mL) medium. The samples were immersed in solution containing TEA (1.48 g, 14.6 mmol) followed by the addition of BiB (3.05 g, 13.3 mmol). The reaction was allowed to proceed overnight on a shaking device at room temperature followed by washing the samples twice in the following media: 200 mL ethanol, 200 mL acetone and 200 mL THF. The samples were left as rolled for the first ethanol wash and was opened up for the subsequent washes. The samples were then dried in a vacuum oven at 40 °C overnight.

### 2.7.1.4 Grafting of *N*-Isopropylacrylamide from initiator functionalised substrate

The glassware used were first washed with de-ionised water followed by ultra-pure water. The typical procedure was to add PNIPAAm (4 g, 35.3 mmol) to degassed water (46 mL) in a Schlenk flask in-line followed by stirring till completely dissolved. The solution was then degassed by three cycles of freeze-pump-thaw using liquid nitrogen and heat gun. The solution was then moved to another round bottom flask in the line containing CuBr (25 mg,  $17.4 \times 10^{-2}$  mmol) and HMTETA (48  $\mu$ L,  $17.6 \times 10^{-2}$  mmol) under argon. CuBr and HMTETA was added into the flask in an inert fume hood and sealed with a rubber septum prior to connecting to the line. The mixture was then ultra-sonicated till completely soluble. The solution was then transferred to another flask containing BiB-modified paper samples (rolled-up) followed by ultra-sonication. The polymerisation was allowed to continue under argon atmosphere at room temperature for 24 hrs while stirring. The reaction was quenched by exposure to air. The samples were then opened, washed thoroughly in ultra-pure water, ethanol and dichloromethane respectively followed by drying in a vacuum oven at 40 °C overnight.

FTIR and Scanning electron microscopy (SEM) analysis were carried out on the dried samples to confirm the grafting of *N*-Isopropylacrylamide. A comparison of FTIR spectra of Sekishu 30gsm (control) and grafted samples are shown in Figure 2.23. The FTIR analysis of the samples confirmed the successful chemical grafting of thermoresponsive polymer as anticipated in the schematic as the steep reduction (blue box) in the hydroxyl stretch in grafted specimens at wavenumber  $3500 \text{ cm}^{-1}$  corresponds well with the additional stretch (green box) introduced by the double bonds in the thermoresponsive polymer.

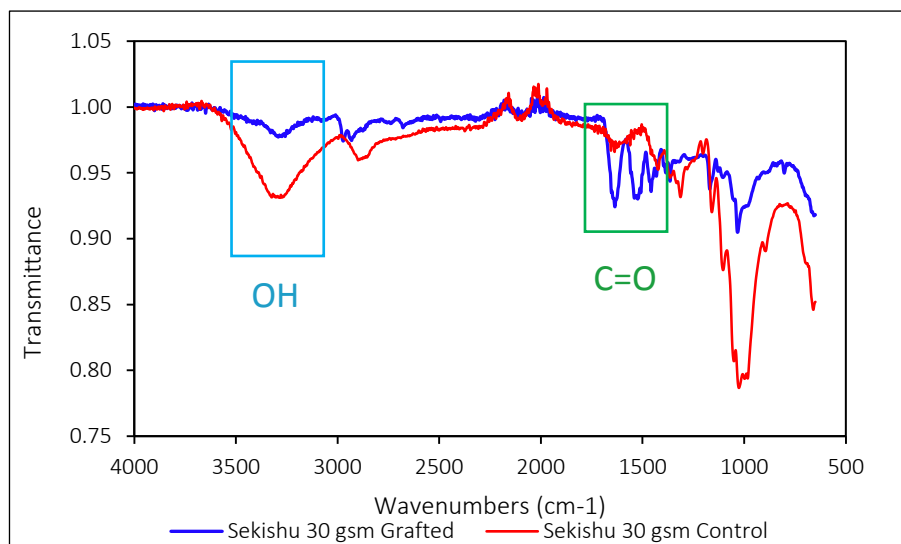


Figure 2.23: FTIR spectra of Sekishu 30 GSM (Control) and Sekishu 30 GSM grafted with PINAAPm.

The presence of the thermoresponsive polymer and the resulting changes in the substrate microstructure was also observed through microscope and the results are presented in Figure 2.24. The reduction in pore volume in grafted samples (Figure 2.24b) was evident when compared to the control (Figure 2.24a). This figure also confirms that the polymers were grafted onto the fibres itself rather than form a supporting matrix as filler. Chemically grafting the polymer is essential as opposed to other techniques such as dip coating because it ensures that the thermoresponsive polymer does not get washed away and the modified substrate can support multiple transition cycles.

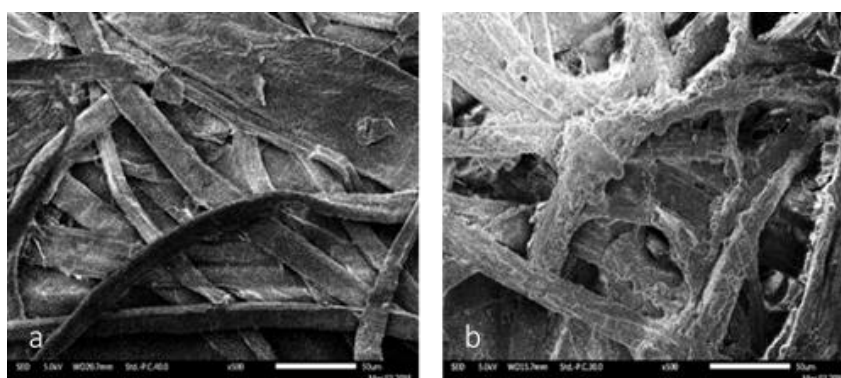


Figure 2.24: SEM images of Sekishu 30 GSM paper (a) before and (b) after grafting with PNIPAAm. (Scale bar = 50  $\mu\text{m}$ ).

### 2.7.2 Contact angle measurements of modified paper substrate

Contact angle analysis deliver a comparative measure of hydrophilicity and is representative of surface properties such as micro-structure and roughness of the substrate. Therefore, contact angle measurements were carried out using KRÜSS DSA 100 to characterise the functionalised paper substrate. As with other paper types, dynamic contact angle analysis was

carried out on functionalised substrates at room temperature (below LCST) and at a temperature above the LCST of the thermoresponsive polymer (53 °C). The experimental setup is shown in Figure 2.25. The samples were placed on the aluminium heater-block heated by circulating hot water in a loop from a reservoir with temperature-controlled heating elements. Temperature equilibrium prior to taking measurements were ensured by means of a thermal camera (FLIR T650 sc) before dispensing the droplet.

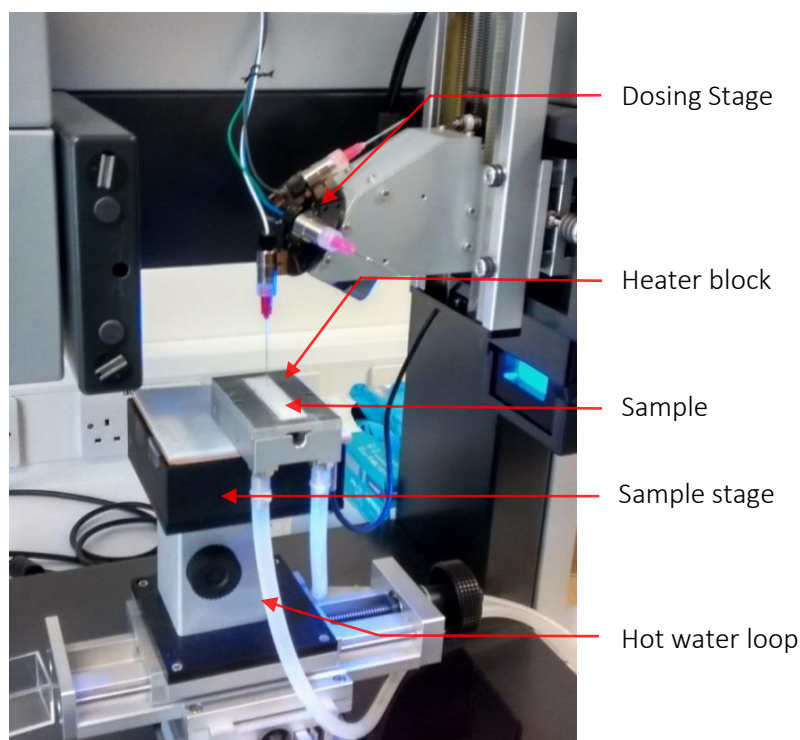


Figure 2.25: Experimental set-up for contact angle analysis at elevated temperatures.

The results are presented in Figure 2.26 and the contact angle measurements of chemically un-altered Sekishu 30 gsm (control) samples are also presented for comparison. The changes in microstructure and pore volume owing to chemical grafting is evident from the contact angle analysis of grafted and un-altered Sekishu 30 gsm samples at room temperature. For temperatures below LCST, slower droplet absorption and higher initial contact angle was observed in grafted samples with comparable water absorption characteristics to unaltered Sekishu 30 gsm. However, raising the temperature of the sample and its environment above the LCST of PNIPAAm triggered the hydrophobic response as evidenced by the higher initial contact angle and slower water absorption rate into the substrate. The droplet absorption dynamics appear to be completely different to that of both grafted and unaltered Sekishu 30 gsm at room temperature. These results confirm the effectiveness of hydrophilic-hydrophobic transition on a thermal trigger in controlling the water transport into the substrate.

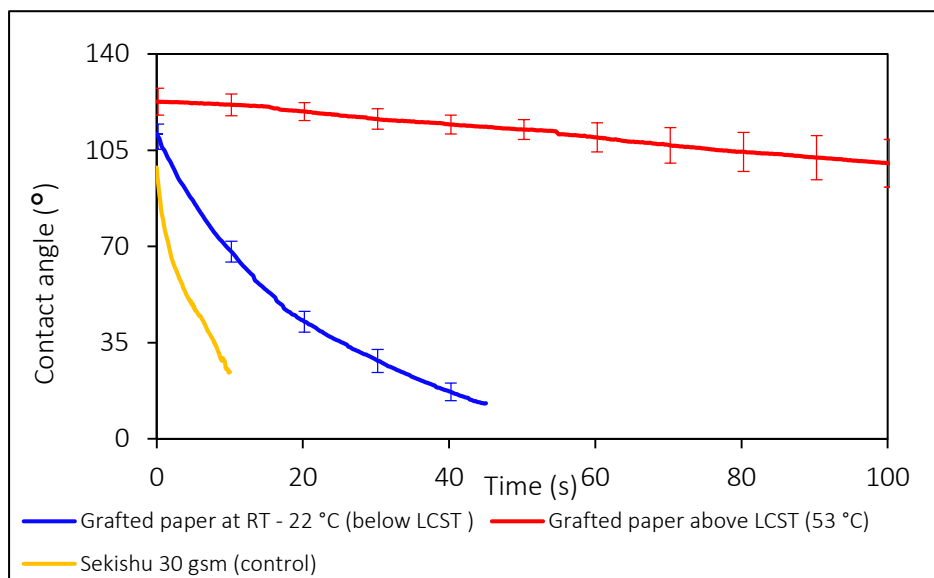


Figure 2.26: Contact angle measurements for polymer grafted samples above and below the LCST along with control.


### 2.7.3 Actuation of functionalised paper substrates

Fully reversible actuation of the model cross shape could not be realised even after raising the temperature of the actuation medium above the LCST. It was concluded that the surface tension of water (actuation medium) was inhibiting the shape recovery as observed during natural drying of the samples (Figure 2.11). In order to minimise the effect of surface tension, it was decided to simplify the architecture to a single fold effectively reducing the surface area in contact with water. Consequently, the model shape was reduced to a rectangle of 40 mm x 15 mm folded in the middle along the short-edge. The actuation response of this model shape when hydrophobic behaviour was evoked (above LCST) is summarised in Table 2.5. The actuation times are also reported with the error showing standard deviation of 5 samples. The final position of fold deployment above LCST is presented in insert (red). It was observed that the deployment of PNIPAAm grafted samples stopped midway when actuated in water bath above the LCST, clearly demonstrating that impregnation of water into the substrate had ceased owing to thermally induced hydrophobicity and thus inhibiting full deployment. Below LCST, the grafted PNIPAAm brushes assume a stretched conformation resulting in hydrophilic behaviour. Hence, the folded architecture from PNIPAAm grafted samples were able to deploy (in  $23 \pm 4$  s) in water bath below LCST. However, at LCST, the brushes undergo a phase transition where the PNIPAAm brushes collapse to form globules resulting in reduced wettability of the surfaces [148]. It must be noted that the samples were kept at room temperature (below LCST) prior to deployment; as such the initial deployment was credited to water ingress prior to the hydrophobic transition within the samples. The influence of temperature in facilitating increased flow and thus resulting in faster deployment was

documented in 2.5.2 *Temperature* for unaltered substrates. As such, the probable response at higher temperature is faster actuation leading to full deployment of folded samples and the control samples of Sekishu 30 gsm paper deployed within a second above the LCST temperature as expected. In comparison, PNIPAAm grafted architectures did not fully deploy but maintained its position (deployment arrest) in excess of 2 minutes above LCST. Therefore, the deployment arrest in the folded samples observed in this study can be attributed to the hydrophobic transition of PNIPAAm above its LCST and its influence on the water ingress into the modified paper substrates. This actuation behaviour with thermoresponsive polymer grafted samples are testament to the effectiveness of this strategy of exploiting hydrophobic transitions in controlling deployment as well as to the versatility of cellulosic substrates for further functionalisation. Perhaps, thermal trigger to induce hydrophobicity to fully reverse the deployment is not ideal as an increase in temperature also increases the vapour pressure and fluid flow favouring faster deployment which is attempted to be countered by triggering hydrophobic transition resulting in deployment arrest. Therefore, this strategy is best suited for controlling actuation response mid-deployment and for reducing the drying time (for recovery) after deployment had attained and outside the influence of activating stimulus.

Table 2.5: Actuation times for a single fold of PNIPAAm grafted paper

Actuation time for single folds (s)		
Samples	Below LCST	Above LCST
Neat (control)	$5 \pm 1$ s	<1 s
Grafted	$23 \pm 4$ s	>120* s



\* samples opened up from folded configuration and stopped mid full deployment

## 2.8 Discussion and Conclusion

The main aim of this chapter was to characterise the deployment of a 'model' folded paper architecture using the medium of water for self-actuation. The motivation to undertake this in-depth characterisation as well as investigating the underlying mechanisms and chemistry involved was to capture the 'design rules' of active morphing in natural fibrous systems for translation into a synthetic counterpart. This study has identified the key parameters that governs the actuation of folded fibrous architectures through the medium of paper. Folding and subsequent deployment in paper architectures are by virtue of its hierarchal structure



and the chemical nature of cellulose which forms the main constituent in paper. Hydrogen bonding in cellulose chains forms fibrils which further associate to form the fibres; these fibres form an interlaced network resulting in the hierarchical structure of paper [150]. The cellulose chains are closely packed in the highly ordered crystalline phase compared to the amorphous regions and the hydrogen bonding within is very stable [151]. The introduction of water or moisture can interact with the amorphous regions along the fibrils by weakening or 'relaxing' the inter-fibre hydrogen bonding by occupying the vacant spaces within the disordered amorphous regions. Along with water retained within inter and intra fibre pores, these intercalating water molecules results in swelling throughout the fibres. As the water front propagates through the thickness direction of the paper substrate, the swelling across the fibre network in effect cause the paper to behave like a bi-layer film. The through-thickness strain gradient first develops on the surface in contact with water and approaches zero when the substrate is fully saturated. As such the bi-layer behaviour is a function of saturation time which is essentially the time required to deploy any folds in the substrate. The resultant stress relaxation at the folds promotes fold deployment, since it is no longer capable of supporting the bending stress stored at the folds during the process of manual folding. The fluid transport mechanism in the paper substrate was found to be a combination of diffusion and capillary effect through inter-intra fibre pores; the diffusion-based mechanism was found to be even more prominent at higher temperatures due to increased partial vapour pressure.

The influence of porosity and grammage was very clearly demonstrated in the deployment experiments. Apart from influencing the actuation times, it was also observed that the microstructure and filler materials played a significant part in facilitating the shape recovery. The role of different stimuli (activating) media was also considered. It is evident that molecular interactions are crucial for deployment in these architectures alongside fluid flow and substrate saturation. The impetus to try glycerol was due to comparable surface tension value to that of water and the number of OH groups present in the molecule. It is believed that glycerol was capable of interacting with the hydroxyl sites on the cellulose chain as all the paper types investigated in this study were successfully activated, albeit over significantly longer time periods than the samples triggered by water. As the experiment was left for a significantly longer time period (12 hrs); deployment of the fold lines occurred as the samples sank and become saturated with glycerol resulting in unfolding and relaxation of the folds. It should be noted that the Printer paper 90 gsm and Lokta 60 gsm did not open to the same extent as the lighter paper types (30 gsm) and it is speculated that the filler content and higher fibre  $V_f$  hindered the ingress of the glycerol limiting access to the fibrils. Perhaps this variation

in the extent of opening is also a consequence of weak glycerol interactions with cellulose in comparison with water. The role and influence of surfactants were also investigated and quantified to establish whether it had any effect on the mass propagation of the water molecules into the cellulose architecture. Interestingly, the addition of surfactants (whether anionic or non-ionic) does have a decreasing effect on the actuation time of the samples tested. However, the actuation time at a given surfactant concentration was found to be comparable regardless of the difference in surface tension. Therefore, it is speculated that the decreasing effect is believed to be a function of the number of surfactant molecules and their physical arrangement at the water surface-substrate boundary, and the control this molecular arrangement imparts on the rate of fluid transport into the substrate, as opposed to the reduction of surface tension which is the primary consequence of surfactant addition [117].

Actuation of multi-layered paper composites ascertained the significance of the base unit in achieving fast actuation times. Although the previous experiments with homogenous lamina sheet samples indicated a proportional relationship with paper weight (grammage) and activation times; the actuation experiments with multi-layered composites showed that this trend is not directly translated. Architectures with smaller base units actuated faster despite being heavier in grammage. This behaviour upon substrate saturation is believed to be compound effect of hygroscopic adhesive inter-layers on the strain gradient and hornification effect of increased fibre spacing during composite paper fabrication which includes wetting out the individual lamina sheets with water-based adhesive followed by drying. It can be concluded that multi-layer composite approach utilising smaller lamina base units is an efficient way of promoting water transport into the substrate resulting in swelling and actuation, but poses serious limitations in the context of repeatable actuation. The samples were removed from water surface once full deployment was achieved regardless of whether full saturation had occurred. Such procedure of multiple wetting/drying cycles will result in non-uniform hornification across the samples when re-folded for subsequent deployments. The physical changes in fibres and paper microstructure induced in this manner cannot be controlled or monitored due to the nature of multiple drying/wetting cycles involved in the manufacture of these paper composites. Investigation into multiple actuation cycles across a range of temperatures also indicated a large standard deviation in 2<sup>nd</sup> actuation times at higher temperatures for the paper composites and further confirmed the inadequacy of this strategy for repeatable deployment of folds in the context of cyclic actuation. The effect of temperature on the adhesive layer and water absorption properties is an area which requires further investigation. As such, layering with adhesive inter-layers are not ideal for making

composites of cellulose substrates despite the greater strain gradients permitted by the use of hygroscopic adhesive. Ideally, the matrix should have better integration between the different layers to promote uniform flow and saturation, whilst providing better cohesion and substrate stability to overcome the limitations of hornification during actuation cycles. One way to limit the effects of hornification is to subject the cellulose fibres to multiple cycles of wetting and drying to the point where the effects are negligible prior to fabrication of composites and actuating forms. Conversely, a compliant matrix which can potentially counter the hornification effects in fibres by extending itself to compensate for the shrinkage can also be utilised. This strategy could also aid in stabilising the substrate during multiple actuation cycles.

Immediate reversal of actuation could not be realised as envisaged through functionalising the cellulose fibres with thermoresponsive polymer, but control over the rate of actuation has been attained. Surface tension of water was identified as the main inhibitor of reversibility whilst on the activation medium. Hydrophobic transition of the ATRP modified cellulose was confirmed through contact angle measurements and deployment arrest on activation medium above the LCST of PNIPAAm. However, this transition itself is understood not to be sufficient to overcome the surface tension forces keeping the deployed facet to the surface of water bath. The recovery and reversibility of samples modified this way will be more efficient outside the influence of surface tension forces as hydrophobic transition repels water from the bulk of substrate thus aiding in faster drying. Furthermore, this attempt at grafting is also testament to the versatility of cellulose to be functionalised to have a multitude of useful properties.

The main drawback of using paper as such for harnessing its potential as a smart material is the lack of reliability limiting its programmability. Additionally, the initial 2D to 3D transformation required intervention of manually folding the paper substrates to locally modifying the microstructure. Furthermore, the paper making processes are optimised for parameters that are not critical for actuation such as ink absorption and whiteness whilst having no control over critical parameters such as uniformity in microstructure. In order to take full advantage of cellulosic materials as smart materials for programmable actuation, new manufacturing strategies have to be developed. Such strategies should enable control of microstructure by enabling functionally graded architectures as well as support for functional materials to be incorporated during fabrication. Ideally, these strategies should also contemplate on bypassing manual intervention of programming (*e.g.* manual deformation in shape memory materials and manual folding in paper architectures) by incorporating this step in to the manufacturing process. The following chapters will aim to address these points to

---

realise reactive morphing architectures based on the paper actuators investigated in this chapter. The significance of the work presented here is that as well as validating the efficacy of cellulose as a responsive smart material, the physical changes in microstructure (both natural and intentional), manipulation of the stimuli or surrounding environment are shown to influence the actuation response of paper architectures. The factors affecting this actuation and the understanding of underlying mechanisms in operation generated from this body of work can be employed to realise robust and reliable engineering analogues of the cellulose actuators and also to program a desired morphing response from them.

---

## Chapter 3 Realising 4D architectures through strain differential

---

### 3.1 Introduction

Re-configurable architectures and the materials that facilitate inherent transformations have immense potential. Having more than one physical configuration simply maximises the usefulness of a given architecture or form by substituting the need to have distinct multiple configurations, thus minimising the cost, resources (*e.g.* energy, materials and time) and space. Some examples of these re-configurable or morphing structures include humble household foldable furniture to complex stowed away solar sails used in space exploration. Combining self-sensing and self-actuation with re-configurable structures results in responsive or reactive morphing systems with multiple useful configurations. There is compelling research push to achieve such smart systems and some of the key proposed examples from the literature have been covered in previous chapters especially in Chapter 1. These strategies on morphing can be summarised as shape memory materials [122,152], tensegrity structures [153], modular self-assembly [154] and folding [126,155,156]. The process of folding to realise 3D shapes has great significance in biological and synthetic worlds alike.

This chapter looks at the current approaches in realising morphing or actuation with specific focus on folding and self-actuation. The term fold and what it embodies in relation to stimuli responsive (or reactive) morphing is presented along with some fold performance parameters which could be used to quantify the process. This is primarily aimed to standardise and clarify the terms used in origami engineering with respect to self-actuation. The concept of strain gradient/differential/mis-match is also elaborated as a simple but effective means to realise shape re-configuration through programmable self-folding. Additive fabrication techniques to program a strain gradient into a 2D membrane through the novel adoption of hydration and membrane forces to actuate or morph between the shape configurations are also presented. The factors affecting the creation of folds, the design rules for programmable morphing and some model morphing architectures fabricated using these techniques are also reported in the following sections of this chapter. The strategy presented in this chapter is aimed to supplant human interventions similar to manual folding of paper architectures (as employed in Chapter 2) or mechanical deformation required to fix a shape in smart materials capable of actuation. The strategy of programming localised strain gradients in a substrate to realise self-folding and the subsequent stimuli responsive deployment is mediated through the principles of prevailing folding techniques such as origami and kirigami. Self-folding response of some model architectures are also presented to prove the efficacy of this methodology to fabricate

comparable architectures realised through other strategies reported in literature. It is envisaged that the design guidelines developed for morphing in fibrous substrates such as paper can be digitised to be incorporated into a reliable material system. The advantages of 3D printing in enabling greater control of material placement in creating programmable strain gradients are also discussed.

### 3.2 Classification of folds in origami inspired stimuli responsive morphing

Realising 3D forms through folding primarily concerns 2D membranes and sheets, provided they can maintain the folded configuration even after the removal of the impetus to fold. Several definitions for folds, bends and creases can be found in the literature and can be confusing at times as they are often used synonymously. This is primarily due to stimuli responsive re-configurable materials being an emerging field of research and standardisation of terms has not been accomplished. Furthermore, the definition of terms and their characteristic features as defined in traditional paper-origami are not always valid for stimuli responsive re-configurable materials. Following the naming convention proposed by Abbott *et al.* [157] for covering origami inspired folding in polymer substrates, folds can be classified into two: *bend* (elastic deformation, non-localised and recoverable) and *crease* (plastic deformation, localised and permanent). However, pertaining reconfigurable materials and origami engineering, these definitions of *bend* and *crease* are limited in the sense that creases can be removed (deployed) regardless of permanent or temporary deformations in the membrane/sheet microstructure as evidenced by actuations of paper architectures (reported in Chapter 2) and shape memory materials respectively. Furthermore, a bend can also be locked into the structure without having to supply constant external force to maintain the bend. Lauff *et al.* offers an alternative definition to clarify the terms based on the curvature produced as a result of deformations [158]. This nomenclature is more fitting concerning re-configurable materials. Here, a *bend* is defined as having a **distributed curvature** caused by deformation whilst *fold* entails a **localised curvature** caused by deformation along a crease pattern. This classification treats bend and fold as separate entities adhering to the traditional origami lines but fails to encompass the ubiquity of the term 'folding' as used in nature and other pertinent works as the primary driver for morphing. Therefore, the classification proposed by Lauff *et al.* has to be combined with that of Abbott *et al.* [157] to appropriately define the terms pertaining to the morphing of re-configurable materials.

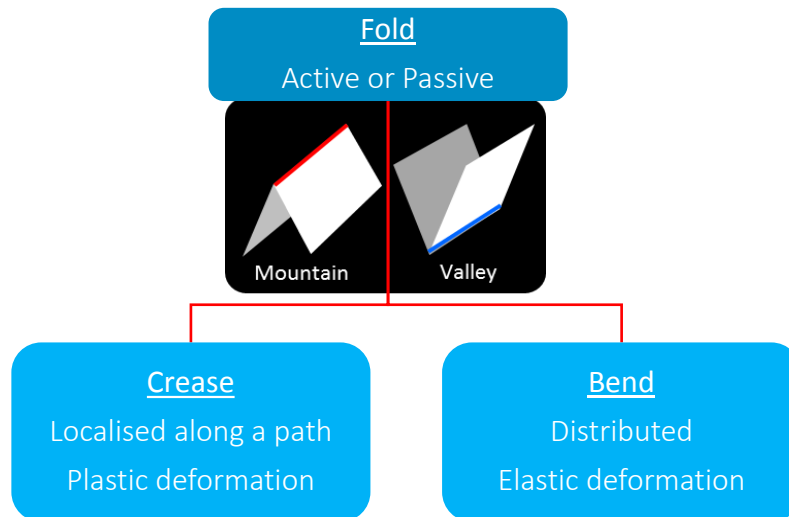


Figure 3.1: Classification of fold and related terms with their characteristic features.

Figure 3.1 presents the schematics of proposed classification and key characteristics of the means of realising a 3D shape from 2D through ‘folding’. Within the context of re-configurable systems, *folds* can be defined as any out of plane deformation that results in a 3D form. Folds thus formed, whether mountain or valley can be either active or passive, depending on whether it can be activated (actuated) by releasing the stored strain energy during the folding process. Further to this point, active folds can be one-way, two-way or capable of cyclic actuations before having to undergo the process of creating the fold again. The programming of an active or passive fold in a substrate is usually a design choice but it is also affected by geometric factors. For example, over constraining the free-edge boundaries or the presence of other adjoining folds can often render an otherwise active fold passive: either by restricting actuation along the pre-determined path or by permitting actuation through more favourable actuation pathways. A *Crease* is classified as a type of fold characterised by its localisation along a prescribed path. As a consequence of this localisation, creases are typically characterised by plastic deformation along its prescribed path known as crease pattern or fold lines. To accommodate a crease in 2D substrate, the material on the inside of the path (for a valley fold) will deform through compression whilst the outside of the path deforms through tension. Actuation of the crease back to the initial configuration does not necessarily reverse the plastic deformation for all substrate types. For example, in shape memory materials the plastic deformation can be recovered by initiating a phase change within the material itself. As for fibrous substrates such as paper investigated in Chapter 2, the deformation (or the energy of folding) was observed to be accommodated through localised fibre buckling, delamination and microstructure rearrangement along the prescribed crease path resulting in non-recoverable plastic deformations. Architectures with such non-recoverable plastic

deformation was shown to be reverted to its flat configuration by harnessing the actuation forces of swelling and hydration as presented in Chapter 2. However, *Bends* are characterised by their distributed curvature and thus being more benign on the substrate compared to *creases* as the material is not deformed permanently. Hence the substrate is said to be elastically deformed to realise a bend. As the 3D forms generated through a bend are elastically recoverable, provisions must be made to 'lock-in' the resultant architecture. Contrary to the notion that constant external forces or energy had to be supplied to maintain a bend (*e.g.* continued heating to maintain curvature in bi-metallic strips), internal forces such as membrane forces or stored strain energy can be utilised to fix the form through adept material design. Specific examples validating this point will be presented in Section 3.4 *Harnessing volumetric changes in cellulosic hydrogels for morphing*.

In order to fully quantify morphing through folding, certain performance parameters have to be defined and investigated. Further to this point, Abbott *et al.* proposes some parameters to quantify the fold performance in polymers for adaptive origami. These are crease memory, reversibility, accuracy, hold, energy required to fold, fatigue, relaxation time and recoil force [157]. These parameters can be expanded and advanced to capture the fold performance encompassing self-actuation and responsiveness. Fold performance parameters relevant to self-actuation are listed and defined as follows.

1. *Fold memory* concerns with the ability of the material system to revert to the initial folded state once actuated. A key criterion for exhibiting shape memory.
2. *Reversibility* refers to the ability of the fold to reverse its direction *i.e.* mountain fold to a valley fold or vice versa.
3. *Fold accuracy* defines the ability of the material to fold along the prescribed path. Surface features, anisotropy and texture of the material substrate greatly affect the fold accuracy. A straight line connecting two points would be the easiest to fold and any deviation of the straight-line path would impose geometrical restrictions on the fold along the deviated fold path.
4. *Fold retention or Hold* is the property which relates to the ability of the material or material system to maintain the programmed fold when not being influenced by activating stimuli. The plastic deformations as with creases can be relied onto provide some retention of the created fold; though relaxation at microstructure level could eventually cause the material to liberate the folds over time. Therefore, fold retention should be defined for a material system within a time frame.



5. *Energy of folding* refers to the energy (force) required to create a fold. This would depend on the material, total area required to be folded and the extent of folding itself.
6. *Fatigue behaviour* aims to capture the ability of fold to withstand subsequent actuation cycles (*i.e.* subsequent folding and un-folding). This is a crucial parameter for folds capable of multiple actuations.
7. *Block force* refers to the force generated by virtue of fold deployment or actuation. This parameter is usually measured by restricting the actuator motion and measuring the force generated as a result. Block force is a useful means to compare the force output of actuating materials.
8. *Actuation time* is the time required to deploy a fold from one configuration to the other from the onset of activating stimuli. This parameter represents the response speed of the material and morphing architecture.

These performance parameters (especially parameters 1-5) predominantly depend on the inherent material properties and geometry of the specimens, whereas, parameters 6-8 captures the influence of the activating stimuli (*i.e.* responsiveness) in addition to the material and geometric specifications. Even though some of these performance parameters cannot be quantified directly, they can be used in a qualitative sense to compare between re-configurable materials. Along with the fold classification and definition of related terms, these parameters will help to gain an in-depth understanding of stimuli responsive morphing systems particularly the one presented in this chapter.

### 3.3 Significance of simplistic approaches in materials and fabrication

A vast number of examples detailing the actuation of folded structures capable of morphing are reported in the literature with some relevant examples already covered in Chapter 1. This section however, is focussed on a subset, specifically on examples covering self-actuation in response to some stimulus and thus adhering to actuation in the time domain (4<sup>th</sup> dimension-4D). Folding results in compressive deformation on the inside and extensional deformation on the outside for a valley fold (inverse for a mountain fold), thus setting up a strain gradient or strain mismatch through the thickness direction. Realising this strain gradient and being able to control it is key to programmable morphing. However, there are different ways to realise a strain differential in a substrate.

The temperature response of a bi-metallic strip is an early but prominent example of harnessing strain gradient to realise 3D forms [129]. Lithographically patterning a similar bilayer offers more design freedom as photomasks can be applied intelligently in fabricating

morphing structures [159,160]. Another common approach is to use shape memory (SM) materials (alloys and polymers) at the fold regions to act as hinges but these materials require complex pre-programming steps to define the shape configurations. These pre-programming steps typically vary from pre-stretching to temperature treatments followed by deformation into a new configuration. These memory materials respond to the stimulus of heat. Sustained heating above a threshold temperature results in atomistic or molecular rearrangement prompting the shape memory materials to recover the earlier shape configuration. For shape memory alloys this atomistic rearrangement is called a phase transition and the temperature at which it transpires is termed as phase transition temperature. In shape memory polymers the molecular rearrangement occurs at the temperature where molecules begin to flow and is termed as glass transition temperature ( $T_g$ ). This heat-initiated reorganisation releases the locked in strain energy from the pre-programming step resulting in 'shape memory'. Figure 3.2a shows the schematics of actuation response in a patterned pre-stretched polystyrene in response to infrared (IR) radiation, where patterning with black ink results in selective IR absorption and localised heating within the substrate resulting in morphing [124]. Different approaches utilising shape memory (SM) hinges can be seen in open literature: Tolley *et al.* described a composite style fabrication where pre-stretched shape memory material was sandwiched between stiffer materials whilst selectively exposing SM regions in patterns defining the hinge regions [51], and Neville *et al.* reported a kirigami approach to deployable honeycomb structure where thermoformed flat-folded (forming hinges) and corrugated strips (forming honeycomb walls) of SMP were bonded with cyanoacrylate adhesive to form the cellular structure which deployed upon heat activation [161]. Depending on the actuation strategy, the hinges can be activated wholly (uniform heating) [51,161] or through selective resistive heating controlled through electronics [156]. Selective heating of the shape memory hinges (either specifically designed or patterned) enables programmed sequential actuation response. As covered in Chapter 1 (1.6.1 *Shape memory materials-based approach to 4D printing*), 3D printing of shape memory polymers can also be used to achieve similar morphing response and digital mixing of materials permits hinges with tuneable  $T_g$  resulting in selective and sequential activation in response to the stimulus of heat [101,125]. Combining materials in the bulk or in discrete layers/sections within a global substrate results in dissimilar volumetric swelling response to organic or inorganic solvents. This strategy allows for additional features besides morphing to be integrated into the system by selecting appropriate initial materials to be combined, provided sufficient cohesion at the interfaces can be guaranteed. The inclusion of photonic crystals which change colour in response to the morphing strains [162], functional thermo-responsive polymers that can release held solution

beyond a critical temperature [163,164] and structural lamina elements within a laminate are some examples [125].

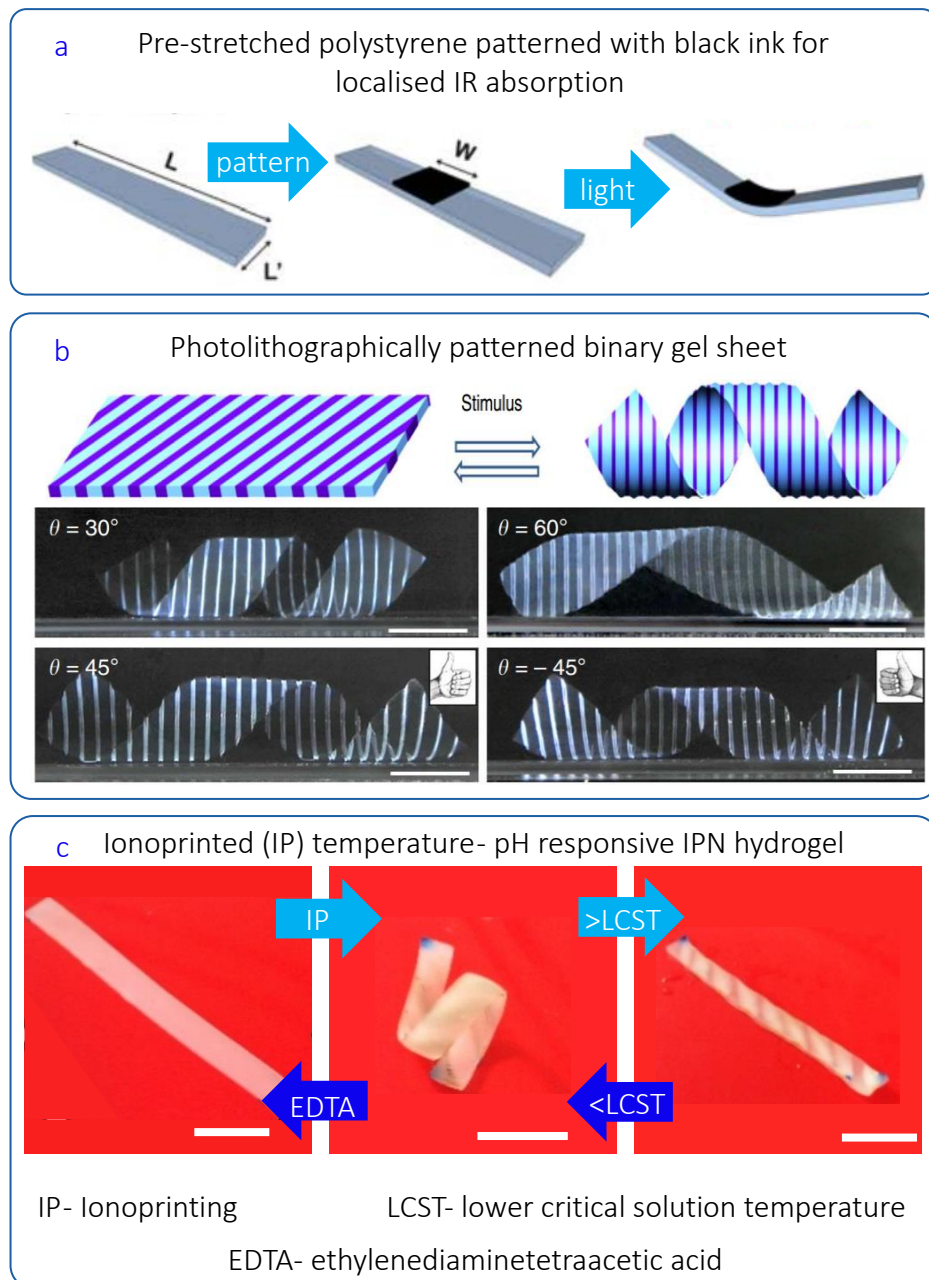


Figure 3.2: Examples of morphing responses from open literature; (a) Morphing of pre-stretched polystyrene (Shrinky-dinks) patterned with black ink due to localised heat absorption. Image adopted from [124] with permission from Royal Society of Chemistry (b) Morphing response of a UV crosslinked composite (regions of primary gel and binary gel achieved by the use of photo mask) hydrogel sheet to the stimuli of heat or ionicity. Image adopted from [166] with permission from Springer Nature (c) Formation of a helix through ionoprinting on an interpenetrating polymer network hydrogel and morphing response above and below LCST in 0.1 M LiCl solution. Image adopted from [167] and reproduced under Creative Commons Attribution 4.0 International License. (Scale bar = 10 mm).

Strain gradient can also be realised in uniform materials without having a layered arrangement. Restricting the otherwise homogeneous swelling/shrinking of the host material through the incorporation of a stiff phase or oriented reinforcing elements is yet another

means to achieve morphing. Desirable reinforcement orientations achieved through the application of magnetic fields [1], ultrasound [165] and shear forces that arise during extrusion [93] are reported in literature. Hydrogels represent a material class that is of tremendous significance with regard to morphing of soft materials due to their ability to volumetrically swell and shrink. Strain mismatch can be initiated within the hydrogels by restricting the swelling via a rigid phase. This could be through localised crosslinked points, interfacing with another (compliant) material or through the use of short fibres embedded within the swellable matrix. Wu *et al.* report programming strain gradients using photomasks and UV to selectively create crosslinked patterns into poly (N-isopropylacrylamide (PNIPAAm)) based hydrogel containing photo-initiators [166]. Figure 3.2b shows the morphing response of a selectively crosslinked hydrogel strip forming a helix. Ionoprinting, the process of electrically embedding ions in polyelectrolyte hydrogels to create ionic crosslinks can be effectively used to create 3D geometries as demonstrated by Palleau *et al.* [67]. Here, a metal anode is used to pattern regions (usually lines) of ionic crosslinks in hydrogel (placed on an aluminium foil cathode to set up current flow through the gels) and consequently morph out-of-plane. These crosslinks not only restrict chain mobility but also provide localised stiffness as well. Ionoprinted regions can be erased by immersing in a chelating medium and can be printed again. Sequential actuation using this methodology is realised by means of embedding different cation species at the hinges to form the 3D geometry and subsequent immersion in chelating agents erasing specific a cation species. Only the hinges patterned with the cation specific to the chelating agent is erased (actuated) whilst retaining the other hinges. With the ionic crosslinks removed and the hydrogel restored to its virgin state, it can be ionoprinted again to a different configuration. Incorporating thermoresponsive polymer such as N-isopropylacrylamide (NIPAAm) to form the hydrogel substrate allows for reversible thermally induced actuations along with ionoprinted shapes. Figure 3.2c shows the fabrication of a helix through ionoprinting on an interpenetrating polymer network (IPN) hydrogel substrate and its thermally induced actuation [167]. Gladman *et al.* demonstrated the fabrication and actuation of 3D printed plant-inspired architectures consisting aligned cellulose nanofibrils (NFC) within a thermoresponsive acrylamide ink containing photoinitiators among other additives. When exposed to UV, the ink crosslinked to form hydrogel and upon hydration, these architectures actuated as a result of preferential swelling in the host hydrogel owing to the shear alignment of NFC along the print path [93].

Even though the aforementioned strategies and examples enable time dependant (4D) morphing, they are characterised by their complexity in materials, fabrication steps or the

chemistry involved. For example, patterning discrete regions to generate strain gradients can be time consuming (multi-step lithography) or require specialist tools to impart inhomogeneity. Exploring morphing science using novel materials or proprietary technologies are essential to accelerate the push to advance the boundaries of knowledge and demonstrate what is possible. However, simplistic but effective approaches could be easily overlooked to utilise the latest and sophisticated technologies as the latter are often perceived to guarantee success. This could significantly drive up the cost and potentially reduce the real-world impact by restricting the wider adoption of a strategy. The significance of the strategy developed in this project is that morphing is realised without the complexity in terms of material, fabrication and underlying chemistry. Here, a bio-inspired approach to realising morphing is adopted by combining stimuli responsiveness and specific active regions with programmed strain gradients in compliant substrates. This approach relies on the placement of compatible materials in 3D space along a pre-defined (programmed) path to realise morphing. Furthermore, using bio-derived materials in an environmentally friendly way for the synthesis reduces the ecological footprint of this approach and the bio-inspired design rules of realising form ensures relevance and adaptability.

### 3.4 Harnessing volumetric changes in cellulosic hydrogels for morphing

The following sections details the experimental work carried out in harnessing the volumetric changes in hydrogel to realise morphing fibrous architectures. The characteristic feature of hydrogels is the ability to retain large amounts of water by expanding to multiple times its initial volume. The dehydration of the gel results in shrinking: to a solid mass devoid of water. This range of volumetric expansion realised by directing the water flux within the gel is utilised to create a strain gradient and consequently result in folding and un-folding along a prescribed path. In the preceding work of characterising the deployment of paper architectures (Chapter 2), the energy to create the folds in first place was imparted through manually folding the substrates. This folding energy can be substituted with the membrane forces arising from shrinking hydrogel strategically placed on a paper surface. The resultant strain gradient of this 'bi-layer' will result in out of plane transformation and the 3D geometry thus created can be actuated back to the initial configuration through hydration. Here, the microstructure of paper substrate will essentially act as a valve for the controlled release of strain energy stored in the structure by regulating the influx of water into the substrate and to the gel. Figure 3.3 shows the schematics for shrinking-initiated morphing through the strategic placement of hydrogel on paper substrates and resulting examples of *crease* and *bend* fabricated in this manner. The hydrogel used here is carboxymethyl cellulose (CMC) of molecular weight (Mw) 700,000

dissolved in water with a mass ratio of CMC:H<sub>2</sub>O = 1:20. The specific details of the gel are presented in detail in Chapter 4 (4.2.1 *Materials and formulation*). The regions within paper were patterned with a specific formulation of hydrogel to define folds (along the fold line) and the forces developed within the hydrogel as it dried initiated the 2D to 3D transformation. Confining the hydrogel deposition to the fold line resulted in crease whereas spreading of hydrogel produced a bend. Drying at room temperature resulted in morphing which was then maximised by drying at higher temperature due to enhanced dehydration.

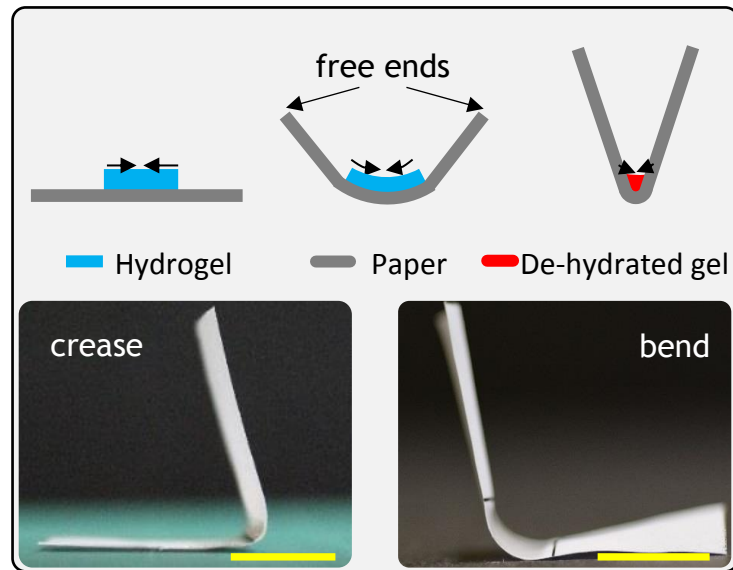


Figure 3.3: (top) Schematic of folding with hydrogels; (bottom) Examples of crease and bend fabricated as per the schematic. (Scale bar = 10 mm).

Here, the prepared hydrogel was manually extruded through a syringe (nozzle diameter( $\varnothing$ ) = 1 mm) along the fold line and allowed to shrink (natural drying at room temperature -21 °C) to realise out-of-plane deformations. The gel can be visualized as a polymer network with water bound to and in between the network. Initially, water diffuses out to the surrounding environment exposing solid-vapor interfaces within the hydrogel resulting in the liquid (water) to flow from the bulk to the exterior along the concentration gradient. The capillary forces stretch the exterior liquid in tension and are balanced by the compressive stresses in the network that cause shrinkage. Therefore, the 'exposed' network collapses into the liquid phase and the process continues till equilibrium. The surface tension of the hydrogel could also control the direction of collapse of network towards the middle. It is hypothesised that in this system of hydrogel and cellulosic fibrous substrate such as paper, the gel is anchored to the pores and cellulose fibers through hydrogen bonding and drives the open ends as it shrinks towards the middle. There are several factors that affect the extent of deformation (morphing) in this material system: substrate stiffness, amount of gel forming polymer (concentration), gel-spread, area that needs to be folded, adhesion between the gel and paper substrate (gel-

paper interface) and swelling/shrinking capacity of the gel. Understanding these parameters will further inform the design principles to realise stimuli responsive morphing using paper or compliant substrates.

### 3.4.1 Factors affecting fold creation on paper substrates

#### 3.4.1.1 Substrate stiffness

The work done by the hydrogel to fold or deform a stiffer substrate material will be greater than for a material of less stiffness. Consequently, for a given amount of hydrogel, relatively greater morphing behaviour can be realised for compliant substrates of lower stiffness. The relevance of substrate stiffness is significant in the design problem as there will be an upper limit either by grammage (weight) or by elastic modulus (intrinsic to the material itself) above which the proposed methodology using hydrogel shrinking cannot initiate folding. Kirchhoff-Love's classical theory on bending of plates can be broadly applied here to easily understand this relationship even though the theorem is limited to elastic and small deformations. The theory derives bending stiffness or flexural rigidity ( $D$ ) of a plate ( $L \gg t$ ;  $L$  represents in-plane length or width dimensions and  $t$  is thickness in transverse plane) as follows [168]:

$$\text{Bending stiffness } (D) = \frac{Et^3}{12(1-\nu^2)} \quad (3.1)$$

where  $E$  is the Young's modulus (Elastic modulus) and  $\nu$  is the Poisson's ratio. Equation (3.1) implies that the stiffness is proportional to elastic modulus and cubic function of substrate thickness and consequently folding will become progressively more difficult for stiffer and thicker substrates. The forces developed by drying the hydrogel and the resultant strain gradient created in the substrate is responsible for folding. Even though the forces are applied normal to the plate in classical plate theory as opposed to the axial forces exerted by the shrinking gel on paper substrate, the deformation profile is similar and justifies using the bending stiffness equation from the classical theory to illustrate the influence of thickness and elastic modulus on folding. The average thickness of the paper types were  $0.113 \pm 0.002$  mm,  $0.084 \pm 0.008$  mm and  $0.077 \pm 0.005$  mm for Printer paper 90 gsm, Lokta 30 gsm and Sekishu 30 gsm. Figure 3.4 shows the actuation of paper substrates (of same planar dimensions)

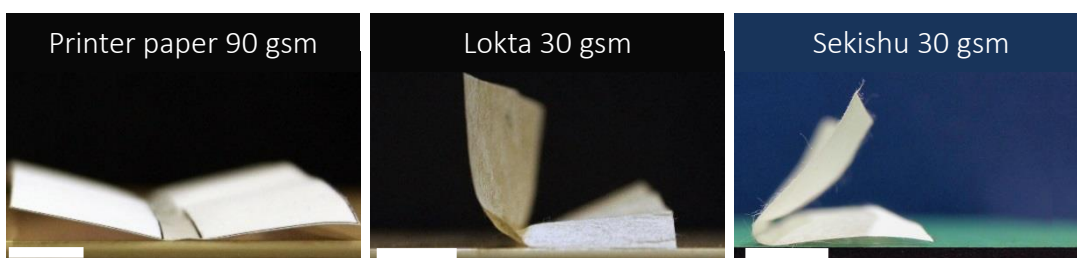


Figure 3.4: Actuation response of different paper substrates to same amount of hydrogel. (Scale bar = 10 mm).

characterised by their grammage, thickness and origin in response to identical amount of hydrogel placed in the middle along the length to initiate a fold. As expected, lighter paper types (Sekishu 30 gsm and Lokta 30 gsm) had morphed to a greater extent than the heavier and stiffer printer paper 90 gsm. The material properties of these cellulosic substrates apart from grammage were not available from the open literature. As these experiments were carried out to understand the substrate behaviour in response to hydrogel deposition rather than to derive precise relationships, mechanical characterisation of the paper types was not carried out to obtain materialistic parameters such as Elastic modulus and Poisson's ratio. Hand-held deposition of hydrogel through a syringe itself is rather challenging to ensure even gel distribution and the surface tension of the deposited hydrogel could also lead to agglomeration as it beads-up along the fold line/region. This will considerably affect how the forces are developed when the deposited hydrogel is dried to initiate folding. These scenarios will certainly influence folding as these will result in non-uniform strains along the fold line promoting sections of greater or lesser folding.

#### 3.4.1.2 Amount of gel per unit area

The energy to 'fold' the paper substrates are supplied by the membrane forces of dehydration of the deposited hydrogel. Therefore, having more hydrogel applied to a fold line should naturally result in greater folding provided the dimensions, type and grammage (weight or stiffness) of the paper substrates remains the same. An experimental study was carried out on 90 gsm printer paper of dimensions 90 mm (length) x 45 mm (width) with the fold line along the length direction through the middle. Hydrogel was uniformly deposited as a line through a syringe (nozzle  $\varnothing$ 1 mm) on to the fold line. Three iterations were investigated; 1x (one line), 4x (four lines) and 7x (seven lines), where multiple gel lines were laid on top of each other in a stack rather than deliberately spread around the fold line. All three sets were left to dry at room temperature (21 °C) under the same conditions. Once dried, the morphed folds were photographed, and the resulting fold angles were measured using ImageJ (version 1.50g) software. The visual results are presented in Figure 3.5. The fold angle is defined as the angle realised between the facets due to the shrinking of hydrogel placed on the fold line.

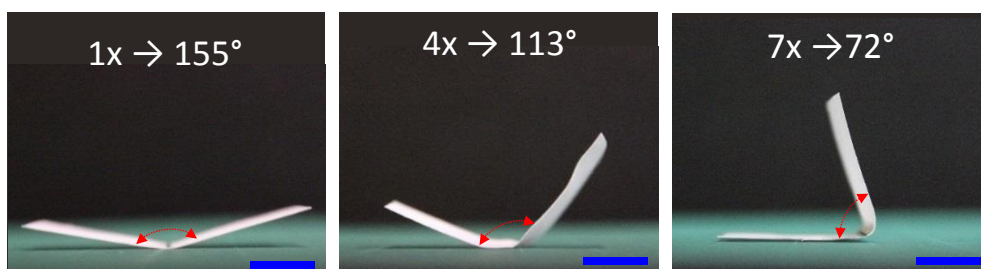


Figure 3.5: Relationship between amount of hydrogel and resulting fold angle. (Scale bar = 10 mm).



The substrate type and dimensions were chosen arbitrarily and kept same across the sample spectrum ensuring the amount of hydrogel as the only variable in determining the resulting fold angle under same environmental conditions. Since the *crease* and *bend* are defined in this project based on the local curvature, distribution of hydrogel is critical to designing a crease or a bend. Here, hydrogel deposition was confined to the fold line resulting in higher concentration of gel per unit area along the fold line for each iteration and consequently resulted in the formation of crease. Figure 3.6 demonstrates the influence of relative amount of hydrogel and the resulting fold angle in a graphical format. As expected, the extent of folding increases (*i.e.* decrease in fold angle) with the amount of hydrogel deposited. Even though the amount of gel was proposed as the influencing factor, it is the forces developed within the hydrogel system during dehydration that perform the work of folding. As such, the fold angle is the result of balance between bending stiffness of the substrate and the shrinking forces developed during the dehydration process for which the equilibrium is dependent on ambient conditions. By keeping the substrate and drying conditions identical across the sample set, the influence of the amount of gel on fold angle was isolated. The amount of gel deposited is merely an indirect and simple way to capture the effect of membrane forces of shrinking hydrogel on these substrates. As manual extrusion was employed in placing hydrogels, consistent and repeatable deposition could not be guaranteed for multiple sets. Therefore, the fold angles reported are from a single sample for each of the sets. Fold angle is expected to follow a linear trend as shown in Figure 3.6, but in order to validate this and to quantify the precise relationship, more reliable hydrogel deposition methods than manual extrusion has to be employed.

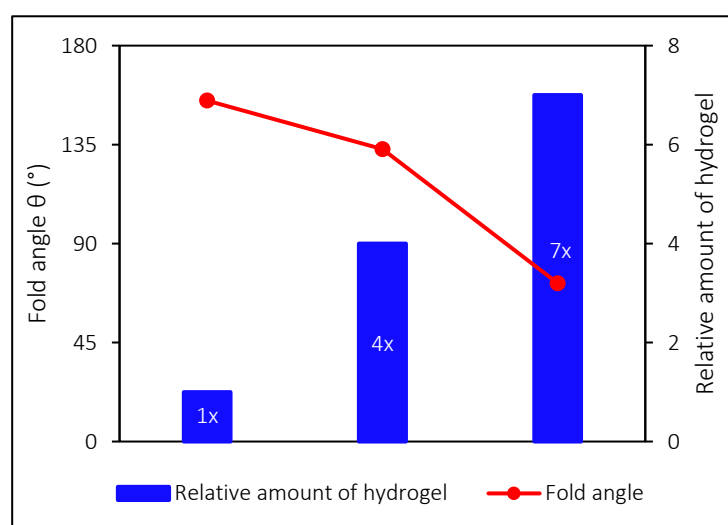


Figure 3.6: Fold angle as a function of relative amount of hydrogel confined to the fold line.

### 3.4.1.3 Distribution of hydrogel (spread)

The effect of spreading the hydrogel across a fold line in a bid to create distributed curvature was also investigated. Samples of dimensions 90 mm (length) x 45 mm (width) with the fold-regions along the length direction through the middle was also chosen here. Note that as opposed to the term fold line in the previous study, fold-region is used as hydrogel distributions of 5 mm, 10 mm and 15 mm width are investigated. Here, the concentration or amount of hydrogel per unit area in the fold-regions was kept as constant. To ensure this,  $\approx 1$  mL of hydrogel was used to cover the region of 5 mm x 90 mm,  $\approx 2$  mL for 10 mm x 90 mm and  $\approx 3$  mL for 15 mm x 90 mm. The volume of deposited gel was monitored by the eye and the resolution of the syringe used was 1 mL which diminishes the confidence in volume measurements of the deposited hydrogel. It must be noted that this study does not isolate the effect of 'substrate area that needs to be folded'; as the sample geometry is fixed, an increase in fold-region width results in an equal decrease in the width of the facets that forms the fold. The physical significance of this limitation is that it becomes progressively easier for the hydrogels to fold (bend) the substrates as the area of the facets that needs to be folded decreases. This influence will be de-coupled in the following study concerning the area to be folded. The uneven deposition of the hydrogel had resulted in some distortion along the length in the fabricated samples. Therefore, sections devoid of such distortions were extracted from the samples after drying at room temperature. These sections were then dried in the oven at an elevated temperature (140 °C for 5 minutes) to maximise the morphing response prior to imaging. The resulting folding response is presented in Figure 3.7 where it was characterised by fitting a circle to the fold region curvature and measuring the diameter using ImageJ (version 1.50g) software. It is evident from Figure 3.7 that the diameter of the fold regions becomes progressively smaller and the free ends (facets) try to wrap around the imaginary cylinder transcribed by the distributed curvature of fold regions. Consequently, the facets on either side of the fold region are coming closer resulting in greater extent of folding for increasing hydrogel spread.

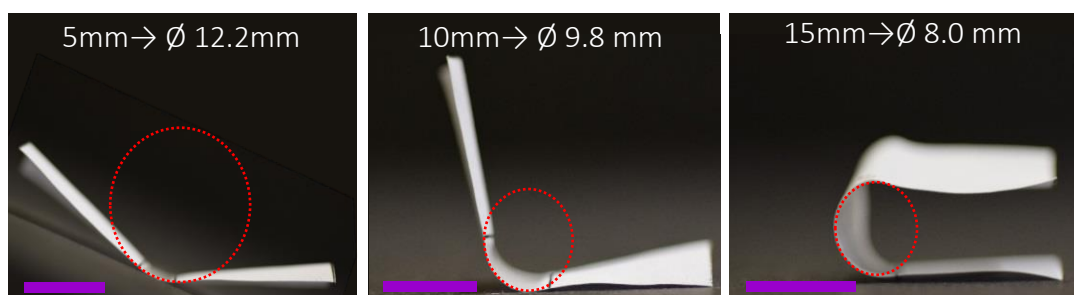


Figure 3.7: Effect of Hydrogel distribution (spread) in folding. (Scale bar = 10 mm).

#### 3.4.1.4 Open area to be folded

This is a straight forward parameter as more work needs to be done by the hydrogel to fold larger surfaces of the same stiffness. The useful work done by hydrogel in folding the substrate is limited to the amount of hydrogel deposited on the substrate, the hydrogel-substrate interface and the interface area. Since the area of facets to be folded tends to be an open design problem, the experiments to demonstrate the influence are limited to observations rather than attempting to derive precise relationship between hydrogel deposition and the area to be folded for vast compliant substrates. To ascertain the relationship between hydrogel spread and area (of the facets) to be folded, self-folding experiments were carried out with gel spreads of 5 mm, 10 mm and 15 mm over a range of specimen width. The length of the samples was kept constant (45 mm) and gel was applied through the middle along the length direction. Facet widths of 15 mm, 25 mm and 35 mm on either side of the fold region were investigated. Figure 3.8 summarises the folded curvatures of the samples after drying at room temperature.

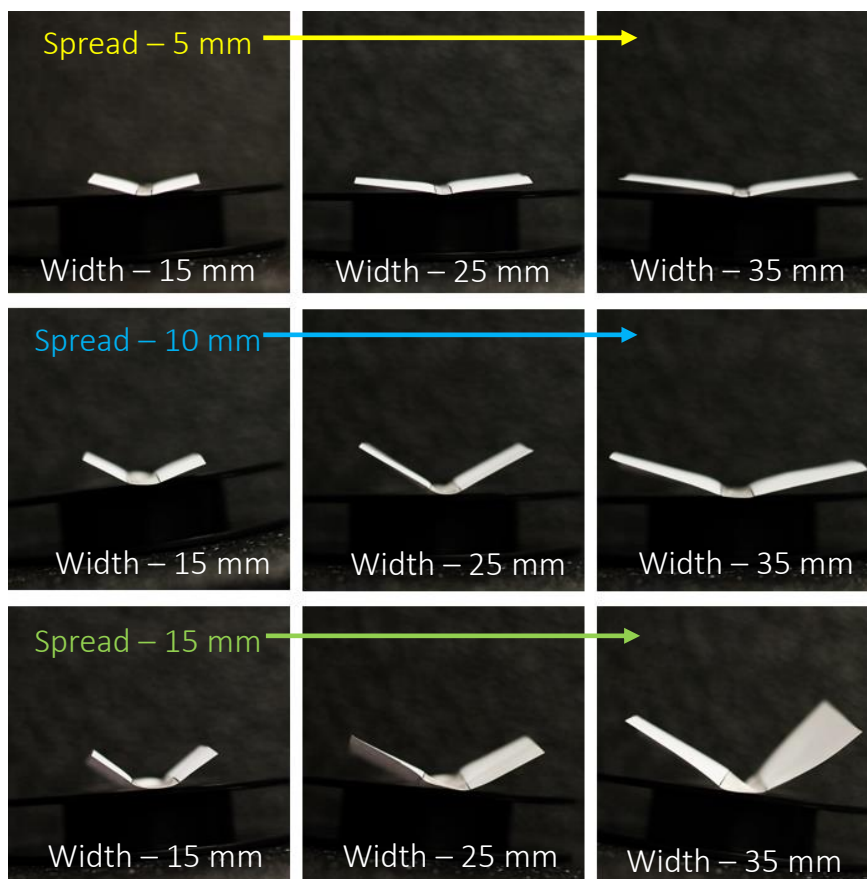


Figure 3.8: Effect of fold region width (hydrogel spread) and facet width on folding.

It can be seen that for fold region (spread) of 5 mm and 10 mm, the extent of folding is progressively lower as the facet width increases. Figure 3.9 shows the relationship between gel spread and facet width on the angle formed upon drying at room temperature (21 °C) for

Printer paper 90 gsm. Owing to limitations presented by manually filling the fold regions, it was hard to ensure even deposition of hydrogel along the length especially for fold region widths of 10 and 15 mm respectively. Additionally, the relatively large amount of gel deposited in these cases led to agglomeration owing to surface tension effects and dried as such. This resulted in uneven folding responses as well as distortion along the length of fold region. The fold angle was measured from the photographs of the folded samples using ImageJ (version 1.50g) and the method used to determine the angle is presented in Figure 3.9 (insert). As expected, a greater folding response is observed (*i.e.* decrease in fold angle) as the gel spread increases for a given facet width. Since the open areas to fold remains same on either side of the fold region, increase in gel spread results in greater membrane forces to develop at each of the 15 mm, 25 mm and 35 mm facet widths as the hydrogel dries. The influence of gel spread on the area to be folded is also evident for 5 mm and 10 mm spread as the fold angles are greater as the facet width increases from 15 mm to 35 mm on either side of the fold region demonstrating the progressive difficulty in folding wider substrates with the same amount of deposited gel. Similar trends cannot be observed for 15 mm spread between facet widths of 25mm and 35 mm. This was due to the samples being distorted and the folds not being properly manifested due to the aforementioned limitations associated with manual gel deposition (Figure 3.8 (bottom row)). The higher standard deviation in the fold angle for samples with 10 mm gel spreads were also attributed to this. However, rationale implies that similar response to that of 5 mm width would be observed if uniform distribution of gels could be ensured. The error bars represent the standard deviation among three samples for each set. With reliable substrates and gel deposition, the chart presented in Figure 3.9 can possibly be expanded to a look-up table to aid the design of morphing architectures where substrate dimensions and amount of gel required could be selected to program a specific fold angle. Another aspect not de-coupled in this study using a single fold is the effect of the second moment of inertia (more precisely the ratio of length and width) of the substrate. Even though a simplified implementation of plate buckling under uni-axial compression could be employed to see the influence of length and width on the critical buckling load (the minimum force needed to fold the paper), its influence is believed to be much smaller compared to other factors studied here. Furthermore, one of the benefits of origami is that it is scalable, so folds could be designed so as to realise similar responses by using smaller folds but in a greater number or vice versa. Furthermore, the substrate thickness was kept same throughout the set and thus the influence of length to width ratio can be expected to be minimal as thickness of the substrate is the most significant dimensional parameter affecting the bending stiffness of a plate geometry.

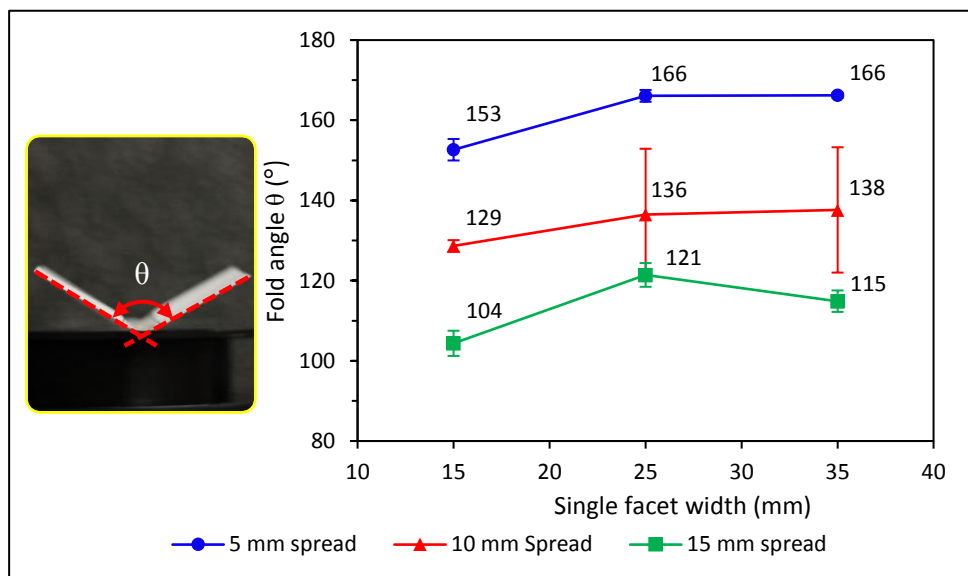


Figure 3.9: Fold angle as a function of facet width and gel spread. Method of determining fold angle is shown in insert.

#### 3.4.1.5 Interface between the hydrogel and substrate

The morphing of bi-layers depends on the integrity of the interface between the layers as lack of cohesion results in sliding interfaces and an absence of through thickness strain gradient. As for the paper-hydrogel systems presented here, the microscopic surface features of the paper (pores and undulations) provide anchor points for the hydrogels to attach onto through hydrogen bonding. Once dried and consolidated through crosslinking, the gels cannot be cleanly separated. Attempts to separate interfaces resulted in removing a thin layer of paper attached to the dried gel demonstrating that the cohesion between layers of paper is weaker than the adhesion between dried gel and paper (Figure 3.10a). The interface between the gel and paper is affected by hydration but still pertinent to initiate morphing through swelling. Figure 3.10b shows the residue layer of paper left on the hydrogel once separated after hydration and subsequent swelling. This confirms the robustness of hydrogel-paper interface and the links formed during drying and thermal crosslinking.

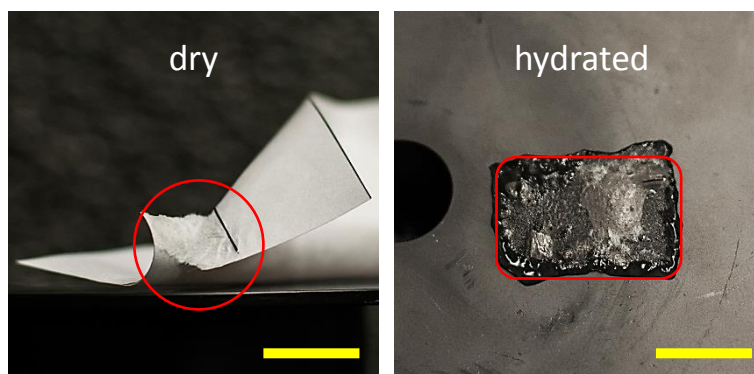


Figure 3.10: Hydrogel-paper interfaces. (a) Separated after drying and crosslinking. (b) Separated after saturation of crosslinked samples in water. (Scale bar = 10 mm).

#### 3.4.1.6 *Strain potential of the gels*

The significance of strain-differential in morphing has been established previously in 3.3 *Significance of simplistic approaches in materials and fabrication*, where examples of anisotropic swelling responses resulting in shape changes were presented from open literature. The shrinking/swelling potential of the gels directly affects the through thickness strain-differential that develops along the fold line and ultimately the folding and unfolding responses. Since the range of volumetric changes within the hydrogel controls folding and unfolding, being able to control or program this range is critical. The ability of the hydrogel to shrink or to swell depend on many factors: surrounding environment, the presence and direction of stimuli are most important. As for matters that are intrinsic to the hydrogel system, the ability to hold and release water and the rate at which this transfer can proceed are vital. The dynamics of hydration and dehydration will be covered in detail in the following section. As the water transport out of the hydrogel in this system is diffusion dominated, the rate and extend of the flow are affected by the relative water concentration gradients. Thus, the shrinkage of the gel is dominated by the relative humidity in the surrounding environment especially at room temperature. Drying of the paper architectures at elevated temperatures and the subsequent enhanced dehydration results in greater shrinking. This translates to greater folding of the architectures. The volumetric changes realised in a hydrogel can be controlled through different crosslinking strategies and modifying the gel formulation. Programming the swelling potential of the gels can not only result in opening of folded architectures but also reversal in the direction of folding or realisation of new orthogonal folds when allowed to swell without restriction. Figure 3.11a-d illustrates how volumetric changes induced in the hydrogel affects a fold. Figure 3.11a shows the programmed fold after drying at room temperature (21 °C). Figure 3.11b shows the same sample after drying at an elevated temperature (enhanced dehydration). The greater extent of folding is evident. Once immersed in water to facilitate unrestricted swelling, the fold reverts to its flat configuration as seen in Figure 3.11c. Further hydrogel swelling results in transverse folding in this configuration. This behaviour is believed to be due to unrestricted hydrogel swelling at the ends causing the paper substrate to fold (roll) orthogonal to the initial fold region. The swelling and shrinking characteristics of the gel are characterised in great detail in the following Chapter 4 (*4.3 Characterisation of the material formulations*). In conjunction with the experimental work carried out in Chapter 4, in programming the extent of volumetric changes in the hydrogel, Figure 3.11 demonstrates the potential of programmable strain to realise additional shape configurations.

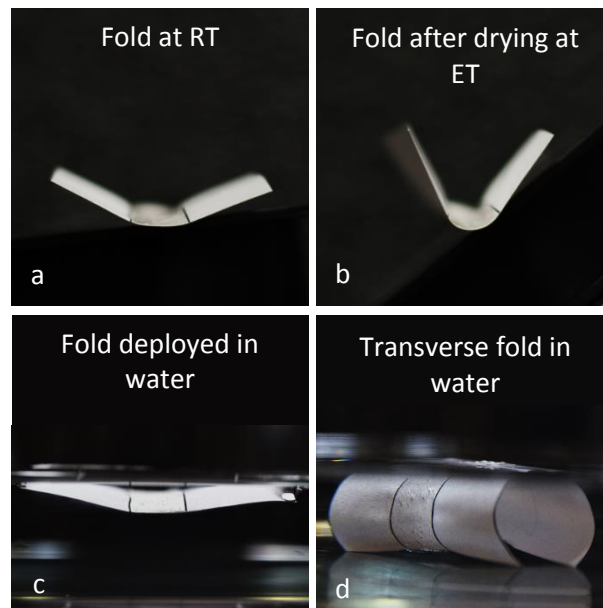


Figure 3.11: Effect of shrinking/swelling potential on realising folds (a) Fold at room temperature (b) Increased folding after drying at elevated temperatures (ET) (c) Fold deployed to flat configuration once fully immersed in water (d) Further unrestricted swelling results in transverse fold.

### 3.4.2 Dynamics of hydrogel dehydration and hydration

Dehydration and hydration of the gel and paper substrate plays a significant part in the realisation of 3D architectures and its actuation (4D) as investigated in this study. Understanding the role of water in carboxymethyl cellulose hydrogel and its effect (localised) on the fold line is key to understanding the dynamics of shrinking and swelling. Water in hydrogel can be classified into bound, semi-bound, interstitial and free water [169]. The water molecules attached to the most hydrophilic and polar groups in the polymer chain are called bound water or primary bound water. During the synthesis of hydrogel, hydration of these functional groups ensues immediately, further opening the network and exposing more functional groups (hydrophobic) to which water can attach through weak interactions. These water molecules are classified as semi-bound or secondary bound water. Even though they have weaker interactions than bound water, these water molecules are connected to the main polymer network structure of the gel. Interstitial water, whilst not attached to the hydrogel structure but exists in spaces between the network chains, pores and voids. The water in the outermost layer is called free water. As interstitial and free water are not attached to the polymer network, they can be easily removed. These water molecules are imbibed as a result of osmotic forces driving the hydrogel towards infinite dilution. The crosslinks present in the gel resist swelling and further absorption of water into the gel ceases once the retraction force of the gel network and osmotic forces reaches an equilibrium. If the polymer chains are held together by means of weak physical interactions or if the crosslinks are degradable, then the gel will disintegrate as the networks swells further in the absence of a restorative force.

Swelling is driven along the water concentration gradient and on the application of the stimulus of water, the hydrophilic and polar functional groups of the polymer in dry gel hydrates first resulting in primarily bound water followed by secondary bound water. The extent of free water absorbed during actuation sequence depends on the programmed swelling potential of the hydrogel mediated through formulation and crosslinking and is reported in Chapter 4 (4.3.2 *Swelling ratio*). The continued absorption of water into the hydrogel towards infinite dilution is resisted by the crosslink points in the hydrogel thus controlling the strain potential and providing aqueous stability to the actuated architectures.

Natural drying of the hydrogel at room temperature and atmospheric conditions removes the free and interstitial water from the network. This dehydration and resultant shrinking of the gel placed on paper substrates result in the initial out of plane deformation (Figure 3.11a). Drying of the gels at higher temperatures results in further shrinking due to enhanced dehydration and maximises the morphing or deformation of the substrate (Figure 3.11b). The extent of water loss in the gel during such dehydration processes are reported in Chapter 4 (4.3.3 *Shrinking ratio*). Hydration and parameters governing the actuation of manually folded paper substrates were investigated and reported in Chapter 2 (2.5 *Factors affecting deployment*). As for the hydrogel-paper system presented here, the paper substrate is envisaged to act as a valve that controls the exposure of gel to the stimulus of water by virtue of its properties such as grammage and porosity especially when placed on a water bath to actuate. Hydration and de-hydration of the carboxymethyl cellulose polymer is a diffusion driven process mediated by water concentration gradients between the substrate and its environment. This determines the rate at which hydration and dehydration of the samples and subsequent swelling or shrinking can occur to morph between the programmed states. Therefore, the environmental conditions are also important. Manipulating the water concentration in the environment can influence the speed of actuations of the architectures fabricated in this manner by controlling the rate of swelling/shrinking. For example, drying the samples morphed at room temperature and ambient conditions at an elevated temperature promoted further de-hydration at a faster rate resulting in enhanced morphing behaviour. Deployment of folded samples in an aqueous environment also promoted faster hydration of the gel devoid of water. This offers wider possibilities of controlling the speed of actuations by using activating media (stimuli) of varying water concentration gradients.

### 3.5 Examples of shrinking driven morphing on fibrous structures

This section is aimed to demonstrate the capability of this proposed methodology to realise programmable morphing architectures without the complexity of the strategies covered in



Section 3.3 *Significance of simplistic approaches in materials and fabrication*. Since these examples are presented as a proof of concept, manual extrusion was used to deposit hydrogels along the prescribed fold path. The results presented here are more of a visual study as opposed to an in-depth investigation into the design parameters in creating these architectures. Limiting the responsiveness of folds through geometry, design and over-constraining have been discussed earlier in Section 3.2 *Classification of folds in origami inspired stimuli responsive morphing* to convert an active fold into passive. However, these limitations are also valuable design tools to generate intermediate or traditionally hard to access shape configurations. The examples presented here can be categorised into independent and coupled, based on how the key deformations for morphing are realised.

### 3.5.1 Independent morphing response

Typically for a hydrogel placed on paper substrate, drying results in a positive curvature due to the shrinking of gels (valley fold) whereas, the inverse configuration results in a negative curvature (mountain fold). Figure 3.12 shows the schematics of these responses. These behaviours are used to create and actuate some common morphing shapes that consist of creases and bends.

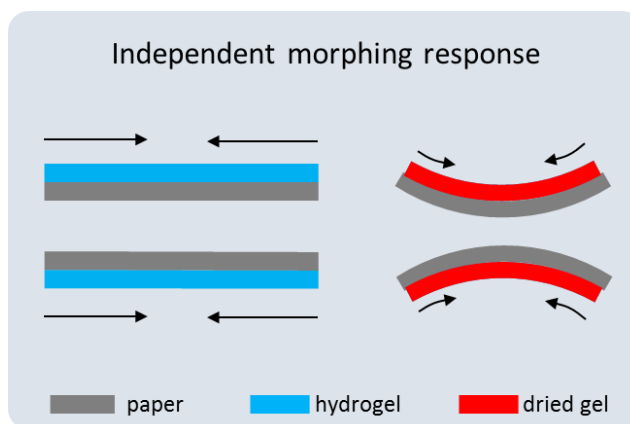


Figure 3.12: Schematic of independent morphing response of shrinking hydrogels on paper. Arrows indicate membrane forces of shrinking.

*Helix*: The fabrication of helix from a 2D geometry has been effectively used to demonstrate the potential of various morphing material systems [166,167]. Fabrication of similar helical shapes utilising hydrogel shrinking initiated morphing offers a direct comparison between the various strategies of realising morphing architectures. The geometric parameters defining the helix are presented in Figure 3.13(top row).

Fabrication of helices from flat substrates traces its origin to the recreational habit of paper folding, where a paper strip (length  $\gg$  width) folded perpendicular to the length direction along the entire length transcribing a circular shape. Varying the fold line spacing and angle

between the length axis results in helices of varying shapes and sizes. The geometric criteria of length  $\gg$  width is critical to the formation of helices from substrates as low aspect ratio substrates would only fold upwards. Whereas, the high aspect ratio strips can fold and turn over to complete the rotation and pitch. Same principles of folding the strip along the length direction are adopted for realising morphing helices. Figure 3.13(bottom row) shows the schematics of geometrical and fold parameters concerning helix formation from a strip. These parameters especially the fold line spacing ( $a$ ) and angle ( $\theta_s$ ) can be varied to create helices of varying length ( $L$ ), diameter ( $D$ ) and helix angle ( $\alpha$ ).

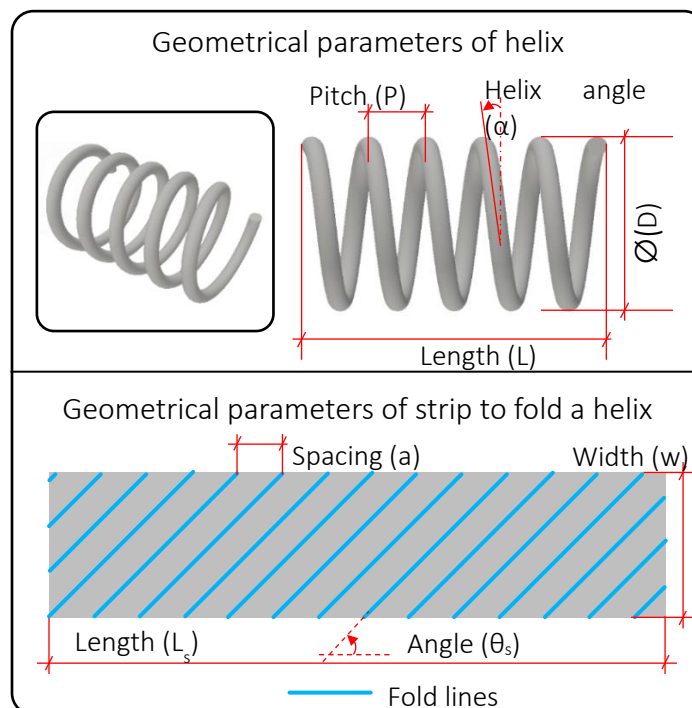


Figure 3.13: (Top row) Schematic of helix and its geometrical parameters. (Bottom row) Schematic of fold line and geometrical parameters of paper strip to fold a helix.

Results from a parametric study on varying the fold line angle and spacing is presented in Figure 3.14. All helices were fabricated from strips of same dimensions. Hydrogel was deposited on the substrate using a syringe (nozzle  $\varnothing = 1$  mm) and utmost care was taken to ensure even distribution along the fold lines for all samples. The uniform and even deposition of gel minimised the effect of amount of hydrogel per unit area as the focus here was on geometric and design parameters on helix formation. Self-folding of helices from a paper strip is an example of how geometric limitations can affect morphing responses. These results demonstrate the possibility of programming a specific helix by varying the design parameters on the paper substrate in shrinking initiated morphing.

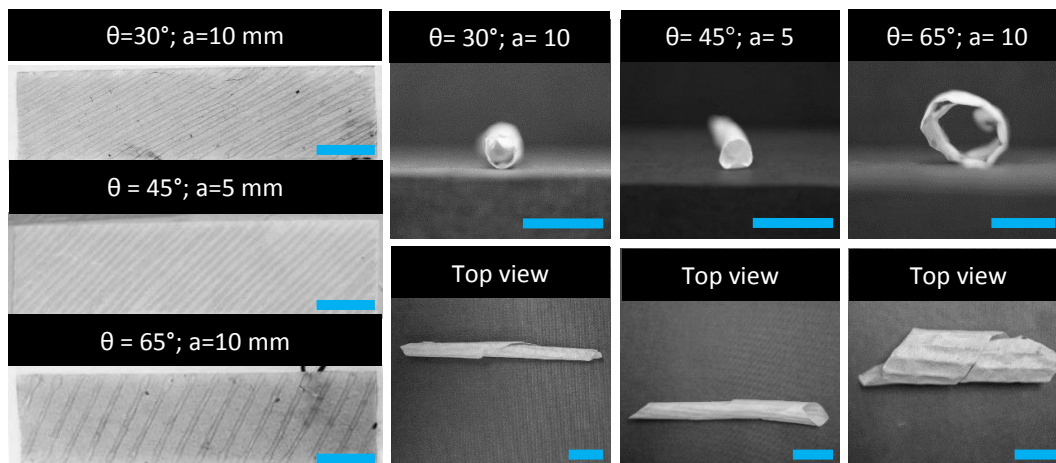


Figure 3.14: Programmable self-folding helices. Geometric parameters such as fold line angle ( $\theta$ ) and spacing ( $a$ ) are varied to create helices of varying diameter ( $D$ ) and length ( $L$ ). Images are presented in black and white to enhance the visibility of gel placements on fold lines. (Scale bar = 25 mm).

*Saddle shape:* Fold accuracy, one of the performance parameters of folding has been previously defined as the ability of a material to fold along the prescribed fold path, and any deviation from a straight-line path would impose geometrical frustration on the folds created. This characteristic feature of folding has been deliberately taken advantage of to create decorative and artistically pleasing features using paper. This type of folding is usually referred to as curved crease origami. Among such architectures, folding of annular strips of paper along a central curve have interested artists and researchers alike as the resulting folded structure is heavily dictated by the geometric frustrations that arise from the curved crease.

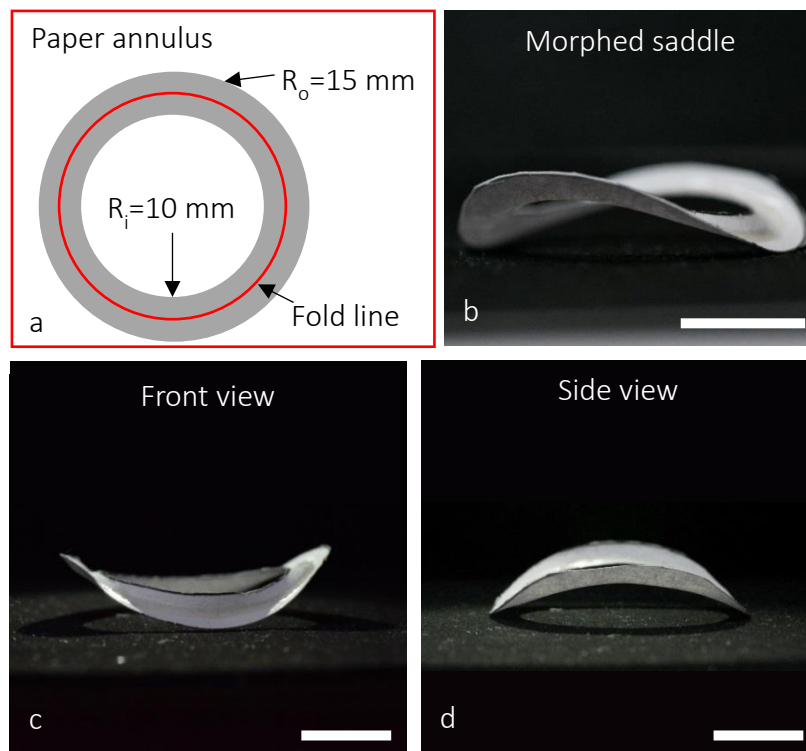


Figure 3.15: Morphing of annular strip. (a) Schematic of paper annulus. (b) Morphed saddle after drying of the hydrogel at room temperature (21°C). (c) Front view (d) Side view. (Scale bar = 10 mm).

Dias *et al.* has published an in-depth analysis of the geometric mechanics of an annulus folded along a central circular curve [170]. In order to demonstrate the feasibility of hydrogel shrinking mediated folding in realising curved creases, an annular strip of paper was folded using the hydrogel shrinking strategy. Figure 3.15a and b show the schematic and dimensions of the annular strip and the morphed shape. Figure 3.15c and d show the front and side views respectively. Figure 3.15 clearly shows that the hydrogel shrinking along the fold path resulted in a curved crease which transformed the flat annular ring to a buckled structure (saddle) driven by geometrical frustration. This morphing response further emphasises the significance of initial geometry choice and fold paths as powerful design tools in realising unique morphing responses and architectures.

### 3.5.2 Coupled morphing response

Programming of morphing architectures by exploiting geometric constraints of the substrate has been covered in the examples of helices and saddles. Here, the independent morphing response of gel on paper is antagonistically coupled to initiate novel morphing responses. Designing the material configuration is key along with fabrication to initiate these new responses from hydrogel-paper systems. The schematic of material configuration and resulting morphing response is presented in Figure 3.16.

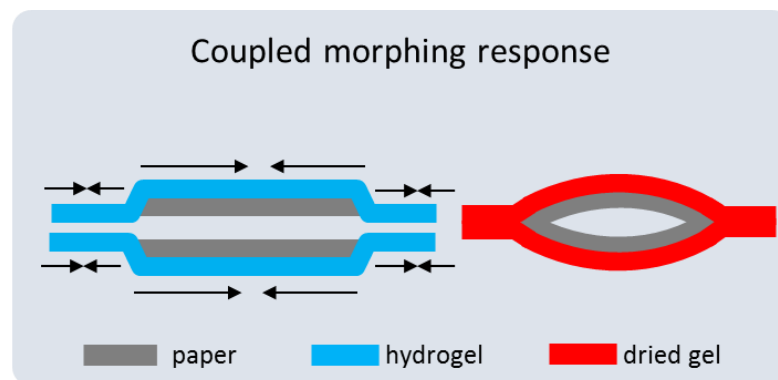


Figure 3.16: Schematic of Coupled morphing response.

These morphing responses can be utilised to create pop-up structures as seen in Figure 3.17. The structure is flat once fabricated and pops into 3D after heating in the oven. Design of these structures involves sandwiching two overlapping paper cut-outs (of any closed geometric shape) in between two layers of hydrogel followed by drying. The hydrogel layers on top and bottom must fully cover and extend beyond the boundaries of the paper cut-outs in order to fully encapsulate them. The opposing morphing responses during room temperature drying balances out resulting in a flat composite substrate as shown in Figure 3.17. Enhanced dehydration at higher temperatures results in shrinking and greater strain differential across

the paper-hydrogel substrate. This frustrates the flat configuration and result in popping of the paper cut-outs as this is the lowest energy configuration as shown in Figure 3.17a and b. Taken in isolation, shrinking gel should result in a positive curvature on the top paper layer and negative on the bottom; however, the resulting structure in the coupled response has negative curvature on the top layer and positive on the bottom. This antagonistic response is by virtue of coupling. Using circular cut-outs results in an ellipsoidal shape with each cut out forming opposing domes on either side of the substrates mid-plane.

Morphing response of a floral configuration using circular cut-outs are shown in Figure 3.17a and b. Using square (or any parallelogram) cut-outs results in a pillow like shape (Figure 3.17e) to be morphed out of the flat configuration. The domes formed are resilient as they are capable of supporting mass much greater than itself (Figure 3.17c and d). The curvatures of the dome are locked in place by the membrane forces of shrunk hydrogel and they do not collapse when cut open (Figure 3.17e). These types of closed structure that pop-up from a flat configuration cannot be fabricated through independent responses of hydrogel shrinking alone. These morphing responses forming closed structures demonstrate that through the design of material configuration in 3D space and coupling, more complex and diverse architectures can be achieved using the methodology presented here.

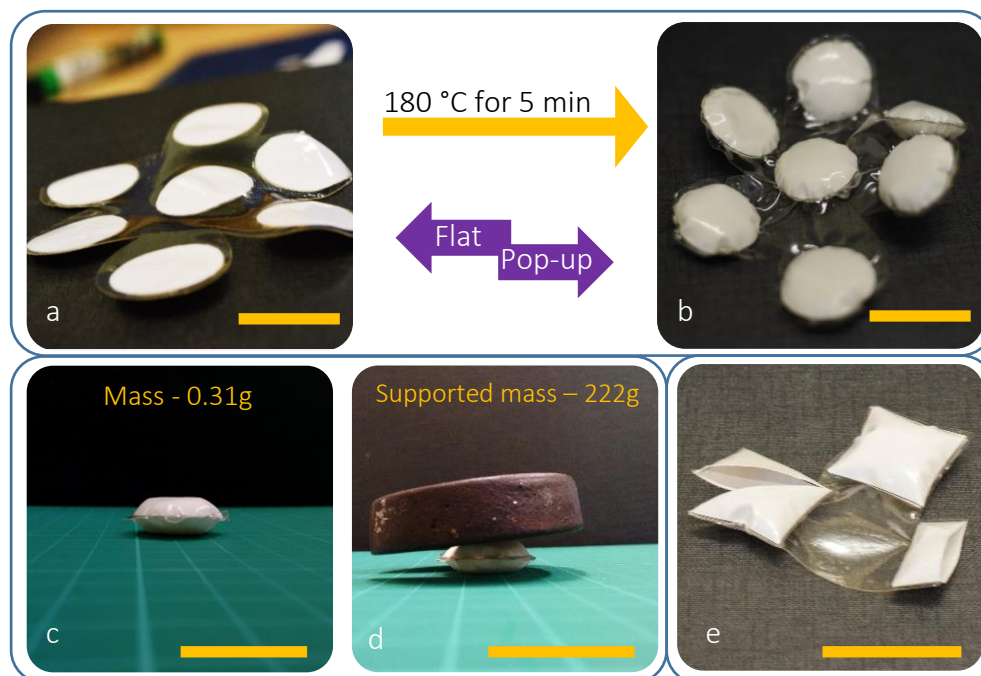


Figure 3.17: Hydrogel shrinking initiated pop-up morphing response. Transformation of (a) flat floral configuration into (b) pop-up configuration in response to the stimuli of heat. (c) Individual unit isolated from the floral architecture. (d) Resilient individual unit supporting mass much greater than itself. (e) Cut-open square pillow structure showing locked in curvatures after transformation. (Scale bar = 30 mm).

### 3.6 Potential of strain differential beyond hydrogel on paper systems

The significance of simplistic approaches in realising morphing utilising the volumetric changes in hydrogel and some of the shape configurations possible through this methodology had been presented in the previous sections. By way of examples, it was demonstrated that this technique could be employed to fabricate similar architectures achieved using other self-actuation strategies such as ionoprinting, shape memory materials and photolithography without the complexity in terms of materials used and fabrication steps. The significance of having control of material configuration in 3D space to achieve programmable morphing with this strategy is evident. Paper as a material is not reliable enough to program predictable and consistent morphing responses owing to its numerous constituents and inherent anisotropy. Therefore, a programmable material with known ingredients and predictable response in terms of stability and swelling is essential to realise complex and reliable morphing architectures using the strategies developed here. The same can be said of manually depositing hydrogel onto paper substrates to define fold lines. The repeatability as in terms of achieving the same degree of morphing has been challenging due to inherent difficulties associated with repeating manual extrusion despite utmost care taken to ensure even gel deposition.

Along with the ability to program the strain differential, initial substrate geometry and material configuration in 3D space is central to realising morphing and 4D actuation with this strategy as evidenced by the examples presented in the previous sections. In order to maximise the usefulness of the strain differential mediated morphing using volumetric changes in hydrogel, paper substrates have to be replaced with a more controlled and consistent substrate. Integration of such materials into the 3D printing landscape is essential to realise wider material configurations in 3D space. For example, realising specific geometrical criteria, kirigami-esque cuts and curved fold lines in substrates can be carried out easily and more precisely with additive manufacturing processes as opposed to casting or cutting out specific shapes and using manual patterning or photomasks. Therefore, it can be concluded that additive manufacturing techniques are essential to fully realise the potential of cellulosic materials in morphing as envisaged in this project.

### 3.7 Discussion and Conclusion

This chapter presented a detailed definition of folds and what it entails along with fold performance parameters relevant to self-actuation. This was aimed to clarify the misperception surrounding the specific terms used in origami, origami engineering and stimuli

---

responsive morphing architectures. The concept of strain differential as the driving force of morphing and a comparison of different approaches found in the open literature regarding the programming of strain differential to realise morphing was also presented. The simplistic approach to the materials used and fabrication strategies adopted in this study was emphasised whilst demonstrating that using volumetric changes in a hydrogel to realise morphing is more than adequate in terms of shapes created and compared, and to establish its potential. The fold performance parameters offer great insight into the realisation and understanding of responsive morphing architectures facilitated through folding. Some of the directly measurable parameters can be used to quantify the material system by investigating a model architecture and its response to a stimulus. The factors affecting the creation of folds were also investigated. The folding responses to the variation of these factors on a single valley fold was depicted and was aimed to serve as guidelines or reference points for programming architectures and morphing behaviours of increasing complexity. Fibrous architecture of paper and cellulose is still at the heart of these morphing responses and thus the deployment of the morphed architectures back to the initial flat configuration in response to the stimulus of hydration should adhere to the parameters identified in Chapter 2 *Morphogenesis through folding - Potential of paper*.

Dynamics of dehydration and hydration of the hydrogel, and its influence on the extent of folding was also reported. Examples of some morphing architectures fabricated with the hydrogel on paper system and the significance of design parameters, substrate geometry and coupling effects in realising unique, programmable morphing responses were also presented. However, the investigation was carried out mainly to capture the design rules to realise morphing architectures than to fully characterise the response for a specific substrate. This is justified as the paper substrate and manual deposition of hydrogel were used as tools to understand the morphing behaviours by harnessing volumetric changes in hydrogel on a fibrous cellulosic substrate. The results from this study helped to further understand the morphing potential of cellulosic substrates and supplement the understanding of actuation principles of three-dimensional cellulosic architectures.

The presented programming guidelines have been proven to be effective through examples of morphing and deploying paper architectures. The natural progression of the work presented here would be to take advantage of computer aided designing (CAD) and 3D printing. The programming guidelines presented in this chapter allows to digitally create intricate architectures through CAD with dedicated morphing pathways along origami and kirigami principles. Whereas, 3D printing allows to realise these architectures with great

---

precision. Even though relatively simplistic whilst showing potential, 4D architectures realised in this manner is plagued with inconsistency and is clearly inferior to comparable systems observed in nature such as pinecones. The challenge is to overcome the limitations presented by inconsistent material substrates and lack of spatial control of key material components by developing novel material systems tailored for purpose and adopting the technological advancements presented by additive manufacturing.



---

## Chapter 4 Cellulose – hydrogel composites for 4D Printing

---

### 4.1 Introduction

The scientific understanding from the work carried out in characterising the paper actuators formed the foundation of developing a new smart material system suited for morphogenesis manufacturing. As proposed in Chapter 1 (*1.3 Morphogenesis manufacturing*), nature's design of smart systems can be encapsulated by the following: (1) inherent design either embedded into organisms' genetic code or shaped through the interacting natural forces; (2) core building materials embedded with multi-functionality; (3) growth as a process which enables precise placement of various building blocks in hierarchical order to realise form as per the embedded design under the influence of environmental stimuli. The design rules for folding flat paper substrates into 3D forms as presented in Chapter 3 could be coded into CAD files to be 3D printed. It was previously established in Chapter 1 that albeit new functional and responsive materials currently being developed for 4D printing, there is scope for further improvement especially with respect to the ecological footprint, sustainability and cost of responsive 4D materials. This chapter seeks to address this noticeable lack in the research field whilst meeting the second criteria to enable the third point in nature's design strategy for smart systems. Despite commercial paper making processes having to adhere to certain industrial standards, the microstructure and constituents of paper is known to vary across a single sheet itself [137]. Even though variability was minimum in handmade paper types as proven in Chapter 2, greater degree of control over the microstructure is paramount in order to realise predictable and reproducible actuation as seen in nature's actuators. Developments in additive manufacturing technology enables unparalleled capability in placing materials in 3D space and thereby resulting in the realisation of hybrid or hierarchical structures that are characteristic of functional biological systems. Intricate 3D designs can be fabricated with remarkable accuracy (resolution) as a direct result of continued progress in both software and hardware developments in this field. Furthermore, the technology is also becoming increasingly affordable to the general consumers as well as researchers outside of traditional 3D printing markets owing to its mass-adoption across a multitude of disciplines outside of engineering such as rapid prototyping, fashion, design, animation, and general hobbyists. This chapter describes the development of a paper inspired cellulosic smart composite that is readily suited for extrusion-based 3D printing thereby facilitating the 4D printing of cellulosic materials. The smart composite is inspired by nature's actuators such as pinecones not only in its cellulosic nature but also in terms of its activation stimuli and strain gradient mediated actuation. This smart composite consists of reinforcing cellulose fibres embedded within a

swellable host hydrogel matrix derived from cellulose. The constituents and construction of the composite is built upon the understandings from the characterisation of actuating paper architectures as well as the design rules for realising morphing through generating strain-differential as investigated in the previous chapters. The following sections present a processing route which permits 3D printing of cellulosic materials. The formulations were developed to facilitate ease of extrusion, good dispersion of the cellulose fibres within the host matrix and stability of the constituents in mixture as well as in aqueous medium. Even though the formulations developed are that of hydrogel and hydrogel composites, the characterisation performed were on the flow (*i.e.* for extrusion in 3D printer) and actuation (*i.e.* swelling, shrinking and force generated due to swelling) parameters as opposed to more conventional procedures such as gelation or morphological analysis as they were deemed less critical for 3D printing and morphing. The developed cellulosic hydrogel composite formulations can be extruded through a syringe and satisfies the traits of materials suited for morphogenesis manufacturing by virtue of its responsiveness and low ecological footprint.

#### 4.1.1 Cellulose as a smart material

The potential of paper of which cellulose is the principal component, as a precursor for a cost-effective, sustainable, bio-degradable and programmable smart material have been presented in the previous chapters and supported by [117]. The hierarchical structure of cellulose fibre is presented in Figure 4.1. The presence of hydroxyl groups (OH) in the molecule results in inter-molecular hydrogen bonding between molecules and intra-molecular hydrogen bonding

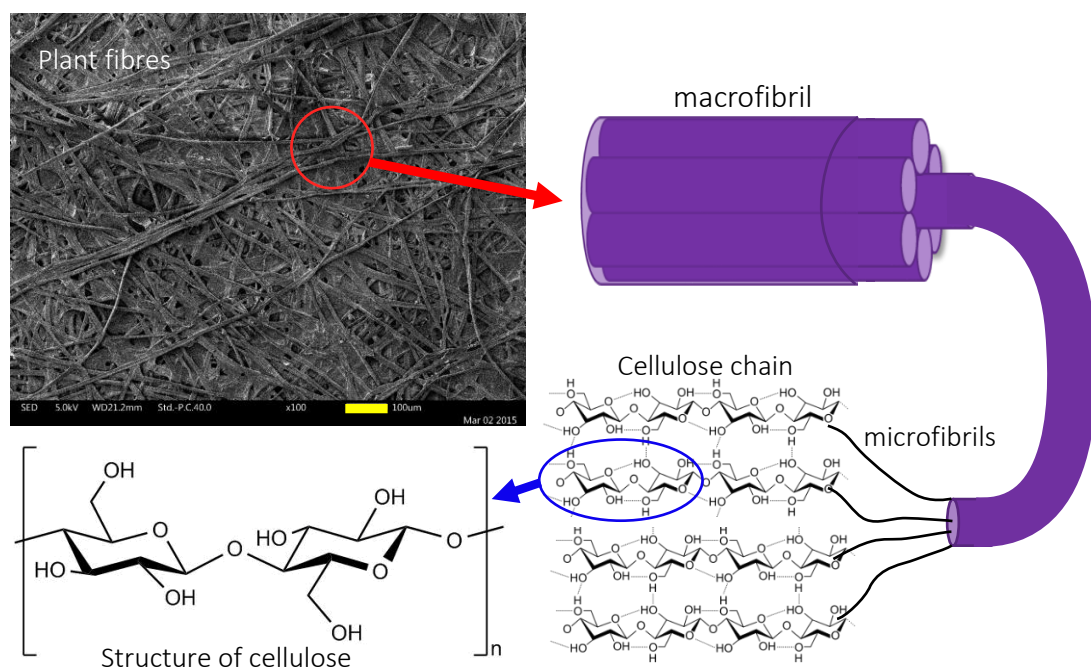


Figure 4.1: Schematic of hierarchical structure of cellulose fibres. (Scale bar = 100  $\mu\text{m}$ ).

between the cellulose chains leading to the formation of fibrils which further associate to form naturally occurring fibres in a true hierarchical fashion. In fibrils, cellulose exists in highly ordered crystalline and disordered amorphous phases [38]. These intercalating water molecules can interact with the amorphous regions and result in swelling throughout the material, which is used to drive the actuation of specific architectures created by these materials.

#### 4.1.2 Cellulose fibres

Cotton based pulp linters were chosen as the reinforcement phase for the composite as they have high cellulose content ( $\approx 99\%$ ) compared to fibres from other plant sources such as flax (65%-87%) [171]. Cotton derived pulp linters are highly desirable in paper making industry for its high cellulose content ( $\approx 99\%$ ), purity and colour [172]. The farming impact of producing cotton such as substantial use of water and other resources were overlooked at this stage as it was the readily available natural fibre source with high cellulose content. Even though less resource demanding crops with high enough cellulose content such as hemp fibres (73%-77%) exists, they are not easily available and are not produced in large scale owing to legal limitations prevailing in most countries [173]. However, the legal restrictions associated with growing industrial hemp are being relaxed or removed in most countries paving way for an efficiently sustainable cellulosic fibre source than cotton. As the actuation in paper architectures were proven to be a consequence of hygroscopic swelling of cellulose regardless of its biological origin, any cellulosic fibre should suffice as the reinforcement in the smart composite.

#### 4.1.3 Enabling functional cellulose 3D printing

Thermal melting of polymer filaments and laser sintering of ceramic/metal/polymer beads via laser beam, are the prevailing commercial approaches employed in the field of additive manufacturing. Despite the environmental benefits and abundance of cellulose, 3D printing cellulose in its native form is not viable as it cannot be melted and extruded like existing 3D printing polymer feedstocks, nor sintered with a laser. Therefore, new approaches had to be employed to add cellulose to the domain of 3D printing materials. These approaches have already been reviewed in Chapter 1 (1.7 *Additive manufacturing with cellulose*). However, the following presents more specific details pertaining these different methodologies of enabling cellulose printing. A common approach is to use 3D printing filaments with cellulosic materials (e.g. sawdust and recycled wood) forming fillers ( $\approx 30\text{-}40\%$ ) within a polymer matrix such as PLA (Poly lactic acid) [109,110]. However, this strategy is not ideal for morphing applications due to the limited exposure to stimuli and lack of consistency [111]. Another practical

approach is to dissolve cellulose in suitable solvents to enable printing as reported by Markstedt *et al.*, where different types of cellulose (namely bacterial nanocellulose, Avicel-PH-1-1 and dissolving pulp) were dissolved in ionic liquids (IL) and printed. This was followed by coagulation in non-solvents such as water by printing directly onto a coagulating bed (agar gel), resulting in 2D and multilayer 3D gel structures. Ionic solutions with cellulose concentrations of 1 %, 2 % and 4 % (w/w) were 3D printed. After the complete removal of IL followed by freeze drying, the resulting print was shown to be amorphous cellulose aerogels [112]. Composite bio-inks prepared by combining cellulose nanofibrils (NFC) dispersions in alginate-based hydrogels consisting of 95-99 % water was also reported. The cellulosic content of the reported bio-ink varied from 1.5 %-2.25 % w/v and was crosslinked by immersion in calcium chloride ( $\text{CaCl}_2$ ) solution [174]. Hakansson *et al.* reports similar bio-inks where the 3D dry state shape was achieved by means of freeze drying the printed form [113]. Similar approaches in cellulose printing were also reported from Aalto University (Finland) and VTT research (Finland) as part of their joint DWOC (Design Driven Value Chains in the World of Cellulose) program [114]. Even though these approaches facilitated 3D printing of cellulose, the final shapes which could be achieved were fixed. More recent work from Gladman *et al.* demonstrated the fabrication of plant-inspired architectures using cellulose nanofibrils (NFC) within a thermo-responsive acrylamide ink. The final 3D shapes were not fixed in this case, but capable of transforming in the time domain as envisaged in 4D printing. These architectures actuated as a result of preferential swelling of the acrylamide gel guided by the shear alignment of NFC along the print path. A 0.8% wt of NFC was used to prepare the composite ink [93]. Even though adapting cellulosic materials to the 3D printing domain was achieved, there is scope for further innovation especially with regard to realising printed composites with higher cellulosic content.

The design of cellulosic fibrils to preferentially control the swelling of an embedding matrix thus creating a through-thickness strain gradient is inspired by nature's design of the hierarchical structure of pinecones [26,115]. The significance of porosity and the resulting network structure of pulp fibres in controlling the opening and closing of folds and also in aiding fold recovery (after actuation) in paper architectures had been reported in Chapter 2. Such a microstructural network would not only enhance the mechanical properties of hydrogel substrates but also provide additional parameters such as porosity and anisotropic stiffness which can be programmed to tailor the response to stimuli. The importance of a stable matrix in supporting multiple actuation cycles and fold recovery has also been established. Combining a cellulose derived hydrogel with pulp fibres will permit the

development a cost-effective, all cellulosic smart composite whilst providing chemical homogeneity ensuring greater compatibility between the constituents (*i.e.* enhanced reinforcement-matrix compatibility). Some examples of cellulose derived polymers forming hydrogels are hydroxypropyl cellulose (HPC), hydroxypropyl methylcellulose or hypomellose (HPMC), carboxymethyl cellulose (CMC), hydroxyethyl cellulose (HEC), methyl cellulose (MC) and ethyl cellulose (EC) [36,59]. The pulp fibres were combined with a suitable cellulose derived gel forming polymer to realise a cellulosic hydrogel composite with the attributes to be 3D printed and the following sections reports the development, characterisation and its feasibility of morphing in the time domain.

## 4.2 Development of hydrogel composite

The idea of a composite hydrogel is not entirely new. Historically, several additives of various aspect ratios have been incorporated into base hydrogel in order to enhance their mechanical properties [57,74,175] and some examples were as reviewed in Chapter 1 (1.5.2.4 *Hydrogel composites*). Carboxymethyl cellulose (CMC) is a hydrophilic cellulose derivative with carboxymethyl groups bound to the hydroxyl groups of glucose unit and was chosen for this study. The functional properties of this biocompatible carbohydrate depend on its degree of substitution (*i.e.* the average number of sodium carboxymethyl groups substituted per anhydroglucose unit of cellulose). The polar nature of carboxylic group makes CMC soluble in water resulting in the formation of gel. This polymer is widely used in food, skin care and drug industry as a thickening agent and rheological modifier. The cellulose fibres derived from cotton pulp linters are envisaged to form a structural and functional network within CMC hydrogel resulting in an all cellulosic composite. This cellulosic pulp-hydrogel composite is responsive to the stimulus of water due to its hygroscopic nature and control over the rate of stimulus ingress imparted by virtue of the pulp fibre network enabling programmability. The following sections detail the development of this composite including the optimisation steps undertaken to ensure stability and also to facilitate 3D printing of these material systems.

### 4.2.1 Materials and formulation

Reagent grade water from Fisher Scientific was used as received. Carboxymethyl cellulose sodium salt (CMC) with degree of substitution (DS) of 0.9 in molecular weight (Mw) of 700,000 and 250,000 were obtained from Arcos Organics. Hydroxyethyl cellulose (HEC) was obtained from Merck Millipore. Montmorillonite clay (naturally occurring mineral) and citric acid (99%) were purchased from Alfa Aesar and Sigma Aldrich respectively. Poly acrylic acid (PAA) in molecular weight (Mw) of -450,000 was purchased from Sigma Aldrich. All the materials were

used as supplied. Pressed pulp linters (plant source-cotton) for papermaking was purchased from George Weil Art & Craft Supplies ([www.georgeweil.com](http://www.georgeweil.com)).

Nomenclature shown below was used to indicate the respective ingredients and their amount (in grams) in each formulation.



For example, a sample [1]/[2]/[3]/[4]/[5] = 30 / 1.5 / 0 / 0 / 0.15 indicates that the formulation contains 30 g of water, 1.5 g of gel polymer, 0 g of dried pulp, 0 g of clay and 0.15 g of crosslinking agent. For samples crosslinked with citric acid, the total amount of polymers in [2] were in a 3:1 (CMC: HEC) mass ratio.

#### 4.2.2 Processing

To attain a balance between the benefits of fibrous network without compromising the gel nature, a 50% fibre  $V_f$  (volume fraction) of the final composite (*i.e.* half fibre-half CMC polymer) was deemed appropriate and desired. Cellulose fibres (as used for paper making) were obtained as pressed pulp linters (Figure 4.2 (top row) a) and was saturated in water for  $\approx 24$  hrs (Figure 4.2(top row) b), ), to disrupt the hydrogen bonding between individual fibres. This step was followed by breaking up of linters into smaller pieces by gently scraping with a spatula and drying at room temperature (Figure 4.2(top row) c). The uniform dispersion of pulp fibres in water is crucial for smooth extrusion through syringe nozzles without clogging which is the dispensing system envisaged. The saturation and breaking up of pulp linters (fibres) were essential to aid the uniform dispersion of fibres during processing as pulp in its supplied form was almost impossible to disperse due to its compacted nature. In traditional paper making process, dispersion of pulp requires large volume of water and mechanical agitation to separate the fibres from each other. This is essential to 'relax' the hydrogen bonding between individual fibres resulting in the formation of fibre suspensions suitable for subsequent processing to make paper. The caveat in adopting a similar approach here is that such large volume of water would not only result in low fibre  $V_f$  but also prevent the formation of hydrogel matrix when CMC is added to the pulp. The strong hydrogen bonds present at both intermolecular and intramolecular levels in cellulose pulp promotes aggregation, and to prevent this in limited volume of water requires introduction of shear force. A characteristic rheological feature of suspensions (pulp in water) is that they exhibit shear thickening - an increase in viscosity when forced to flow. Addition of CMC polymer not only resulted in bypassing this undesirable shear thickening by changing the nature of the material system (*i.e.* from suspension to a gel or paste form) but also enabled effective transfer of shear forces to

separate pulp fibres. Based on preliminary dispersion trials it was deemed that within a laboratory environment only a minimal amount of pulp fibres (significantly lower than the target  $V_f$ ) could be evenly dispersed in a beaker before starting to compromise the gel nature of the composite as the addition of more fibres to improve the  $V_f$  inevitably required further addition of water to facilitate dispersion. The gel nature is crucial to enable extrusion as suspensions tend to exhibit shear-thickening under stress [176]. As such, a balance is required so as to maximise the fibre  $V_f$  without compromising the gel nature of the composite.

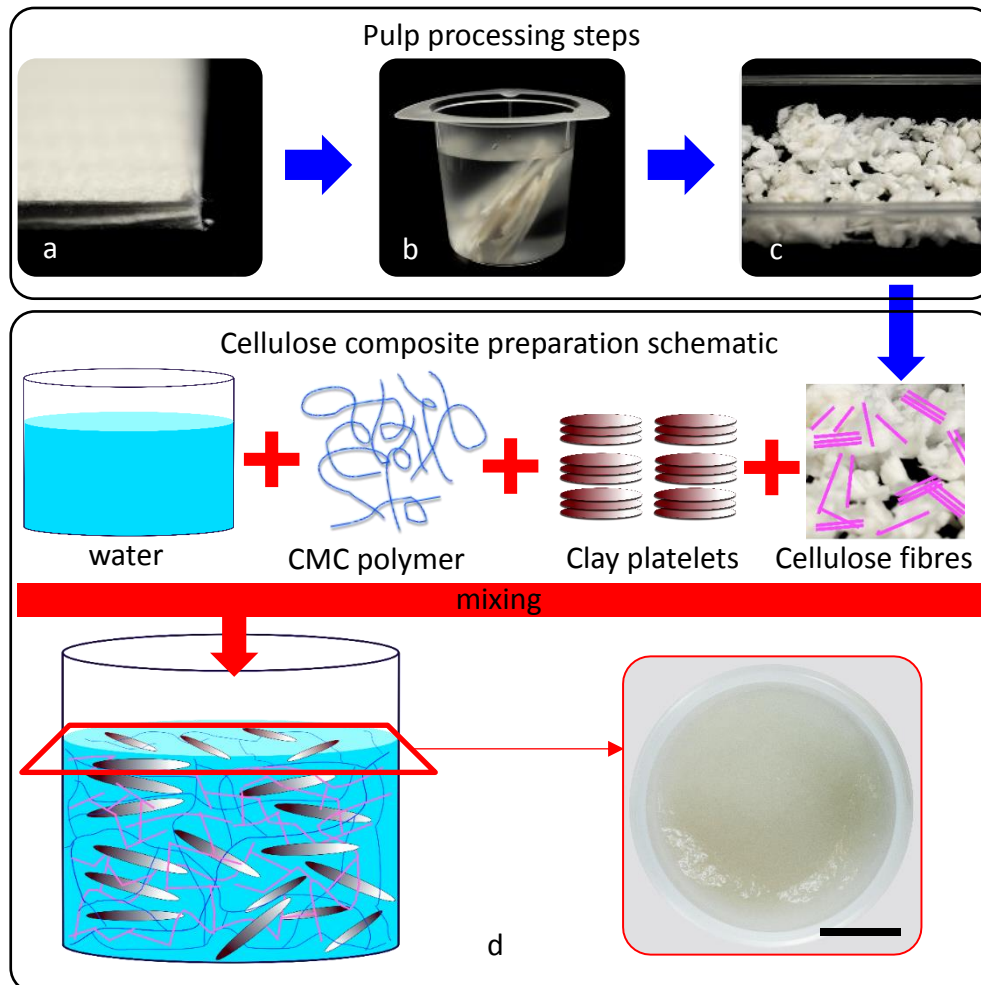


Figure 4.2: (top) Processing of cellulose fibres from pulp linters. (a) Pressed pulp linters as received. (b) Pieces of pulp linters saturating in reagent grade water prior to breaking up and (c) scraped up pulp in the process of drying at room temperature. (bottom) Schematic of the preparation of hydrogel composite and (d) final mix shown in insert. (Scale bar = 20 mm).

For the proposed syringe-based extrusion system, uniform dispersion of fibres is crucial to avoid any clogs in the syringe nozzle as well as to promote even extrusion. The general schematic of the composite preparation is presented in Figure 4.2 (bottom row). A number of mixing strategies were explored ranging from sonication (Figure 4.3b) and shear mixing (Figure 4.3c) besides mechanical agitation (Figure 4.3a) in beaker but yielded less than ideal results evidenced by the fibre agglomeration observed in prepared films. However, adding a

hydrocolloid such as CMC before and during the mixing of pulp in water showed promising results when extruded to form thin films (Figure 4.3c). This strategy was further refined to yield improved extrusion results.

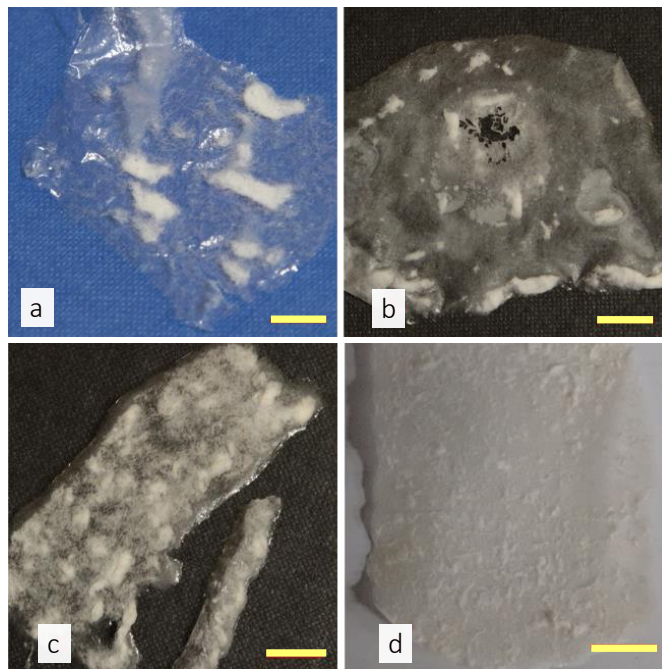


Figure 4.3: Pulp-CMC composite films illustrating the improvements in pulp dispersion as a result of optimised mixing strategies: (a) Mechanical agitation with spatula, (b) Ultra-sonication, (c) Shear mixer and (d) Non-contact planetary shear mixer. (Scale bar = 10 mm).

The composition of the final composite was 0.025 g each of pulp and CMC polymer per 1 mL of water. The best dispersion results (Figure 4.3d) for this formulation was obtained with a non-contact planetary mixer<sup>1</sup> (Thinky (ARE-250) Mixer, USA). The excellent dispersion was obtained due to the efficient shear transfer of centrifugal forces facilitated by the addition of gel forming polymer in separating and dispersing the pulp fibres. The mixing procedures with Thinky mixer is as follows: The pulp, water and CMC were added in small quantities ( $\approx$  15-20 % wt of total batch (30 mL of water)) and mixed for 30 seconds at 1600 rpm before adding further up to the required amount as per the recipe. Once all the ingredients are in, the mixture is further mixed for 3-4 minutes (depending on the total volume) till a uniform paste was formed (Figure 4.2d (bottom row- insert image)). The specified mixing procedures and parameters were developed through experimenting with various settings followed by visually analysing the results and checking the feasibility for manual extrusion through a syringe. CMC forms gels when added to water by virtue of physical interactions and the amount used in the formulations were more than enough to facilitate gel formation. The cellulose-hydrogel

<sup>1</sup> Planetary mixer – A centrifugal mixer that mixes materials employing "rotation" and "revolution".



composite would then be manually extruded through a syringe (as in a 3D printer print head) of diameter  $\approx 1\text{mm}$  and dried to form thin films. Figure 4.3 shows the improvements in pulp dispersion in hydrogel composite and clog free extrusion owing to optimised mixing strategies. The progressive lack of transparent (*i.e.* hydrogel only) regions in prepared films are evident. Even though manual extrusion through a syringe was feasible albeit with some difficulty, lumps of fibres can be seen scattered through the films as well as transparent CMC only regions (Figure 4.3a-c). Such lack of consistency in material distribution is detrimental to programmability of actuation responses as well as the material placement benefits of 3D printing this material is poised to take advantage of. Therefore, the pursuit of excellent dispersion and smooth extrusion is paramount and is justified on those two fronts.

#### 4.2.3 Stability of hydrogel composites

Long term (structural) stability of the gel and composite formed is also critical to the ability to extrude through a syringe. It was noted that a significant reduction in the hydrogels and composites gelling properties and viscosity had occurred after a week. Evidently, this is not an ideal feature as the materials then had to be prepared immediately before extruding and thus lacks flexibility for storage for later use. This time dependant viscosity behaviour would affect the extruder parameters such as flow rate to be adjusted prior to each extrusion resulting in extensive tuning to achieve consistency and good repeatability of the forms created. Therefore, storage stability was deemed essential for the materials developed. Montmorillonite clay was added (0.5 % wt of water) as a filler in order to stabilise the hydrogel in this regard. An inversion test on one-week old samples proved the effectiveness of clay in stabilising the hydrogel. An off-white colour was imparted to hydrogel composite when clay was added. Montmorillonite is a layered silicate with a lamellar structure and commonly used as an additive to improve the mechanical properties of polymers in general. The layers of montmorillonite platelets can be effectively exfoliated by water and through adequate agitation. Once exfoliated, these platelets can effectively intercalate between the polymer chains and fibres. The schematic of this process is presented in Figure 4.2 (bottom row). The exfoliation of the platelets in water is by virtue of layer separation brought about through hydration forces as well the hydration of the cations ( $\text{Fe}^+$ ,  $\text{Fe}^{2+}$ ,  $\text{Mg}^{2+}$  and  $\text{Al}^{3+}$ ) present in montmorillonite [177]. Chemically modified clays such as organoclays with desirable surface properties such as low surface energy facilitating faster dispersion with improved colour can also be substituted for montmorillonite to achieve storage stability. This was confirmed through experiments carried out using a commercially available organoclay obtained from Baltimore Innovations ([www.baltimoreinnovations.co.uk](http://www.baltimoreinnovations.co.uk)). This improved-clay was not

considered further in the study as its exact chemical modification was not specified in its datasheet. The significance of functional fillers such as modified clay was not overlooked entirely, but perhaps it presents an opportunity to further the mechanical or actuation potential of the material system developed. The molecular weight (Mw) of CMC used was also increased from 250,000 to 700,000 to improve viscosity and stability.

The stability in aqueous medium is paramount for hydrogel based actuators. Standard films (dry) of CMC polymer disintegrated (soluble) in water when left overnight. Whereas, films of cellulose-hydrogel composite (see Figure 4.3) retained their 'shape' in an aqueous medium overnight but disintegrated when handled confirming that just the pulp network alone is insufficient in holding the shape. In order to provide the vital stability in aqueous (stimuli) medium, it was decided to crosslink the hydrogels. Crosslinking reactions involving self-crosslinking [178], with PAA (poly acrylic acid) [75,179] and citric acid [180,181] as crosslinking agents were carried out and evaluated.

*Self-crosslinking of CMC:* This methodology is based on the self-crosslinking properties of CMC by virtue of its many carboxyl and hydroxyl groups resulting in the formation of ester at high temperatures (above 180 °C). The reaction is essentially a thermally induced dehydration reaction. Although simple and viable as it enabled fixing of shapes without the need to add any additional crosslinking agents, the reaction required temperatures above 180 °C (for 30 minutes) to form crosslinks [178]. The primary concern with the reaction parameters was the crosslinking temperature and its influence on polymer properties (degradation temperature of CMC -290 °C). The reaction time could be reduced to 5 minutes when the temperature was increased to 200 °C. A hint of charring was observed in the samples after self-crosslinking at these temperatures but disappeared after hydration and swelling. Figure 4.4 (a-c) illustrates this observation. A £1 coin is presented next to charred (Figure 4.4 b) and hydrated (Figure 4.4 c) samples to contrast the discolouration as result of crosslinking and its subsequent

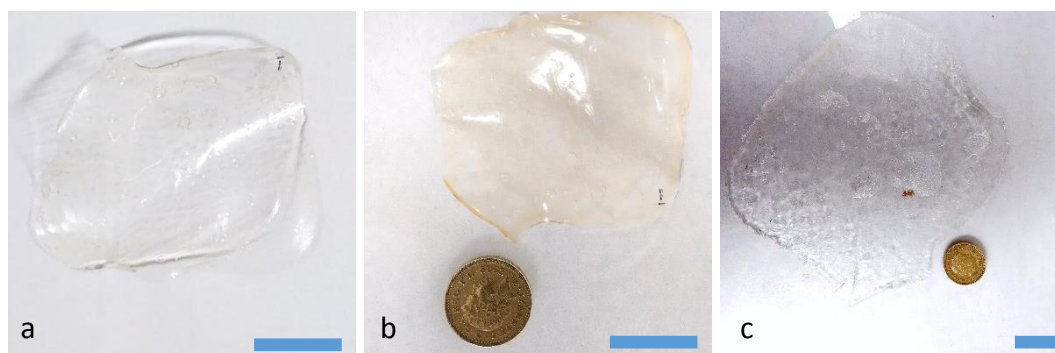


Figure 4.4: Self-crosslinking induced charring (a) before crosslinking (b) after crosslinking at 180 C for 30 minutes (c) after swelling in reagent grade water for 24 hours. (Scale bar = 20 mm).

disappearance after hydration. The crosslinked samples were allowed to swell in reagent grade water (same as the type used for the synthesis). The reasons to why the colour was “washed away” is not known but the observations indicate that the discoloration was either a surface phenomenon which was either washed away or the water somehow restoring original transparency (*i.e.* clear colour) to the samples by hydrating apparently charred regions. However, other crosslinking options were explored in order to lower the temperature at which the reaction could be carried out without being detrimental to the samples.

*Crosslinking with Poly acrylic acid (PAA):* This is a common method to produce hydrogel films through solvent casting and subsequent heat induced esterification. Here, the crosslinking reaction involves the formation of ester bonds between the carboxyl groups of PAA and hydroxyl groups (of cellulose and CMC). The reaction was carried out at 140 °C for 30 minutes. The reaction parameters were obtained from [75] and modified to suit the processing and materials developed in this study. PAA amounting to a 10 % wt of total solid content (or 0.5 % wt of water) was used in formulations as this concentration was found to have greatest bridging effect from open literature. Varying the amount of crosslinking agent affects the swelling capacity of the films formed through solvent casting. The effects of varying PAA (crosslinker) concentration and its influence on hydrogel swelling were not characterised because it has been extensively reported in open literature. The neat CMC films crosslinked with PAA exhibited visibly more shrinkage after drying and thus developed macroscopic surface cracks. As for composites, the pulp fibres stabilised the film from cracking and shrinking. They also exhibited a more severe tint possibly due to charring which was not entirely removed through hydration as in the case of self-crosslinked samples. However, these surface cracks aggravated and developed into cracks that ripped apart the substrate during swelling in water. This is possibly due to the amount of PAA used being excessive and resulting in far too many crosslink points in the substrate. Figure 4.5 shows the PAA crosslinked samples after swelling in water exhibiting severe cracks and tint. PAA used was designated as mild carcinogen due to possible traces of benzene used in its preparation. Therefore, it was decided not to proceed further with PAA crosslinking for the hydrogels and composites due to the cracking of substrates upon hydration and also because it represents nonconformity from the philosophy of morphogenesis manufacturing by using ingredients with potential adverse effects.



Figure 4.5: Cracking observed in PAA crosslinked samples after swelling. (Scale bar = 20 mm).

*Crosslinking with citric acid (CA):* An environmentally friendly polycarboxylic acid such as citric acid could also be employed to crosslink CMC hydrogels. Multiple examples of citric acid mediated crosslinking of cellulose derivatives can be seen in open literature [180–184]. The reaction involves dehydration kinetics comparable to the previous two methodologies but proceeds at a lower temperature of 120 °C for 10 minutes. The dehydration of citric acid results in the formation of highly reactive acid anhydride which combines with the hydroxyl groups in cellulose to form crosslink points. The reaction parameters were obtained from [180] and modified to suit the cellulosic hydrogel composite processing developed in this study. A mixture of CMC and HEC (hydroxyethyl cellulose), with weight ratio equal to 3:1 was used to form the hydrogel. The presence of HEC is necessary to promote intermolecular rather than intramolecular crosslinking. The formulations containing 10% wt (of total polymer content) citric acid was chosen in this study.

Even though all three methodologies presented here resulted in aqueous stability, the reaction involving citric acid was chosen as the way forward as it was more environmentally friendly, bio-compatible and benign. The crosslinking reactions were successfully carried out at 120 °C for 10 minutes as opposed to 180 °C for 30 minutes for self-crosslinking and 140 °C for 30 minutes when PAA was used. The selection of citric acid as the crosslinker also alleviated the potential health risks associated with PAA. The lower reaction temperature also meant less risk of polymer degradation. The neat hydrogel films formed were stable and devoid of cracks unlike the films crosslinked with PAA. The films were also devoid of any discoloration as observed in self-crosslinked and PAA crosslinked samples. The difference in hydrophilicity in CMC and HEC could also enable manipulation of swelling characteristics. Even though not explored/ tested in this study, the CMC hydrogel formulations involving citric acid has demonstrated self-healing properties when immersed in citric acid solution for 3 hrs [185]. This would be an interesting feature for the hydrogel composites as well.

### 4.3 Characterisation of material formulations

The formulations with citric acid as crosslinking agent were subjected to full characterisation. This section presents the 'as-prepared' flow characteristics and mechanical properties; swelling and shrinking characteristics of the hydrogel and associated hydrogel composite formulations. Rheology is a suitable method for characterising the mechanical properties of a hydrogel owing to its quick, responsive and sensitive data gathering. It can also be used to comparatively differentiate properties such as degree of crosslinking, molecular weight, structural homogeneity, glass transition and flow characteristics. The rheological analysis carried out in this study focuses on the mechanical characterisation as well as the flow characteristics of the formulations developed. The swelling behaviour of the crosslinked samples (films) are also quantified to investigate the influence of crosslinking agent, pulp and clay in governing the actuation response of the formulations. The shrinking behaviour of as-prepared formulations due to drying and crosslinking were also evaluated using thermogravimetric analysis. The swelling and shrinking characteristics of the formulations would give an insight into the range of volumetric changes and consequently the strain gradients achievable within the formulations. The force generated during the swelling response was also characterised for the formulations. The force response, and the time required to generate force response are crucial in gauging the effectiveness of developed formulations as an actuator.

#### 4.3.1 Rheology

The technique predominantly used to characterise hydrogels is small-amplitude oscillatory shear (SAOS) test. In SAOS, the sample is tested in between parallel disks (medium viscosity) or a cone and disk (low viscosity) based on the nature of material being tested. The critical measurement data is collected from the linear visco-elastic regime (LVER) with respect to the strain rate where the material shows a proportional relationship with the applied strain. The protocol used to characterise the rheological behaviour and consequently the mechanical properties of the hydrogel and composites are outlined as follows: (i) amplitude sweep; (ii) frequency sweep; (iii) steady-state shear tests and (iv) stress-ramp tests were performed. This protocol was adapted from [186,187] and the gelation times were not determined using rheological parameters as the gel formation with CMC was observed as a function of loading capacity and constantly resulted in the formation of gels during the synthesis step of the formulations investigated (see Table 4.1). A rheometer (Kinexus Pro) from Malvern Instruments with a parallel plate geometry (PU20) of diameter 20 mm was used throughout the characterisation and all the samples were tested at 25 °C. Each sample was used only once,

and the tests were performed in triplicate with the error bars representing the corresponding standard deviation. A standard loading procedure (sequence) was used to guarantee reliable and precise loading protocol.

Table 4.1: Sample nomenclature and respective formulations

Gel+CA (low)	Gel+CA	Gel+Clay+CA	Composite+CA	Composite+Clay+CA
30/0.75/0/0/0.15	30/1.5/0/0/0.15	30/1.5/0/0.15/0.15	30/0.75/0.75/0/0.15	30/0.75/0.75/0.15/0.15

Gel+CA (low) has the same polymer content (2.5% wt of total water content) as the composite samples and the polymer content in the other two gel samples is equivalent in weight to the solid (polymers and pulp) content of the composite samples (5% wt of total water content). This spectrum of samples would demonstrate the effect of pulp, clay and polymers forming the gel in governing the rheological characteristics and mechanical properties of these formulations. The effect of amplitude, frequency and shear rate on elastic (storage) modulus  $G'$  (representing the solid-like characteristics) and viscous (loss) modulus  $G''$  (representing the liquid-like characteristics) will give a good indication of the nature and flow characteristics of the samples.

The relative importance of  $G'$  and  $G''$  is represented by phase angle ( $\delta$ ) as follows:

$$\tan(\delta) = \frac{G''}{G'} \quad (4.1)$$

When  $\delta > 45^\circ$  (*i.e.*  $G''/G' > 1$ ), it can be said that liquid-like behaviour dominates within the sample. For  $\tan(\delta)$  values  $< 1$ , solid-like behaviour dominates within the sample.

#### 4.3.1.1 Strain sweep

A strain sweep from 0.01%-100% at a frequency of 1Hz was performed on gelled samples. Figure 4.6 shows the elastic modulus ( $G'$ ) (top) and phase angle ( $\delta$ ) (bottom) as a function of shear strain for the samples tested. The loss modulus ( $G''$ ) values were not presented for clarity but is embodied in the phase angle ( $\tan \delta$ ) data presented. The phase angle data also demonstrates that  $G' > G''$  ( $\tan(\delta) < 1$ ) for most of the applied strain regime indicating that the samples are structured (gel). Elastic modulus values measured within the LVER (linear visco-elastic regime) shows the highest value for Gel+Clay+CA (1.15 kPa) samples as expected. The presence of clay results in a higher elastic modulus and viscosity when compared to Gel+CA (0.9 kPa) samples. Contrary to what was observed in gel samples, the addition of clay in composites did not increase the elastic modulus ( $\approx 0.7$  kPa) but resulted in gradual decay of the modulus and viscosity at lower strains followed by a rapid decay of modulus which signified the critical strain %. The onset of non-linearity is termed as critical strain % and the

---

gel structure is disrupted when strain values exceed beyond this point. It is assumed that the structural interactions of intercalated clay and dispersed pulp fibres resulted in this flow behaviour. As the samples were not chemically crosslinked, the gel nature was by virtue of physical crosslinks such as hydrogen bonds. Montmorillonite is of layered structure and could reduce the effective hydrogen bonding between cellulosic pulp, polymers and water by intercalating between them. This is reflected in the phase angle plot as the rapid rate of increase in  $\tan(\delta)$  indicate more fluid like behaviour under increasing applied strain. Although further investigations as to why this behaviour arises are necessary, these characteristics are ideal for the proposed composite extrusion system as it not only provides long term stability to the material system but also the composite gel containing the clay flows more easily when compared to other formulations in this study. It is also noted that the modulus and thus  $\tan(\delta)$  for Gel+CA (low) are particularly noisy at strain (0.01%-0.1%) as expected due to weaker response at this strain range from the sample.

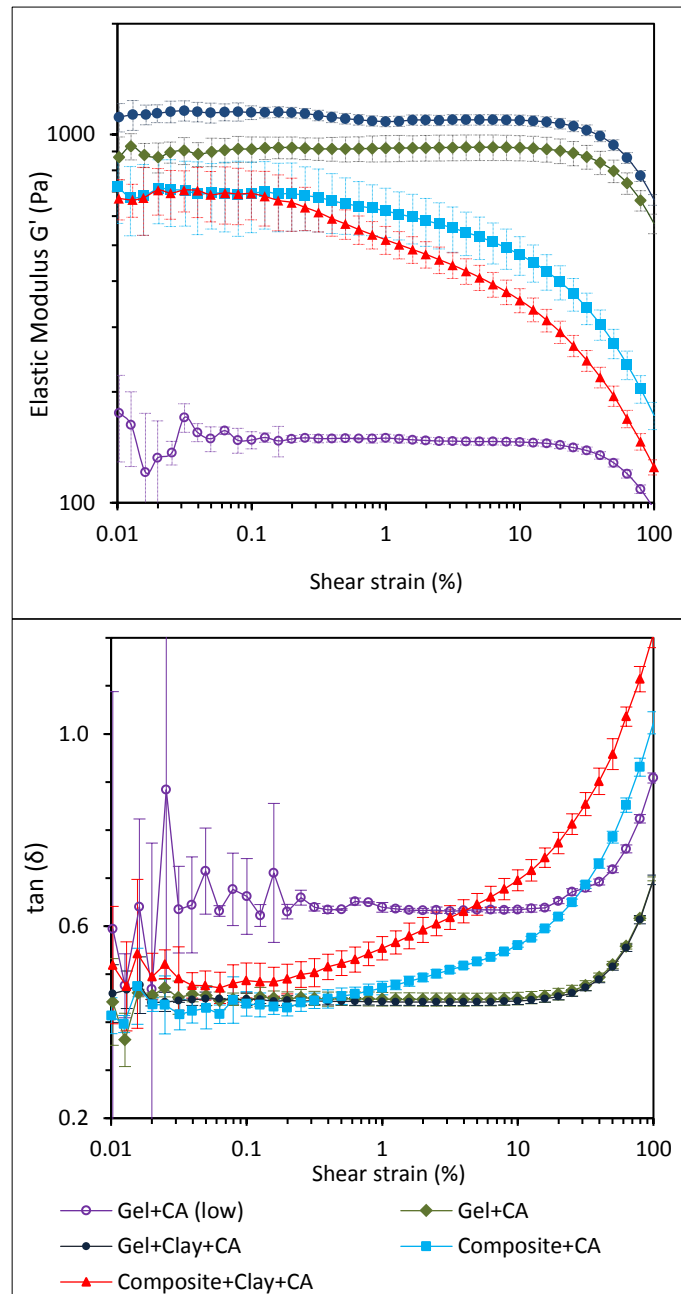


Figure 4.6: Amplitude sweep data showing (top) Elastic modulus ( $G'$ ) and (bottom) phase angle ( $\delta$ ) as the function of shear strain.

#### 4.3.1.2 Frequency sweep

Frequency sweeps from 0.1 Hz-10 Hz were performed on the samples at 0.5 % strain (within LVER) and the results are presented in Figure 4.7. The results demonstrate the  $G'$  (top) and phase angle (bottom) variation across the probed frequency range. Loss Modulus ( $G''$ ) values were omitted for clarity and relative significance of elastic and viscous modulus is presented as  $\tan(\delta)$  dependence on frequency. It can be seen that the elastic modulus values at 1 Hz shown in Figure 4.7 (top) matches the  $G'$  values in LVER regime in amplitude sweep results presented in Figure 4.6 (top). The recorded slope in  $G'$  indicates that the modulus is dependent



on the frequencies probed and implies some structural relaxation where stored elastic energy is dissipated with time. There is no crossover between  $G'$  and  $G''$  as evidenced by  $\tan(\delta)$  values less than 1 within the frequency range investigated. However, analysis of the phase angle trends in Figure 4.7 (bottom row) implies possible crossover frequencies  $\ll 0.1$ . The precise crossover frequencies and thus relaxation time were not determined due to time-related impracticalities in running frequency scans at such low frequencies. The  $\tan(\delta)$  data also shows  $G' > G''$  validating the presence of structured gel as observed in amplitude sweep results.

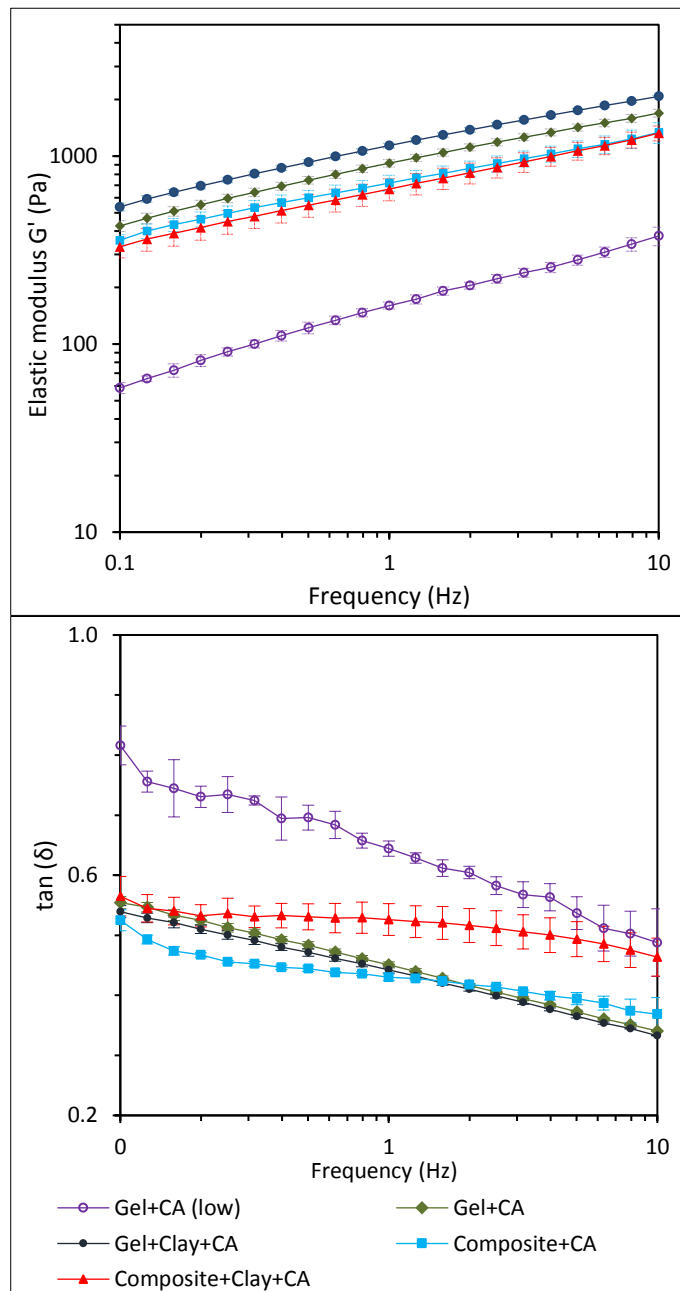


Figure 4.7: Frequency sweep data showing (top) Elastic modulus ( $G'$ ) and (bottom) phase angle ( $\delta$ ) as a function of frequency.

#### 4.3.1.3 Shear rate

The results from the steady state shear measurement are presented in Figure 4.8; as viscosity (top) and shear stress (bottom) as a function of shear rate. The highly shear thinning nature of the samples are evident from the shear viscosity-shear rate plot (Figure 4.8 (top row)) and confirms pseudo-plastic behaviour. Therefore, the developed formulations could be extruded (through a syringe) on the application of continued force. It can also be observed that the viscosity and stresses of Composite+Clay+CA samples are closer to that of Gel+CA (low) samples especially at higher shear rates (representing short times) despite the increased amount (more than twice as high) of solid content within this composite formulation. This behaviour underlines the suitability Composite+Clay+CA formulation for short-time processes such as extrusion. The comparison of viscosity and shear stress developed in Composite+Clay+CA, Gel+CA and Gel+Clay+CA confirms the observation made in amplitude sweep analysis regarding the combined effect of pulp and clay in facilitating better extrusion. The relationship between shear stress developed and the applied shear rate are also presented (Figure 4.8 (bottom row)). Comparatively low shear stresses are developed within the Composite+Clay+CA formulation as the presence of layered clay platelets aids in cleaving the physical interactions on the application of external force to cause the material flow. The shear stresses developed in the gel formulations indicate that higher forces have to be supplied to cause flow in these materials. This is expected as the gels were found to be very structured from the amplitude results. However, the rate of developed shear stresses (*i.e.* slope) in (Figure 4.8 (bottom row)) can be seen to decrease in the shear rate region between 1-5 ( $s^{-1}$ ) followed by an increase. Structural changes within the hydrogel network, possibly break down and re-organisation in response to the applied forces are presumed to occur at this transition region. The physical implications of these induced structural changes are not well understood and perhaps this indicates a 'sweet-spot' which can enable easier flow with the gel materials. However, the key point from shear-rate experiment was the response of Composite+Clay+CA formulation as these results showed the effectiveness of pulp-gel composite system in having ideal extrusion characteristics for 3D printing as a homogenous phase of either of the two would not have yielded necessary high viscosity (solid-like) at rest and declining at higher shear rates (*i.e.* when deformed).

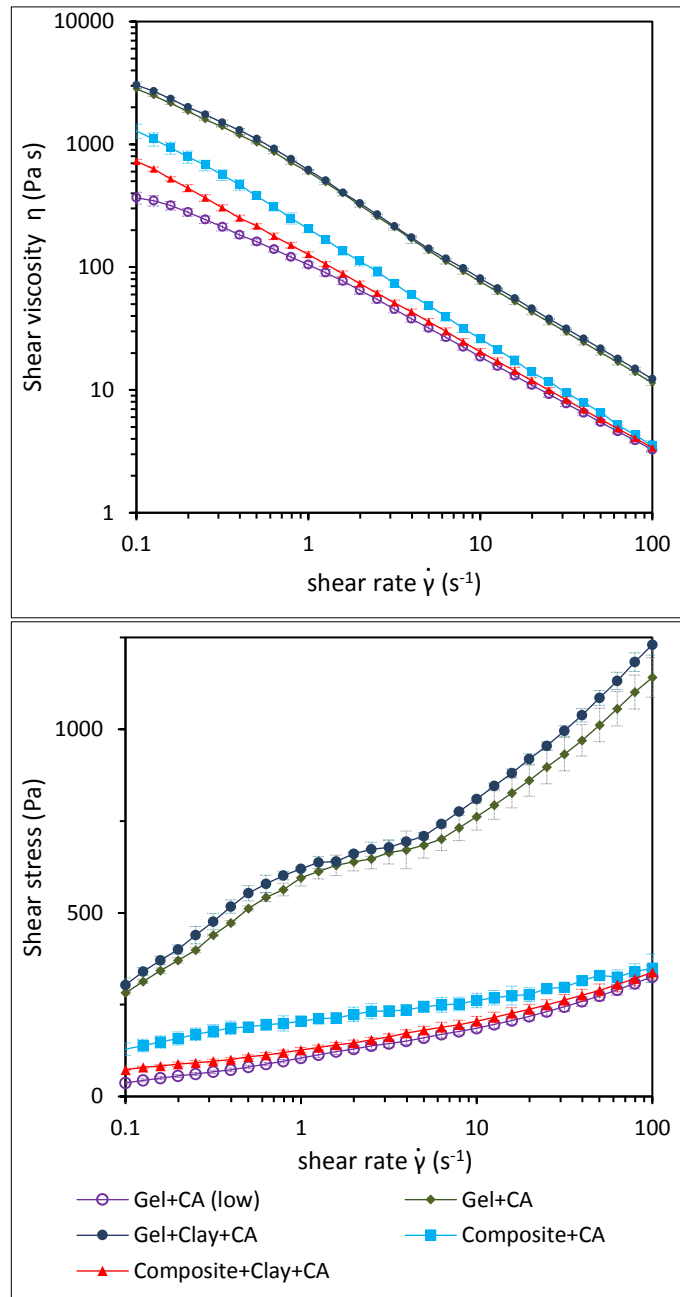


Figure 4.8: Steady state (top) shear viscosity ( $\eta$ ) and (bottom) shear stress ( $\tau$ ) as a function of shear rates.

#### 4.3.1.4 Stress ramp

Yield stress signifies the stress required to break the physical interactions that give materials their solid like characteristics to cause material flow. In other words, the material will not flow unless the applied stress exceeds a critical threshold value, typically referred to as the yield stress of that material; below this threshold the material deforms elastically and above it plastic deformation (*i.e.* flow) occurs. In regard to the material systems studied here, it means the ease with which the formulations can be extruded from the syringe of the printer when force is applied through the plunger.

A stress ramp is one of the commonly used test methods to estimate the yield stress of materials where the instantaneous viscosity of the sample is measured against an increasing applied shear stress. The shear stress corresponding to the peak viscosity (point of yield) is estimated as the yield stress of the sample. The (averaged) stress ramp data and measured shear viscosity of the formulations are presented in Figure 4.9. The data acquisition was carried out in triplicates and each sample was only used once. The ramp duration was kept as 100 s for all formulations but to different final stress (from zero) in order to adequately capture the peak viscosity change and response beyond yielding. The Gel+CA and Gel+Clay+CA samples were subjected to 0-300 Pa, whereas Composite+CA and Composite+Clay+CA samples were subjected to 0-200 Pa during the test. The error bars for viscosity from averaged triplicate run have been omitted from Figure 4.9 for clarity, with representative values reported in Table 4.2. Gel+CA (low) samples were omitted from the stress ramp test to estimate yield stress because the formulation was deemed too weak (low  $G'$ ) to hold the extruded shape even though its low viscosity would make it easier to extrude through the syringe.

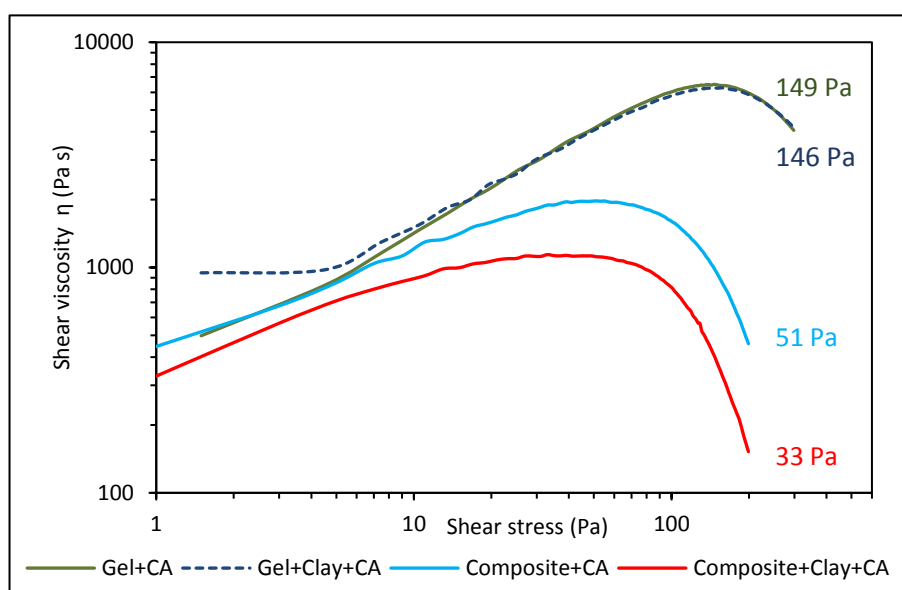


Figure 4.9: Stress ramp plots showing Yield Stress of formulations at peak viscosity.

The yield stress for each of the formulations was obtained from the shear stress value corresponding to the peak viscosity for each test run and is tabulated in Table 4.2. The data presented here is more reliable as they represent actual test data as opposed to results from the time averaged response plotted in Figure 4.9. It is noted that the values presented in Table 4.2 cover the peak values presented in the plot (Figure 4.9) thus confirming minimal yield stress variation due to loading discrepancies. As expected Gel+CA and Gel+Clay+CA formulations have the highest yield stress and thus would be harder to extrude from the

syringe compared to the other formulations with lower yield stress. The combined effect of clay and pulp fibres in facilitating easier flow is evident from the yield stress values.

Table 4.2: Yield Stress of the formulations

Formulation	Peak viscosity (Pas)	Yield Stress (Pa)
Gel+CA	7000 ± 800	140 ± 9
Gel+Clay+CA	6300 ± 380	147 ± 8
Composite+CA	2000 ± 290	46 ± 8
Composite+Clay+CA	1150 ± 230	38 ± 8

#### 4.3.2 Swelling ratio

Strain mismatch within a substrate is the driving force for many of the transformations in nature as well as for many synthetic actuators upon activation by the stimuli. Swelling is one of the simplest ways to realise strain differential in a substrate. Therefore, characterising the swelling behaviour of the developed formulations is vital to better inform the design choices for morphing and equilibrium swelling ratio (ESR) is one way to capture this response. Even though equilibrium swelling ratio does not directly relates to the strain differential developed in response to the stimulus in any of the co-ordinate axis (direction) of the sample, it can be used to quantify the maximum swelling potential by means of change in weight. The equilibrium swelling ratio (ESR) is related to the weight of the sample as described in equation 4.2. The equilibrium swelling ratio (ESR) of the crosslinked hydrogels and composites were investigated in de-ionised water with a focus on formulations containing citric acid as it was chosen to be the ideal crosslinking option. The samples (minimum of 3) were weighed and immersed in de-ionised water for 24 hrs to reach equilibrium swelling at room temperature (21 °C). The samples were recovered from water and weighed after removing excess water from the surface by gently patting down with tissue paper.

The ESR was calculated as follows:

$$ESR = \frac{W_s - W_d}{W_d} \quad (4.2)$$

where  $W_s$  is the weight of the swollen hydrogel/ composite, and  $W_d$  is the weight of the dried sample. Table 4.3 summarises the results of swelling ratio investigation. The standard deviation is presented as error. The swelling ratios of comparable self-crosslinked samples (without citric acid) are also presented to better understand the effect of crosslinking agent in restricting the swelling. The effectiveness of citric acid in crosslinking at relatively lower

temperature is clear when compared to self-crosslinked samples. The effect of pulp fibres on the swelling ratio is also evident. This confirms the presence of pulp network that restricts the swelling of hydrogel matrix resulting in a lower swelling ratio. The addition of montmorillonite clay was found to have no impact on swelling ratio. In swelling-induced shape transformations, the ESR results presented might come across as an apparent limitation as they are significantly lower than for the self-crosslinked samples. However, what is more significant is the ability to realise the strain gradient in substrates in a controlled manner. The versatility of this approach is that the amount of crosslinking agent or the ratio of cellulosic polymers (CMC:HEC) can be varied so as to achieve desirable swelling specific for a structure.

Table 4.3: Equilibrium swelling ratio of formulations with CA after crosslinking

Crosslinked with CA (10 min @ 120 °C)	Swelling ratio	Self-crosslinked (30 min @ 180 °C)	Swelling ratio
30/1.5/0/0/0.15	2.6 ± 0.2	30/1.5/0/0/0	38.3 ± 1
30/1.5/0/0.15/0.15	2.8 ± 0.1		
30/0.75/0/0/0.15	1.4 ± 0.3		
30/0.75/0.75/0/0.15	0.85 ± 0.02	30/0.75/0.75/0/0	4.1 ± 0.1
30/0.75/0.75/0.15/0.15	0.82 ± 0.03	30/0.75/0.75/0.15/0	6.2 ± 0.2

#### 4.3.3 Shrinking ratio

As seen in Chapter 3, shrinking of hydrogels can also drive the transformations of suitable substrates. Thermal analysis, specifically TGA (thermogravimetric analysis) was carried out on the prepared formulations to characterise the mass loss due to drying and crosslinking. TGA is a thermal analysis technique in which the mass of the sample is measured over time as a function of temperature. The equilibrium swelling ratio reported in the previous section provided an insight into the volumetric changes during swelling by means of capturing the mass increase due to water absorption. Similarly, TGA was used to capture the mass change within the prepared formulations as they shrink during the drying and crosslinking steps due to dehydration. The thermal analysis was carried out on a TGA Q500 from TA Instruments and standard analysis protocols and default gas flow rates were utilised. The samples were analysed in a platinum pan and nitrogen was used as the purge gas for the balance and samples. For ‘as-prepared’ formulations namely Gel+CA, Gel+Clay+CA, Composite+CA and Composite+Clay+CA, the following steps were used in TGA: (1) samples were heated up at (temperature ramp) 10 °C /min to 120 °C followed by (2) holding the temperature (isothermal) for 10 minutes. These steps were taken in consideration to the selected crosslinking reaction involving citric acid which occurs at 120 °C for 10 minutes. The sample size was one for all the formulations and the average sample weight was approximately 35 mg. The TGA results were analysed using Universal Analysis software (version 4.5A) from TA instruments.

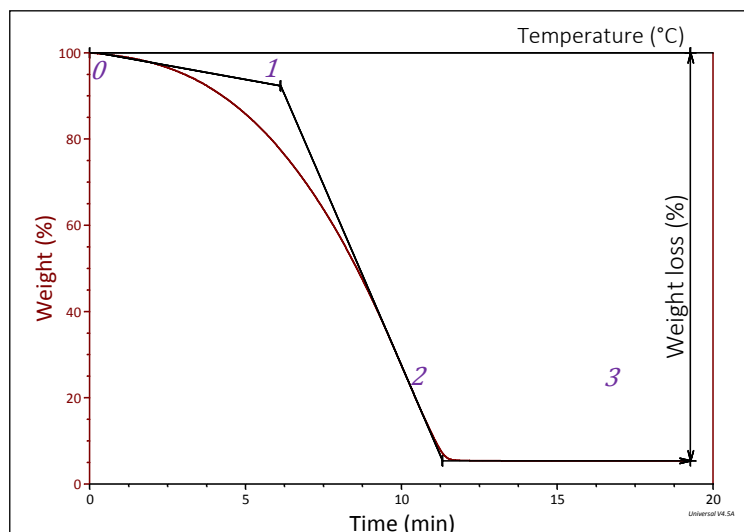


Figure 4.10: Typical thermal data of the samples indicating distinct weight loss regions (0-1,1-2 and 2-3) during the analysis steps.

The typical response of ‘as-prepared’ samples when subjected to the aforementioned thermal analysis steps is presented in Figure 4.10. Three distinct weight loss regions could be identified from the chart. The first two stages (0-1 and 1-2) occur during the temperature ramp from RT (21 °C) to 120 °C and the third stage (2-3) indicates the isothermal step held at 120 °C for 10 minutes. The weight loss in samples at the end of analysis was obtained from the TGA thermograms using Universal Analysis software as indicated in Figure 4.10 and was used to calculate the ‘shrinking ratio’ akin to the swelling ratio calculated in the previous section. The equation used to calculate shrinking ratio is as follows.

$$\text{Shrinking ratio} = \frac{\text{final weight (\%)} - \text{initial weight (\%)}}{\text{initial weight (\%)}} \quad (4.3)$$

The results from thermal analysis are tabulated in Table 4.4. The TGA thermograms of the formulations with weight loss (%) as function of time are presented in Figure 4.11a. It can be seen that the samples have identical weight loss and consequently similar shrinking ratio as well. It must be noted that the total water content in the prepared formulations are 94.4 %. Therefore, the weight loss in the samples can be attributed to the removal of water added during the synthesis step and perhaps also as a by-product from crosslinking reaction. This confirms that drying and crosslinking reactions result in dehydration as intended and do not degrade the samples. Furthermore, the shrinking ratio also implies that the developed formulations show no preference in retaining water by virtue of its constituents during the drying and crosslinking steps employed and thus modulation of the shrinking responses are not possible.

Table 4.4: Summary of thermal analysis results

Sample	Weight loss (%)	Shrinking ratio	% weight lost after each stage			Peak weight loss temperature (°C)
			1	2	3	
Gel+CA	93.17	-0.93	22.6	68.1	2.5	109.1
Gel+Clay+CA	94.87	-0.95	25.3	67.7	1.8	119.2
Composite+CA	94.66	-0.95	22.6	70.4	1.7	120.3
Composite+Clay+CA	94.10	-0.94	25.1	67.3	1.7	112.4

Analysing the weight loss % after each of stage in the thermal data reveals that significant weight loss occurred in the second stage. The first derivative of TGA curves with respect to time signifying the rate of change in weight loss is presented in Figure 4.11b. Note that the region in the chart past the 120 °C mark corresponds to the temperature hold step. The temperatures corresponding to the peak in dTGA curves collated in Table 4.4 imply that significant weight loss occurred towards the end of stage 2 for all formulations. Gel+CA and Composite+Clay+CA samples dried at room temperature were also subjected to thermal analysis at an increased ramp rate of 20 °C /min to 120 °C followed by isothermal conditions for 10 minutes. These two samples were chosen for this particular analysis as they are relevant to the proceeding work of fabricating morphing architectures (Chapter 5). The increased temperature ramp rate for this set of samples were to replicate the heating of RT dried samples as presented in Chapter 3 and Chapter 5. The sample size was one for these two formulations and the average sample weight was approximately 1.8 mg. A weight loss of 6.2 % and 5.2 % was noted for Gel+CA and Composite+Clay+CA samples respectively.

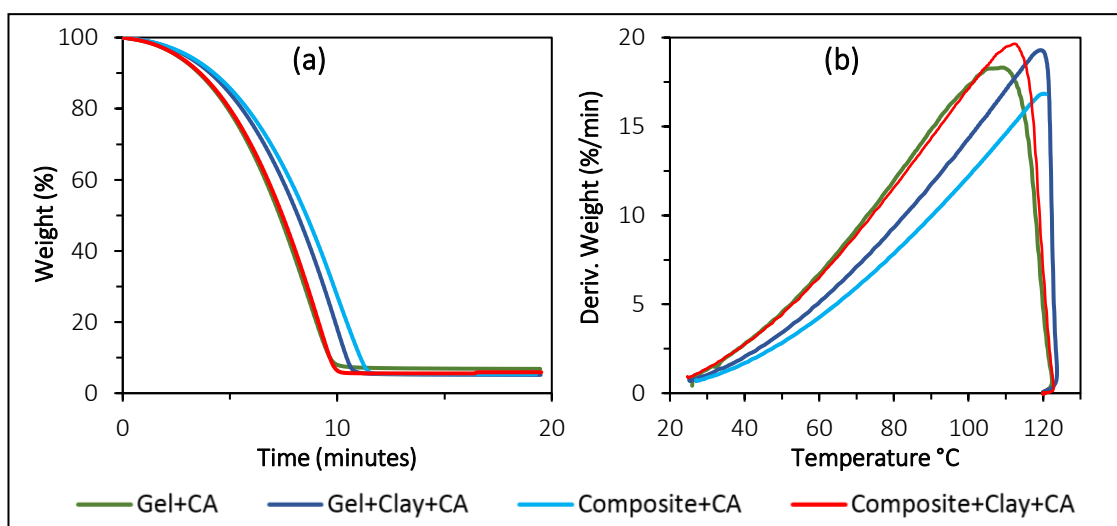


Figure 4.11: TGA curves (a) Weight (%) expressed as function of time. (b) First derivative ( $d(TG)/dt$ ) of weight (%) expressed as a function of temperature.

Even though distinct stages in the thermal data could be identified, these cannot be directly attributed to the removal of different types of water (*i.e.* free water, semi-bound and bound



water) within the hydrogel without further analysis. Such in-depth thermal analysis as well as thermal degradation studies were deemed not critical at this stage as quantifying the mass changes within the material systems and gaining an insight into the extent of volumetric changes during drying were given priority. Chang *et al.* reports the degradation temperature of CMC polymer and cellulose based on TGA studies as 290 °C and 360 °C respectively [188]. Therefore, the drying and crosslinking strategies adopted in this study are clearly outside of the degradation temperatures of the key material ingredients.

#### 4.3.4 Force characterisation

The force exerted by an actuator is a key parameter in characterising and comparing its efficiency as well as an indication of its usefulness. This section aims to characterise the force response from the developed formulations namely Gel+CA, Gel+Clay+CA, Composite+CA and Composite+Clay+CA. Blocking force is defined as the maximum force generated by an actuator and is obtained by restricting the actuator displacement and measuring the corresponding force generated. For hydrogel systems upon hydration, displacement occurs in all directions due to isotropic swelling. Crosslinking and composite construction was shown to impart anisotropic swelling response to hydrogel systems and consequently result in directionality of the blocking force (*i.e.* maximum force generation in each direction) based on the actuator shape and construction. Simultaneously limiting gel expansion in all directions for the sake of measuring blocking force could also limit the exposure to water thus inhibiting the development of blocking force to its maximum. Therefore, measuring the force response of the samples would require limiting the displacements in certain directions whilst allowing continued hydration (thus expansion as well) in the free directions. A crucial factor in the development of blocking force in hydrogel systems is the time required to develop the maximum force. This is typically dictated by the rate of hydration of the sample along the diffusion (or water concentration) gradient. Therefore, the time required to develop the blocking force would be the time taken to fully saturate the sample. This will certainly be different for various hydrogel systems especially for the gel and composite formulations developed in this study. Owing to this variation, it was decided to characterise these systems based on the force generated for a specific period of time rather than the maximum force generated as this approach will give an insight into the rate of hydration and force development across the formulations. Although measures such as encapsulating gel in a rigid mesh or in a suitable membrane allowing hydration whilst limiting expansion could potentially be devised, such attempts are incredibly sophisticated and would require a custom test rig and apparatus to implement. A simplified test set-up using a rheometer based on the one

described by Illeperuma *et al.* was devised to carry out the force characterisation of the formulations developed [189]. Here, the force transducer attached to the rheometer top-plate was used to measure the swelling force generated by the formulations as it hydrates. The materials were extruded through a nozzle ( $\varnothing=0.8$  mm, tapered) to form circular discs and were dried flat in between glass slides at room temperature (25 °C) followed by crosslinking at 120 °C for 10 minutes. Even though the circular discs were prepared with a diameter of  $\approx 20$  mm and thickness of 2 mm, shrinking associated with drying and crosslinking resulted in final sample dimensions much smaller than the prepared dimensions. The dried, shrunken samples were then trimmed with scissors to circular discs with approximately 15 mm in diameter. The dried gel (xerogel) and composite discs weighed from 0.035-0.042 g on average with thickness in the range of 0.3-0.5 mm. The experimental set-up and results are discussed in the following sections.

#### 4.3.4.1 Experimental set-up

An oscillation single frequency experiment was set up in a rheometer (Kinexus Pro, Malvern Instruments) with default shear rate (25 %) and frequency (25 Hz). A schematic of the experimental set-up is shown in Figure 4.12. A parallel plate geometry (PU20) of diameter 20 mm was used as the top-plate with the gap zeroed in relation to an empty petri dish as the bottom plate. This procedure zeros the gap between the top-plate and bottom of petri dish as well as the normal force on the top-plate. A custom procedure was devised to carry out the experiment after numerous trials. Prior to loading, the samples were glued to the base of a petri dish using epoxy glue (Superglue) in order to prevent the samples slipping from underneath the top-plate.

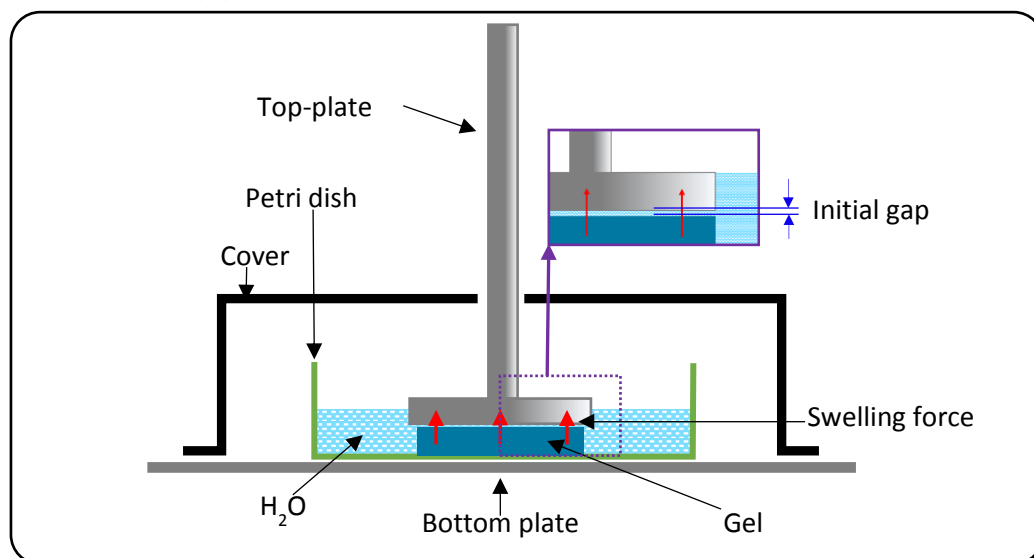


Figure 4.12: Schematic of experimental set-up for force characterisation using rheometer with close-up of the top-plate and sample is shown in insert.

The steps involved in fixing the samples to the base of petri dish as shown in Figure 4.13. The disc shaped samples were glued to the base using superglue to prevent them from slipping through the sides and invalidating the test. A small bead of Superglue was applied at the centre of petri dish using a precision applicator and allowed to dry for 10 seconds (Figure 4.13b). The disc shaped samples were then carefully dropped in on top of the glue and the weight of the samples spreads the glue and eventually solidifies (Figure 4.13c). Epoxy based glue was used as it would not react or swell in water and thus influence the swelling of the formulations when hydrated during the test.

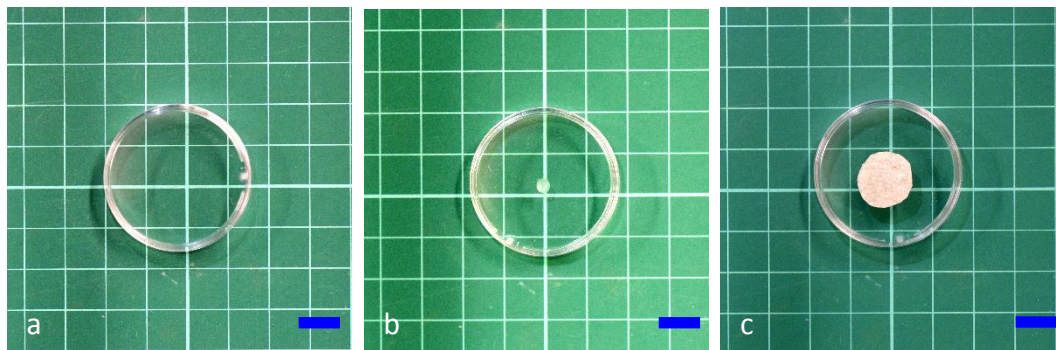


Figure 4.13: Series of images showing the sample set-up for characterising swelling force (a) empty petri dish (b) with glue applied in the middle. (c) Final set-up with a Composite+Clay+CA sample fixed at the base of petri dish. (Scale bar = 10 mm).

The petri dish with the sample was placed at the centre of bottom plate followed by lowering of top-plate to just above the sample surface. The petri dish was then aligned so that the sample would sit directly underneath the geometry. The top-plate position was then adjusted using manual gap command in combination with monitoring the live normal force experienced at the geometry so as to have a small gap between the top-plate and sample (Figure 4.12, insert). This gap was usually set to 0.1 mm and was achieved by first lowering the top-plate onto the sample so that the top-plate just registers a normal force followed by raising the top-plate by 0.1 mm. The dry samples were allowed to swell by introducing de-ionised water through a syringe into the petri dish (up to top-plate level) and was immediately followed by recording of the normal force data. The set-up was then covered as shown in Figure 4.12 to minimise external influence. Here, the swelling in thickness direction was restricted by the base of petri dish and top-plate. The samples were hydrated from the sides and free to swell in that direction. The force exerted by the swelling samples against top-plate was measured as normal force experienced by the rheometer top-plate and recorded every 30 seconds. The gap and normal force were zeroed relative to an empty petri dish prior to each test.

#### 4.3.4.2 Swelling force

The normal force data were recorded every 30 seconds for the duration the test. The saturation of the samples from the sides resulted in circumferential swelling against the top-plate combined with some relaxation of the disc. This resulted in uneven normal force to be experienced at the top-plate initially. As the hydration continued further, swelling response of the samples were stabilised and consequently the swelling force exerted on the top-plate gradually increased. The Gel+CA and Gel+Clay+CA samples dried evenly and flat compared to Composite+CA and Composite+Clay+CA samples due to the lack of reinforcing fibres. Typical swelling force response of the tested formulations are presented in Figure 4.14. Note that the chart shows the response of a representative sample for each formulation. Owing to circumferential swelling and anisotropy in composite samples, the initial force experienced at the top-plate after 30 seconds (the first measurement point) into data collection was different for each sample. The composite samples had the most variation due to inherent anisotropic swelling. Therefore, the normal force data collected by the instrument for all the samples were normalised so that the lowest normal force point was off-set to zero (*i.e.* the lowest force value was subtracted from all the force readings from the raw test data). Albeit being a conservative approach, this aids to analyse the average response of the formulations as a whole. The maximum force exerted by the samples at the end of one hour was obtained and reported in Table 4.5. A minimum of four samples were used for each formulation. The corresponding stress was obtained by dividing the peak force with the area of the sample (assuming circular disc of diameter 15 mm for all samples). This conservative assumption was made to simplify the analysis. The results presented in Table 4.5 indicates that Gel+CA is the ideal option as an actuator due to the development of large swelling force (12.57 N) within the time frame investigated whereas the composite formulations especially Composite+Clay+CA is ideal when stability and slow development of swelling are desirable. Therefore, the use of Gel+CA formulation to define the active regions (fold lines) to realise self-folding paper architectures as reported in Chapter 3 is justified.

Table 4.5: Summary of swelling force generated by the formulations after an hour

Sample	Corrected swelling force after 1 hr (N)	Stress*after 1 hr (MPa)
Gel+CA	12.57±1.94	0.071
Gel+Clay+CA	7.48±1.53	0.046
Composite+CA	0.40±0.15	0.002
Composite+Clay+CA	0.37±0.04	0.002

\*A generous nominal area of 176.7 mm<sup>2</sup> was used assuming the discs are circular with a diameter of 15 mm. In reality some samples were much smaller after trimming.

As expected, Gel+CA generates the highest force at the end of 1 hr mark with the swelling force decreasing with the increase in reinforcement content (clay and fibre). The presence of reinforcements restricts the swelling of hydrogel and results in lower force development during the time period investigated here. Analysing the trends presented in Figure 4.14 reveals the nature of force generation in these formulations. The swelling in Gel+CA samples are only limited by the crosslink points and there is no hindrance to the propagation of hydration front within the samples. Whereas, the presence of reinforcements could hinder the flow and rate of swelling resulting in a lower force response. It can be seen from Figure 4.14 that the force generated in Gel+CA and Gel+Clay+CA are reaching saturation values (blocking force) towards the end of 1-hour mark. Understandably, the force generated by the composite samples are low owing to the presence of the fibrous network and by only having half the amount of CMC resulting in less swelling. However, the response characteristics does not suggest saturation close to the hour mark implying that over time the swelling force from the composite formulations could increase further before reaching saturation (blocking force).

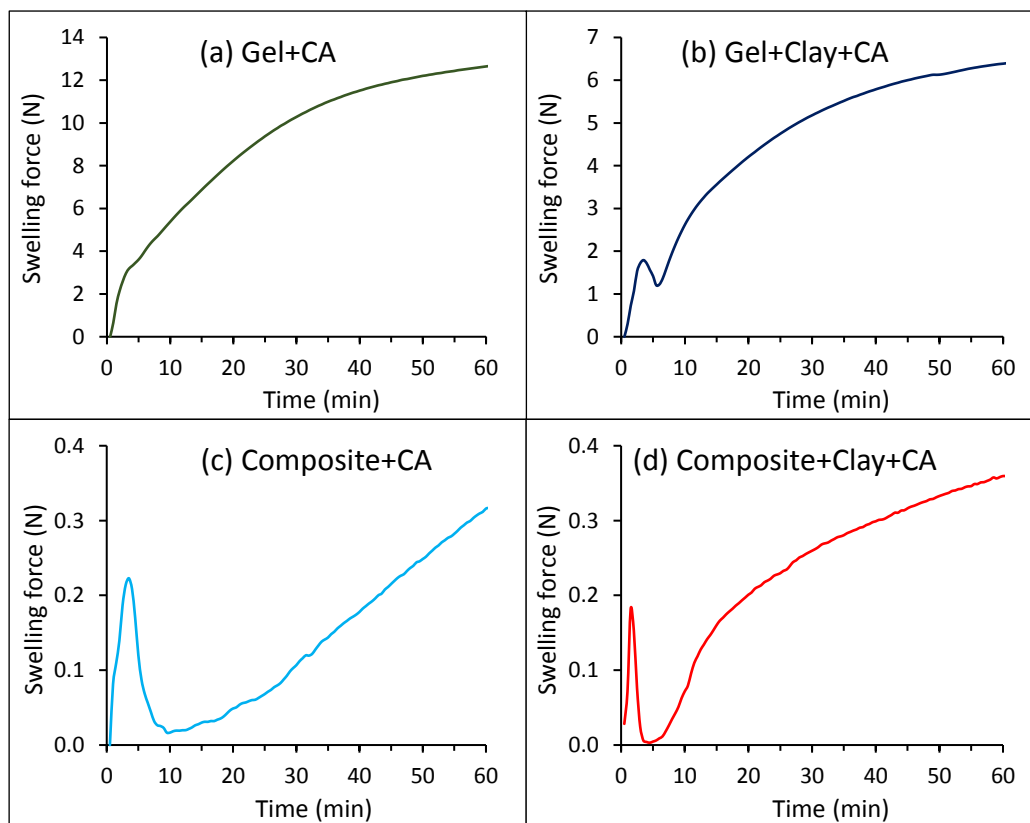


Figure 4.14: Typical swelling force response over time for the investigated formulations. Each chart shows the response of one sample.

As rheometer protocols for charactering viscous media using the oscillation single frequency test were adapted than using test fixtures specific for capturing the swelling force of gel materials, it can be argued that the experimental set-up devised here was not ideal albeit

being adequate to capture the force response of the formulations. For instance, even though the default frequency of 25 Hz and shear strain of 25% applied by the top-plate are relatively small to disrupt the swelling dynamics of the samples, they were not stationary. If anything, the applied default frequency and shear strain values would result in a conservative capture of the actual swelling forces developed by the samples. As the test specifics were kept the same for all samples, this departure from ideal set-up does not diminish the confidence in this methodology adopted to evaluate and compare force characterisation of the formulations developed here. Furthermore, the force and corresponding stress generated by the formulations will actually be greater than the values reported in Table 4.5 due to the cautious approaches taken in processing the test results

#### 4.4 Strain differential mediated morphing of cellulosic architectures

The natural progression of the work presented here would be attempting to control the microstructure and final form through 3D printing. The materials developed and characterised in this study enable extrusion through a syringe which is the proposed dispensing method for integrating with open-source 3D printing hardware. As a way of example, preliminary results demonstrating the actuation of a manually fabricated flower architecture is presented in Figure 4.15 to ascertain the stimuli responsive behaviour of the developed material systems and also to validate that the strain differential mediated folding presented in Chapter 3 could be expanded to the hydrogel composites as well. The form was fabricated through hand-held syringe extrusion of Composite+Clay+CA (for the substrate) and Gel+CA (at the base of the petals) by carefully following the trace of flower outline produced from a CAD drawing. The critical dimensions and a schematic of the fabrication process are outlined in Figure 4.15 (top row). This architecture has a programmed actuation pathway (Figure 4.15 (bottom row) a) - highlighted in yellow) around the base of petals where a layer of gel (Gel+CA) formulation was deposited to define the fold line. The choice of Gel+CA formulation for the actuation pathway is justified as it was found to produce the highest forces in response to hydration. This design was aimed to take advantage of the programmed 'through-thickness strain mis-match' which is the driving force for shape transformations. The drying of samples at room temperature (21 °C) initiate the transformation (Figure 4.15 (bottom row) b) which was maximised by drying at elevated temperature (140 °C for 5 minutes) fixing the new configuration (Figure 4.15 (bottom row) c). This new configuration is by virtue of greater strain differential achieved by means of enhanced dehydration of the materials at elevated temperatures. This transformed shape is deployed back to the flat configuration by placing on a water bath at room temperature (Figure 4.15 (bottom row) d) in a similar fashion to that of the preceding work reported in

Chapter 2. The asymmetric folding and waviness observed in dried petals are attributed to uneven amount of composite and hydrogel deposited - an implicit consequence of hand-held syringe extrusion. This uneven deposition of materials affects the through thickness strain differential within the global substrate. This observation further strengthens the argument for a smooth and controlled extrusion system to realise the full potential of this material system in creating controlled architectures. These features can be achieved through an automated extrusion system powered by stepper motors or pneumatics as found in 3D printers and industrial fluid dispensers respectively.

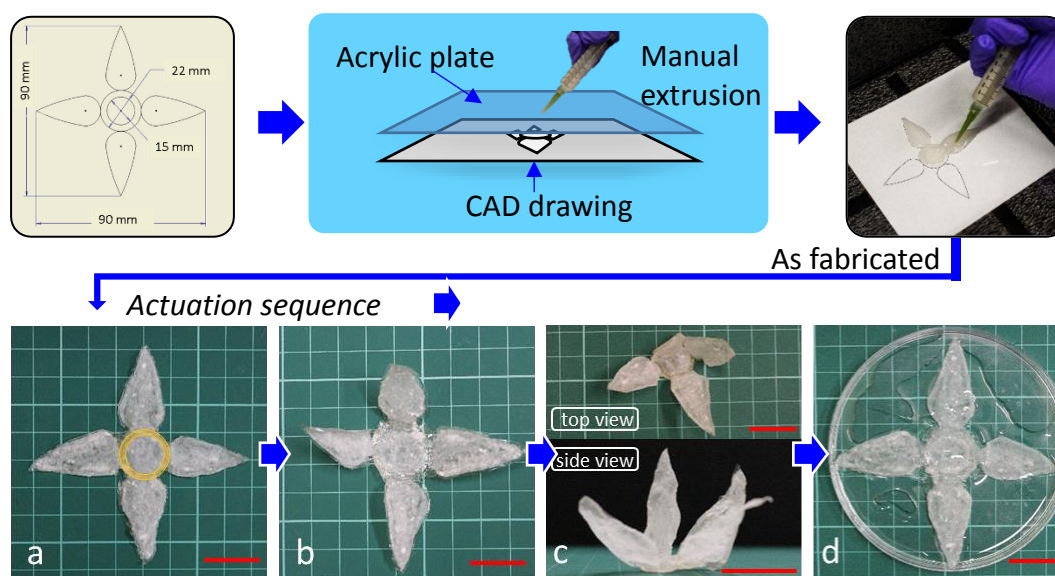


Figure 4.15: (top) Schematic of flower architecture fabrication (bottom) Actuation of flower architecture. (a) During drying at RT (21 °C) (b) dried at RT –initiation (c) after drying at elevated temperature– fixing shape (d) deployed back to flat configuration in water at RT. (Scale bar = 20 mm).

#### 4.5 Discussion and conclusion

The main hurdle in the development of the 3D printable cellulosic fibres was the dissociation of pulp fibres. The addition of cellulosic hydrogels overcame the issue of the inherent hydrogen bonding in the fibres resulting in a shear thickening suspension that frequently clogged when attempts were made to extrude with precision. Dissociation of pulp fibres in the hydrogels not only imparted necessary shear thinning properties but also aided in the dissociation and distribution of pulp fibres through optimised mixing strategies. This directly resulted in the ability to use higher loading capacities of pulp fibres without clogging, allowing the development of 3D printable cellulosic fibres. It was observed that permitting the crosslinking of these composites did not adversely affect the extrusion and swelling characteristics. Furthermore, it was imperative that the extruded/printed shapes are stable in an aqueous environment and do not disintegrate over the duration of experiments. The choice of citric acid as a crosslinker enabled lower crosslinking temperatures (after the fabrication of

shape), stable swelling without cracks and discolouration and an ecologically friendlier direction for further material development.

The rheological characterisation of the formulations containing citric acid confirmed that the samples were shear thinning which is essential for smooth and controlled extrusion in any syringe-based 3D printing extrusion set-up. The low critical strains for composite samples indicate that they flow readily when deformed which is desirable. The yield stress characterisation enabled quantifiable measurement of the force required to extrude the formulations. These results would better inform the selection process of the extruder system for the integration of this material system into the domain of 3D printing. Even though montmorillonite clay was added to stabilise the formulations for long term storage, but an additional complimentary effect on the composite formulation was also noted. Conventionally, the addition of filler materials results in an increased solid like characteristics and viscosity thus hindering the material flow, but as demonstrated in the amplitude sweep and shear rate results, the combination of pulp and clay resulted in an increasingly liquid like behaviour when deformed. The positive effect of clay-pulp interactions in lowering yield stress was also noted. It is believed that the intercalating clay platelets inhibits or even cleaves the physical interactions between pulp, CMC and water when deformed. Further characterisation of the pulp-clay interaction and the micro-structure in Composite+Clay+CA samples is required to confirm this hypothesis. However, the rheological characterisation of the samples confirms that the addition of clay improves the solid-like characteristics at rest and enhances the flow characteristics in formulations with pulp fibres. These are ideal features for a 3D printing material as a liquid like behaviour (flow) is desired for ease of extrusion and solid like behaviour to hold the shape after extrusion (rest).

The swelling ratio of samples were determined after crosslinking to investigate the swelling potential of the samples as well as their aqueous stability. As expected, the citric acid formulations had considerably lower swelling ratio when compared to the self-crosslinked samples. However, it is of paramount importance to generate controllable swelling without degrading the material. Additionally, the presence of crosslinking agent as opposed to self-crosslinking enables control over the extent of crosslinking and was found to influence the swelling potential. This was evidenced by the low ESR of Gel+CA when compared to self-crosslinked samples as reported in Table 4.3. The role of pulp network in restricting the swelling of gel the matrix was also noted. The thermal analysis of the samples yielded useful insight into the drying and crosslinking processes. In conjunction with the swelling ratios, the shrinking ratios calculated from TGA revealed the extent of volumetric changes in the



formulations through mass variations. This gave an insight into the strain gradients achievable from these materials for morphing applications. The characterisation of swelling force revealed the time dependent nature of swelling force development with the force decreasing with an increase in the amount of reinforcements. Furthermore, the influence of reinforcements especially the pulp network in controlling the hydration rate and consequently the development of swelling force was evident. The ratio of volumetric changes and swelling force characterisation revealed why bare gel formulations (Gel+CA) were effective in defining fold lines in morphing paper architectures presented in Chapter 3.

The morphing example of the flower architecture presented in Figure 4.15 not only demonstrates the ability of the developed material system to be extruded through a syringe but also its ability to morph out-of-plane by virtue of programmed strain differential via dehydration/hydration. As demonstrated in Chapter 2, cellulose within an already existing fibrous architecture (*i.e.* paper) has morphing potential, whilst this work aims to enable bespoke architectures beyond the limitations of two-dimensional paper. Whilst the architectures presented in Chapter 2 was manually folded in to three-dimensional configuration from flat (2D), the material system developed in this chapter demonstrate the ability to morph from flat (2D) to a three-dimensional configuration following the design rules developed in Chapter 3 and subsequent stimuli responsive deployment. The material system developed here permits a greater control of programming the strain-differential which enabled 2D to 3D and back to 2D transformation. The adoption of pulp and cellulosic hydrogel in a composite form enabled integration of the cellulosic material into the domain of shear thinning materials without compromising its functionality to create morphing architectures whilst retaining the tuneable parameters such as varying micro-structure, porosity, temperature and volume fraction ( $V_f$ ). These parameters can be controlled to attain a programmable response from a global substrate through varying inherent 'through thickness strain differential' upon hydration/ dehydration. The characterisation of the hydrogel and composite formulations presented in this chapter also identifies swelling potential as a programmable parameter inherent to the materials as opposed to the geometrical or system programmable parameters. The swelling potential of the materials presented here can be varied by changing the amount of crosslinking agent (citric acid) in the formulation essentially allowing further modulation of the morphing response. Implementation of these materials into 3D printing will not only ensure greater precision in the placement of materials but also facilitate fabrication of more complex architectures and actuation pathways for 4D printing. Owing to the novelty and characteristic paste nature of this bespoke material system, new

material dispensing systems are required to facilitate 3D printing of these materials as the conventional systems based on melting or sintering are not feasible. It is envisaged that in conjunction with the versatility of additive layer manufacturing methods varying microstructures within an overall shape can be achieved. Whereas, the responsive nature of material along with its tuneable parameters would result in hierarchical structures within a global form that can actuate in complex forms. The responsive material system, tuneable material parameters and programming guidelines broadens the design choices to program creases and bends thereby being capable of realising unique morphing responses from the material system.

---

## Chapter 5 Cellulosic composites and 4D transformations

---

### 5.1 Introduction

This chapter reports the morphological and mechanical characterisation of 3D printed cellulosic composites and their 4D transformations. Owing to the novelty of the developed material system, custom hardware and firmware modifications had to be carried out on an open source 3D printer to enable additive manufacturing. The developmental work to facilitate this is summarised and the deployment as well as self-folding parameters identified in Chapter 2 and Chapter 3 were validated by means of a representative 4D morphing example. Prior to fabricating complex morphing architectures, it is imperative to gain more understanding of the material system and how 3D printing influence some of the key material properties. The influence of process (3D printing) variables on key material properties such as microstructure and mechanical properties were thoroughly investigated and quantified through experimental testing. Some 4D morphing examples actuating in the thickness direction (pop-up) are also presented to show the efficacy of the strategies adopted here to realise transformations beyond the familiar folding and un-folding responses. This is aimed to validate the potential of the material system and additive manufacturing process as adopted here to realise morphing architectures of increased complexity and programmable responses.

### 5.2 Enabling additive layer manufacturing (ALM) of cellulose

This section details the work carried out in adapting an open source 3D printer to print with the developed hydrogel and hydrogel composite formulations. 3D printing with a non-standard material involves a fair amount of custom modifications to be carried out to the hardware, firmware and the controlling software. The open-source 3D printing technology encourages and facilitates such modifications to be realised and shared through an active community of users and developers, the Reprap movement being a prime example [86,116]. A commercially available open source FFF 3D printer for printing plastics such as PLA (polylactic acid) and ABS (Acrylonitrile butadiene styrene) was taken as the foundation and onto which necessary modifications were carried out to realise syringe-based paste extrusion. This was primarily due to cost and accessibility considerations as FFF printers are cheaper and have more support through open-source compared to other 3D printing options. A 3D printer is yet another numerical control machine which can take a digital computer aided design (CAD) file to a physical form. Specialist software called slicers (*e.g.* Slic3r, Cura, Simplyfy3D and Matter Slice) usually bundled with the printer's control software convert the CAD file to a set of 'layer by layer' machine commands called G-codes to be read by the 3D printer based on

the input preferences. The G-codes are specific machine commands issued to a numerical controlled machine and contains specific information about how to realise the given task. Some of these slicers are available for free whilst others required purchase of a license. However, these control software and slicers are universal in nature that they can be used to operate a wide range of 3D printers conforming to the open source Marlin or Repetier firmware.

### 5.2.1 Specifications

The following specifications were drawn up for the 3D printing system to be able to print cellulosic hydrogel and composites:

- Ability to extrude high viscosity ‘paste like materials’ without clogging
- Provisions for accommodating various nozzle sizes and ease of handling
- A simple, light-weight and easy to replicate extrusion solution
- Support for large capacity syringes up to 60 mL
- Support multi-material extrusion

### 5.2.2 3D Printer hardware

Even within the open source fused filament fabrication (FFF) landscape, there are different styles of printers namely Cartesian and delta style printers as shown in Figure 5.1a and b respectively. These styles are characterised by their method of movement while printing an object. In Cartesian style printers, the print bed (build platform) is not stationary but moves at least in one of the axes (mostly Y or Z), whereas the delta style printers are characterised by their fixed build platform. This has certain advantages such as added stability to the print during 3D printing and less inertia associated with print-head resulting in faster print speeds.

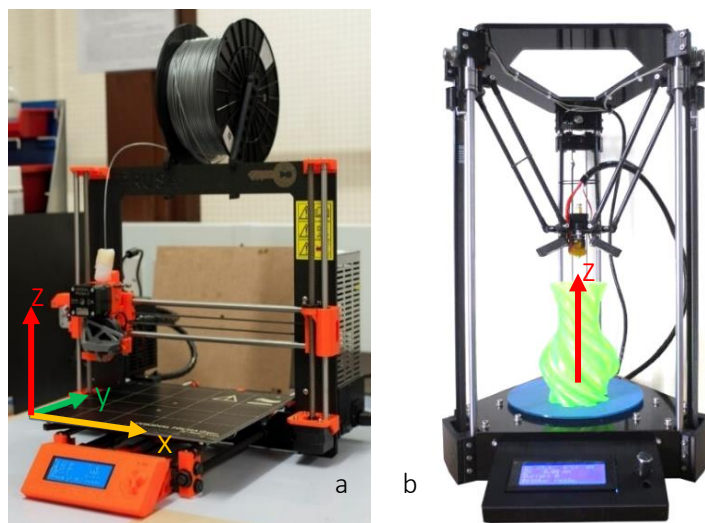


Figure 5.1: (a) Cartesian style Prusa i3 MK2S (b) A generic delta-style 3D printer. (Image adapted from source: [www.alibaba.com](http://www.alibaba.com))

The Cartesian systems excel in being more compact, general ease of use and maintenance; and having a simplified approach to 3D printing. Therefore, a Cartesian style open source printer (Prusa i3 MK2S) was selected to be modified for this project. A self-build kit was purchased directly from the developers and assembled in the lab (Figure 5.1a).

The Prusa i3 MK2S cartesian style printer has the built platform free to move in the Y axis whereas the X and Z axis movements are managed at the extruder carriage through stepper motor driven belt and lead screw assembly respectively. Owing to the precision-machined threaded lead screws in combination with micro stepping enabled NEMA 17 stepper motors, Z axis resolutions from 0.05 mm onwards are possible with this printer. The open frame design also permitted ease of access to the electronics and provisions for modifications to the printer as well. Furthermore, the printer utilises a RAMBo (RepRap Arduino compatible Mother Board) Mini control board based on an open source design. The RAMBO Mini 1.3a used in this printer is manufactured by Ultimachine, USA and is well supported through forums thus ideally suited for modifications and experimentation. Figure 5.2 shows the schematic of the motherboard indicating key connection points. In the firmware, the plastic extruder is treated as the fourth axis (E axis) along with the three co-ordinate axes (XYZ) and controlled via stepper motor drivers on the motherboard. The printer can be operated at default configuration via the control knob and LCD display, but more complex operations required interfacing with the control software on a PC through USB. As the motherboard houses an Arduino Mega at its heart, discreet commands to program various printer parameters could be sent through Arduino IDE or through dedicated G-code terminals on most 3D printer control software.

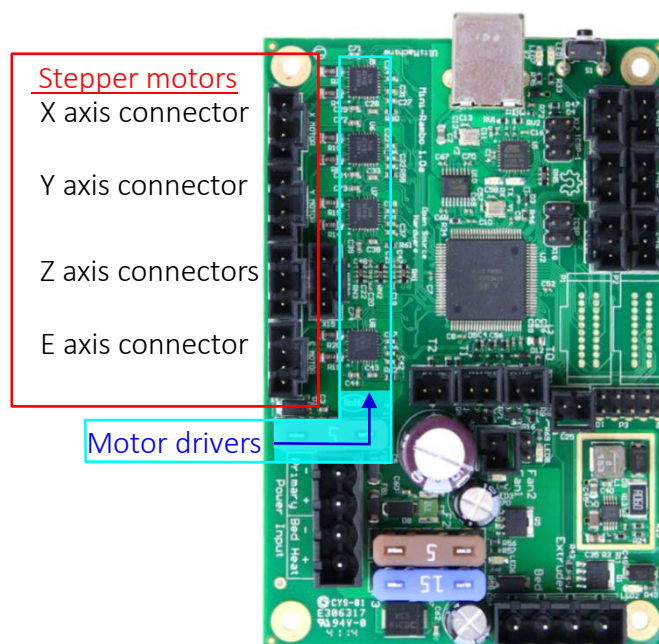


Figure 5.2: Schematic of Mini-RAMBo v1.3 a. (Image adapted from source: [www.matterhackers.com](http://www.matterhackers.com))

### 5.2.3 Design of paste extruder

There are several open-source paste extruder designs readily available within the Reprap community. Most of them are stepper motor driven for simplicity as opposed to hydraulics or pneumatics. These designs can be classified into stepper belt-driven and stepper direct-drive based on how the paste material is moved towards the nozzle. Classification can be made based on the mounting point for the extruder as well; namely direct mount and off-axis. Some generic examples of paste extruders are presented in Figure 5.3. Figure 5.3a shows the Universal Paste extruder (developed by Richard Horne), a compact extruder that can be directly mounted on to the print-head of 3D printer [190], whereas Figure 5.3b shows an example of direct driven extruder mounted outside the perimeters of 3D printer [191]. This style of extruder pushes the printing material through compliant tubing towards the nozzle mounted on the X-carriage thus minimising the weight of the carriage assembly. This permits faster carriage movements and less inertial effects ultimately resulting in faster print times and stable operation. This design also facilitates incorporating larger syringe sizes without limiting print-head movements. Theoretically, the direct-driven designs allow for certain degree of retraction by reversing the stepper direction and thus retracting the plunger. However, as the drive is further away from the nozzle, there is a delay for the actions at the paste extruder's stepper end to influence the conditions at the nozzle/print end.

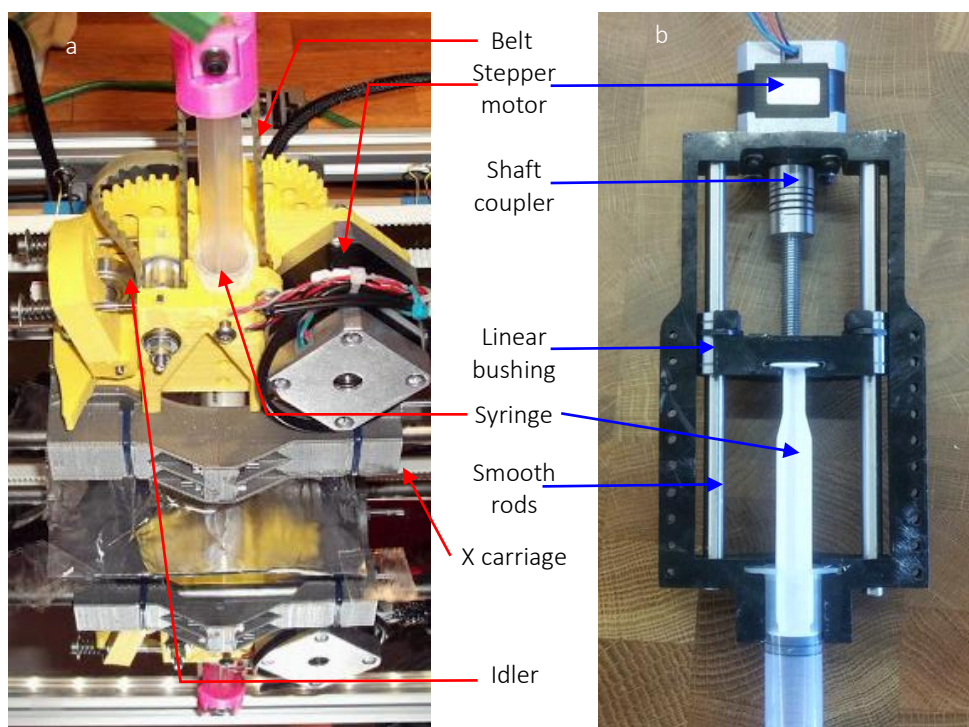


Figure 5.3: (a) Direct mount belt driven Universal Paste extruder. Image adapted from [190]. (b) Off-axis direct driven syringe extruder. Image adapted from [191] and reproduced under Creative Commons Attribution-NonCommercial-ShareAlike 2.5 Generic License.

Owing to the novelty of the materials developed, it was challenging to select the best extruder solution as they are all being optimised specifically for certain material types. Therefore a new extruder adhering to the direct drive off-axis design was designed and built to meet the developed specifications for paste extruder. Figure 5.4(a and b) shows the developed extruder and its key components. The extruder functions akin to a syringe pump and benefits from the precision threaded drive screw for efficient power transmission. The corresponding driven-nut pushing the syringe plunger prevents backlash and resulting loss of built-up pressure in the syringe when the extruder (motor) is paused/stopped. The precision machined linear smooth rods in conjunction with linear bushings ensure smooth travel along the lead screw length. The syringe cap aids to further stiffen the syringe holder as well as secure the syringe in place during extruder operation. The NEMA 17 stepper motor driving the paste extruder directly replaces the stepper motor driving the plastic extruder at the motherboard. More information about the operation of stepper motors are included in Appendix A.1.1 *Introduction to stepper motors* The NEMA 17 (48 oz) stepper, bushings and rods were all purchased from Oozenest ([www.oozenest.co.uk](http://www.oozenest.co.uk)) whereas, the rest of the components were

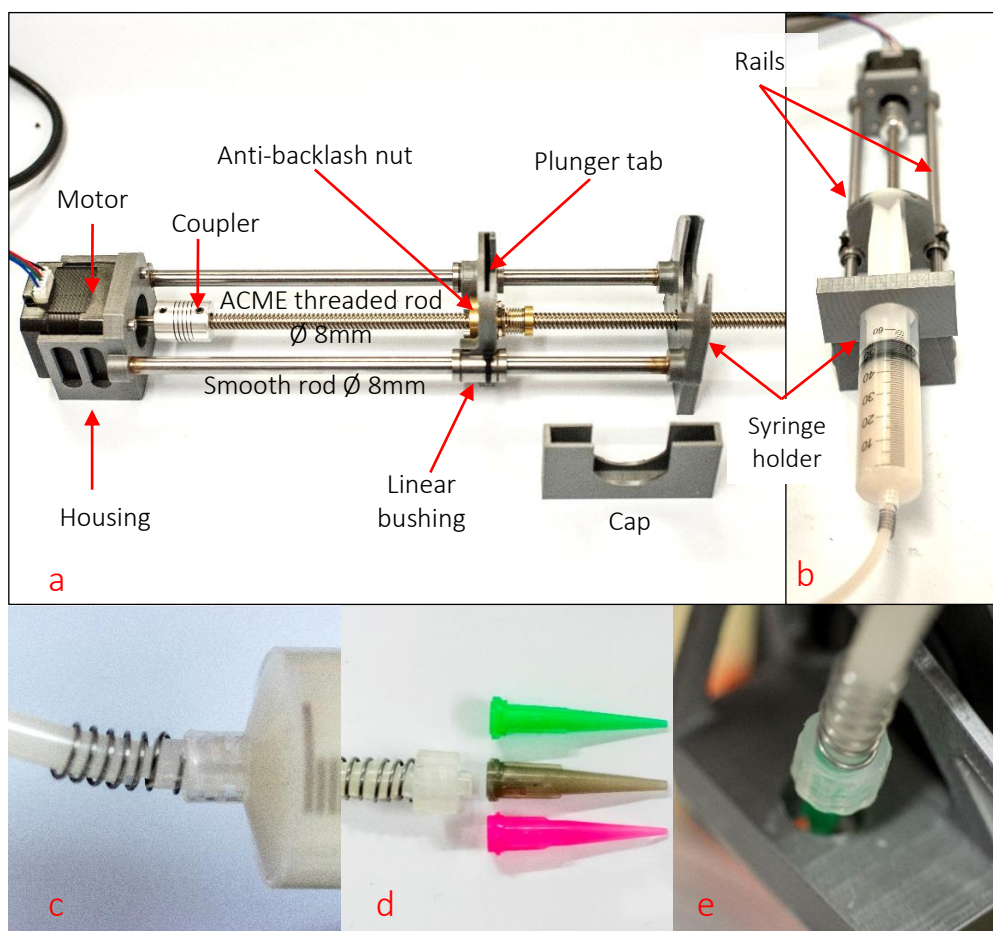


Figure 5.4: Paste extruder. (a) Key components, (b) loaded with syringe containing hydrogel composite, (c) female luer barb lock and PTFE tubing assembly, (d) male luer nozzle assembly and a selection of nozzle sizes, and (e) Push-fit nozzle assembly into the housing attached to the X carriage.

designed and 3D printed in-house from PLA using the Prusa MK2S printer. The design is best suited for 60 mL syringes, however, it can accommodate other syringes of lower volumes effortlessly. The off-carriage extruder design not only allows for large syringe volumes (upto 60 mL) to be utilised but also preserves the original plastic filament extrusion set-up of the printer. This dual capability is a useful feature to have and the extruder of choice can be engaged easily by plugging in the corresponding stepper leads at the motherboard.

The final extruder setup with the printer is shown in Figure 5.5. The material extruded from the syringe is directed towards the printer and nozzle by means of a flexible PTFE tubing of 4 mm inner diameter. The paste extruder housing mounts directly on to the part cooling fan on the 3D printer extruder carriage as shown in Figure 5.5(insert). The luer assembly with PTFE tubing at the syringe and nozzle end is shown in Figure 5.4c and d respectively. The luer adapter connected to the PTFE tubing is then inserted into the 3D printed paste extruder housing (Figure 5.4e) with the design allowing for the paste extruder nozzle to have a pre-defined off-set from the plastic extruder (metal hotend) as shown in Figure 5.5(insert). This prevents the inactive plastic extruder (metal hotend) interfering with the print during printer operation. As the paste extruder nozzle is designed to be 'push-fit', it can be easily removed from the housing for the plastic extruder to be engaged. This design also enables easier and faster loading of materials (pre-assembled syringe+tubing) in to the printer.

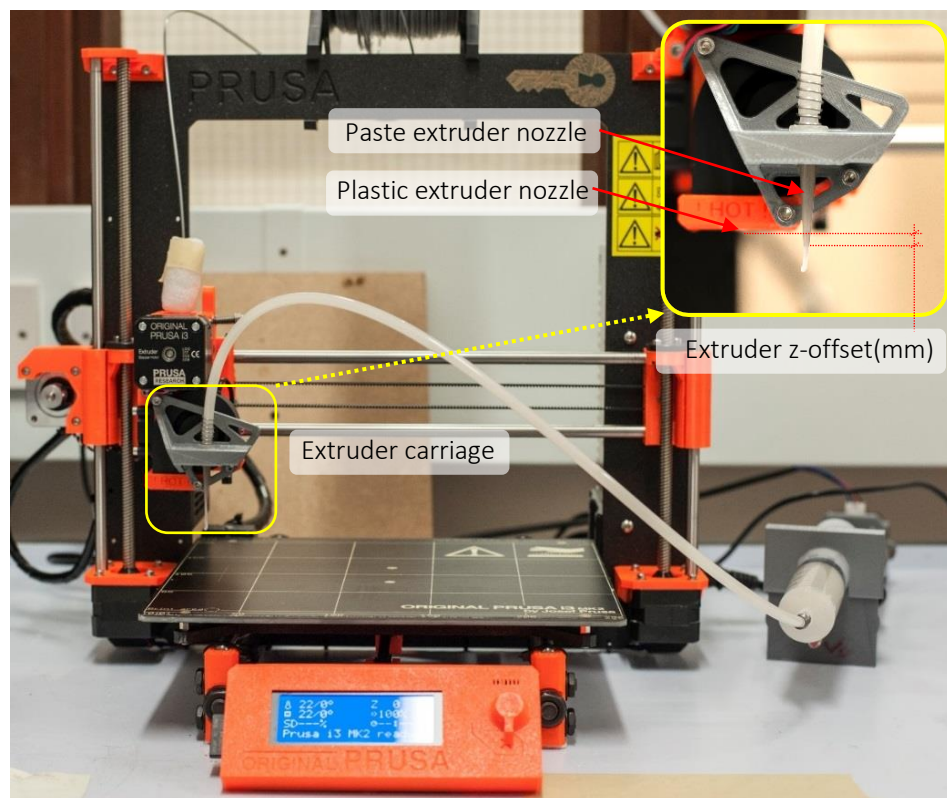


Figure 5.5: 3D printer and extruder set-up; Extruder housing is shown in insert.



#### 5.2.4 Printer and extruder set up

MatterControl, a free open source software package was used to control and send commands to the 3D printer. This software was chosen amongst alternatives such as Repetier-Host and Cura mainly due to its user-friendly interface as well as the ease of access to the printer and CAD file settings. Furthermore, it also incorporates a range of slicer software such as MatterSlice, CuraEngine and Slic3r and supports seamless switching between them to generate the necessary G-codes.

By default, the printer is tuned to extrude thermoplastics. In order to extrude cellulosic gel and hydrogel composites, certain parameters of the stepper motor driving the paste extruder had to be modified. The torque output of the extruder assembly could be improved by incorporating appropriate gearing to the motor output or by using stepper motors with internal gearing. Therefore, a second paste extruder (Discov3ry from Structur3D) powered by a stepper motor with internal gearing was also utilised in this project alongside the paste extruder shown in Figure 5.4a and b for convenience and also to explore multi-material printing. The motor input current, voltage and steps are controlled by the on-board stepper motor driver and thus is the performance limiting factor. The on-board drivers are rated for maximum 2 A (ampere) current; however, the default set current for the stepper motors are much lower. This value is usually set depending on the motor load, system inertia, noise level and operational time among other things. The step count of the motor specifies the number of steps required to move 1 mm of the filament or in this case advance the lead screws by 1 mm. As the default is set for extruding thermoplastic filaments, this parameter needs to be reconfigured to enable paste extrusion. The ideal step count was obtained through experimentation with the materials and extruders. For example, the extruder motor step count and current were varied through G-code commands until smooth and continuous material flow was established depending on the material type and the stepper motor used. A detailed explanation of motor parameters, the necessary G-codes and the turning process utilised to achieve smooth and reliable extrusion are presented in Appendix A.1 *Optimisation of paste extruder and print settings for 3D printing*.

The typical procedures to enable paste extrusion and 3D printing are outlined as follows. The print bed was calibrated without the paste extruder nozzle using in-printer calibration routine. This allowed the induction sensor at the print-head to be utilised in conjunction with the factory code to achieve print bed levelling and record skew or misalignment so as to compensate during actual print operation. The calibration sequence ended with the plastic extruder nozzle at the default 0.15 mm off the levelled print bed. The nozzle was brought back

to zero using the control dials followed by connecting to a laptop with MatterControl software. This action synchronised current printer configurations with the software and allowed the printer to be controlled through the software. The paste extruder nozzle was then engaged, and the required Z-offset was determined by adjusting the Z axis via the software to a point where the paste extruder nozzle was flush with the print bed. The raised Z axis distance was noted as the z-offset for extruder in the software and this effectively zeroed the Z axis in relation to the paste extruder nozzle and print bed. The default setting to prevent cold extrusion was overridden and the extruder steps re-configured through specific G-codes commands to the desired values. Refer to Appendix, (*A.1.2 Optimisation of print parameters*) for exact values.

The extruder operates by first building up pressure within the syringe in response to the advancement of lead screw compressing the plunger. Once the yield stress as well as resistive forces along the PTFE tubing and the syringe barrels had overcome, the material will flow along the tubing and through the nozzle onto the print bed. Even though the extruder design allowed for syringe retraction, the effects of such an action was not immediate as the flow control (stepper motor) was carried out further from the delivery (nozzle). An ideal paste extruder should also have options to allow for flow control adjacent to the nozzle as well. Commercial fluid system dispensers utilise such an approach with auger screws providing finer control of material dispensing and retraction closer to the nozzle. This particular improvement will be addressed in the Future work chapter (*6.2.3 Extruder upgrades for reliable and integrated multi-material printing*). Furthermore, integrated multi-material printing could not be realised due to the lack of additional stepper motor ports on the printer motherboard. This was mitigated to an extent by adopting an inter-layer multi-material approach where the architectures were designed such that the materials were not varied within a layer but only in between the layers. The designs were split (de-coupled) in CAD based on the material arrangement in 3D and was coupled back together by printing on top of each other. Even though this solution certainly limited the design freedom, multi-material printing and more importantly programmable strain gradients could be realised this way. As for the scope for this project, feasibility of 3D printing and characterising the morphing of the printed architectures were deemed more critical than the development of an ideal paste extruder at this stage.

#### 5.2.5 Print results

Once the nozzle calibration and paste extruder parameters were assigned, the modified printer was ready to print hydrogels and hydrogel composites. The CAD file (see Figure 5.6a)

was then imported into printer control software (MatterControl) and sliced to generate the G-codes. The layered schematic in Figure 5.6b shows the visualisation of the G-code print-path. The materials were extruded and laid on to the print bed at room temperature as per the G-code sent to the printer. However, the bed temperature could be increased up to 80 °C to aid faster drying. Once dried and removed from the print bed, the prints can be crosslinked in an oven as per the material specifications. Shrinking of prints are inevitable when dried or dehydrated, but the shapes can also be de-hydrated through freeze drying and then crosslinked to preserve the printed dimensions. Figure 5.6 confirms the successful integration of the paste extruder and feasibility of 3D printing with the materials developed.

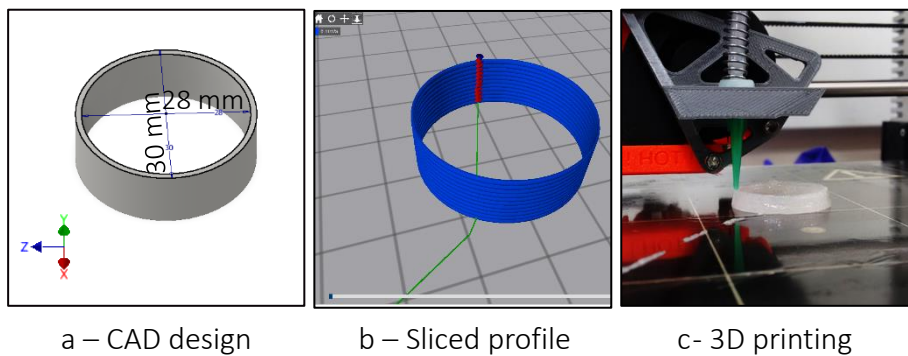


Figure 5.6: 3D printing of a cylinder (dimensions in mm) using paste extruder. (a) CAD design with dimensions. (b) Sliced layer by layer profile of the cylinder. (c) 3D printing of the cylinder using Composite+Clay+CA formulation.

### 5.2.6 4D printing of cellulosic composites

As a way of example, a flower architecture similar to that of manually fabricated in Chapter 4, (Figure 4.15) was printed using the custom 3D printer + paste extruder set-up. The manufacturing and actuation steps are presented in Figure 5.7a-f. The form was fabricated from a CAD model and prepared for 3D printing (sliced) with MatterControl software. The base of petal was printed from Composite+Clay+CA with an additional annular layer of Gel+CA at the base of the petals forming the region of localised strain differential. A tapered nozzle with 0.8 mm diameter was used for printing. The corresponding print path is shown in Figure 5.7a (blue - Composite+Clay+CA and red - Gel+CA) and the printed form is shown in Figure 5.7b. Similar to the hand-made flower architecture, the drying of the specimen at room temperature (RT-21 °C) initiated the transformation (Figure 5.7c) which was maximised by crosslinking at 120 °C for 10 minutes fixing the new configuration as shown in Figure 5.7d. This new configuration is generated by virtue of greater strain differential achieved by means of enhanced dehydration of the materials at elevated temperatures. The transformed shape is deployed back to the flat configuration by placing in water bath at room temperature (21 °C) (Figure 5.7e) in a similar fashion to that of the preceding work reported in Chapter 4. Upon drying, the petal architecture reverts to its 3D configuration as shown in Figure 5.7f exhibiting

fold recovery first observed in Chapter 2, 2.4 *Fold recovery upon drying*. The actuation between flat and 3D configuration is cyclic and can be repeated multiple times thus exhibiting shape memory behaviour. Unlike the manually fabricated form in Figure 4.15, the form in Figure 5.7 is devoid of asymmetric folding and waviness. This confirms the previous assertions on the limitations of hand-held syringe extrusion and that it had been rectified through adopting 3D printing as predicted.

The example presented in Figure 5.7 not only demonstrates the ability of the developed material system to be 3D printed but also its ability to morph out-of-plane by virtue of programmed strain differential via dehydration/hydration. This demonstration also represents the successful culmination of some of the key objectives pursued in Chapter 2, Chapter 3 and Chapter 4 as a reliable cellulosic smart material system with inherent programmable parameters was used to fabricate a digital design capable of morphing in the time domain. As predicted in Chapter 2, 2.4: *Fold recovery upon drying*, the presence of a stable matrix in between the fibrous network was crucial in achieving cyclic actuation and shape memory behaviour of the fabricated forms through fold recovery. The aqueous stability imparted through formulation and crosslinking strategies were also evident as envisaged. However,

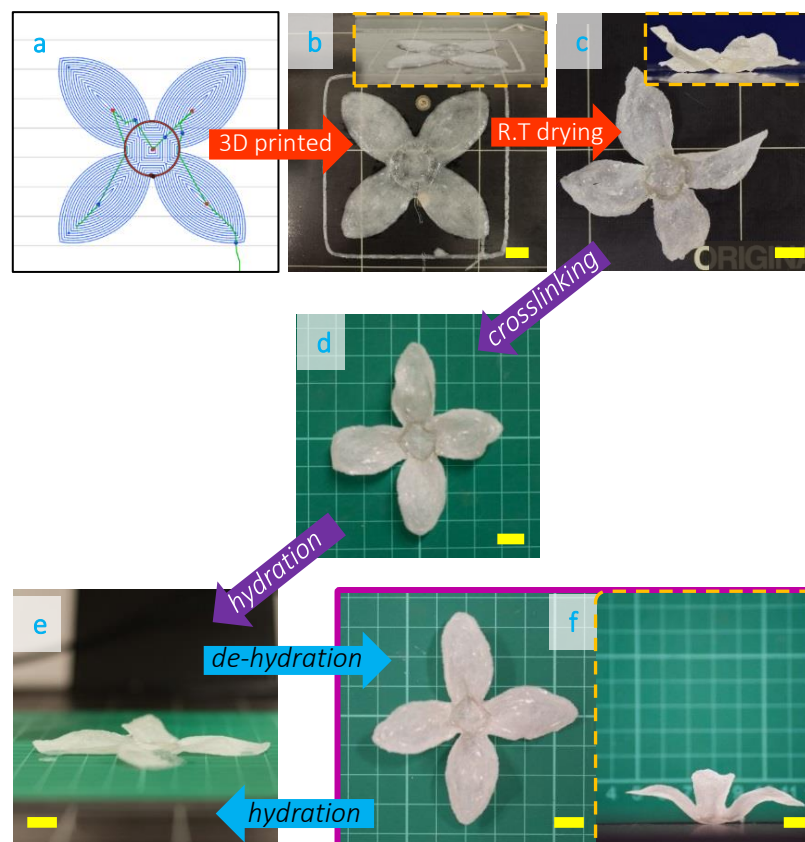


Figure 5.7: Fabrication of petal architecture. (a) Generated print-path from CAD model. (b) 3D printed form. (c) Drying at room temperature initiating morphing. (d) After crosslinking to maximise and fix the 3D shape. (e) Deployed to flat configuration upon hydration and (f) drying (dehydration) recovers the 3D petal shape. The side views are shown in inserts. (Scale bar = 10 mm).

owing to the novelty of 3D printing this unique material system, further characterisation is required to fully understand the influence of processing and materialistic parameters.

### 5.3 Characterisation of 3D printed cellulosic composites

As mentioned earlier, the composite formulations were envisaged to form the stable substrate and the gel formulations to form active fold lines along which the printed forms can actuate. Therefore, it is crucial to investigate the fabricated forms and identify the influence of manufacturing process in governing its key material and responsive parameters. The following sections report the efforts carried out to characterise the microstructure, hydrophilic nature and mechanical properties of the material systems after 3D printing.

#### 5.3.1 Microscopy

The printed forms were observed under a microscope (Zeiss Imager M.2) after drying at room temperature (RT 21 °C). A single extruded line comprising one layer (Figure 5.8a), a cross print with overlapping extruded lines at 0° and 90° from Composite+Clay+CA (Figure 5.8b) and a Gel+CA fold line on Composite+Clay+CA substrate (Figure 5.8c) were investigated. Figure 5.8a shows the basic composition of the printed composite with the CMC polymer occupying the inter-fibre spaces whilst encapsulating them. A degree of fibre alignment in the print direction is also evident and this aspect was examined in-depth in Section 5.3.3 *Fibre alignment in-print*. Figure 5.8b shows a cross over point in the print operation and the resulting changes to the inter-fibre spacing as a result. The inter-fibre spacing was significantly reduced at this region

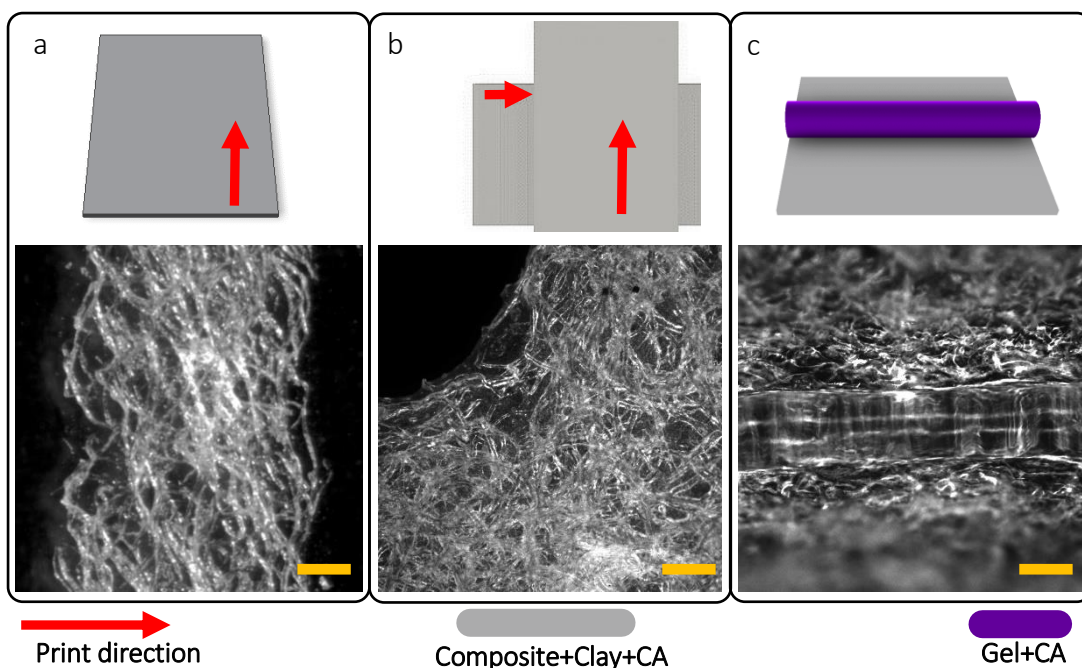


Figure 5.8: Microscope images of 3D printed specimens. (a) Single extrusion line of Composite+Clay+CA (1-layer). (b) Overlapping lines of Composite+Clay+CA (1-layer) and (c) Gel+CA laid on top of Composite+Clay+CA defining fold line. (Scale bar=200  $\mu\text{m}$ ).

accompanied by an increase in the grammage due to the increased amount of fibres (Composite+Clay+CA) present in the crossover region. Figure 5.8c shows the detailed view of fold line created on the printed composite surface using hydrogel (Gel+CA). It can be seen that as the printed form dries, the deposited gel is anchored to the fibres and the matrix occupying inter-fibre spaces driving the open surfaces closer forming a fold. This is ideal as the fold lines are essentially integrated in to the substrate. These observations showcase the changes in substrate microstructure as a result of 3D printing and programming strain gradients.

### 5.3.2 Contact angle measurements of 3D printed formulations

An understanding of the material response to the stimulus of hydration is essential to generate clear design rules for this morphing system. The study of fibrous architectures in paper types revealed that the contact angle measurements are indicative of the rate of actuation as hydrophilicity and substrate architecture plays a crucial role in fluid - substrate interactions and fluid transport. As for paper substrates, a dynamic approach to assessing contact angle was used (Section 2.2.3 *Contact angle measurements of paper substrates*) to investigate the hydrophilicity (*i.e.* wettability) and droplet absorption where contact angle measurements over a set time period was carried out. A similar approach using a Drop Shape Analyser (KRÜSS DSA 100) could not be extended to the dried and crosslinked gel and composite samples. The droplet absorption on these substrates resulted in immediate swelling directly underneath the droplet due to its hygroscopic nature and the DSA could not distinguish between the decline in droplet size and subsequent swelling. Figure 5.9 shows the photograph of Gel+CA substrate swollen into the droplet. It can be seen that such a response cannot be distinguished by DSA over time which measure contact angle based on contrast detection alone. Other samples Gel+Clay+CA and Composite+Clay+CA also exhibited this response but to a relatively lesser extent.

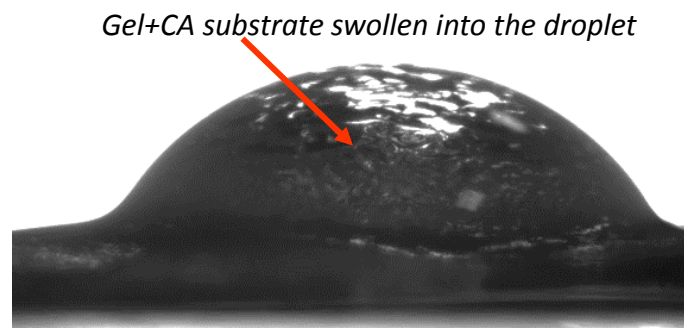


Figure 5.9: Example of substrate swollen into the droplet for Gel+CA.

Therefore, the static contact angle of the 3D printed films of Gel+CA, Gel+Clay+CA and Composite+Clay+CA were evaluated using Drop Shape Analyser (KRÜSS DSA 100) and

accompanying analysis software ADVANCE. Standard practices and loading protocols were observed and the contact angle measurements were taken after 15 seconds from droplet deposition on the substrate allowing the droplet to be stable and in equilibrium. Even though droplet absorption is expected to commence almost immediately due to the hygroscopic nature of the substrates, it is even more important to allow the droplet to be stable within its environment. The same protocols were also applied in the assessment of contact angle for the paper substrates.

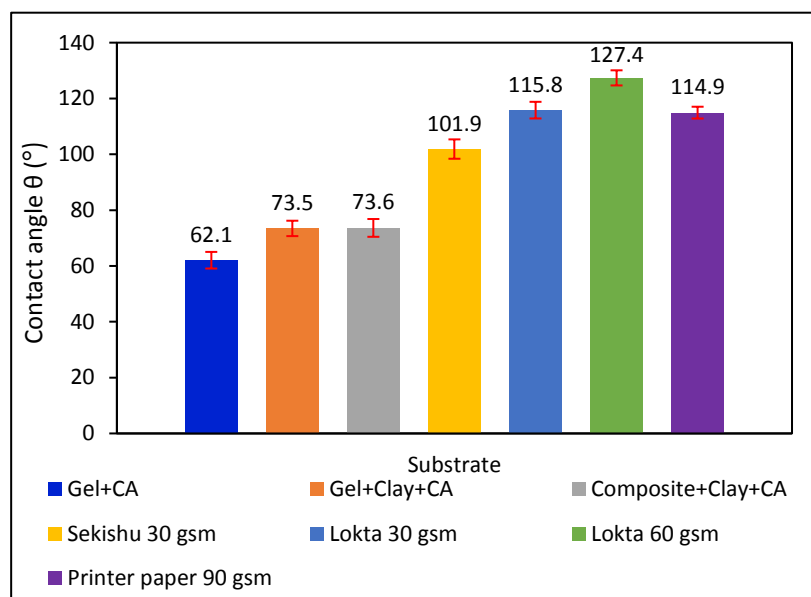


Figure 5.10: Contact angle of the substrates investigated in this study.

Figure 5.10 shows the contact angle measurements for 3D printed films along with the contact angle of different paper substrates for comparison. A total of 5 measurements were taken from different regions on the substrate and the standard deviation is presented as error. As expected, Gel+CA films are the most hygroscopic and relatively more wettable as evidenced by their low contact angle. Gel+Clay+CA and Composite+Clay+CA samples have approximately same affinity towards water as they have similar contact angle. When compared to the paper substrates, the contact angle for the materials developed in this study is lower indicating more affinity and responsiveness to the stimuli of water. The contact angle values presented here are indicative of factors such as surface chemistry and surface roughness than the influence of microstructure (especially for paper substrates). This is supported by the low standard deviation between the measured contact angles for the paper substrate types.

Swelling of the substrate and subsequent wrinkling due to random anisotropy inhibited the capture of complete droplet absorption in paper substrates leading to full wetting. As for the Gel+CA, Gel+Clay+CA and Composite+Clay+CA films, it was the swelling directly underneath the droplet that inhibited the measurement of contact angle decay leading to full wetting. The

saturation and flow propagation in substrates developed in this study and that of paper are different owing to the differences in its microstructure. Hand-made paper substrates are characterised by their porosity and in printer paper the inter-fibre spaces are occupied by filler matrix which is often formulated to resist water absorption. In porous substrates, the droplet could occupy the inter-fibre spaces whilst being absorbed by the randomly aligned fibres resulting in anisotropic swelling leading to twisting as well as wrinkling. In printer paper, primary flow path for the droplet was through absorption into the fibres eventually resulting in anisotropic swelling as they were more hygroscopic than the filler matrix. The materials developed in this study (by virtue of CMC polymer) clearly has a greater capacity to absorb water and therefore can accommodate greater amount of water directly underneath the droplet than propagate further radially. This localised influence of hydration has some advantages. Firstly, it directly results in a greater substrate stability as only the substrate regions directly in contact with the water are affected. It could also open-up new possibilities of creating specific hydration path ways such as micro channels (thus taking advantage of capillary effects) in 3D printed architecture with these materials as confinement of hydration effects within incident points are favoured than radial propagation. Furthermore, no wrinkling or warping was observed with films of gel and composite samples as they were programmed to be stable and fabricated in layers arranged in  $[0^\circ, 90^\circ]$  configuration in the 3D printer. The  $[0^\circ, 90^\circ]$  print-path configuration minimises the anisotropy in the films leading to further stability.

### 5.3.3 Fibre alignment in-print

Alignment of high aspect ratio particulates during shear and extensional flow within a fluid medium has been studied and reported before [93,111,192]. Here, the alignment of cellulose fibres within the hydrogel matrix during 3D printing is investigated. The paste extruder pushes hydrogel composite along a flexible PTFE tubing and through a tapered nozzle. The converging profile of the nozzle aids in the smooth and clog-free flow and results in shear induced alignment of the particulates. The extent of shear induced alignment depends on factors such as particle size, volume fraction ( $V_f$ ), nozzle geometry (length and diameter) and printing speed [93]. As for the cellulose composite and extrusion system developed in this study, parameters such as particle size (fibre diameter ( $D$ ) =  $13.4 \pm 1.34 \mu\text{m}$ ; length ( $L \gg D$ )), volume fraction ( $V_f = 0.5$ ) and nozzle length and style are optimised for smooth flow and remains invariant. Thus, for a fixed printing speed, only the nozzle diameter affects the alignment. Nozzle diameter is a crucial parameter in 3D printing as it dictates the print resolution as well as the time (duration) to make a print as it influences the amount of material that can flow through the



nozzle. Therefore, the fibre alignment through different nozzle diameters were investigated and characterised to optimise the nozzle diameter to facilitate maximum alignment, resolution and ease of printing.

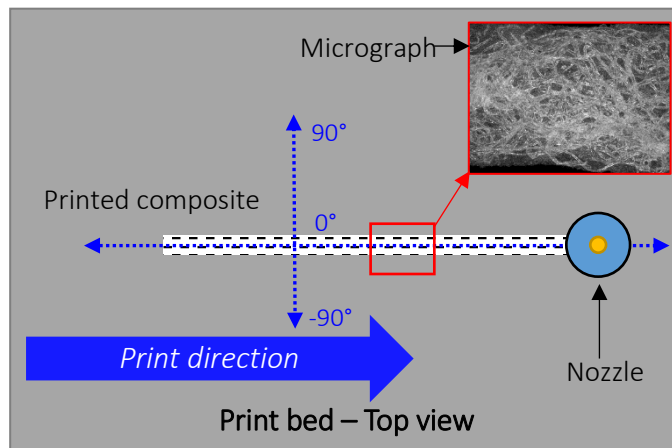


Figure 5.11: Schematic (top down view) of 3D printer bed and principal printing direction relative to the nozzle movement. (Insert) Microscopic image (10x) of the 3D printed cellulose- hydrogel composite line.

In order to quantify alignment, lines of cellulosic hydrogel composite (Composite+Clay+CA) were extruded on to the print bed at room temperature (RT 21 °C) at a speed of 8 mm/s (1-layer height). Nozzle diameters of 0.6 mm, 0.8 mm, 1.2 mm and 1.6 mm were investigated. As the layer height is limited by the nozzle diameter, the lines were printed such that the nozzle would just press down and flattens the laid material as the print head moves. Typically, layer heights within 50 % - 80 % of the nozzle diameter were feasible without spreading the material excessively. Figure 5.11 shows the schematic of the cellulose-hydrogel composite deposition and relative angles with respect to the print direction. The printed lines were allowed to dry at room temperature and was visualised under the microscope (as shown in Figure 5.11 (insert)). The printed lines were imaged using a microscope (Zeiss Imager M.2) at 10x magnification. Five micrographs were taken from various zones along the printed lines for each nozzle diameter such that the images were aligned with the print direction. These micrographs were then processed in image analysis software Fiji, a distribution of ImageJ (v1.51s) bundled with useful scientific plugins and was used to determine the alignment of cellulose fibres in the print. Directionality (creator: Jean-Yves Tinevez) plugin was used to determine the alignment of fibres in this study. A series of pre-processing steps were applied to the micrographs in order to improve the efficacy of image analysis. They are as follows:

- Converted the micrographs to 8-bit image (*i.e.* monochrome/grey scale image) to be compatible with the plugin
- Aligned the images with the print direction using rotate and/ transform functions

- Duplicated a region of interest (ROI) within an image followed by brightness and contrast adjustment. Sharpness and Window/level parameters of the image were also adjusted as necessary. These steps were carried out to enhance contrast-based pixel differentiation on which the image analysis software relies upon to generate results.
- Applied a bandpass filter of max 40 and min 3 pixels; this procedure digitally isolated and enhanced the features for better detection
- Analysed the ROI using Directionality plugin generating the alignment histogram and dominant direction of particulates.

These pre-processing steps were necessary to obtain the best contrast possible in order to generate accurate directionality results and did not introduce any digital artefacts in the image. The directionality of the fibres was determined by the plugin using a local gradient method (based on Sobel filter which is an (contrast based) edge detection algorithm). Analysis using the plugin yielded the following results: a directionality histogram with the highest peak fitted by a Gaussian function, aligned direction ( $^{\circ}$ ), the amount of aligned fibres in the principle direction within the range of its standard deviation (measured data as opposed to fitted), Dispersion ( $^{\circ}$ ) which denotes the standard deviation of the Gaussian fit and its goodness on a scale of 1= good, 0=bad. The averaged (across five different regions) directionality results for each of the nozzle diameters investigated are tabulated in Table 5.1 and the directionality histograms presented in Figure 5.12.

Table 5.1: Aligned direction of the cellulose fibres and the amount of alignment for different nozzle diameters

Nozzle diameter (mm)	Aligned direction ( $^{\circ}$ )	Amount (%)	Gaussian fit	
			Dispersion ( $^{\circ}$ )	Goodness
0.6	1.0	53	22.7	0.79
0.8	2.5	79	32.3	0.98
1.2	-0.7	76	29.2	0.99
1.6	-2.1	79	31.4	0.98

It can be seen that the cellulose fibres align in the direction of printing (nozzle translation) for all nozzle diameters ( $\pm 2.5^{\circ}$ ) due to the shear and extensional flow through the nozzle. Nozzle diameters of 0.8mm, 1.2 mm and 1.6 mm had relatively high amount of fibres (>75%) aligned in the print direction compared to the 0.6 mm nozzle (53%). This observation is contrary to what is reported in the literature as smaller nozzle sizes typically enhances the alignment due to the increased shear stress developed within the nozzle. However, the size of fibres relative to the nozzle diameter is key here as the 0.6 mm nozzle clogged up frequently during printing and is believed to have disrupted the extent of alignment. The other nozzle diameters

exhibited smooth extrusion and resulted in substantial alignment of the fibres in excess of 75% in the print direction. The implications of this shear induced anisotropy are significant. Aside from the strength and stiffness tailoring mediated by programmable print-paths, shear alignment of fibres will also dictate the strain differential upon swelling/shrinking which is crucial for stimuli responsive morphing. A bi or multi-layer configuration using different materials was employed to realise the strain differential within an architecture for the morphing examples reported in this project. However, the shear induced alignment of cellulose fibres enable programmability of strain differential within each layer without bi or multi-layer strategies through guided print paths thus enabling more functional hierarchical levels within a 3D printed architecture.

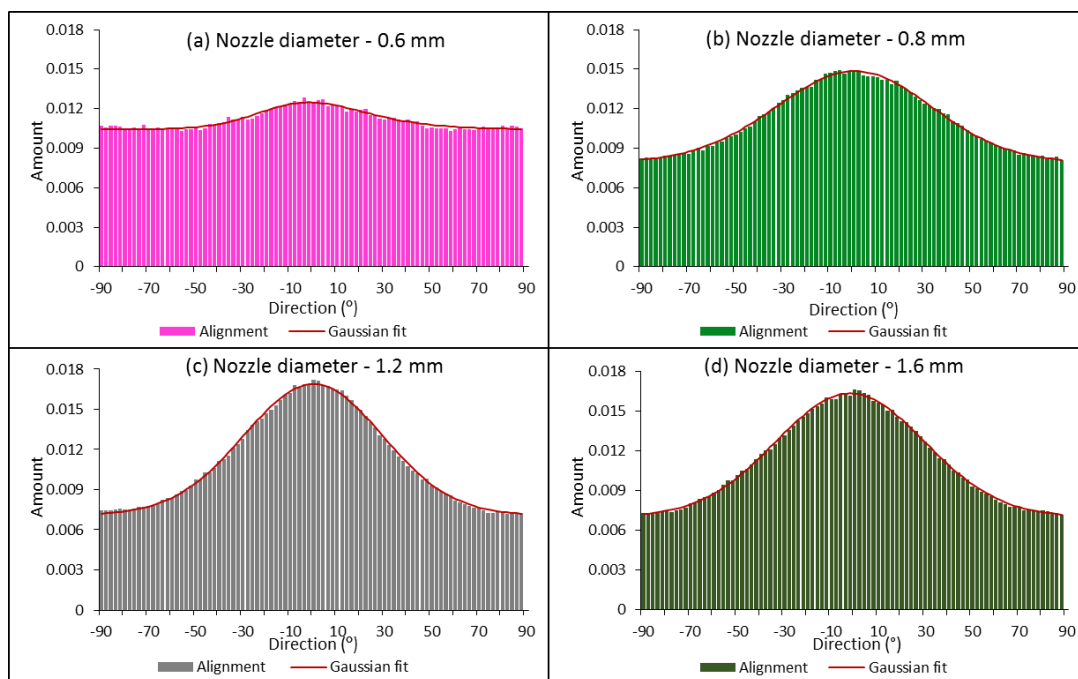


Figure 5.12: Directionality histograms for the various nozzle diameters investigated showing the dominant alignment direction and the relative amount.

#### 5.3.4 Mechanical characterisation of printed composites – Tensile testing

It is essential to characterise the key mechanical properties of the hydrogel composite material to better understand this novel system. The materials utilised in this material system undergoes distinct changes in its nature during the course of realising an architecture that can morph in response to stimuli. These distinct stages can be roughly classified as initial stage (raw materials in their pristine form), intermediate stage (after combining to form a well-dispersed shear thinning media) to enable 3D printing and the final stage where the material is dried and crosslinked after forming a shape. The physical and chemical properties of the composite at the intermediate and final stage are programmed to serve the purpose of

realising programmable morphing architectures. The (rheological) characterisation carried out in Chapter 4 only concerns the properties of this material system in its intermediate state *i.e.* facilitating extrusion. The properties of the material system especially that of hydrogel composite will vary significantly after 3D printing, drying and crosslinking. The shear alignment of fibres within the hydrogel composite during 3D printing itself will give rise to anisotropy in its properties whereas drying and subsequent crosslinking result in the removal of water and consequently an increasing solid like behaviour of the composite through consolidation. The printed composites effectively condense to form a solid composite with dry cellulose fibres as reinforcement embedded within dry carboxymethyl cellulose (CMC) polymer matrix. This final state of the material system was formulated to have 1:1 ratio of fibres and CMC polymer in order to optimise the benefits of both reinforcement and matrix. The following sections details the mechanical characterisation of printed composites (after drying and crosslinking). The main objective of this characterisation was to capture and validate the variation in material properties by virtue of the print-path (directions) within a composite.

#### 5.3.4.1 Test standards

Due to the novelty of material system developed in this project, there are no recognised testing standards that could be readily implemented to characterise the relevant mechanical properties. Therefore, a review of internationally recognised ASTM (American Society for Testing and Materials) standards pertaining paper-cardboard systems, polymers and composites was carried out to identify the key parameters relevant to the cellulose-hydrogel composites developed here. The primary motive to investigate testing standards relevant to paper industry was due to the cellulosic component in the developed system and the dependence of materials properties on water/humidity due to its responsiveness and ensuing indirect dependency on temperature. However, the lack of a suitable temperature and humidity-controlled testing chamber within the mechanical testing lab limited the material characterisation independent of humidity and temperature variables. This was mitigated by monitoring temperature and relative humidity during the course of mechanical testing in ambient conditions. The tests were also carried out as close together as possible to minimise the variation in ambient conditions. The material properties obtained should also be reported in relation to the temperature (T) and relative humidity (RH) during the course of testing. The stimuli responsiveness of the material system and its influence on material properties could not be captured in this manner, but it is a necessary compromise which had to be made.

The additive layer manufacturing of hydrogel composites as realised in this project draws parallels to that of polymers and the testing standards for characterising such 3D printed

polymers are in its premature state due to the infancy of this technology. The anisotropy in the additive manufacturing of otherwise isotropic polymer arises primarily due to the interface or microstructure realised within the 3D printed shape. Placing a line of molten polymer next to a solid line of polymer at a lower temperature results in discrete interface between the lines of laid-out polymers and influence the overall mechanical characteristics of the printed shape. Therefore, characterisation protocols concerning that of composite materials are more appropriate in order to quantify 3D printed polymers. Since there are no thermal gradients arising during the additive layer manufacturing of hydrogel composites, there is no such issue of weak interfaces. Furthermore, the material system was developed to have chemical homogeneity and the hydrogen bonds within the material ensure a coherent system devoid of weak interfaces. The anisotropy within the hydrogel composite is a function of shear alignment of fibres during the 3D printing process as opposed to weak interfaces arising from thermal gradients. Furthermore, the final state of the material system after printing, drying and crosslinking is quintessential composite and justifies using protocols pertaining composites to characterise them. As such a combination of test standards pertaining plastics and reinforced composites were adopted to obtain the relevant material properties. These specific standards are referred to in the following sections when used.

#### *5.3.4.2 Tensile testing of composite samples*

Tensile testing is a fundamental characterisation technique employed to obtain key material properties such as ultimate tensile strength, stiffness and elongation at break. Due to the limitations inherent to typical directional (anisotropic) composites, mechanical testing protocols for these materials calls for coupon testing as opposed to dog bone or dumbbell geometry of test samples as machining fibre reinforced plastics results in delamination and edge defects. However, one of the advantages of 3D printing is its flexibility in realising shapes and a dumbbell/dog bone geometry can be realised devoid of the aforementioned limitations affecting typical reinforced composites. This is however a more suitable and appropriate geometry for tensile testing as it ensures that the failure of test specimens could occur within the gauge length. Samples with the print direction along longitudinal and transverse directions of the dumbbell geometry will be investigated to obtain the mechanical properties in those directions. An additional sample set with a symmetric, cross-ply orientation will also be investigated.

#### *5.3.4.3 Sample details*

A dumbbell geometry adhering to ASTM D638 Type V was designed in CAD. The in-plane dimensions were then scaled up with an offset of 2mm to account for the shrinking during the

drying process. The printed dimensions of the samples are reported in Figure 5.13(top row). ASTM D638 pertains the mechanical characterisation of plastics and Type V sample dimensions are to be used when limited material is available and thickness of specimens are less than 4 mm. The thickness of the printed specimens was set to be 2 mm to mitigate the adverse deformations observed when 4 mm printed samples were naturally dried. With these considerations, the samples as shown in Figure 5.13 were 3D printed. The desired print path and stacking sequence for the samples were generated by adjusting the infill angle (0° and 90°) and layer thickness within the MatterControl software. Infill of 100% with a layer height of 0.5 mm was chosen and the CAD geometry was sliced using the embedded slicer (MatterSlice). The samples were sliced with zero perimeter so that only the directional infill print-paths contributing to the sample geometry. Owing to the novelty of the materials and shrinkage upon drying, a large number of samples (total - 16) were fabricated for each set for tensile testing. The samples were printed at the speed of 8 mm/s and material retraction as well as Z-lift was turned on to avoid the nozzle interacting with laid out layers during print operation. The print-paths, retraction and the Z-lift points were automatically generated by the slicer software based on the shape of dumbbell geometry. The generated print path for all the three sets of samples are presented in Figure 5.13(bottom row) along with their stacking sequence. Once printed, the samples were dried at room temperature underneath microscope slides to prevent warping. This was followed by crosslinking at 120 °C for 10 minutes.

It should be noted that the slicer software and embedded algorithms are optimised for 3D printing thermoplastics with the priority given to external finish than optimised infill print-paths. This is counterintuitive for 3D printing anisotropic materials such as the cellulose hydrogel composites as control over the print-path especially in the infill regions are essential to program principle strength and stiffness directions and desired responses to stimuli. Some untenable print moves and retractions believed to be influenced by the shape of the printed samples were observed in the generated G-codes which deposited small amount of material outside the sample profile in some cases. However, these minor incursions were removed with a sharp scissors after drying and crosslinking. Furthermore, the large sample size gives flexibility to mitigate the variation in samples during characterisation.

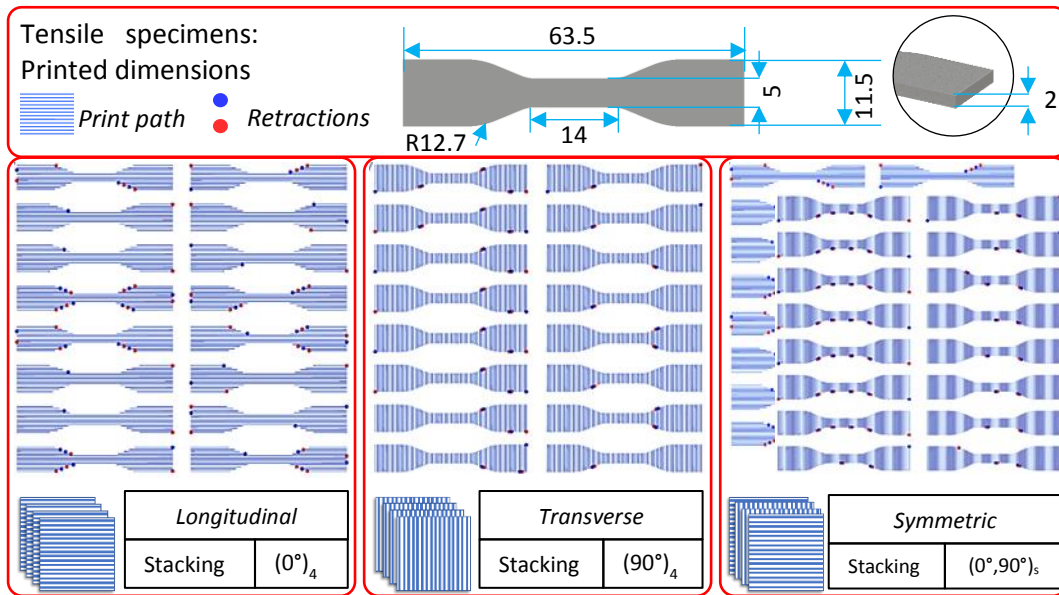


Figure 5.13: (top row) Test specimen dimensions as per ASTM D638 Type V (dimensions in mm). (bottom row) Print-path and stacking sequence of the samples fabricated for each set.

#### 5.3.4.4 Sample preparation

Once dried and crosslinked underneath microscope glass slides, the samples were carefully inspected and had the excess material outside the dumbbell profile trimmed off. Longitudinal samples were labelled from B1-B16, transverse samples from C1-C16 and symmetric cross-ply samples from 1-16 and is shown in Figure 5.14 before being tested. This ensures full traceability of each sample and its failure response when tested. Tracking points for digital image correlation (DIC) were marked 15 mm apart within the grip region encompassing the gauge region. Even though all samples were printed from the same CAD file to the exact dimensions, it can be seen from Figure 5.14 that the anisotropy in samples (due to directionality of printing process) resulted in different shrinking response in each of the sample sets. Samples were left adjacent to the test machine in the lab to condition overnight.

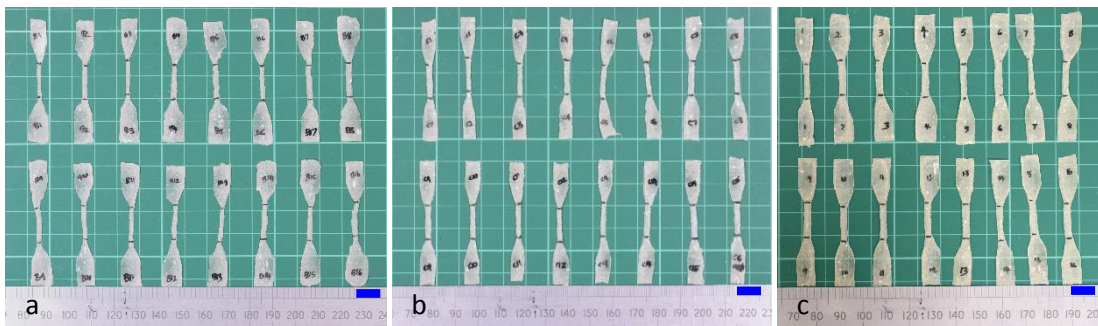


Figure 5.14: Samples before being tested to failure in tension. (a) Longitudinal orientation, (b) Transverse orientation and (c) Symmetric cross-ply orientation relative to print direction. (Scale bar= 10 mm).

#### 5.3.4.5 *Test details*

All samples were tested in tension until failure using a Shimadzu (AG-X) test rig and 1kN load cell. An extension rate of 1mm/minute was used for all tests. Each sample's thickness was measured using a micrometer at three points (top, middle and base) along the gauge region and averaged prior to testing. A similar approach was used to measure the gauge width of the samples but ImageJ (v1.51s) was used to measure the width. The gauge length of the specimens was also measured using ImageJ. Photographs shown in Figure 5.14 was used to obtain the dimensions. Due to the variation between the samples, it was deemed more appropriate to measure the length and width of the gauge region using image analysis. The photographs were taken on a calibrated sample stage (using Nikon D5500) and the optics (Nikon AF Micro (1:1) NIKKOR 60mm f/2.8D Lens) used had minimal distortion. The test machine grips were aligned prior to securing the samples to eliminate bending and out of plane testing. Temperature (T) and relative humidity (RH) were monitored using a sensor (Sensiron SHT2x) throughout the tests and the readings were taken at three instances during the course of each set. Due to uneven thickness and texture in the grip regions, samples had to be secured properly within the grips which resulted in some pre-load prior to the test. The loads and extensions were zero-ed before securing the samples in the grips in order to gauge the amount of pre-load each sample was subjected to prior testing. A deliberate attempt was made to minimise variation in pre-load on the samples. Pre-load in the region of 4-7 N was required at the grips to prevent samples from slipping during the test. The tensile tests were recorded (video) with a DSLR camera (Nikon D5500). Once the test had finished, raw data (namely force (N), extension (mm) and time (s)) from the test were exported for post processing. These procedures were kept the same for all three sets of longitudinal, transverse and symmetric cross-ply samples.

#### 5.3.4.6 *Data post-processing*

Validation and calculation procedures outlined in ASTM D3039 were used to process raw data from the test. ASTM D3039 covers the determination of in-plane tensile properties of reinforced polymer matrix composites and thus more suited to the cellulose hydrogel composites tested here. Raw test data comprising load (N), extension (mm) and time (s) were used to generate corresponding stress (MPa) and strain values for each data sets in Microsoft Excel using the following equations (5.1 and 5.2). The failure mode and slipping at the grips were used as the key parameters for validating the test data. Therefore, samples that failed outside the gauge region was discarded from being used for the calculation of ultimate



properties. Samples that had excessive slippage (as evidenced in the test specimen's force-stroke plot) were also discarded.

$$\sigma_i = F_i / A \quad (5.1)$$

$$\varepsilon_i = \delta_i / L_g \quad (5.2)$$

where:  $\sigma_i$  = tensile stress at  $i^{\text{th}}$  data point (MPa),  $F_i$  = force at  $i^{\text{th}}$  data point (N),  $A$  = cross-sectional area of the gauge region ( $\text{mm}^2$ ),  $\varepsilon_i$  = strain at  $i^{\text{th}}$  data point,  $\delta_i$  = extension at  $i^{\text{th}}$  data point (mm),  $L_g$  = gauge length (mm)

The stress and strain data thus generated was used to plot the stress-strain plot for each sample and the tensile chord modulus within the recommended strain range was calculated according to the test standard as follows:

$$E^{\text{chord}} = \Delta\sigma / \Delta\varepsilon \quad (5.3)$$

where:  $E^{\text{chord}}$  = tensile chord modulus of elasticity (GPa),  $\Delta\sigma$  = difference in applied tensile stress between two strain points (MPa) and  $\Delta\varepsilon$  = difference between the corresponding strain points. ASTM standard D3039 suggests these strain points to be close to 0.001 and 0.003 provided no transition region occurs within this range in the stress-strain plot. However, some samples had minor slippage within this range, consequently the range was varied for such samples to exclude such transition regions. The strain range taken for chord modulus was always kept to the lower-half of the stress-strain plot as per the test standard guidelines with the difference in strain ( $\Delta\varepsilon$ ) being close to 0.002.

The ultimate tensile strength ( $F^{\text{tu}}$ ) was calculated according to equation (5.4). The strain at failure ( $\varepsilon_{\text{fail}}$ ) was obtained from the analysis of test video using DIC software (Video gauge from imetrum). The time of sample failure from the video file and synchronously the time point of ultimate tensile strength was used to obtain the strain at failure from the DIC results.

$$F^{\text{tu}} = P^{\text{max}} / A \quad (5.4)$$

where:  $F^{\text{tu}}$  = ultimate tensile strength (MPa),  $P^{\text{max}}$  = maximum force before failure (N) and  $A$  = cross-sectional area of the gauge region ( $\text{mm}^2$ )

The statistical analysis of the test data were carried out as per test standard guidelines and the sample mean ( $\bar{x}$ ), standard deviation ( $S_{n-1}$ ) and coefficient of variation (CV, %) were obtained and reported in Table 5.2.

## 5.3.4.7 Results

Table 5.2 summaries the ultimate material properties obtained from the tensile testing of cellulosic composite samples in longitudinal, transverse and symmetric cross-ply configurations. The mean, median, standard deviation ( $S_{n-1}$ ) and coefficient of variation (CV) are reported. Even though ASTM standard D3039 does not call for median values, it is reported to show actual test result than average value across the population. Poisson's ratio was not derived because no transverse strain measurements could be made during the test. The relative humidity and temperature during the course of testing is also reported in Table 5.2 for each configuration. Therefore, the ultimate material properties reported here are to be taken in consideration with the relative humidity and temperature measured during the tensile test. Only the samples that adhered to the validation criteria was used in the calculation of the ultimate properties reported. The samples that did not meet the criteria are highlighted in Figure 5.15.

Table 5.2: Tensile testing results

Sample set	Properties	Mean	Median	$S_{n-1}$	CV (%)
<i>Longitudinal</i>	$E^{\text{chord}}$ (GPa)	1.531	1.518	0.2	13.2
	$F^{\text{tu}}$ (MPa)	29.22	27.15	4.76	16.3
	$\epsilon_{\text{fail}}$	0.011	0.011	0.004	36.5
	RH (%)	36.72	37.25	2.67	7.3
	T (°C)	21.54	21.70	0.79	3.7
<i>Transverse</i>	$E^{\text{chord}}$ (GPa)	0.904	0.923	0.140	15.4
	$F^{\text{tu}}$ (MPa)	14.22	14.69	2.65	18.7
	$\epsilon_{\text{fail}}$	0.008	0.007	0.002	26.2
	RH (%)	33.68	33.87	0.72	2.1
	T (°C)	22.32	22.33	0.03	0.1
<i>Symmetric Cross-ply</i>	$E^{\text{chord}}$ (GPa)	1.561	1.559	0.202	12.9
	$F^{\text{tu}}$ (MPa)	26.18	26.73	2.72	10.4
	$\epsilon_{\text{fail}}$	0.008	0.008	0.002	29.2
	RH (%)	33.39	33.65	0.47	1.4
	T (°C)	20.99	20.86	0.24	1.1

As expected, the transverse configuration where the print path and fibres are orthogonal to the loading direction has the lowest of modulus (0.904 GPa), when compared to the other configurations. Symmetric cross-ply samples had the highest chord modulus (1.561 GPa) despite having lower amount reinforcements aligned in the loading direction compared to longitudinal samples; the longitudinal samples were not far behind in its chord modulus (1.531 GPa). The RH measurements taken during the test could perhaps give an insight into this difference. RH measured during the testing of longitudinal and symmetric cross-ply samples were at 36.72 % and 33.39 % respectively. Since these cellulosic composites are hygroscopic, it is possible that the increased moisture content had influenced the results. As water and moisture absorption has a softening effect on the material, the longitudinal samples were believed to be influenced by this effect albeit having more fibres aligned in the loading direction. The strain at failure ( $\epsilon_{fail}$ ) is also greater (0.011 compared to 0.008) for longitudinal samples as the consequence of this moisture induced softening is increased ductile behaviour. However, the strain at failure results has to be considered with caution as the coefficient of variation is relatively high across all sample sets. This is believed to be due to video gauge strain measurement being too noisy. The chord modulus is free from the aforementioned strain noise as the chords were taken from regions devoid of slippage in the stress-strain plot from test machine raw data. The ultimate tensile strength was the highest for longitudinal (29.22 MPa) samples followed by symmetric cross-ply (26.18 MPa) and transverse (14.22 MPa) sets as the longitudinal samples have most layers oriented in the direction of loading capable of supporting the applied load.

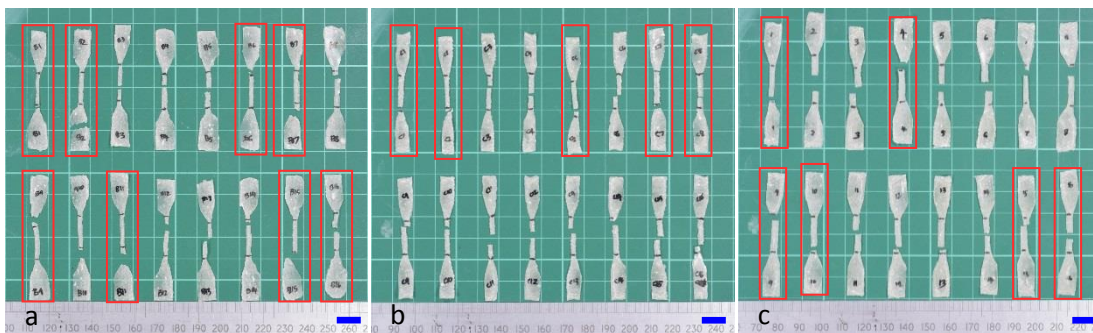


Figure 5.15: Samples after testing to failure in tension. (a) Longitudinal orientation, (b) Transverse orientation and (c) Symmetric cross-ply orientation relative to print direction. Highlighted are the discarded samples as they failed to meet the validation criteria. (Scale bar = 10 mm).

Figure 5.15 also demonstrates the failure mode of each samples as well. The longitudinal sample set had the greatest number of samples failing outside of validation criteria (50%) whereas transverse and symmetric cross-ply sets had failures of 31 % and 38 % respectively. The translucent sections in the grip regions are indicative of sample irregularities arising due to drying underneath glass slides, where the glass shears the material underneath possibly

due to extra material deposited owing to G-code anomalies. Another source of sample irregularity is the anisotropic shrinking by virtue of directionality of the print paths. Regardless of the samples being printed from the same CAD file with same dimensions, the final dried and crosslinked shape is not the same across the sets. This however cannot be alleviated as it is inherent to the material system under investigation.

#### 5.4 Shape transformations

This section reports the investigation into realising some morphing architectures as envisaged in this study *i.e.* combining origami principles and cellulose 3D printing. Since the feasibility of fabricating conventional folded architectures were demonstrated in Section 5.2.6 *4D printing of cellulosic composites*, forms that actuate in the thickness direction (pop-up) were designed and investigated here. Furthermore, there is a lack of morphing examples in the open literature that actuate in this manner. These pop-up morphing architectures are selected as they demonstrate the embodiment of origami principles and stimuli responsive morphing. It must be emphasised that a wide variety 2D to 3D morphing architectures could potentially be realised using this strategy and material system and are only limited by the designers' creativity. The architectures were realised in CAD based on the understanding of self-folding responses and design guidelines presented in the previous chapters. As mentioned previously in 5.2.5 *Print results*, the current set-up realised in this project lacks integrated multi-material capability within the hardware and firmware due to the shortage of additional on-board stepper control ports. Therefore, the architectures were designed in CAD as separate parts for the substrate and fold lines respectively and treated as two separate print jobs. For example, the substrate part was printed first with the extruder laden with the desired material. Once completed, the extruder piston was wound back through G-code commands to release the syringe and loaded with the syringe containing second material. The nozzle and tube were purged with second material and the fold lines were printed with a z-offset matching the z-height (thickness) of first part. This methodology relies on the firmware centering the prints on the print-bed each time. Albeit not ideal, this strategy enabled inter-layer multi-material printing and thus resulted in localised strain gradient regions required for morphing response as designed. The architectures were printed on to the print-bed heated to 35 °C. This was chosen arbitrarily and to speed up the drying process. Once printed, the designs were left to dry at room temperature (24 °C) before crosslinking.

### 5.4.1 Connected concentric annuli

This architecture was designed based on curved crease origami but also takes advantage of the geometric constraints in guiding the overall shape transformation. A connected concentric annuli architecture was designed in CAD and 3D printed from Composite+Clay+CA as the substrate material and Gel+CA defining the fold lines (Figure 5.16). The CAD is shown in Figure 5.16a with the blue indicating fold lines. The curved fold lines are continuous in this architecture. The composite substrate elements connecting the annular rings are designed to guide the saddle formation. Figure 5.16b shows the architecture after drying and crosslinking; the waviness observed around the periphery of the rings are edge-effects as drying initiates from the edges. Figure 5.16c and d show the morphing response when submerged in a water bath. As envisaged, the connecting elements guides the morphing response. The middle annular ring is over constrained by the connecting elements from the outer and inner annuli and does not morph out of plane despite the presence of a central circular curve. This however, enables the innermost annulus to morph to an extent as seen in Figure 5.16c when submerged in water bath. The top view of the actuated architecture is presented in Figure 5.16d. It can be seen that once submerged, the architecture was devoid of the waviness around the periphery as seen in Figure 5.16b and confirms that they are not permanent in nature.

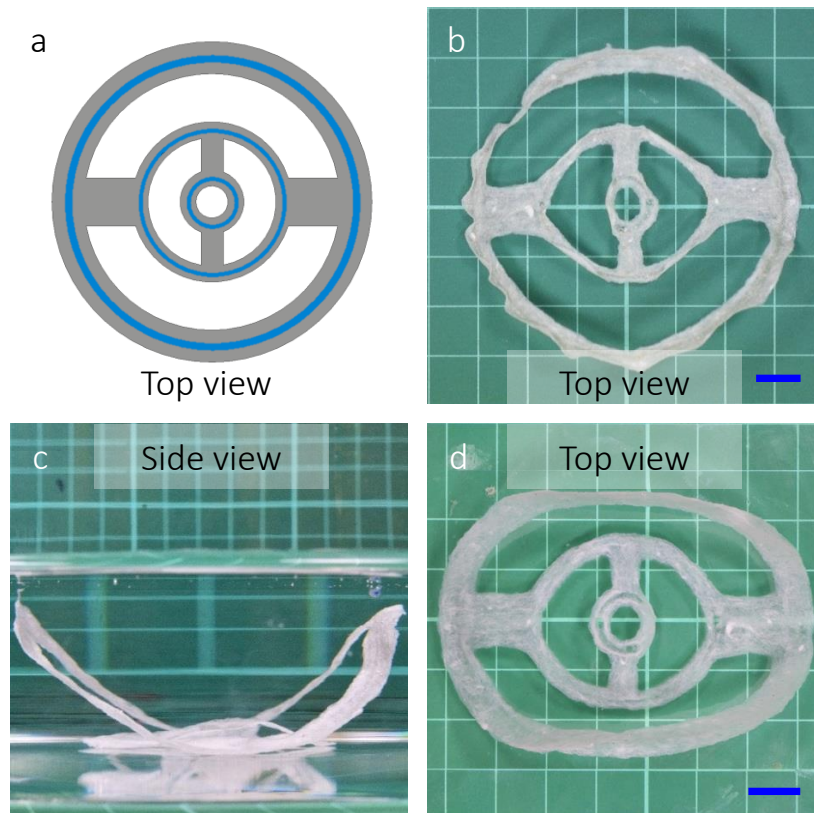


Figure 5.16: Connected concentric annuli. (a) CAD with blue lines indicating curved fold line. (b) 3D printed architecture after drying and crosslinking. Morphing response when submerged in water (c) Side view and (d) Top view. (Scale bar = 10 mm).

### 5.4.2 Connected annulus-coil

This architecture is also based on curved crease origami but incorporates valley folds in a coil pattern following the substrate underneath. Figure 5.17a shows the architecture as designed in CAD. It was designed to enable the coil shape to morph upwards in a similar fashion to that of a spiral staircase with the annular rings providing a stable but morphed (through geometry frustrations arising from curved fold line) base. Unlike the concentric connected annuli shape in Figure 5.16, this design incorporates discontinuous fold lines to fold the spirals. Figure 5.17b shows the slicer generated print path of the fold lines overlaid on the substrate geometry with the green lines indicating 'non-extruding' print moves and the blue lines indicating extruding moves. It can be seen that a substantial amount of print-head pass-overs occur over the coiled section of the substrate. Figure 5.17c shows the shape after drying and crosslinking. Similar to connected annuli architecture, waviness originating from the edge-wise drying is evident in this architecture as well. However, the distortion observed in some folding elements in the spiral component was not programmed and thus undesirable. This was caused by the material oozing out of the nozzle during the 'non-extruding' print moves (stringing) due to the inherent limitation (lack of flow control at the nozzle) of the extruder designed in this study. This resulted in Gel+CA lines to be laid on the substrate as the print-head moved around to deposit valley-fold lines.

The morphing response of the architecture when immersed in water is shown in Figure 5.17d and e. It can be seen the coil did pop up in the thickness direction albeit not to the extent or shape envisaged. This is due to the non-programmed deposition of Gel+CA material during 'non-extruding' print moves affecting the overall morphing response. As reported previously in Section 5.2.5 *Print results*, the material flow-control is further away from the point of deposition, and the attempts to retract the syringe plunger to stop the flow for non-extruding' print moves were not as effective as a result. Even though morphing response was achieved, the new fold lines and thus the morphing pathways created in this manner are detrimental to the programmability of the material system and is a serious limitation of the extruder developed in this project. This limitation and the suggested solutions to mitigate the lack of finer flow control are reported in Future work, Section 6.2.3 *Extruder upgrades for reliable and integrated multi-material printing*.

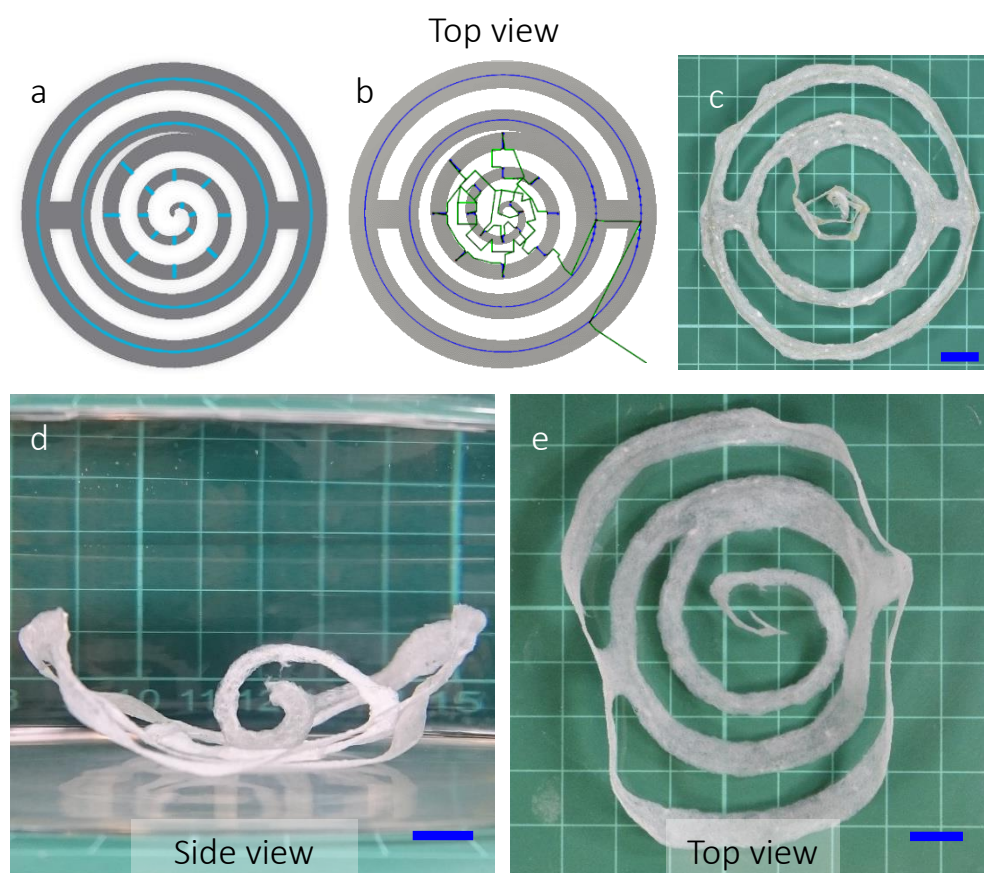


Figure 5.17: Connected annulus-coil. (a) CAD with blue indicating fold lines. (b) Slicer generated print path for the fold lines (dark blue - extruding moves; green - non-extruding moves) (c) 3D printed architecture after drying and crosslinking. Morphing response when submerged in water (d) Side view and (e) Top view. (Scale bar = 10 mm).

## 5.5 Discussion

This chapter demonstrated the feasibility of 3D printing utilising the developed material formulations, reported the characterisation of mechanical properties and showcased the shape transformations of 3D printed architectures in the time domain (4D). The custom work carried out in developing and adapting a paste extruder to an opensource 3D printer to enable 3D printing of the formulations were also reported. This was essential to the fabrication of cellulosic architectures with programmed morphing pathways (fold lines). The strategy of drying and crosslinking of the printed formulations resulted in the formation of relatively high volume fraction ( $V_f = 50\%$ ) composites capable of morphing compared to other approaches.

The microscopy and contact angle studies revealed that the printed composite substrates displayed the critical features of paper such as network structure and responsiveness to hydration whilst providing the ability to easily modify these parameters. Unlike the radial propagation of water droplets in paper microstructure, the constituents and its arrangements in the developed material formulations demonstrated localised hydration effects during the

contact angle analysis. This feature could potentially be utilised in the creation of morphing architectures with dedicated hydration channels for complex morphing responses. The inter-fibre spaces are occupied by the hygroscopic CMC polymer matrix in printed composites and was proven to effectively stabilise the substrates during hydration and minimise wrinkling and twisting observed with the paper architectures. The significance of this stabilising matrix in shape recovery was also evident in the actuation of composite morphing flower architecture. The shear induced alignment of pulp fibres along the print path was also established and quantified. As such, the work presented here clearly demonstrate that the limitations of paper such as lack of programmable microstructure and stabilising matrix, controlled flow propagation and wrinkling effects of hornification had been alleviated by developing this novel cellulosic material system.

The tensile testing of the printed composites confirmed the influence of fibre alignment along the print path in determining the structural properties. This strength tailoring along with graded microstructures enabled by additive manufacturing will have a compound effect in fabricating complex morphing architectures. The effect of fibre alignment in controlling the strain was also observed as the equilibrium shapes of three sets of tensile samples were different despite being printed to the same dimensions. The gel formulations used to define fold lines were not subjected to mechanical characterisation like Composite+Clay+CA formulation because of the difficulties in preserving the 3D printed test geometry during drying. This is justified as they are not envisaged as the strength bearing elements and used locally in a morphing architecture to supply the actuation force. The mechanical properties of the composite are not compared to other materials mainly due to the inadequacies of the test strategy such as lack of unified test protocols, environmental chamber and suitable load cell for testing. A 1kN load cell was used for the tensile tests but the results indicated specimen failure at loads less than 5-7% of the load cell limit indicating that a 100N load cell would be the ideal load cell choice.

The shape transformation examples presented demonstrate the programmable actuation of the architectures realised from CAD. The pop-up actuations in particular showcase the ease with which the principles of origami and kirigami can be combined to realise stimuli responsive morphing architectures as envisaged in this project. Minor waviness (albeit temporary) as edge-effects were observed on annular rings in the pop-up architectures as drying initiates from the edges. This issue was observed predominantly for thin and narrow sections such as the annular ring and can be mitigated by carrying out the printing process in a heated enclosure to promote even drying from the surfaces. Even though morphing architectures had



been successfully fabricated, the 3D printing as realised in this project leaves a lot to be desired. Firstly, greater control of the material flow at the nozzle end is crucial for precise placement of materials and the current implementation utilised in this project was shown to be inadequate for discontinuous fold lines where excessive non-extruding print-head pass-overs occur. Although continuous fold lines and architectures without complex print manoeuvres were realised as desired, the current implementation of the extruder is a serious limitation. Secondly, the 3D printing process is currently optimised for preserving the exterior features of CAD and have limited options to tune the print-paths (specifically the in-fill) in the slicer software. As the field of 4D printing matures, this aspect is expected to be addressed and greater control over the print-paths especially for the inside of a structure could be realised with ease.

---

## Chapter 6 Conclusions and Future work

---

### 6.1 Conclusions

The main objective of this research was to develop a bio-inspired smart material system capable of morphing. An introduction to as well as the significance of the research carried out in this project and its place in the wider landscape of morphing smart materials were presented in Chapter 1. Typically, biological functions or features serve as inspiration for synthetic analogues. However, this research goes beyond just the functionality and seeks inspiration from nature in its sustainable approach, use of benign materials and the way they are combined to realise forms. The chapter-specific summaries and conclusions are reported at the end of each chapter. The key findings from the experimental chapters are as follows.

Cellulose and its potential as an ecological and cost-effective programmable smart material was explored and validated in Chapter 2 where several programmable parameters were identified pertaining to the actuation of manually folded paper architectures in response to the stimulus of hydration. Whilst these material and stimuli parameters could be effectively controlled to govern the actuation response of the paper architectures, the inevitable permanent physical changes in fibres due to cyclic wetting and drying (hornification) are undesirable for the repeatability of actuation responses. Therefore, the strategy of incorporating a compliant matrix which can potentially lessen the hornification effects in fibres was devised and implemented for the development of cellulose-hydrogel composite. This strategy could also aid in stabilising the substrate during multiple actuation cycles. Here, the significance of a fibrous architecture and grammage as programmable features in controlling the speed of actuation was established. Hornification effects and lighter paper substrates permit greater access for the water to occupy inter fibre spaces and permeate them to release the stored strain energy of folding. Even though switchable deployment arrest was achieved through grafting PNIPAAm polymer on cellulose substrate, immediate reversal of deployment was not possible. Since hydration and de-hydration are diffusion-dominated processes advancing along the water concentration gradients, the speed of actuation especially that of fold recovery will depend on the factors affecting the water concentration gradients and diffusion. In this context, the thermoresponsive functionalisation of cellulose can be adopted to promote faster drying rates once outside of the influence of stimuli than to achieve immediate reversal of deployment in the presence of activating stimuli.

Whilst Chapter 2 detailed the characterisation of the actuation parameters of manually folded paper architectures, Chapter 3 presented the work carried out to realise 3D architectures from

2D paper substrates through programmed self-folding in the time domain (4D). Dehydration and hydration mediated volumetric changes in hydrogels were harnessed to generate localised strain gradients within the global paper substrate to generate self-folding 3D forms. Efficacy of this simplified approach was demonstrated by fabricating some common morphing architectures (such as spirals and flower architectures) realised in open literature for comparison. The design rules for self-actuating origami folds as well as the factors affecting the creation of such folds were also identified. Even though adequate in its ability to realise 2D to 3D forms, dehydration mediated morphing responses are considerably slower than that of action potential and phase transition mediated responses. This is primarily due to drying being a slow diffusion based process proceeding along the water concentration gradients between the hydrophilic gel and its environment at room temperature and atmospheric pressure. Therefore, new strategies are required to improve the response speed in dehydration mediated morphing.

The development of a novel material system for the 4D printing carried out in Chapter 4 was based on the results obtained from the preceding chapters where reliable programmable substrates and a greater control of realising localised strain gradients were identified as key parameters towards programmable cellulosic morphing architectures. Hence, this chapter elucidated the work carried out in integrating cellulose into the domain of 3D printing materials as additive manufacturing was identified as a powerful means to create intricate forms through programmed and controlled arrangement of materials in 3D space akin to growth in natural systems. The materials development to exhibit ideal flow characteristics for paste extrusion based 3D printing, a formulation based approach (programmable materials) to control the swelling characteristics and the force generated by the materials in response to hydration were also attained. The dispersion of pulp fibres in a hydrogel matrix was the challenging and crucial part of this study as composite formation was imperative for the integration of cellulose into the domain of additive manufacturing without limiting its stimuli responsive properties. The synergy of pulp fibres dispersed in a CMC matrix resulted in stable substrates minimising the hornification effects during cyclic actuation. Whilst the extent of strain differential (shrinking ratio) that could be generated through dehydration is limited by the water content in as-prepared formulations, the strain gradients achieved through hydration can be varied by modifying the crosslinking agent in the formulations. Through adept design, the extended range of volumetric changes achievable in hydration phase could potentially be employed to access new configurations with respect to time.

Chapter 5 reports the 3D printing of cellulosic material systems developed in the previous chapter, mechanical characterisation and its potential to realise programmable transformations. The shear alignment of pulp fibres during printing and the resulting anisotropy in mechanical properties were characterised. This chapter demonstrated the 4D printing of cellulosic architectures that actuate along the fold lines realised by adhering to the origami and kirigami principles. The superiority of this morphing system to that of the actuation responses exhibited by the folded paper architectures are evident. Incorporating cellulosic fibres within a cellulose derived matrix resulted in numerous advantageous: coherent interfaces supported by hydrogen bonds and esterification and stable response to hydration and dehydration are a few. The composite construction of the constituents and 3D printing enabled control over substrate microstructure without compromising the flow characteristics of the activating stimuli as observed in Section 2.6 *Multi-layered composite paper systems*. Furthermore, the strategy of printing a hydrogel composite followed by drying and crosslinking permits high  $V_f$  structures with relative ease. The ability to integrate both the substrate and strain gradient regions in digital designs and realise them through additive manufacturing enhances the capability of this approach to create morphing architectures compared to other approaches such as ionoprinting or photolithography patterning. The speed of actuation especially in dehydration initiated responses have been discussed previously. The structures can be designed in CAD so as to maximise the surface area exposed to the surrounding environment to facilitate greater diffusion of water in and out of the material. Grading the structure by optimising the infill properties prior to printing is one way to promote porosity in structures and thereby increasing the surface area exposed to the environment. The resolution of such fine details and the ability to fabricate complex morphing architectures are reliant on ensuring greater control of material flow in the extrusion system.

It can be concluded that the project has indeed achieved its objectives of realising programmable morphing architectures by harnessing the potential of cellulose as a cost-effective and sustainable smart material. The bio-inspired approach of generating localised strain gradients to generate 3D forms, the formulations utilised in the material system and the additive manufacturing process bringing together digitised design and programmability for manufacturing are in agreement with the philosophy of morphogenesis manufacturing as envisaged. The ability to generate localised strain gradients within a global substrate is the key to achieving the morphing responses realised in this study. As such, this methodology and design guidelines are not strictly limited to cellulosic substrates but can also be applied to other compliant substrates capable of supporting localised strain gradients.

## 6.2 Suggestions for future work

Albeit demonstrating its potential, the understanding of material behaviour within this system is not yet adequate or even comparable to the likes of shape memory materials (polymers and alloys) widely employed in morphing application. Therefore, the next phase in the research should focus on raw material optimisation and further understanding of the material responses. Developments to current 3D printing software and hardware could immensely improve the 4D printing process and result in morphing architectures beyond the levels of complexity explored in this study. The limitations presented by the lack of control in selectively varying the 'infill regions' in the slicer software were previously discussed. This is primarily due to additive manufacturing as it exists today prioritising the external features over internal which is understandable for static 3D printed shapes. However, for 4D printing control of internal architecture is key for programmability and should be given adequate priority as the technology matures. As for future work more closely tied to the work carried out in this project, optimising the materials and 3D printing process, especially multi-material 3D printing are reasoned to generate the most significant of improvements. These suggestions for future work are considered in the following sections.

### 6.2.1 Improved material strategies

The materials used in this project were often aimed for other purposes than to be used as a smart material in 4D printing. For instance, improvements in the quality of raw materials such as pulp fibres and clay such that they are developed specifically for the purpose of smart applications will immediately enhance the system presented in this study. The limiting step in the preparation of hydrogel composite is the dispersion of pulp fibres in the hydrogel matrix which was mitigated by using a non-contact planetary shear mixer. Only up to 350 g of the material could be prepared at once due to the volumetric limitations of the mixer. The non-contact shear mixer is also a significant financial investment worth £5000-£6000 which may not be feasible for some research labs despite the other elements in this project costing significantly less. Perhaps, it is wise to balance these limitations by incorporating composite preparation with the process of pulping which usually is a large-scale process compared to mixing 400 g of materials in a non-contact shear mixer. Furthermore, the process of pulping also relies on shear forces to separate the cellulosic fibres, therefore it is desirable to have the process of composite preparation as an auxiliary operation to existing pulping facilities for large scale operation. This would ensure quality control of the fibres and offset the cost of the shear mixer albeit resulting in an increase in the cost of raw materials. It is envisaged that separating materials development from the fabrication of architectures will also aid in the

faster adoption of the morphing material systems presented here. Incorporation of functionalised reinforcements or matrix could further the potential of the system developed here by adding intermediate or hidden shape configurations that could be selectively accessed. Functionalising pulp fibres with thermoresponsive polymer similar to the work presented in Chapter 2 (*2.7 Reversible deployment through functionalisation*) would be a good starting point to explore this further.

### 6.2.2 Sequential actuation

The ability to program sequential actuation of the active regions are crucial in realising more complex morphing architectures. Even though not directly explored in this project, several inherent options to program sequential actuation to a uniform stimulus are available. Varying the amount of crosslinking agent or by varying the  $V_f$  in composites to create new formulations should achieve this. The swelling behaviour (ESR) was shown be dependent on the extent of crosslinking. Locally varying the microstructure (graded microstructures) with composite formulations by controlling the infill amounts is yet another way to impart time-dependant swelling behaviour at the fold regions. Multi-material printing and greater control over the internal structure during 3D printing is vital to realising sequential actuation.

### 6.2.3 Extruder upgrades for reliable and integrated multi-material printing

The main limitation of the 3D printing set-up as devised in the project was the lack of integrated multi-material printing and lack of finer flow control due to the absence of multiple stepper motor ports at the RAMPS 1.3a printer motherboard. The multi-material printing achieved in this project relied on switching between the syringes and printing over an existing material thus essentially limiting it to inter-layer than intra-layer. Using a 3D printer inherently supporting multi-material printing or using stepper expansion boards (as available for the Prusa MK2S used in this project) should permit this as the open-source software packages for controlling the printers already have the provisions to support multi-material extrusion.

The main drawback of the off-axis direct driven extruder adopted here was the lack of finer control of material deposition through retraction. As the pressure to cause flow of the materials is further away from the nozzle, any level of retraction assigned to the paste extruder motor did not prevent the material oozing out of the nozzle during non-extruding print-head manoeuvres. Consequently, this resulted in inaccurate material deposition at times, especially for more complex architectures. FFF printers where the push/pull on the polymer filament is controlled closer to the nozzle are also prone to this issue known as stringing, albeit not as severe. Having a smaller and less powerful motor driving a screw extruder just above the

nozzle can easily mitigate this issue by enabling control of material flow very close to the nozzle. Thus, the ability of the printer motherboard to drive multiple motors is also key to achieving finer control. Furthermore, the smallest layer height (resolution) achieved with the current set-up was close to 0.5 mm despite the electronics (theoretically) being capable of supporting layer heights from 0.05 mm onwards. The next iteration of the extruder should incorporate inherent multi-material printing as well as finer control of material deposition. This was broadly explored as a concept during the development of the paste extruder. Figure 6.1 shows the schematic of this recommended set-up. In this set-up, the off-axis syringe extruder (as realised in the current printing system) will do the majority of work in moving the material towards the inlets on the print-head whilst the smaller motor (Figure 6.1b) mounted on the print-head assembly driving the extruder screw provides finer deposition control and efficient retraction (Figure 6.1c).

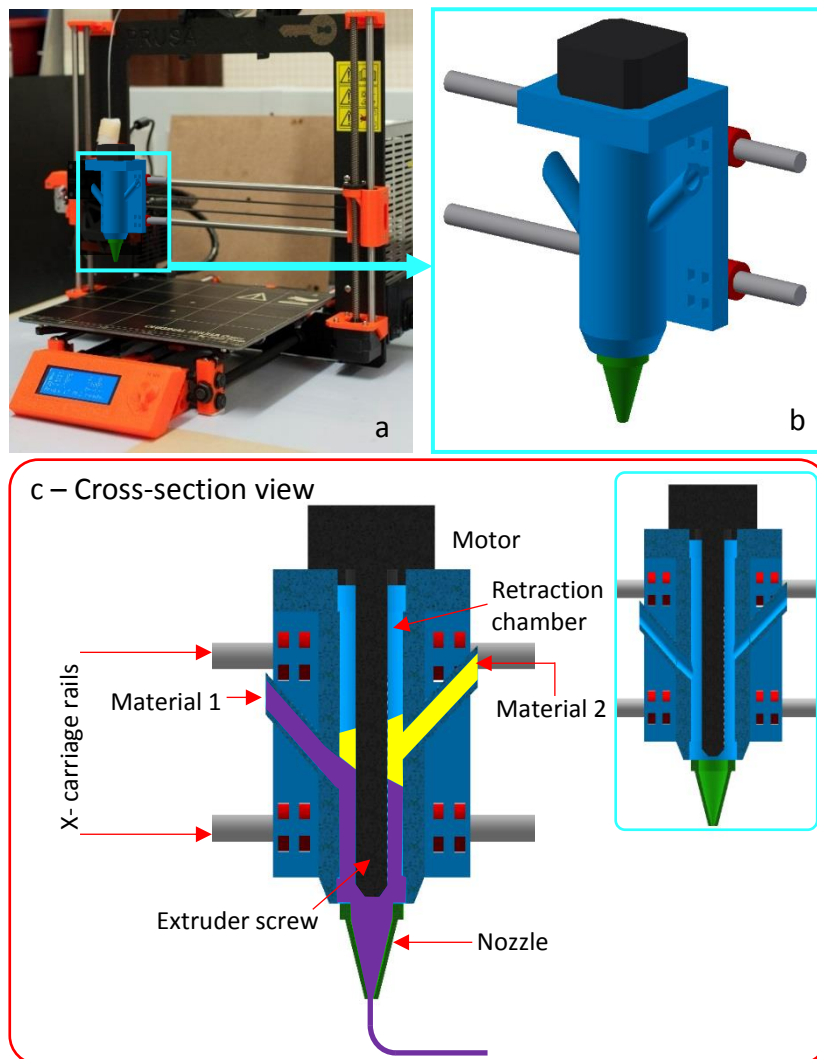


Figure 6.1: Schematic of suggested multi-material paste extrusion set-up with finer deposition. (a) Visualisation of the print-head with Prusa MK2S (b) close-up view of the print-head housing motor and deposition nozzle (c) cross-section view of the print-head showing the extruder chamber during multi-material printing with an empty chamber shown in insert.

#### 6.2.4 Structures with increased complexity in form and actuation response

Fabrication of complex architectures presents another area of scope to further this project. For example, the complexity of origami and kirigami shapes currently realised in paper and also in engineering are far superior to the basic shapes explored here in this study. Increasing the complexity of a morphing shape or its actuation pathways through localised programming was increasingly inhibited by the challenges explained earlier. Aforementioned works regarding improved materials and multi-material printing should mitigate the challenges inhibiting the realisation of such complex architectures. Investigating increasingly complex architectures is crucial to establish the limitations of the design landscape and thus formulate specific application scenarios utilising this material system. For example, the unique properties of meta-materials are attributed to their arrangements and overall geometry. Investigating stimuli responsive complex morphing architectures could result in on-demand meta-properties mediated through stimuli.

This work has provided the fundamentals of realising programmable morphing responses from sustainable cellulosic architectures through 4D printing. The experimental results and fabricated morphing structures demonstrate the potential to create complex morphing architectures capable of sequential multi-stage deployment. Furthermore, architectures where intermediate configurations which could be selectively activated can also be achieved by taking advantage of shear alignment of fibres and specific actuation pathways within a global architecture through additive manufacturing techniques.



---

## References

- [1] Erb RM, Sander JS, Grisch R, Studart AR. Self-shaping composites with programmable bioinspired microstructures. *Nature Communications* 2013;4:1712. doi:10.1038/ncomms2666.
- [2] Elbaum R, Zaltzman L, Burgert I, Fratzl P. The role of wheat awns in the seed dispersal unit. *Science (New York, NY)* 2007;316:884–6. doi:10.1126/science.1140097.
- [3] Peraza-Hernandez EA, Hartl DJ, Malak Jr RJ, Lagoudas DC. Origami-inspired active structures: a synthesis and review. *Smart Materials and Structures* 2014;23:094001. doi:10.1088/0964-1726/23/9/094001.
- [4] Giesecke K. *Deployable Structures Inspired by the Origami Art*. Massachusetts Institute of Technology, 2004.
- [5] Saito K, Agnese F, Scarpa F. A Cellular Kirigami Morphing Wingbox Concept. *Journal of Intelligent Material Systems and Structures* 2011;22:935–44. doi:10.1177/1045389X11416030.
- [6] Lang RJ. *Tree Maker* 2004. <http://www.langorigami.com/article/treemaker> (accessed April 2, 2017).
- [7] Tachi T. *Freeform Origami* 2010. [www.tsg.ne.jp/TT/software/](http://www.tsg.ne.jp/TT/software/) (accessed May 17, 2017).
- [8] Tachi T. *Origamizer* 2008. [www.tsg.ne.jp/TT/software/](http://www.tsg.ne.jp/TT/software/) (accessed April 2, 2017).
- [9] Tachi T. *Rigid Origami Simulator* 2007. [www.tsg.ne.jp/TT/software/](http://www.tsg.ne.jp/TT/software/) (accessed May 17, 2017).
- [10] Scott JL, Unali G. Chemicals from Biomass. In: Letcher TM, Scott JL, editors. *Materials for a Sustainable Future*, The Royal Society of Chemistry; 2012, p. 279–324. doi:10.1007/978-1-4419-7991-9\_28.
- [11] Gerrard J, Kandlikar M. Is European end-of-life vehicle legislation living up to expectations? Assessing the impact of the ELV Directive on “green” innovation and vehicle recovery. *Journal of Cleaner Production* 2007;15:17–27. doi:10.1016/j.jclepro.2005.06.004.
- [12] Akampumuza O, Wambua PM, Ahmed A, Li W, Qin XH. Review of the applications of biocomposites in the automotive industry. *Polymer Composites* 2017;38:2553–69. doi:10.1002/pc.23847.
- [13] Mohanty AK, Misra M, Drzal LT. Sustainable Bio-Composites from renewable resources: Opportunities and challenges in the green materials world. *Journal of Polymers and the Environment* 2002;10:19–26. doi:10.1023/A:1021013921916.
- [14] Labet M, Zakir Hossain KM, Ahmen I, Thielemans W. Biomass in Composite Materials. *Materials for a Sustainable Future*, 2012, p. 698–739.
- [15] Valsiliev V V., Morozov E V. *Mechanics and Analysis of Composite Materials*. First Edition. Elsevier Science; 2001.
- [16] Mallick PK. *Fiber-Reinforced Composites: Materials, Manufacturing, and Design*. Third Edit. CRC Press; 2007.
- [17] Chen P-Y, McKittrick J, Meyers MA. *Biological materials: Functional adaptations and*

- bioinspired designs. *Progress in Materials Science* 2012;57:1492–704. doi:10.1016/j.pmatsci.2012.03.001.
- [18] Autumn K, Gravish N. Gecko adhesion: evolutionary nanotechnology. *Philosophical Transactions Series A, Mathematical, Physical, and Engineering Sciences* 2008;366:1575–90. doi:10.1098/rsta.2007.2173.
- [19] Meyers MA, Chen P-Y, Lin AY-M, Seki Y. Biological materials: Structure and mechanical properties. *Progress in Materials Science* 2008;53:1–206. doi:10.1016/j.pmatsci.2007.05.002.
- [20] Wegst UGK, Bai H, Saiz E, Tomsia AP, Ritchie RO. Bioinspired structural materials. *Nature Materials* 2014;14:23–36. doi:10.1038/nmat4089.
- [21] Openstax. Muscle Tissue. *Anatomy & Physiology, OpenStax*; 2013, p. 405–30.
- [22] Studart AR, Erb RM. Bioinspired materials that self-shape through programmed microstructures. *Soft Matter* 2014;10:1284–94. doi:10.1039/C3SM51883C.
- [23] Sanchez C, Arribart H, Guille MMG. Biomimetism and bioinspiration as tools for the design of innovative materials and systems. *Nature Materials* 2005;4:277–88. doi:10.1038/nmat1339.
- [24] Burgert I, Fratzl P. Actuation systems in plants as prototypes for bioinspired devices. *Philosophical Transactions Series A, Mathematical, Physical, and Engineering Sciences* 2009;367:1541–57. doi:10.1098/rsta.2009.0003.
- [25] Le Duigou A, Requile S, Beaugrand J, Scarpa F, Castro M. Natural fibres actuators for smart bio-inspired hygromorph biocomposites. *Smart Materials and Structures* 2017;26. doi:10.1088/1361-665X/aa9410.
- [26] Dawson C, Vincent JF V., Rocca A-M. How pine cones open. *Nature (London)* 1997;390:668. doi:10.1038/37745.
- [27] Scorza LCT, Dornelas MC. Plants on the move: Towards common mechanisms governing mechanically-induced plant movements. *Plant Signaling & Behavior* 2011;6:1979–86. doi:10.4161/psb.6.12.18192.
- [28] Guo Q, Dai E, Han X, Xie S, Chao E, Chen Z. Fast nastic motion of plants and bio-inspired structures 2015. doi:10.1098/rsif.2015.0598.
- [29] Martone PT, Boiler M, Burgert I, Dumais J, Edwards J, MacH K, et al. Mechanics without Muscle: Biomechanical inspiration from the plant world. *Integrative and Comparative Biology* 2010;50:888–907. doi:10.1093/icb/icq122.
- [30] Kim S, Laschi C, Trimmer B. Soft robotics: A bioinspired evolution in robotics. *Trends in Biotechnology* 2013;31:287–94. doi:10.1016/j.tibtech.2013.03.002.
- [31] Schmitt S, Haeufle DFB, Blickhan R, Günther M. Nature as an engineer: one simple concept of a bio-inspired functional artificial muscle. *Bioinspiration & Biomimetics* 2012;7:036022. doi:10.1088/1748-3182/7/3/036022.
- [32] Capadona JR, Shanmuganathan K, Tyler DJ, Rowan SJ, Weder C. Stimuli-Responsive Polymer Nanocomposites Inspired by the Sea Cucumber Dermis. *Science* 2008;319:1370–4. doi:10.1126/science.1153307.
- [33] Guo Q, Dai E, Han X, Xie S, Chao E, Chen Z. Fast nastic motion of plants and bio-inspired structures 2015. doi:10.1098/rsif.2015.0598.

- [34] Azizi Samir MAS, Alloin F, Dufresne A. Review of Recent Research into Cellulosic Whiskers, Their Properties and Their Application in Nanocomposite Field. *Biomacromolecules* 2005;6:612–26. doi:10.1021/bm0493685.
- [35] Malmström E, Carlmark A. Controlled grafting of cellulose fibres – an outlook beyond paper and cardboard. *Polymer Chemistry* 2012;3:1702. doi:10.1039/c1py00445j.
- [36] Kang H, Liu R, Huang Y. Cellulose-Based Gels. *Macromolecular Chemistry and Physics* 2016;1–13. doi:10.1002/macp.201500493.
- [37] Zhang K, Geissler A, Standhardt M, Mehlhase S, Gallei M, Chen L, et al. Moisture-responsive films of cellulose stearyl esters showing reversible shape transitions. *Scientific Reports* 2015;5:11011. doi:10.1038/srep11011.
- [38] Habibi Y, Lucia LA, Rojas OJ. Cellulose nanocrystals: Chemistry, self-assembly, and applications. *Chemical Reviews* 2010;110:3479–500. doi:10.1021/cr900339w.
- [39] Rose M, Palkovits R. Cellulose-based sustainable polymers: State of the art and future trends. *Macromolecular Rapid Communications* 2011;32:1299–311. doi:10.1002/marc.201100230.
- [40] Shokri J, Adibkia K. Application of Cellulose and Cellulose Derivatives in Pharmaceutical Industries. *Cellulose – Medical, Pharmaceutical and Electronic Applications* 2013:47–66. doi:45635.
- [41] Courtenay JC, Sharma RI, Scott JL. Recent advances in modified cellulose for tissue culture applications. *Molecules* 2018;23. doi:10.3390/molecules23030654.
- [42] Yamabe T, Fujinami K, Nakajima T. Experience with building sentient materials using various sensors. *Proceedings of the 24th International Conference on Distributed Computing Systems* 2004:445–50. doi:10.1109/ICDCSW.2004.1284070.
- [43] Schaudel B, Guermeur C, Sanchez C, Nakatani K, Delaire JA. Spirooxazine- and spiropyran-doped hybrid organic–inorganic matrices with very fast photochromic responses. *Journal of Materials Chemistry* 1997;7:61–5. doi:10.1039/a606859f.
- [44] Lampert CM. Chromogenic smart materials. *Materials Today* 2004;7:28–35. doi:10.1016/S1369-7021(04)00123-3.
- [45] Tzou HS, Lee HJ, Arnold SM. Smart materials, precision sensors/actuators, smart structures, and structronic systems. *Mechanics of Advanced Materials and Structures* 2004;11:367–93. doi:10.1080/15376490490451552.
- [46] Diane T. Smart Materials. *Institute of Materials, Minerals and Mining Schools Affiliate Scheme* 2003;10:129–43.
- [47] Stoeckel D. Nitinol medical devices and implants. *Minimally Invasive Therapy and Allied Technologies* 2000;9:81–8. doi:10.3109/13645700009063054.
- [48] Baughman RH. Materials science. Playing nature’s game with artificial muscles. *Science (New York, NY)* 2005;308:63–5. doi:10.1126/science.1099010.
- [49] Zhou J, Sheiko SS. Reversible shape-shifting in polymeric materials. *Journal of Polymer Science, Part B: Polymer Physics* 2016;54:1365–80. doi:10.1002/polb.24014.
- [50] Leng JS. Multi-Functional Soft Smart Materials and their Applications. *Advanced Materials Research* 2011;410:25–25. doi:10.4028/www.scientific.net/AMR.410.25.
- [51] Tolley MT, Felton SM, Miyashita S, Aukes D, Rus D, Wood RJ. Self-folding origami:

- shape memory composites activated by uniform heating. *Smart Materials and Structures* 2014;23:094006. doi:10.1088/0964-1726/23/9/094006.
- [52] Yu Y, Nakano M, Ikeda T. Directed bending of a polymer film by light. *Nature* 2003;425:145. doi:10.1038/425145a.
- [53] Ware TH, McConney ME, Wie JJ, Tondiglia VP, White TJ. Voxelated liquid crystal elastomers. *Science* 2015;347:982–4. doi:10.1126/science.1261019.
- [54] Yoshida R, Okano T. Stimuli-Responsive Hydrogels and Their Application to Functional Materials. In: Ottenbrite RM, Park K, Okano T, editors. *Biomedical Applications of Hydrogels Handbook*, New York, NY: Springer New York; 2010, p. 19–44. doi:10.1007/978-1-4419-5919-5.
- [55] Wichterle O, Lím D. Hydrophilic Gels for Biological Use. *Nature* 1960;185:117–8. doi:10.1038/185117a0.
- [56] Ullah F, Othman MBH, Javed F, Ahmad Z, Akil HM. Classification, processing and application of hydrogels: A review. *Materials Science and Engineering C* 2015;57:414–33. doi:10.1016/j.msec.2015.07.053.
- [57] Ahmed EM. Hydrogel: Preparation, characterization, and applications: A review. *Journal of Advanced Research* 2015;6:105–21. doi:10.1016/j.jare.2013.07.006.
- [58] Sannino A, Demitri C, Madaghiele M. Biodegradable cellulose-based hydrogels: Design and applications. *Materials* 2009;2:353–73. doi:10.3390/ma2020353.
- [59] Chang C, Zhang L. Cellulose-based hydrogels: Present status and application prospects. *Carbohydrate Polymers* 2011;84:40–53. doi:10.1016/j.carbpol.2010.12.023.
- [60] Omidian H, Park K. Hydrogels. In: Siepmann J, Siegel R, Rathbone M, editors. *Fundamentals and Applications of Controlled Release Drug Delivery*, Springer, Boston, MA; 2012, p. 75–105. doi:10.1007/978-1-4614-0881-9.
- [61] Pérez S, Samain D. *Structure and Engineering of Celluloses*. vol. 64. 2010. doi:10.1016/S0065-2318(10)64003-6.
- [62] Cash MJ, Caputo SJ. Food Stabilizers, Thickeners and Gelling Agents. In: Imeson A, editor. *Food Stabilizers, Thickeners and Gelling Agents*, Wiley-Blackwell; 2010, p. 95–115.
- [63] Osada Y, Matsuda A. Shape memory in hydrogels. *Nature* 1995;376:219. doi:10.1038/376219a0.
- [64] Noda Y, Hayashi Y, Ito K. From topological gels to slide-ring materials. *Journal of Applied Polymer Science* 2014;131:1–9. doi:10.1002/app.40509.
- [65] Stoychev G, Guiducci L, Turcaud S, Dunlop JWC, Ionov L. Hole-Programmed Superfast Multistep Folding of Hydrogel Bilayers. *Advanced Functional Materials* 2016;26:7733–9. doi:10.1002/adfm.201602394.
- [66] Dicker MPM, Rossiter JM, Bond IP, Weaver PM. Biomimetic photo-actuation: sensing, control and actuation in sun-tracking plants. *Bioinspiration & Biomimetics* 2014;9:036015. doi:10.1088/1748-3182/9/3/036015.
- [67] Palleau E, Morales D, Dickey MD, Velez OD. Reversible patterning and actuation of hydrogels by electrically assisted ionoprinting. *Nature Communications* 2013;4:2257.

- doi:10.1038/ncomms3257.
- [68] Wu ZL, Moshe M, Greener J, Therien-Aubin H, Nie Z, Sharon E, et al. Three-dimensional shape transformations of hydrogel sheets induced by small-scale modulation of internal stresses. *Nature Communications* 2013;4:1586. doi:10.1038/ncomms2549.
- [69] Haraguchi K, Takehisa T. Nanocomposite hydrogels: A unique organic-inorganic network structure with extraordinary mechanical, optical, and swelling/De-swelling properties. *Advanced Materials* 2002;14:1120–4. doi:10.1002/1521-4095(20020816)14:16<1120::AID-ADMA1120>3.0.CO;2-9.
- [70] Okay O. General Properties of Hydrogels. In: Gerlach G, Arndt K-F, editors. *Hydrogel Sensors and Actuators: Engineering and Technology*, Berlin, Heidelberg: Springer Berlin Heidelberg; 2010, p. 1–14. doi:10.1007/978-3-540-75645-3\_1.
- [71] Bao Y, Ma J, Li N. Synthesis and swelling behaviors of sodium carboxymethyl cellulose-g-poly(AA-co-AM-co-AMPS)/MMT superabsorbent hydrogel. *Carbohydrate Polymers* 2011;84:76–82. doi:10.1016/j.carbpol.2010.10.061.
- [72] Ma J, Xu Y, Fan B, Liang B. Preparation and characterization of sodium carboxymethylcellulose/poly(N-isopropylacrylamide)/clay semi-IPN nanocomposite hydrogels. *European Polymer Journal* 2007;43:2221–8. doi:10.1016/j.eurpolymj.2007.02.026.
- [73] Kokabi M, Sirousazar M, Hassan ZM. PVA-clay nanocomposite hydrogels for wound dressing. *European Polymer Journal* 2007;43:773–81. doi:10.1016/j.eurpolymj.2006.11.030.
- [74] Abe K, Yano H. Cellulose nanofiber-based hydrogels with high mechanical strength. *Cellulose* 2012;19:1907–12. doi:10.1007/s10570-012-9784-3.
- [75] Spoljaric S, Salminen A, Luong ND, Seppälä J. Crosslinked nanofibrillated cellulose: poly(acrylic acid) nanocomposite films; enhanced mechanical performance in aqueous environments. *Cellulose* 2013;20:2991–3005. doi:10.1007/s10570-013-0061-x.
- [76] Spoljaric S, Salminen A, Luong ND, Seppälä J. Stable, self-healing hydrogels from nanofibrillated cellulose, poly(vinyl alcohol) and borax via reversible crosslinking. *European Polymer Journal* 2014;56:105–17. doi:10.1016/j.eurpolymj.2014.03.009.
- [77] Han N, Johnson J, Lannutti JJ, Winter JO. Hydrogel-electrospun fiber composite materials for hydrophilic protein release. *Journal of Controlled Release* 2012;158:165–70. doi:10.1016/j.jconrel.2011.09.094.
- [78] Schuurman W, Khristov V, Pot MW, Van Weeren PR, Dhert WJA, Malda J. Bioprinting of hybrid tissue constructs with tailorable mechanical properties. *Biofabrication* 2011;3. doi:10.1088/1758-5082/3/2/021001.
- [79] Etches JA, Bond IP. Development of a self-actuating fibre reinforced ionic epoxy gel polymer composite. *Smart Materials and Structures* 2011;20:045020. doi:10.1088/0964-1726/20/4/045020.
- [80] Leeuwenburgh SCG, Jansen JA, Mikos AG, Leeuwenburgh SCG, Jansen JA, Mikos AG. Functionalization of oligo ( poly ( ethylene glycol ) fumarate ) hydrogels with finely dispersed calcium phosphate nanocrystals for bone- substituting purposes 2012;5063.

- [81] Diba M, An J, Schmidt S, Hembury M, Ossipov D, Boccaccini AR, et al. Exploiting Bisphosphonate – Bioactive-Glass Interactions for the Development of Self- Healing and Bioactive Composite Hydrogels 2016;1–8. doi:10.1002/marc.201600353.
- [82] Fujishiro Y, Hench LL, Oonishi H. Quantitative rates of in vivo bone generation for Bioglass?? and hydroxyapatite particles as bone graft substitute. *Journal of Materials Science: Materials in Medicine* 1997;8:649–52. doi:10.1023/A:1018527621356.
- [83] Nejadnik MR, Yang X, Bongio M, Alghamdi HS, Van den Beucken JJJP, Huysmans MC, et al. Self-healing hybrid nanocomposites consisting of bisphosphonated hyaluronan and calcium phosphate nanoparticles. *Biomaterials* 2014;35:6918–29. doi:10.1016/j.biomaterials.2014.05.003.
- [84] Zhang X, Pint CL, Lee MH, Schubert BE, Jamshidi A, Takei K, et al. Optically- and thermally-responsive programmable materials based on carbon nanotube-hydrogel polymer composites. *Nano Letters* 2011;11:3239–44. doi:10.1021/nl201503e.
- [85] Lewis JA. Direct ink writing of 3D functional materials. *Advanced Functional Materials* 2006;16:2193–204. doi:10.1002/adfm.200600434.
- [86] Jones R, Haufe P, Sells E, Iravani P, Olliver V, Palmer C, et al. Reprap - The replicating rapid prototyper. *Robotica* 2011;29:177–91. doi:10.1017/S026357471000069X.
- [87] Bruijn E De. On the viability of the Open Source Development model for the design of physical objec. *Lessons Learned from the RepRap Project* 2010. doi:10.1002/cbdv.200490137/abstract\nhttp://scholar.google.com/scholar?hl=en.
- [88] Pei E. 4D Printing: dawn of an emerging technology cycle. *Assembly Automation* 2014;34:310–4. doi:10.1108/AA-07-2014-062.
- [89] Tibbits S. 4D printing: Multi-material shape change. *Architectural Design* 2014;84:116–21. doi:10.1002/ad.1710.
- [90] Bakarich SE, Gorkin R, Panhuis M In Het, Spinks GM. 4D printing with mechanically robust, thermally actuating hydrogels. *Macromolecular Rapid Communications* 2015;36:1211–7. doi:10.1002/marc.201500079.
- [91] Wei H, Zhang Q, Yao Y, Liu L, Liu Y, Leng J. Direct-write fabrication of 4D active shape-changing structures based on a shape memory polymer and its nanocomposite. *ACS Applied Materials and Interfaces* 2017;9:876–83. doi:10.1021/acsami.6b12824.
- [92] Momeni F, M.Mehdi Hassani.N S, Liu X, Ni J. A review of 4D printing. *Materials and Design* 2017;122:42–79. doi:10.1016/j.matdes.2017.02.068.
- [93] Sydney Gladman A, Matsumoto EA, Nuzzo RG, Mahadevan L, Lewis JA. Biomimetic 4D printing. *Nature Materials* 2016;1–7. doi:10.1038/nmat4544.
- [94] Raviv D, Zhao W, McKnelly C, Papadopoulou A, Kadambi A, Shi B, et al. Active printed materials for complex self-evolving deformations. *Scientific Reports* 2014;4:1–8. doi:10.1038/srep07422.
- [95] Haberland C, Elahinia M, Walker JM, Meier H, Frenzel J. On the development of high quality NiTi shape memory and pseudoelastic parts by additive manufacturing. *Smart Materials and Structures* 2014;23. doi:10.1088/0964-1726/23/10/104002.
- [96] Walker JM, Haberland C, Taheri Andani M, Karaca HE, Dean D, Elahinia M. Process development and characterization of additively manufactured nickel-titanium shape memory parts. *Journal of Intelligent Material Systems and Structures* 2016;27:2653–

60. doi:10.1177/1045389X16635848.
- [97] Meisel NA, Elliott AM, Williams CB. A procedure for creating actuated joints via embedding shape memory alloys in PolyJet 3D printing. *Journal of Intelligent Material Systems and Structures* 2015;26:1498–512. doi:10.1177/1045389X14544144.
- [98] Ge Q, Qi HJ, Dunn ML. Active materials by four-dimension printing. *Applied Physics Letters* 2013;103:131901. doi:10.1063/1.4819837.
- [99] Zarek M, Layani M, Cooperstein I, Sachyani E, Cohn D, Magdassi S. 3D Printing of Shape Memory Polymers for Flexible Electronic Devices. *Advanced Materials* 2016;28:4449–54. doi:10.1002/adma.201503132.
- [100] Yang Y, Chen Y, Wei Y, Li Y. 3D printing of shape memory polymer for functional part fabrication. *International Journal of Advanced Manufacturing Technology* 2016;84:2079–95. doi:10.1007/s00170-015-7843-2.
- [101] Mao Y, Yu K, Isakov MS, Wu J, Dunn ML, Jerry Qi H. Sequential Self-Folding Structures by 3D Printed Digital Shape Memory Polymers. *Scientific Reports* 2015;5:13616. doi:10.1038/srep13616.
- [102] Ge Q, Sakhaei AH, Lee H, Dunn CK, Fang NX, Dunn ML. Multimaterial 4D Printing with Tailorable Shape Memory Polymers. *Scientific Reports* 2016;6:1–11. doi:10.1038/srep31110.
- [103] Zhao Z, Peng F, Cavicchi KA, Cakmak M, Weiss RA, Vogt BD. Three-Dimensional Printed Shape Memory Objects Based on an Olefin Ionomer of Zinc-Neutralized Poly(ethylene-co-methacrylic acid). *ACS Applied Materials and Interfaces* 2017;9:27239–49. doi:10.1021/acsami.7b07816.
- [104] Zhang Q, Zhang K, Hu G. Smart three-dimensional lightweight structure triggered from a thin composite sheet via 3D printing technique. *Scientific Reports* 2016;6:1–8. doi:10.1038/srep22431.
- [105] Mironov V, Trusk T, Kasyanov V, Little S, Swaja R, Markwald R. Biofabrication: A 21st century manufacturing paradigm. *Biofabrication* 2009;1. doi:10.1088/1758-5082/1/2/022001.
- [106] Arslan-yildiz A, Assal R El, Chen P, Guven S, Inci F, Demirci U. Towards artificial tissue models : past , present , and future of 3D bioprinting Towards arti fi cial tissue models : past , present , and future of 3D bioprinting 2016.
- [107] Mironov V, Boland T, Trusk T, Forgacs G, Markwald RR. Organ printing: Computer-aided jet-based 3D tissue engineering. *Trends in Biotechnology* 2003;21:157–61. doi:10.1016/S0167-7799(03)00033-7.
- [108] Kokkinis D, Schaffner M, Studart AR. Multimaterial magnetically assisted 3D printing of composite materials. *Nature Communications* 2015;6. doi:10.1038/ncomms9643.
- [109] COLORFABB. Product Datasheet. SPECIAL WOODFILL 2017. [https://www.goprint3d.co.uk/colorfabb-woodfill.html?keyword=&gclid=EA1aIQobChMIml68z7CQ1QIVZSJtCh2nOAK2EAQYAIA BEglz9fD\\_BwE](https://www.goprint3d.co.uk/colorfabb-woodfill.html?keyword=&gclid=EA1aIQobChMIml68z7CQ1QIVZSJtCh2nOAK2EAQYAIA BEglz9fD_BwE) (accessed March 5, 2017).
- [110] RSPRO. Product Datasheet. WOOD 2017. <http://docs-europe.electrocomponents.com/webdocs/157c/0900766b8157cfcb.pdf> (accessed March 1, 2017).

- [111] Correa D, Papadopoulou A, Guberan C, Jhaveri N, Reichert S, Menges A, et al. 3D-Printed Wood: Programming Hygroscopic Material Transformations. *3D Printing and Additive Manufacturing* 2015;2:106–16. doi:10.1089/3dp.2015.0022.
- [112] Markstedt K, Sundberg J, Gatenholm P. 3D Bioprinting of Cellulose Structures from an Ionic Liquid. *3d Printing and Additive Manufacturing* 2014;1:115–21. doi:10.1089/3dp.2014.0004.
- [113] Håkansson KMO, Henriksson IC, de la Peña Vázquez C, Kuzmenko V, Markstedt K, Enoksson P, et al. Solidification of 3D Printed Nanofibril Hydrogels into Functional 3D Cellulose Structures. *Advanced Materials Technologies* 2016;1:1600096--n/a. doi:10.1002/admt.201600096.
- [114] Kärki P, Orelma H, Klar V. 3D-printing of cellulose-based materials – CellulosefromFinland.fi 2016. <http://cellulosefromfinland.fi/3d-printing-of-cellulose-based-materials/> (accessed March 1, 2017).
- [115] Reyssat E, Mahadevan L. Hygromorphs: from pine cones to biomimetic bilayers. *Journal of the Royal Society, Interface / the Royal Society* 2009;6:951–7. doi:10.1098/rsif.2009.0184.
- [116] Bruijn E De. On the viability of the Open Source Development model for the design of physical objec. *Lessons Learned from the RepRap Project* 2010. doi:10.1002/cbdv.200490137/abstract\nhttp://scholar.google.com/scholar?hl=en.
- [117] Mulakkal MC, Seddon AM, Whittell G, Manners I, Trask RS. 4D fibrous materials: characterising the deployment of paper architectures. *Smart Materials and Structures* 2016;25:095052. doi:10.1088/0964-1726/25/9/095052.
- [118] Kishimoto N, Natori M, Higuchi K, Ukegawa K. New deployable membrane structure models inspired by morphological changes in nature. *American Institute of Aeronautics and Astronautics* 2006:1–10. doi:10.2514/6.2006-1898.
- [119] Saito K, Yamamoto S, Maruyama M, Okabe Y. Asymmetric hindwing foldings in rove beetles. *Proceedings of the National Academy of Sciences* 2014;111:16349–52. doi:10.1073/pnas.1409468111.
- [120] Lang R, Hull T. *Origami design secrets: mathematical methods for an ancient art*. Springer 2002;27:92–5. doi:10.1007/BF02985811.
- [121] Agbenyega J. Nanostructured origami. *Materials Today* 2009;12:12. doi:10.1016/S1369-7021(09)70106-3.
- [122] Kuribayashi K, Tsuchiya K, You Z, Tomus D, Umemoto M, Ito T, et al. Self-deployable origami stent grafts as a biomedical application of Ni-rich TiNi shape memory alloy foil. *Materials Science and Engineering: A* 2006;419:131–7. doi:http://dx.doi.org/10.1016/j.msea.2005.12.016.
- [123] Harrison FA, Craig WW, Christensen FE, Hailey CJ, Zhang WW, Boggs SE, et al. The Nuclear Spectroscopic Telescope Array (NuSTAR) High-energy X-Ray Mission. *\apj* 2013;770:103. doi:10.1088/0004-637X/770/2/103.
- [124] Liu Y, Boyles JK, Genzer J, Dickey MD. Self-folding of polymer sheets using local light absorption. *Soft Matter* 2012;8:1764. doi:10.1039/c1sm06564e.
- [125] Ge Q, Dunn CK, Qi HJ, Dunn ML. Active origami by 4D printing. *Smart Materials and Structures* 2014;23:1–15. doi:10.1088/0964-1726/23/9/094007.



- [126] Ionov L. Soft microorigami: self-folding polymer films. *Soft Matter* 2011;7:6786. doi:10.1039/c1sm05476g.
- [127] Zhao Q, Dunlop JWC, Qiu X, Huang F, Zhang Z, Heyda J, et al. An instant multi-responsive porous polymer actuator driven by solvent molecule sorption. *Nature Communications* 2014;5:4293. doi:10.1038/ncomms5293.
- [128] Daynes S, Trask RS, Weaver PM. Bio-inspired structural bistability employing elastomeric origami for morphing applications. *Smart Materials and Structures* 2014;23:125011. doi:10.1088/0964-1726/23/12/125011.
- [129] Timoshenko S. Analysis of Bi-Metal Thermostats. *J Opt Soc Am* 1925;11:233–55. doi:10.1364/JOSA.11.000233.
- [130] Alben S. Bending of bilayers with general initial shapes. *Advances in Computational Mathematics* 2014;1110.1007v1. doi:10.1007/s10444-014-9347-2.
- [131] Reichert S, Menges A, Correa D. Meteorosensitive architecture: Biomimetic building skins based on materially embedded and hygroscopically enabled responsiveness. *Computer-Aided Design* 2015;60:50–69. doi:10.1016/j.cad.2014.02.010.
- [132] Cliquet E. Flotilla 2011. <http://ordigami.net/flotilla.php> (accessed August 24, 2015).
- [133] Burgert I, Fratzl P. Actuation systems in plants as prototypes for bioinspired devices. *Philosophical Transactions of the Royal Society A: Mathematical, Physical and Engineering Sciences* 2009;367:1541–57. doi:10.1098/rsta.2009.0003.
- [134] Gronfors J. Use of fillers in paper and paperboard grades. Tampere University of Applied Sciences, 2010.
- [135] Mulakkal MC. Understanding the deployment of Origami architectures for developing Smart materials with Programmable Transformations, 2014, University of Bristol (internal unpublished document).
- [136] Engineering Toolbox. Absolute, Dynamic and Kinematic Viscosity 2003. [https://www.engineeringtoolbox.com/dynamic-absolute-kinematic-viscosity-d\\_412.html](https://www.engineeringtoolbox.com/dynamic-absolute-kinematic-viscosity-d_412.html) (accessed July 12, 2016).
- [137] MacGregor MA. Some impacts of paper making on paper structure. *Paper Technology* 2001;42:30–44.
- [138] Wellisch E, Hagan L, Marker L, Sweeting OJ. Interaction of cellulose with small molecules. Glycerol and ethylene carbonate. *Journal of Applied Polymer Science* 1960;3:331–7. doi:10.1002/app.1960.070030910.
- [139] Minor JL. Hornification -Its origin and meaning. *Progress in Paper Recycling*, vol. 3, 1994, p. 93–5. doi:10.1017/CBO9781107415324.004.
- [140] Fernandes Diniz JMB, Gil MH, Castro J a M. Hornification - Its origin and interpretation in wood pulps. *Wood Science and Technology* 2004;37:489–94. doi:10.1007/s00226-003-0216-2.
- [141] Hubbe M a., Venditti R a., Rojas OJ. What happens to cellulosic fibers during papermaking and recycling? A review. *BioResources* 2007;2:739–88. doi:10.15376/biores.2.4.739-788.
- [142] Brancato AA. Effect of Progressive Recycling on Cellulose Fiber Surface Properties. Institute of Paper Science and Technology 2008.

- [143] Šutý Š, Petriláková K, Katuščák S, Kirschnerová S, Jablonský M, Vizárová K, et al. Change in the Capability of Cellulose Fibres To Retain Water During Thermally Accelerated Ageing of Paper. *Cellulose Chemistry and Technology* 2012;46:631–5.
- [144] Songok J, Salminen P, Toivakka M. Temperature effects on dynamic water absorption into paper. *Journal of Colloid and Interface Science* 2014;418:373–7. doi:10.1016/j.jcis.2013.12.017.
- [145] Rosenholm JB. Wetting of Surfaces and Interfaces: A Conceptual Equilibrium Thermodynamic Approach. *Colloid Stability: The Role of Surface Forces - Part II*, vol. 2, Wiley-VCH Verlag GmbH & Co. KGaA; 2011, p. 1–83. doi:10.1002/9783527631094.ch1.
- [146] Reyssat E, Mahadevan L. How wet paper curls. *EPL (Europhysics Letters)* 2011;93:54001. doi:10.1209/0295-5075/93/54001.
- [147] Hu Z, Cai T, Chi C. Thermoresponsive oligo(ethylene glycol)-methacrylate- based polymers and microgels. *Soft Matter* 2010;6:2115. doi:10.1039/b921150k.
- [148] Lindqvist J, Nyström D, Östmark E, Antoni P, Carlmark A, Johansson M, et al. Intelligent Dual-responsive cellulose surfaces via surface-initiated ATRP. *Biomacromolecules* 2008;9:2139–45. doi:10.1021/bm800193n.
- [149] Gao G, Dallmeyer JI, Kadla JF. Synthesis of lignin nanofibers with ionic-responsive shells: Water-expandable lignin-based nanofibrous mats. *Biomacromolecules* 2012;13:3602–10. doi:10.1021/bm301039f.
- [150] Seery M. Saving paper. *Education in Chemistry* 2013:22–5.
- [151] Zhou C, Wu Q. Recent development in applications of cellulose nanocrystals for advanced polymer-based nanocomposites by novel fabrication strategies. *Nanocrystals – Synthesis, Characterization and Applications properties.*, Rijeka, Croatia: Intech; 2012, p. 103–20. doi:10.5772/46512.
- [152] Sun L, Huang WM, Ding Z, Zhao Y, Wang CC, Purnawali H, et al. Stimulus-responsive shape memory materials: A review. *Materials and Design* 2012;33:577–640. doi:10.1016/j.matdes.2011.04.065.
- [153] Moored KW, Bart-Smith H. The Analysis of Tensegrity Structures for the Design of a Morphing Wing. *Journal of Applied Mechanics* 2007;74:668. doi:10.1115/1.2424718.
- [154] Tibbits S, Cheung K. Programmable materials for architectural assembly and automation. *Assembly Automation* 2012;32:216–25. doi:10.1108/01445151211244348.
- [155] Haghpanah B, Salari-Sharif L, Pourrajab P, Hopkins J, Valdevit L. Architected Materials: Multistable Shape-Reconfigurable Architected Materials (*Adv. Mater.* 36/2016). *Advanced Materials* 2016;28:8065. doi:10.1002/adma.201670255.
- [156] Felton S, Tolley M, Demaine E, Rus D, Wood R. A method for building self-folding machines. *Science* 2014;345:644–6. doi:10.1126/science.1252610.
- [157] Abbott AC, Buskohl PR, Joo JJ, Reich GW, Vaia RA. Characterization of Creases in Polymers for Adaptive Origami. *Proceedings of the ASME 2014 Conference on Smart Materials, Adaptive Structures and Intelligent Systems (SMASIS2014)* 2014:1–7.
- [158] Lauff C, Simpson TW, Frecker M, Ounaies Z, Ahmed S, von Lockette P, et al. Differentiating Bending From Folding in Origami Engineering Using Active Materials.

- Volume 5B: 38th Mechanisms and Robotics Conference 2014:V05BT08A040.  
doi:10.1115/DETC2014-34702.
- [159] Stoychev G, Pureskiy N, Ionov L. Self-folding all-polymer thermoresponsive microcapsules. *Soft Matter* 2011;7:3277. doi:10.1039/c1sm05109a.
- [160] Efimovskaya A, Senkal D, Askari S, Shkel AM. Origami-like Folded MEMS for Realization of TIMU : Fabrication Technology and Initial Demonstration 2015:3–6.
- [161] Neville RM, Chen J, Guo X, Zhang F, Wang W, Dobah Y, et al. A Kirigami shape memory polymer honeycomb concept for deployment. *Smart Materials and Structures* 2017;26. doi:10.1088/1361-665X/aa6b6d.
- [162] Jeong K-U, Jang J-H, Kim D-Y, Nah C, Lee JH, Lee M-H, et al. Three-dimensional actuators transformed from the programmed two-dimensional structures via bending, twisting and folding mechanisms. *Journal of Materials Chemistry* 2011;21:6824. doi:10.1039/c0jm03631e.
- [163] Gallagher S, Florea L, Fraser KJ, Diamond D. Swelling and shrinking properties of thermo-responsive polymeric ionic liquid hydrogels with embedded linear pNIPAAm. *International Journal of Molecular Sciences* 2014;15:5337–49. doi:10.3390/ijms15045337.
- [164] Baker AB, Wass DF, Trask RS. Thermally induced reversible and reprogrammable actuation of tough hydrogels utilising ionoprinting and iron coordination chemistry. *Sensors and Actuators, B: Chemical* 2018;254:519–25. doi:10.1016/j.snb.2017.07.095.
- [165] Garvin KA, VanderBurgh J, Hocking DC, Dalecki D. Controlling collagen fiber microstructure in three-dimensional hydrogels using ultrasound. *The Journal of the Acoustical Society of America* 2013;134:1491–502. doi:10.1121/1.4812868.
- [166] Wu ZL, Moshe M, Greener J, Therien-Aubin H, Nie Z, Sharon E, et al. Three-dimensional shape transformations of hydrogel sheets induced by small-scale modulation of internal stresses. *Nature Communications* 2013;4:1586. doi:10.1038/ncomms2549.
- [167] Baker AB, Wass DF, Trask RS. Thermally induced reversible and reprogrammable actuation of tough hydrogels utilising ionoprinting and iron coordination chemistry. *Sensors and Actuators, B: Chemical* 2018;254:519–25. doi:10.1016/j.snb.2017.07.095.
- [168] Steele CR, Balch CD. Introduction to the Theory of Plates Stretching and Bending of Plates - Fundamentals. *Stanford University Notes* 2009. 1–41. doi:2012938665.
- [169] Weiss P, Fatimi A, Guicheux J, Vinatier C. Biomedical Applications of Hydrogels Handbook. *Business* 2010;c:247–68. doi:10.1007/978-1-4419-5919-5.
- [170] Dias MA, Dudte LH, Mahadevan L, Santangelo CD. Geometric Mechanics of Curved Crease Origami. *Physical Review Letters* 2012;109:114301. doi:10.1103/PhysRevLett.109.114301.
- [171] Wiener J, Kovačič V, Dejlóvá P. Differences between flax and hemp. *Autex Research Journal* 2003;3:58–63.
- [172] Sczostak A. Cotton linters: An alternative cellulosic raw material. *Macromolecular Symposia* 2009;280:45–53. doi:10.1002/masy.200950606.

- [173] Thomsen AB, Rasmussen S, Bohn V, Nielsen KV, Thygesen A. Hemp raw materials : The effect of cultivar , growth conditions and pretreatment on the chemical composition of the fibres. vol. 1507. 2005.
- [174] Markstedt K, Mantas A, Tournier I, Martínez Ávila H, Hägg D, Gatenholm P. 3D bioprinting human chondrocytes with nanocellulose-alginate bioink for cartilage tissue engineering applications. *Biomacromolecules* 2015;16:1489–96. doi:10.1021/acs.biomac.5b00188.
- [175] Buwalda SJ, Boere KWM, Dijkstra PJ, Feijen J, Vermonden T, Hennink WE. Hydrogels in a historical perspective: From simple networks to smart materials. *Journal of Controlled Release* 2014;190:254–73. doi:https://doi.org/10.1016/j.jconrel.2014.03.052.
- [176] Menard KP. *Dynamic mechanical analysis: a practical introduction*. CRC-Press; 1999.
- [177] White WA, Pichler E. Water-sorption characteristics of clay minerals. *Illinois State Geological Survey* 1959;266:20 p.
- [178] Borůvková K, Wiener J, Kukreja S. Thermal Self Cross-Linking of Carboxymethylcellulose. *Academic Coordination Centre (ACC) Journal* 2012;XVIII:6–13.
- [179] Cook JP, Goodall GW, Khutoryanskaya O V., Khutoryanskiy V V. Microwave-assisted hydrogel synthesis: A new method for crosslinking polymers in aqueous solutions. *Macromolecular Rapid Communications* 2012;33:332–6. doi:10.1002/marc.201100742.
- [180] Demitri C, Del Sole R, Scalera F, Sannino A, Vasapollo G, Maffezzoli A, et al. Novel superabsorbent cellulose-based hydrogels crosslinked with citric acid. *Journal of Applied Polymer Science* 2008;110:2453–60. doi:10.1002/app.28660.
- [181] Hashem M, Sharaf S, Abd El-Hady MM, Hebeish A. Synthesis and characterization of novel carboxymethylcellulose hydrogels and carboxymethylcellulose-hydrogel-ZnO-nanocomposites. *Carbohydrate Polymers* 2013;95:421–7. doi:10.1016/j.carbpol.2013.03.013.
- [182] Reddy N, Yang Y. Citric acid cross-linking of starch films. *Food Chemistry* 2010;118:702–11. doi:10.1016/j.foodchem.2009.05.050.
- [183] Raucci MG, Alvarez-Perez MA, Demitri C, Giugliano D, De Benedictis V, Sannino A, et al. Effect of citric acid crosslinking cellulose-based hydrogels on osteogenic differentiation. *Journal of Biomedical Materials Research - Part A* 2015;103:2045–56. doi:10.1002/jbm.a.35343.
- [184] Gorgieva S, Kokol V. Synthesis and application of new temperature-responsive hydrogels based on carboxymethyl and hydroxyethyl cellulose derivatives for the functional finishing of cotton knitwear. *Carbohydrate Polymers* 2011;85:664–73. doi:10.1016/j.carbpol.2011.03.037.
- [185] Zheng WJ, Gao J, Wei Z, Zhou J, Chen YM. Facile fabrication of self-healing carboxymethyl cellulose hydrogels. *European Polymer Journal* 2015;72:514–22. doi:10.1016/j.eurpolymj.2015.06.013.
- [186] Zuidema JM, Rivet CJ, Gilbert RJ, Morrison FA. A protocol for rheological characterization of hydrogels for tissue engineering strategies. *Journal of Biomedical Materials Research - Part B Applied Biomaterials* 2014;102:1063–73.

- doi:10.1002/jbm.b.33088.
- [187] Malvern. Evaluating the rheological properties of hyaluronic acid hydrogels for dermal filler applications 2016. <http://www.malvern.com/en/support/resource-center/application-notes/AN150112-prop-HA-hydrogels-Dermal-Filler.aspx>.
- [188] Chang C, Duan B, Cai J, Zhang L. Superabsorbent hydrogels based on cellulose for smart swelling and controllable delivery. *European Polymer Journal* 2010;46:92–100. doi:10.1016/j.eurpolymj.2009.04.033.
- [189] Illeperuma WRK, Sun J-Y, Suo Z, Vlassak JJ. Force and stroke of a hydrogel actuator. *Soft Matter* 2013;9:8504–11. doi:10.1039/c3sm51617b.
- [190] Horne R. The Universal Paste Extruder 2012. <https://richrap.blogspot.co.uk/2012/04/universal-paste-extruder-ceramic-food.html> (accessed December 22, 2017).
- [191] Lvinger O. Syringe Extruder 2015. <http://www.instructables.com/id/Syringe-Extruder/> (accessed December 22, 2017).
- [192] Raney JR, Lewis JA. Printing mesoscale architectures. *MRS Bulletin* 2015;40:943–50. doi:10.1557/mrs.2015.235.

---

## Appendix

---

### A.1. Optimisation of paste extruder and print settings to for 3D printing

The detailed steps undertaken to enable 3D printing of the developed hydrogel and hydrogel composite formulations are reported in this section. The following sections are aimed to complement and support the work reported in Chapter 5 (*5.2 Enabling additive layer manufacturing of cellulose*).

#### A.1.1. Introduction to stepper motors

Stepper motors are at the heart of enabling movement about the co-ordinate axis and extrusion in 3D printers. A stepper motor is a DC motor that rotates in discrete steps for each pulse of power it receives as the input from the stepper driver. These motors have multiple coils that are organised in 'phases'. Energising these phases in a sequence will produce a propagating magnetic field and rotate the motor (shaft) one step at a time thus providing accuracy in positioning as well as control over the speed. Figure A.1 shows the internal cross-section of a generic stepper motor. The selected NEMA 17 motor has 200 steps with a step angle of  $1.8^\circ$  and micro stepping (1/16) enabled through the driver resulting in fine incremental rotational movement of the shaft. A configurable parameter specific to the stepper motor is step count, which specifies the number of steps required to move 1 mm of the filament (for extruder steppers), or 1mm axial movement (for axis steppers) or in the case of paste extruder, to advance the lead screws by 1 mm. The torque and the rotational speed of the motor depends on the extend and rate of magnetisation in each of the phases which in turn is a function of the input current and number of coil windings at each phase. Since the latter is a design constant specific to each motor, the input current is the only variable that can be used to increase the magnetisation within the motor coils. However, the stepper motors produce low torque at high speeds owing to inductance. Inductance is the property of an electrical conductor by virtue of which it develops an electromotive force (EMF) in response to a change in current. In order to achieve higher speeds, the phases are required to be charged faster. This results in the coils not being fully charged *i.e.* not enough current pass through them to its full capacity before the current is switched over to the next phase to energise its coils. This phenomenon limits the torque output form the motor at higher speeds and hence the paste extruder is operated at comparatively slower speeds to the default settings for thermoplastic filament extruder. This enables extrusion of the material formulations developed in this project.

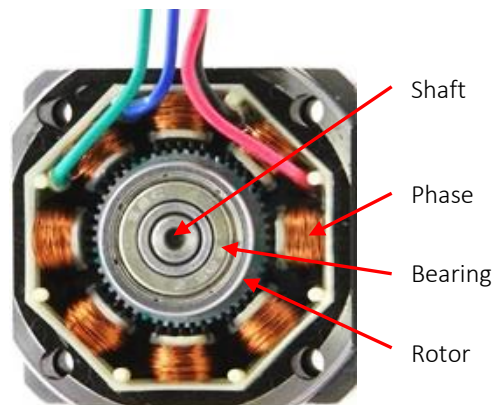


Figure A.1: Internal components of a generic stepper motor showing the phases and coil windings - Front view. (Image adapted from source: [www.pololu.com](http://www.pololu.com))

### A.1.2. Optimisation of print parameters

By default, the printer is tuned to extrude thermoplastics. In order to extrude cellulosic gels and hydrogel composites, certain parameters of the stepper motor driving the developed paste extruder were modified. The rotation of the motor shaft is converted to the linear actuation of the plunger tab through anti-backlash nut assembly on the threaded rod. The stepper motor drivers integrated into the RAMBO mini 1.3 PCB and are configured and controlled through G-code commands. The default setting to prevent cold extrusion for thermoplastic filaments was overridden through G-code command [M302]. The extruder steps were then re-configured through [M92 EXXX] command, where E specifies the extruder motor and XXX implies the step count. Step count of 40 was used for paste extruder with NEMA-17 motor and 4000 was used for the motor with internal gearing. These values were obtained through experimentation where the step count was adjusted in increments in conjunction with the motor current to enable smooth and continuous extrusion of the hydrogel and hydrogel composite. The difference in step count is indicative of the internal gearing. The motor current was adjusted through [M907 EXXX] where XXX denotes the motor current in milliamperes (mA). A motor current of 850 mA was used. The G-codes used are summarised in Table A.1

Table A.1: Summary of G-codes used and its function

No	G-code	Function
1	M302	Enable cold extrusion
2	M92	Adjust stepper motor steps
3	M907	Adjust stepper motor input current

The Matterslice control software permits intuitive modulation (within pre-configured limits) of stepper motor parameters during printing process by allowing user to adjust parameters such as speed and extruder rates from 0.5x-3x of the default values. Rest of the procedures involved in printing cellulosic material are similar to printing thermoplastics where a CAD model is imported and sliced to be 3D printed based on input parameters such as layer height, print-bed temperature and infill properties such as % fill, pattern and overlap.

## A.2. Raw data

The raw data used to derive the results presented in this report are available from the following location.

<https://drive.google.com/open?id=1G3d6GGi3b5SO3pNuwHWslvQR-Kved-Fl>